SCANNING®

The Journal of Scanning Microscopies

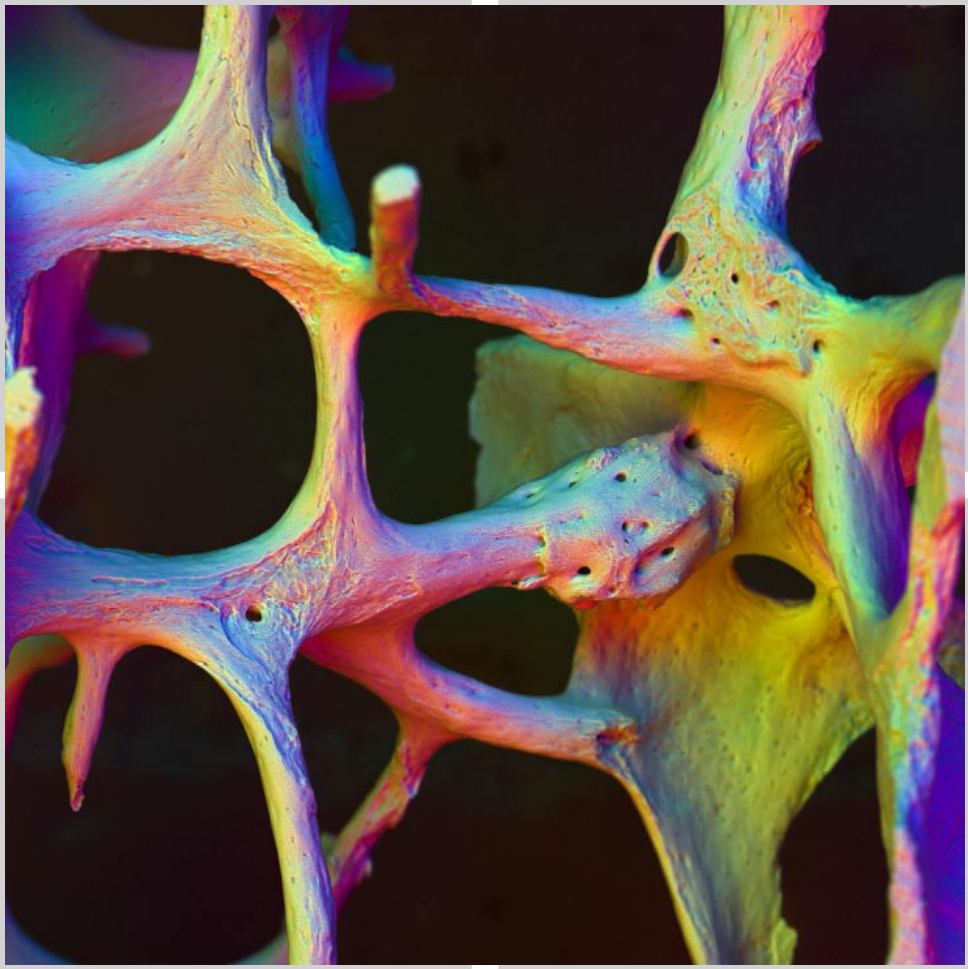

Vol. 23, 2 (2001)
March/April
FAMS, Inc., Mahwah, N.J., USA

Indexed in Current Contents®/Life Sciences, *Index Medicus,*
MEDLINE, and EMBASE/Excerpta Medica

SCANNING®

The Journal of Scanning Microscopies

ISSN 0161-0457

Contents Volume 23, Number 2, March–April (2001)

Proceedings of SCANNING 2001, New York, NY, USA

Robert P. Becker, Guest Editor

Platform Presentations

Cover micrograph: 2.8 mm thick vertical slice through body of fourth lumbar vertebra of 89 year female, after removal of soft tissue elements. This bone shows marked porosis but had not collapsed. 30 kV BSE image taken by Alan Boyde with Zeiss DSM962 SEM, using KE Developments Ltd 4-sector solid state BSE detector. Signal from sectors giving 'apparent illumination' from lower left used for red, from upper left for green and from upper right for blue signal components respectively. Note rods cut away by resorption (not surfaces cut during sample preparation), areas of unrepaired resorption and microcallus (a quick repair tissue phase).

Proceedings of SCANNING 2001

May 5–7, 2001
New York, New York, USA

Saturday, May 5

Electron backscattered diffraction (EBSD)

Electron backscattered diffraction constraints on processes in natural and synthetic rocks: developing technology for demanding materials and problems

D. PRIOR, G. SEWARD, J. WHEELER, DICK PADEN,* DAVID HALLIDAY,* MALCOLM TYE*

Department of Earth Sciences, Liverpool University; *CamScan Electron Optics, Waterbeach, UK

Microstructures and textures of rocks are used to understand:

- Deformation mechanisms,
- Recovery and recrystallization mechanisms,
- Phase changes,
- Pressure-temperature-deformation conditions of high T processes

Electron backscattered diffraction (EBSD) has revolutionised studies of rock microstructure as it enables statistically significant, quantitative microstructural data sets to be collected quickly. Electron backscattered diffraction is rapidly replacing bulk x-Ray techniques and light microscopy in the measurement of textures. It is however, the ability to carry out misorientation analysis that has the biggest impact on understanding the processes. The misorientation information that can be generated by measuring the spatial variation in orientation can be used to test conceptual, numerical, or analytical models for the processes that produce a microstructure. Electron backscattered diffraction is now being used in more than 20 earth science based-labs worldwide. Details of sample preparation and analytical techniques for the application of EBSD to rock forming minerals are outlined by Prior *et al.*[1] The following problems are the focus of current technological development.

Misindexing and Non-Indexing

The degree of non-indexing (patterns that cannot be indexed) and misindexing (patterns that are indexed incorrectly) are a function of pattern quality. Some minerals have misindexing problems, even with patterns of the best quality. Generally, misindexing problems increase as symmetry decreases. It is sometimes possible to optimise software parameters to maximise success or to eliminate unreliable analyses on the basis of some confidence index. Any use of automated EBSD must include an assessment of the degree of misindexing, for the particular experimental set-up and mineral in question, and a discussion as to the possible effects on the data. In minerals with severe misindexing problems, the number of data that are needed to map the microstructure can be reduced significantly by using orientation contrast images.[2-4]

Angular Resolution

Although the misorientation angle has the same order of precision as an individual orientation (~1º), the errors on misorientation axes at small misorientation angles are large.[1] Misorientation axes of low angle boundaries are important in understanding intra- and inter-grain processes, and EBSD users need to be aware of the errors involved. Analysis of data dispersions provides a statistical method to improve angular resolution. However, this only works for data sets (or subsets) with coherent dispersions. New camera technology provides a more general hardware solution for improving angular resolution.

The Biggest Challenge: Using the Data

Electron backscattered diffraction presents us with a new opportunity. We can measure individual orientations, calculate misorientations and reconstruct microstructures. Perhaps the biggest challenge at the moment is in learning how to present and use the data that are provided. Pole figures, inverse pole figures and ODF projections are established in textural studies and can, of course, be generated from EBSD data. The use of individual misorientations, misorientation distributions, and parameters that link texture and microstructure[6,7] are less well established and it is these, rather than the EBSD technique itself, that will be the new tools of microstructure.

Ultimately, we are limited in that processes have to be interpreted from a final, frozen microstructure. Two decades of experiments using transparent polycrystals show that dynamic experiments provide a much better constraint on process than a single snapshot of a microstructure. We have developed an SEM system in which we can conduct high temperature experiments whilst imaging and mea-

suring microstructures. We will show preliminary results of grain growth (in Al) and phase transformation (in Ti, Quartz & brass shape memory alloys) experiments conducted in situ in an SEM to illustrate the potential of this approach.

References

1. Prior DJ, Boyle AP, Brenker F, Cheadle MC, Day A, Lopez G, Peruzzo L, Potts GJ, Reddy SM, Spiess R, Trimby PW, Wheeler J, Zetterstrûm, L: The application of electron backscatter diffraction and orientation contrast imaging in the SEM to textural problems in rocks. *Amer Mineralogist*, 84, 1741–1759 (1999)
2. Prior DJ, Trimby PW, Weber UD, Dingley DJ. Orientation contrast imaging of microstructures in rocks using forescatter detectors in the scanning electron microscope. *Mineralogical Mag*, 60, 859–869 (1996)
3. Day A, Quested TE: A comparison of grain imaging using HOCI, COCI, EBSP and optical methods. *J Microsc* 195, 186–196 (1999)
4. Bartozzi M, Boyle AP, Prior DJ: Automated grain boundary detection and classification in orientation contrast images. *J Structural Geol.* 22, 1569–1579 (2000)
5. Prior DJ: Problems in determining misorientation axes, for small angular misorientations, using electron backscatter diffraction in the SEM. *J Microsc*, 195, 217–225 (1999)
6. Trimby PW, Prior DJ, Wheeler J: Grain boundary hierarchy development in a quartz mylonite. *J Structural Geol*, 20, 917–935 (1998)
7. Wheeler J, Prior DJ, Jiang Z, Spiess R, Trimby PW: The petrological significance of misorientations between grains. *Contributions Mineralogy and Petrology* (in Press)

Significance of electron channeling in the formation of electron backscattering patterns (EBSP)

O. WELLS

NIST, Gaithersburg, MD, USA

An electron backscattering pattern (EBSP) is formed when an electron beam (EB) is focused onto a single-crystal region of the sample. The scattered electrons are incident onto a photographic film or image screen to show lines and bands of contrast formed by the faster scattered electrons. An electron channeling pattern (ECP) is formed by rocking the beam over an area of single crystal, collecting the faster scattered electrons, and by displaying what is a very similar image to the above. The ECP has been explained by supposing that the channeling condition in the entrance Bragg planes modulates the probability of a wide-angle scattering event towards the detector. If indeed the EBSP and ECP are caused by the same phenomenon, then it will be expected that the processes will be related by the reciprocity principle so that the EBSP must be explained by reversing the above sequence of events. In other words the EBSP is formed by the modulation of the probability of a wide-angle scattering event by the channeling condition in the exit Bragg planes — or "channeling in – channeling out."

This suggests that it might be better to refer to the formation of EBSP as channeling (both in and out) rather than diffraction.

Initial electron backscattered diffraction observations of a plutonium-gallium alloy

C.J. BOEHLERT, R.K. SCHULZE, J.N. MITCHELL, T.G. ZOCCO, R.A. PEREYRA

Nuclear Materials Technology Division, Los Alamos National Laboratory, Los Alamos, NM, USA

Introduction

Electron backscattered diffraction (EBSD)[1] analysis of Pu has been elusive to date, relating to several factors including rapid surface oxidation and difficulty in handling because of to its extreme toxicity. The former process results in the buildup of an amorphous surface layer that acts as an obstacle for electron penetration to the underlying crystalline metal. In this work, the first electron backscattered diffraction patterns (EBSPs) of a gallium (Ga) stabilized δ-phase (face-center-cubic [fcc] structure) Pu alloy were captured. This work details the techniques and equipment used to overcome the obstacles preventing EBSD observation of Pu. This demonstrated characterization technique is expected to be a powerful means to further understand phase transformation behavior, orientation relationships, and texture in the complicated Pu and Pu-alloy systems.

Materials and Methods

The Pu-Ga alloy used for this study was chill cast at 450°C in the form of a plate at the plutonium facility of Los Alamos National Laboratory. After casting, a δ-phase homogenization heat treatment was performed. Samples were prepared using standard metallographic and electropolishing techniques that were performed inside gloveboxes and/or other enclosures to prevent spread of radioactive contamination.

Most environmentally sensitive materials, which require sputter cleaning to obtain quality EBSPs, can be transferred from the ion-sputterer through air to the scanning electron microscopy (SEM) chamber.[1,2] In this study, transfer of an ion-sputtered sample through atmosphere did not result in successful EBSP acquisition from the Pu-Ga metal. This was attributed to the formation of a thick amorphous surface oxide layer as a result of air exposure. Design and construction of a vacuum transfer device was thereafter initiated to overcome this obstacle. A scanning auger microprobe (SAM), equipped with an ion gun, was used to characterize and remove surface layers contaminated with chemical impurities (in particular carbon and

oxygen). To remove the surface contaminants, 4 keV argon (Ar) ions at 55 μA/cm^2 were used to bombard the sample surface for up to 1 h. A second sputtering step, with 500 eV Ar ions at 9 μA/cm^2, was performed to reduce the depth of the damage layer caused by the initial sputtering run with higher energy ions. The vacuum transfer device, including a vacuum suitcase and SEM entry-port adapter, was used to minimize oxidation during the sample transfer from the SAM to SEM. The duration of the sample transfer from the SAM to the SEM was approximately 15 min and the maximum atmospheric pressure experienced by the sample was 4×10^{-6} torr. The EBSD patterns were captured using EDAX, Inc. (formerly TSL, Inc.) hardware and software, using the following SEM and OIM parameters: accelerating voltage=30 keV, working distance = 16 mm, specimen tilt angle of 70°, 110 μm objective aperture, absorbed specimen current between 1 and 2 nA, and the CCU averaged 16 video images or frames.

Results

Comparing the Auger spectra, significant reduction in the O and C peaks (including in some cases elimination of these impurities to below detection limits [<0.1 atomic percent]) and the increased height of the Pu peaks were evident for the sputtered condition compared with the as-electropolished condition. The EBSPs of the δ-phase grains were obtained only after sputtering and sample vacuum transfer from the SAM to the SEM. After the initial patterns were captured, the sample was left in the SEM chamber at 4×10^{-7} torr for 68 h. The sample was then reanalyzed and EBSPs were also observed, indicating that the surface oxide did not thicken enough under these conditions to prevent EBSD observation of the Pu-Ga metal. Combining this observation with those for the air transfers, the effect of environment on surface oxidation is illustrated, and this indicates the importance of maintaining a high-vacuum atmosphere after surface cleaning for EBSD observation of Pu-Ga alloys.

Conclusions

(1) The first EBSPs were captured for a Pu-Ga alloy using orientation-imaging microscopy. (2) Sputtering the surface with Ar ions inside an SAM and transferring the cleaned sample to the SEM in a vacuum environment minimized surface oxidation. This maintained the surface integrity of the sample and allowed for the capture of EBSPs of the fcc δ phase.

References

1. *Electron Backscatter Diffraction in Materials Science* (Ed. AJ Schwartz, M Kumar, BL Adams). Kluwer Academic/Plenum Publishers (2000), 301
2. Dingley DJ, Baba-Kishi KZ, Randle V*: Atlas of Backscattering Kikuchi Diffraction Patterns*. Institute of Physics Publishing Ltd., Philadelphia, Pa. (1995) 119

Higher-order laue zone rings in electron backscattering diffraction

A. EADES

Department of Materials Science and Engineering, Lehigh University, Bethlehem, PA, USA

Electron backscattering diffraction (EBSD) patterns obtained in the scanning electron microscope are extremely useful. Its importance arises partly from the general aspect, namely that it brings crystallography into the scanning electron microscope (SEM) in a much easier way than was previously possible. The importance also stems from the value of the two specific types of application that have become most strongly developed, namely orientation mapping and phase identification. All of this is described in a recent book.[1]

Until recently one weakness of the use of EBSD for doing crystallography in the SEM was that the measurement of lattice parameters was imprecise. The angles between zone axes can be rather well measured but lattice spacings could not. This is because lattice spacings were determined from the widths of the Kikuchi bands, and, since Kikuchi bands are narrow and fuzzy, their width could not be determined with much precision.

Joe Michael noticed that some zone axes in EBSD patterns are surrounded by a bright ring. He guessed that these were higher-order laue zone (HOLZ) rings and that they could be used to determine lattice spacings with good precision. It turns out that he was right, though some qualification of these assertions is needed.[2]

The visibility of these rings is a surprise. The nearest equivalent to an EBSD pattern in the transmission electron microscope (TEM) is a large-angle convergent-beam electron diffraction (LACBE) pattern (or perhaps more closely a Kossel pattern). In such patterns in the TEM, HOLZ rings are practically invisible. Even when you know where they are, they are almost impossible to find. This result needs some comment. We are used to seeing convergent-beam electron diffraction (CBED) or selected-area diffraction (SAD) patterns in the TEM in which HOLZ rings are clearly visible. However, these patterns are obtained under conditions in which the HOLZ ring is seen against a dark background. It appears with good contrast even when it is very weak. In LACBED and Kossel patterns as well as in EBSD, the background, by contrast, is very strong–essentially the whole signal—and a HOLZ ring would have to have a much higher relative intensity to be visible.

A HOLZ ring is formed by the combination (the envelope) of a set of lines. The lines are Kikuchi lines, just like normal Kikuchi lines except that, since they are associated with reflection from planes with long g vectors, they are very weak. They become strong enough to see over only a short length where the intensity is enhanced because the reflection couples to dispersion surfaces at a strong zone axis.[3] This phenomenon is more familiar in zone-axis

CBED in the TEM. There, HOLZ lines in the bright-field (direct-beam) disc are seen to fade as the sample is tilted away from the zone axis. In EBSD, the result is that the ring is bright enough to see (in some cases) although the Kikuchi lines that form it are not visible, except where they contribute to the ring. It is not a surprise that the Kikuchi lines that make up the HOLZ ring are invisible except in the ring itself. It is a surprise that the ring is visible at all. This author speculates that the origin of the contrast is related to the idea that Kikuchi contrast in EBSD does not come from a fixed depth but, perhaps, from a self-selected depth related to the extinction distance, which is therefore different for each different reflection. Thus the ratio of the intensity of a HOLZ reflection to the intensity of a low-index reflection will be much higher than the ratio of their structure factors.

Acknowledgments: Support from DOE, under grant DE-FG02-00ER45819, is gratefully acknowledged.

References

1. *Electron Backscatter Diffraction in Materials Science*. (Eds. AJ Schwartz, M Kumar, BL Adams) Kluwer/Plenum, New York **(**2000) I-XVI, 1–339
2. Michael JR, Eades JA: Use of reciprocal layer spacing in electron backscatter diffraction pattern analysis. *Ultramicrosc* 81, 67–81 (2000)
3. Bird DM: Theory of zone axis electron diffraction. *J Electron Microsc Technique* 13, 77–97 (1989)

Scanning probe microscopy

Nanoindentation by atomic force microscopy as a diagnostic tool for soft material

S.V. DUBONOS, V.A. DREMOV, S.I. ZAITSEV

Institute of Microelectronics Technology RAS, Chernogolovka, Russia

We used an atomic force microscopy(AFM)-like device to measure polymer layers by pinning the AFM tip on the layer. For this, the AFM-like device was modified, and a special head (holder) was designed and fabricated. It allows us to use commercially available Si cantilevers whose main advantage is to vary the stiffness allowing the application of a wide range of forces. On the other hand, tips of commercially available cantilevers are not suitable due to rather large tip diameter and cusp angle of the tip. A special procedure was developed to grow fine carbon tips on the Si tip to improve the tip properties. The method of lateral growth under an e-beam was used to obtain a desirable axis angles to compensate for a 10^{o}–20^{o} angle of the cantilever in the commercial holder. The method allows us to grow the tips with a diameter of less than 10 nm with an open angle not $> 10^{o}$. It is well known that carbon tips have strength close to that of a diamond.

At a total force of 10^{-7}N and contact area at about 100 nm^2 the device provides pressure at least 10^9N/m2; this is close to the Young modulus for polymethyl methacrylate (PMMA). So we have a good chance to perform pinning of the resist layer to measure its thickness.

The main advantage of the method is a very rigid and strong carbon tip which allows us to penetrate the PMMA layer at room temperature, measuring the residual thickness with high locality and resolution.

Diagrams of applied force as a function of cantilever displacement during loading (f/ward) and unloading (b/ward) were recorded. The diagram could be interpreted in the following manner. At the contact point a small displacement of the tip resulted in "plastic deformation" of PMMA due to high stress concentration at the carbon tip. Then the tip contacts the substrate and the quazielastic slope is observed. The intersection of the unloading curve with the x-axis allows one to estimate resist thickness. In our case the estimate gives 50 nm, close to the known resist thickness of 60 nm. The experiment shows that resist thickness and some information on deformation process could be obtained by the method developed.

Acknowledgments: The results were obtained in the frame of the SPINUP project. The activity was partially supported by grant number 97-2021

Thin section analysis of the lunar regolith

E.C. HAMMOND

Morgan State University, Physics Department, Baltimore, MD, USA

Thin section Lunar regolith was prepared by the Lyndon B. Johnson Space Center, Planetary Science Branch of lunar samples retrieved by Apollo astronauts (samples #70015.655). The thin sections were milled to approximately 30 μ thicknesses. Using an optical microscope with polarization filters produced dramatic visible transmitted light colonization, which is not seen with terrestrial thin sections of similar minerals. The metallic grains produced complete opacity, while other shocked metamorphic effects were observed in the various basaltic and anorthositic grains. These dramatic effects of polarization were observed because of the absence of water during the early evolution of the moon's formation. This phenomena was not observed until the Apollo astronauts returned with these lunar samples. Images demonstrate cracks in the shocked glass as a function of polarization angle.

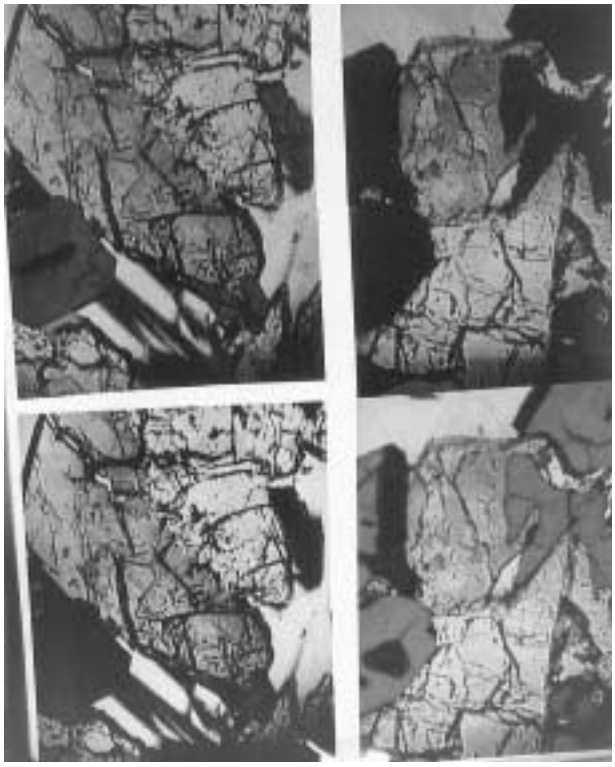

Fig. 1 Shock metamorphosis of thin film of lunar regolith changing the polarization angle. Opaque material indicates metallic thin section.

References

1. Hammond EC, Barron D, Cohen S, Wright-Brown C, Miller T, Russell S: An analysis of the lunar regolith (soils) from the Apollo 11 mission using scanning electron microscopy—energy dispersive system x-ray analysis and atomic force microscopic probe. *Scanning* 20, 136–137 (1998)
2. Hammond EC, Cohen S, Chavis J, Ansari S: An examination of lunar samples from Apollo 11 using atomic force microscopy in tapping mode and other advanced microscopic technologies. Scanning 19, 143–146 (1997)
3. Wood J: Forging the planets: The origin of our solar system. Sky and Telescope 97, 36–48 (1999)
4. Von Englehardt W, *et al*: Shock nelamophism of lunar rocks and origin of the regolith at Apollo 11 landing site. Proceedings *of the Apollo 11 science conference*, I, 363–384

Fast-scanning atomic force microscopy

F.M. SERRY

Digital Instruments/Veeco Metrology Group, Santa Barbara, CA, USA

Atomic force microscopy (AFM) scanning speeds have always been slower than desirable, and this to some extent has limited the number of scientists and technologists who have used and benefited from AFM. For example, until now, AFM tip scanning speeds on most sample types have rarely exceeded 40 μm/s in the most popular mode, TappingMode AFM; typically, scan times are several minutes per frame. There are numerous situations where even though the resolution and wealth of information in a single AFM image surpasses those in many SEM micro-graphs combined, AFMs are bypassed in favor of SEM imaging, in part because of the speed issue. A new AFM technology is discussed which enables scanning speeds much faster—up to 10 times faster—than previously attained. The technology relies primarily on a new electronic feedback architecture (nested feedback loop) and new, micro-actuated, probes. Improvements in scan speeds are illustrated (including in digital video movies showing fast-scanning) on different kinds of sample including Cell-Guard and other polymers, and from the nanometer-scale to several tens of micrometers. Then the technology behind fast-scanning AFM is described, starting with a discussion of the factors that hindered scanning speeds until now. The traditional and popular mode of actuation of the AFM tip out of the plane of the ample (in Z-direction) has been to use a piezoelectric tube or flexure (commonly called the Z-tube or Z-flexure), typically cm's large. It is shown that the size and mass of this actuating element is a major speed bottleneck. The large size and mass basically renders the element too slow to faithfully track the sample surface with the AFM tip at high scan rates. If a second, smaller, more agile actuator, with it's own feedback control is used to assist the Z-tube, then the scanning speed can be increased. There is another benefit to this new scheme: the tip appears to track the surface much better at a given speed when compared with the traditional scheme, suggesting significant positive implications for tip lifetime. This point is illustrated in data from the feedback loop's "error" signal.

MgATP-induced conformational changes of the myosin molecule and periodicity of substructures in the tail observed by atomic force microscopy

M. TANIGUCHI, O. MATSUMOTO,[*] S. SUZUKI, Y. NISHINO,[†] A. OKUDA,[*] T. TAGA,[*] T. YAMANE

Graduate School of Engineering, Nagoya University, Nagoya; [*]Graduate School of Pharmaceutical Sciences, Kyoto University, Kyoto; [†]Graduate School of Human Informatics, Nagoya University, Nagoya, Japan

Muscle contraction results from the sliding movement of thick and thin filaments. The major component of thick filaments is myosin, which is a large unique-shaped molecule with two heads and a long rod-like tail. It is a mechanochemical motor that converts the chemical energy of ATP hydrolysis into mechanical energy and slides on actin filaments. Therefore myosin plays an essential role in the elementary process of muscle contraction. The atomic structure of myosin fragment S1 was solved by crystallography[3]

and the atomic model of the a-helical coiled-coil structure of the tail was proposed based on an amino acid sequence.[1,2] However, relatively little attention was given to the conformational dynamics between the heads and tail. We report on the conformational change of myosin molecules observed directly by atomic force microscopy (AFM). We have previously observed that myosin molecules deposited on mica take extended forms without MgCl2 and ATP and, on the other hand, almost all the molecules take bent and round forms with either MgCl2 or ATP. To understand the orientation transition between two conformers progressively, we tried to take the AFM images of myosin molecules that were exposed under the relaxed solutions with various concentrations of MgATP. We found that the orientation of myosin heads and the tail strongly depends on the concentration of MgATP. The mean-square end-to-end distance of the myosin molecules is much shorter at p[MgATP] = 4 than that at p[MgATP] = 6. The region of myosin rods did not show the same intensity along the long length even in the expended form. They showed discontinuously in clusters to make some domains. The size of compartments in the rods changes at multiple intervals of 14.3-14.5 nm, reflecting the periodicity on a-helical coiled coil. Clustering of the substructures also relates to the spacing of the myosin cross-bridges in the muscle (14.3 nm or 43 nm). These results suggest that the bending of myosin heads seems to couple with the bending or tilting of the helical subdomains. Conformational changes of myosin molecule induced by MgATP seem to reflect the molecular motions of myosin in the force generation.

References

1. McLachlan AD: Structural implications of the myosin amino acid sequence. *Ann Rev Biophys Boiling* 13, 167–189 (1984)
2. Parry D AD: Structure of rabbit skeletal myosin. Analysis of the amino acid sequence of two fragments from the rod region. *J Mol Biol* 153, 459–464 (1981)
3. Rayment I, Rypniewski WR, Schmidt-Base K, Smith R, Tomchick, DR, Benning MM, Winkelmann DA, Wesenberg G, Holden HM: Three-dimensional structure of myosin subfragment-1: A molecular motor. *Sci*, 261, 50–58 (1993)

Materials imaging and characterisation with apertureless second-harmonic scanning near-field optical microscopy

S. TAKAHASHI, D. MCHUGH, A.V. ZAYATS

School of Mathematics and Physics, The Queen's University of Belfast, Belfast, United Kingdom

Continuous trends towards the miniaturisation of electronic devices and components require appropriate, nondestructive techniques for materials characterisation on smaller and smaller scales. Developments in scanning near-field optical microscopy (SNOM) give the possibility for probing optical properties of materials with subwavelength spatial resolution. In turn, second-harmonic generation (second order nonlinear optical process) is widely used for characterisation and investigation of materials and their surfaces as it is extremely sensitive to morphology and surface structure on the atomic scale. Recent experiments on the near-field probing of second-harmonic generation have led to the development of an imaging technique which combines the high spatial resolution provided by SNOM and high optical sensitivity of surface second-harmonic generation. [1-3]

Resolution and throughput of conventional SNOM are limited by the size of a nanometric aperture formed at the end of a tip. The idea of apertureless SNOM is to avoid the use of a small size aperture. This may give the possibility to push the resolution limit of SNOM down to single nanometre scale. At present, two main approaches to apertureless SNOM are being followed based on observation of scattering or fluorescence at the tip–surface junction. The field enhancement effects (both geometric enhancement and localised surface plasmons) are often used in both techniques to achieve better signal-to-background ratio and resolution. A recently proposed apertureless scanning near-field optical microscope employs the enhancement of local second-harmonic generation induced by a probe tip.[4] In this paper the imaging properties of a second-harmonic apertureless near-field microscope are discussed.

Numerical modelling of the second-harmonic generation processes in a probe–sample system shows that the strongly confined sources of second-harmonic light can be achieved due to enhancement of the electromagnetic field at the tip–surface junction. In different realisations, this allows one to probe a local second-harmonic field generated at a sample surface or to use a second-harmonic light source at the apex of a tip for imaging the surface. In these two cases, apertureless SNOM is shown to be the nonlinear analogue of apertureless scanning near-field optical microscopy based on local nanoscopic fluorescence or scattering.

The experimental realisation of this technique has been achieved using gold-coated fibre tips as well as STM gold and tungsten tips to observe the enhanced second-harmonic generation. We have demonstrated apertureless second-harmonic SNOM capabilities for imaging rough metal surfaces, magnetic domains in layered magnetic structures, as well as ferroelectric domains in thin ferroelectric films. A successful scheme for extracting optical information with truly nanometric resolution would have numerous applications in optical studies and characterisation of metal and semiconductor nanostructures as well as biological objects.

References

1. Smolyaninov II, Zayats AV, Davis CC: Near-field second-harmonic imaging of ferromagnetic and ferroelectric materials. *Opt Lett* 22, 1592–1594 (1997)

2. Shen YZ, Swiatkiewicz J, Winiarz J, Markowicz P, Prasad PN: Second-harmonic and sum-frequency imaging of organic nanocrystals with photon scanning tunnelling microscope. *Appl Phys Lett* 77, 2946–2948 (2000)
3. Schaller RD, Roth C, Raulet DH, Saykally RJ: Near-field second harmonic imaging of granular membrane structures in natural killer cells. *J Phys Chem* B, 104, 5217–5220 (2000)
4. Zayats AV, Sandoghdar V: Apertureless scanning near-field second-harmonic microscopy. *Opt Commun*, 178, 245–249 (2000)

Anthropology

Variation in the growth and modeling of the human maxilla as revealed by scanning electron microscopy

M. A. McCollum

Department of Anatomy, Case Western Reserve University, Cleveland, OH, USA

Growth remodeling refers to various combinations of bone deposition and resorption that occur on the inner and outer surfaces of a bony lamina. In the cranium, growth remodeling changes the size of each whole bone, sequentially relocates each of its component regions to allow overall enlargement, and carries out the continuous structural adjustments necessary to adapt bone to the intrinsic and extrinsic changes in their conditions.[1] Current knowledge of human craniofacial growth remodeling derives from (1) histologic studies of a small number (n = 36) of crania,[2] and (2) longitudinal radiographic cephalometric studies in which changes in the external contours of bones are studied relative to stationary radiopaque implants.[3] Through these techniques a general pattern of human craniofacial remodeling has been identified. However, because these data sets are small, little information exists regarding the extent to which craniofacial surface remodeling varies between sexes, and among individuals of differing race/geographic origin.

This study documents variation in nasomaxillary growth remodeling in dentally immature crania housed in the Cleveland Museum of Natural History. This mixed-sex sample of 27 specimens ranges in age from 1 to 20 years, and all but three are of African descent. In each specimen, a negative impression of the periosteal surface of the maxillary incisive alveolar process was made using the President Jet Plus light body impression material (Coltène). Positive surface replicas were made from these impressions using Devcon High Strength 5 Minute Thick Gel Epoxy (Devcon Consumer Products). Low-voltage (10 kV) scanning electron microscopy was used to identify the distribution of fields of deposition and resorption on these high-resolution bone surface replicas.

Results revealed the following five patterns of surface remodeling along the maxillary incisive alveolar process: (1) all depositional, (2) depositional with resorption between tooth roots, (3) depositional with resorption over tooth roots, (4) resorptive with deposition over tooth roots, and (5) all resorptive. The majority of specimens within this sample (17 of 27) displayed a predominantly depositional maxillary incisive alveolar process (Patterns 1, 2, or 3). Although resorption of some portion of the maxillary incisive alveolar process was found to occur at all dental ages, the greatest frequency of surface resorption was observed in those individuals in whom development of the permanent incisors and canines was virtually complete.

The above results can be compared with those obtained by Kurihara *et al.* in their study of 36 subadult human crania purchased from commercial suppliers.[2] Most of the individuals in the latter sample were found to display a predominantly resorptive incisive alveolar process. Indeed, with the exception of individuals under 2 years of age, only 7 of the 27 older individuals (26%) in the Kurihara *et al.* sample showed any evidence of deposition along the incisive alveolar process. In comparison, in the present sample, most of the specimens (17 of 27) were found to display significant deposition along their incisive alveolar process.

Results of this study demonstrate that growth remodeling of the anterior maxilla is more variable than currently recognized. Some of this variation may relate to the ethnic origin, as several cephalometric studies have found a tendency for African Americans to display an anteriorly positioned anterior maxillary surface.[4,5] The possession of a primarily depositional incisive alveolar process may underlie this morphologic tendency of African populations.

Acknowledgments: This research was funded by a grant received from the L.S.B. Leakey Foundation.

References

1. Enlow DH, Hans, MG: *Essentials of Facial Growth*. Philadelphia: W.B. Saunders Company (1996)
2. Kurihara S, Enlow DH, Rangel RD: Remodeling reversals in anterior parts of the human mandible and maxilla. *Angle Orthod*. 50, 98–106
3. Björk A: The use of metallic implants in the study of facial growth in children: method and application. *Am. J Phys Anthropol*, 29, 243–250 (1968)
4. Drummond RA: A determination of cephalometric norms for the Negro race. *Am J Orthod* 54, 670–2 (1968)
5. Faustini MM, Hale C, Cisneros GJ: Mesh diagram analysis: developing a norm for African Americans. *Angle Orthod*, 67, 121–128 (1997)

A three-dimensional visualization model of dental microstructure: Implications for phylogenetic and functional interpretations

G.A. MACHO, I.R. SPEARS*

Hominid Palaeontology Research Group, Department of Human Anatomy and Cell Biology, The University of Liverpool, Liverpool, England; *University of Teeside School of Social Sciences, Middlesbrough, England

Our limited understanding of the three-dimensional (3-D) arrangement of enamel prisms confounds functional interpretations of teeth. Yet, prism decussation has probably evolved to deflect stresses or cracks within enamel and to counteract potentially damaging localised tensile stresses[6]. Ascertainment of the 3-D prism arrangement is only possible through destructive techniques and, hence, not feasible where fossil teeth are concerned. However, an approximation of the amount of enamel decussation is provided by Hunter Schreger bands (HSbs) which are optical phenomena resulting from incident light being reflected (parazones) or absorbed (diazones) in longitudinal (or broken) sections of teeth. Rensberger[5] found a high correlation between the concentration of HSbs and the magnitude of occlusal stress, although detailed information about enamel prism decussation in these areas is still elusive. Furthermore, an assessment of enamel formation time, particularly cuspal enamel, depends on an accurate appraisal of prism decussation which, however, cannot be approximated in longitudinal thick sections of teeth[1]. Ascertainment of the 3-D arrangement of prism arrangement may be overcome by creating 3-D computer models of different enamel organisations and comparing them with HSbs[4]. This proposal was evaluated further in the present study making use of advances in graphics capabilities on modern PCs.

Enamel blocks from the lateral side of teeth of mammals with different dietary strategies (i.e., omnivore, folivore) and–hence–different patterns of enamel decussation, were embedded in epoxy resin. The blocks measured maximally 1 mm mesio-distally, but care was taken that the entire thickness of enamel could be observed. The specimen was then ground down by increments of about 5 to 10 μm and etched in NHCl for 20 s, from the apical aspect towards the cervical part and perpendicular to the dentino-enamel junction. Images were then taken with the scanning electron microscope (I.S.I. 60A) at 24 Kv in backscattered mode (80 s/picture). The images were captured with the iScan software (I.S.S.) and subsequently analysed. Software created with Borland C++ Builder version 4.0 together with OpenGL allows the visualisation models of individual prisms to be generated and duplicated to form virtual enamel blocks. Subsequently, viewing direction, light source, material opacity, and prism orientations are manipulated thus allowing the sub-surface structure of scanning electron microscope images to be approximated.

While the models thus created need to be improved and validated before they can be used to make confident inferences about the 3-D arrangement of prism decussation on the basis of HSBs alone, they demonstrate the feasibility of our approach. Furthermore, the 3-D structures will provide the opportunity to generate mechanical properties[8] and therefore test the biomechanical behaviour of whole teeth (both extant and extinct) more realistically.[2,7,8] In addition, a better appraisal of changes in developmental processes during evolution[3] should be attainable.

Acknowledgments: This work is supported by The Leverhulme Trust.

References

1. Dean MC: A comparative study of cross striation spacings in cuspal enamel and of four methods of estimating the time taken to grow molar cuspal enamel in *Pan*, *Pongo*, and *Homo J Hum Evol* 35, 449–462 (1998)
2. Macho GA, Spears IR: The effects of loading on the biomechanical behaviour of molars of *Homo*, *Pan*, and *Pongo*. *Am J Phys Anthrop* 109, 211–227 (1999)
3. Macho GA, Wood BA: The role of time and timing in hominoid dental evolution. *Evol Anthrop* 4, 17–31 (1995)
4. Osborn JW: A 3-dimensional model to describe the relation between prism directions, parazones and diazones, and the Hunter-Schreger bands in human tooth enamel. *Archs oral Biol* 35, 869–878 (1990)
5. Rensberger JM: *Mechanical adaptation in enamel*. (Eds. W. von Koenigswald, N. Sander. *Tooth enamel microstructure*. (Ed. A.A. Balkema) Rotterdam. 237–257 (1997)
6. Rensberger JM, Pfretzschner U: Enamel ultrastructure in astrapotheres and its functional implications. *Scan Microsc* 6, 495–510 (1992)
7. Spears IR, Macho GA:. Biomechanical behaviour of modern human molars–implications for interpreting the fossil record. *Am J Phys Anthrop* 106, 467–482 (1998)
8. Spears IR: A three-dimensional finite element model of prismatic enamel: A re-appraisal of the data on the young's modulus of enamel. *J Dent Res* 76, 1690–1697 (1997)

The use of laser scanning techniques in paleoanthropology: A preliminary evaluation

M. FRIESS, E. DELSON, L.F. MARCUS, D.P. REDDY

NYCEP Morphometrics Group, Division of Paleontology and Interdepartmental Laboratory, American Museum of Natural History, New York, NY, USA

Introduction

In recent years, the use of three-dimensional (3-D) measuring devices, such as computed tomography (CT) scanners, has become increasingly popular in paleontology and paleoanthropology; however, CT scanning may not always be suitable for a given purpose. For instance, for surface-related data (linear dimensions, volumes, areas), laser scanning appears to better satisfy cost/benefit ratios. Laser

scanning is generally used in rapid prototyping and quality control applications and has recently been extended to paleontological objects.[1,2]

We have evaluated the potential of a laser surface scanner for studies of human and nonhuman primate morphology and evolution. The present evaluation tests accuracy and explores the articular surface morphology of the distal humerus in great apes and humans.

Laser Scanning Technique and Accuracy

We use a Cyberware model 3030 with color registration. The maximum resolution, as specified by the manufacturer, is 0.1mm for a volume of $170 \times 150 \times 150$ mm (xyz).

The principle of 3-D modeling with a laser scanner is based on triangulation of a series of digital views from known positions. A laser beam is scanned across the surface of an object and a series of profiles are captured by a range finder/camera and a color CCD. The user defines the number of positions as steps of angular rotation (0–360°) of the circular platform that holds the object. The resolution is a function of the time interval (spacing) between two adjacent profiles. The final 3-D-model is reconstructed by an automated triangulation and merging process of all profiles over all orientations.

Linear data, such as length, as well as area and volume can be directly obtained using the manufacturer's default software package (CyEat, http://www.headus.com).

We tested the scanner by observation of measurement accuracy (correctness) and dependence on scanning parameters using a standardized object. Accuracy here is taken as the capacity to produce a metrically correct virtual model of a 3-D object. Potential sources of error are the mechanical repeatability of the scanner, the optical resolution of the sensor, and the performance of the merging algorithm. Currently, we have not considered observer-related errors, but will do so as our research continues. The object was scanned with varying resolutions (0.1, 0.2, 0.4 mm). For each scan, 8 measurements (6 linear dimensions, volume, area) were taken and compared. In addition, a series of 14 landmark coordinates were registered directly from the reconstructed mesh. The same landmarks were also registered using a Microscribe 3-D digitizer. These sets of coordinates were then compared with each other using generalized procrustes analysis. Preliminary results yield a measuring error of 0.4–0.5 mm, suggesting that the loss of accuracy compared with maximum resolution is related to observer error.

Application: Exploring Variation in Articular Surface Morphology of Primate Humeri

We compared the morphology of the distal articulation of the humerus, which reflects adaptation to patterns of locomotion, in living primates. This morphology has been described by conventional and landmark morphometrics.[3,4] However, a 3-D model of the surface should contain significantly more information about the functional variability of the distal humerus. We have sampled surface data from several specimens each of the great ape genera (pongo, pan, gorilla) and from living humans of both sexes. These data allow for a comparative analysis of terrestrial versus more arboreal quadrupedal locomotion, as well as the unique bipedal condition of humans. Size-related variations, such as sexual dimorphism, are also taken into account. Area/volume ratios were determined for functional components (trochlea, capitulum, epicondyles) and compared across these taxa.

References

1. Lyons PD, Rioux M, Patterson RT: Application of a three-dimensional color laser scanner to paleontology. *Paleontologia Electronica* 3, 2, 1–16 (2000)
2. Rosenberger AL, Calvo CM: Digital morphology: The Smithsonian's Biovisualization Lab. *Evolut Anthropol* 6(3), 77–78 (1998)
3. Bacon A-M: Principal components analysis of distal humeral shape in pliocene to recent african hominids: The contribution of geometric morphometrics. *Am J Phys Anthropol* 111, 479–487 (2000)
4. Larson SG: Parallel evolution in the hominoid trunk and forelimb. *Evolut Anthropol* 6, 3, 87–99 (1998)

Variability in mineralization density and collagen fiber orientation of the human mid-shaft femur

H.M. GOLDMAN, J.G. CLEMENT,* C.D.L. THOMAS,* T.G. BROMAGE

Hard Tissue Research Unit, Department of Anthropology, Hunter College, CUNY, New York, NY, USA, *Department of Oral Anatomy, Medicine and Surgery Unit, School of Dental Science, The University of Melbourne, Melbourne, Australia

Mineralization density and collagen fiber orientation are both microstructural variables known to affect the mechanical properties of bone. Mineralization is primarily a consequence of time since formation, and hence remodeling rate. When bone is examined using the scanning electron microscope (SEM) in backscattered electron imaging mode (BSE-SEM), grey level values have a positive correspondence to mineralization density. The orientation of collagen fibers in either a more transverse or more longitudinal direction is believed to confer greater resistance to compressive or tensile forces, respectively. When bone is examined using circularly polarized light microscopy (CPLM), fibers transverse in orientation appear bright, while longitudinal fibers appear dark. This study sought to determine whether mineralization and collagen fiber orientation showed spatial organization in the mid-shaft femur that would reflect forces imposed by bipedal standing and locomotion. Variability within each of these microstructural

properties with age and sex was examined, as was the relationship between the two variables.

Cross sections, each 100 μm in thickness, were prepared from an autopsy sample (n=40) of adult femora collected from the Victorian Institute of Forensic Medicine, Australia. Montaged grey-scale images of entire cross sections were first obtained using CPLM under standardized lighting conditions. Specimens were then carbon coated and imaged using BSE-SEM, employing a standard to control for instrument drift over time. Using an automatic routine, each image montage was divided into 48 segments according to anatomical position. Average grey values were quantified for each segment, and one-way analysis of variance (ANOVA) with Tukey HSD post-hoc tests were applied to assess differences between segments for each variable, respectively.

Results of the study of collagen fiber orientation showed statistically significant differences between aspects of the cortex, suggestive of a patterned distribution of collagen fiber orientation. Significantly more longitudinal fibers were found towards the periosteal surface. In addition, the posteromedial aspect contained significantly more transverse collagen fibers than the opposing anterior and anterolateral aspects. This was particularly apparent in the youngest age group. Despite these consistencies, it appeared that a single pattern of collagen fiber orientation patterning did not typify the mid-shaft femur; rather, a large amount of variability was identified both within and between age and sex groups.

Results of the study of mineralization density showed low variability in average mineralization within and between individuals. Mineralization and age correlated negatively. Mineralization was lowest in the periosteal third of the cortex, particularly in the anterolateral aspect, indicative of higher bone turnover in this region. The opposing posteromedial aspect showed much higher mineralization. This pattern was most prevalent among the youngest individuals in the sample. Despite these consistencies, interindividual variation was substantial even within a single age and sex group.

Based on the results of these studies, an average relationship between collagen fiber orientation and mineralization was identified, supporting some of the findings of Portigliatti-Barbos *et al.* (1983). Specifically, regions of longitudinal collagen fibers anteriorly and anterolaterally tended to contain low mineralization bone. On the opposing cortex (postero-medially and medially) high proportions of transverse collagen fibers and high mineralization bone were found. These results appeared consistent with existing knowledge of bending forces in the human femoral diaphysis, and with the average location of the axis of greatest bending rigidity (I_{max}) for the sample. Despite these average consistencies, correlations between the two microstructural variables were very low. Variability within the sample was high, such that very few individuals actually approached this average pattern for either variable.

There are several implications of these results. The differential influences of growth and adaptation, and the complex mechanical environment of the femoral diaphysis, may obscure relationships between microstructural variables. Moreover, individual variations in activities, nutrition, or disease states may result in many possible optimal microstructural configurations. In addition, the variability in microstructural organization and remodeling rates, even within a single individual, has strong implications for the continued use of bone histomorphometry as an aging technique in archaeological or forensic samples.

Acknowledgments: Supported by L.S.B. Leakey Foundation and NSF pre-doctoral awards, and NSF funding to the Analytical Microscopy and Imaging Center in Anthropology. Alan Boyde kindly made available the backscattering electron standard.

References

1. Portigliatti-Barbos M, Bianco P, Ascenzi A: Distribution of osteonic and interstitial components in the human femoral shaft with reference to structure, calcification and mechanical properties. *Acta anat*, 115, 178–186 (1983)

Quantification of dental microwear using scanning electron microscopy: Intraobserver error, interobserver error, and comparison of different techniques

F.E. GRINE, P.S. UNGAR,* M.F. TEAFORD†

Departments of Anthropology and Anatomical Sciences, State University of New York, Stony Brook, NY; *Department of Anthropology, University of Arkansas, Fayetteville, AR; †Department of Cell Biology and Anatomy, Johns Hopkins University, Baltimore, MD, USA

Studies over the past two decades have demonstrated a degree of correlation between dietary habits and the microscopic details of occlusal surface wear on the molar teeth of extant primates. In particular, the incidence of pits and the sizes of microwear feature have been shown to vary among broadly defined dietary categories. These patterns have enabled inferences to be made about prehistoric diets in both archeological and paleontological contexts. Workers have employed several different techniques in the measurement of microwear, but the comparability of these techniques has not been documented. Because occlusal wear defects are irregularly shaped and may lack sharply defined margins, their definition and measurement will necessarily be subject to intra- and interobserver error, both of which have yet to be documented.

The comparability of the three most widely used techniques of microwear quantification, as detailed by Teaford,[1] Grine,[2] and Ungar,[3] was examined. Each of us employed a dif-

ferent method. The average deviation of microwear feature diameter (pit breadth) means was about 25%; that is, the lowest and highest of the three means deviated from the average of the three by some 25%. Incidences of occlusal pitting (where a pit was defined as a feature with a length-breadth ratio of Æ 4:1) showed a somewhat higher average deviation among the three analyses. The difference in the magnification factor employed by these techniques (200× vs. 500×) was not primarily responsible for this magnitude of error.

Interobserver error was examined with each of us using the technique of Ungar[3] to analyze four scanning micrographs. In this study, feature diameters means had an average deviation of about 10%. Pitting incidences also varied with a margin of error of about 10%. The rank ordering of the four micrographs in terms of feature size and the frequency incidence of pitting was consistent among all three observers.

Intraobserver error was determined by the repeated measurement of two micrographs using the technique of Ungar.[3] The micrographs were analyzed with an average interval of some 10 days between each session. An average deviation of about 12% affected the measurement of feature diameters and pitting incidences in this study.

These results suggest that microwear quantification permits the distinction between broad dietary categories, but the margin of intra- and interobserver error should be taken into account when defining pattern differences between species or when documenting seasonally mitigated differences within a species.

Supported by NSF SBR 9804882.

References

1. Teaford MF: Molar microwear and diet in the genus Cebus. *Am J Phys Anthrop* 66, 363–370 (1985)
2. Grine FE: Dental evidence for dietary differences in Australopithecus and Paranthropus: a quantitative analysis of permanent molar microwear. *J Human Evol* 15, 783–822 (1986)
3. Ungar PS: A semiautomated image analysis procedure for the quantification of dental microwear. II. *Scanning* 17, 57–59 (1995)

A new method for histology using backscattered electron imaging of tissue embedded in an iodinated polymer

A. BOYDE, P.G.T. HOWELL, L.H. KOOLE*

Dept. of Anatomy and Developmental Biology, University College London, London, UK; *Center for Biomaterials Research, University of Maastricht, Maastricht, The Netherlands

We describe the utility of methacrylate copolymers with iodine covalently linked to their backbone structure as embedding media. We used mixtures of methylmethacrylate (MMA) and 2-[4'-iodobenzoyl]-oxo-ethylmethacrylate (4-IEMA) (1). Mouse, rat, hamster, dog, and horse bone and soft tissue samples were fixed in NFS or 70% ethanol and embedded using a molar ratio of 4IEMA:MMA which gave an empirical formula of $C_{31}H_{41.8}0_{11.2}I$. Block surfaces were finished by polishing or diamond ultramilling and carbon coating. Digital backscattered electron (BSE) images were recorded using a Zeiss DSM962 SEM. Images with 200 micron field width and 2048 pixel resolution at 20 kV and 0.5 nA beam current showed no evident beam damage. At 30 kV, increasing the BSE yield and thereby the working distance and field of view, wide fields (e.g., 15 mm) could be imaged in a single scan.

The BSE images appear as traditional black and white histology illustrations spanning the range of magnifications used in light microscopy and low-magnification transmission electron microscopy. This arises from the fact that image contrasts in cells and soft tissues reflect the inverse of the mass concentration of organic solids retained after the embedding protocol: proteins, DNA, and RNA are retained: lipids are lost in ethanol and methyl methacrylate monomer, as in conventional histologic processing for light microscopy.

However, the new procedure has significant advantages. Because the material is a solid block, we can prepare surfaces flattened to <0.1 micron roughness. At 20 kV, the information depth is of the order of 0.5 microns. It is not possible to generate very extensive sections that are so thin. Furthermore, physical sections containing tissue types with varying degrees of hardness are deformed and do not lie within a conventional optical section plane. In addition, block surfaces can be finished to have surfaces meeting perpendicularly (or at any other chosen angle), and these can be imaged simultaneously or consecutively to generate an instantaneous 3-D reconstruction with exact matching at joins and correct representation of tissue appearances in contrasting planes of section.

The method has particular application in the field of study of tissue adaptation to (transcutaneous, transmucosal, and intrabony) metallic and ceramic implants, where normal physical sectioning procedures would result in disruption of the interface.

For calcified tissues, we can ultimately destroy the mineralised matrix by successive treatments with acid and alkali, combined with ultrasonication to disrupt and disintegrate, for example, the lacunar-canalicular system in bone. The resultant cast shows the cells that contacted hard tissue surface in a correct 3-D context.

Acknowledgments: The authors thank Mo Arora and Roy Radcliffe for technical assistance and the Horserace Betting Levy Board for support.

References

1. Kruft MA, Benzina A, Bar F, van derVeen FH, Bastiaansen CW, Blezer R, Lindhout T, Koole LH: Studies on two new radiopaque polymeric biomaterials. *J Biomed Mater Res* 28, 1259–1266 (1994)

Current research of the Analytical Microscopy and Imaging Center in Anthropology

T. G. BROMAGE, I. G. CHOWDHURY, P. ELLIS, R. FERRELL,[*] A. MARSHACK,[†] S. MCFARLIN,[‡] R. NUGER,[‡] P. O'HIGGINS,[§] W. PARDI, T. PLUMMER,[¶] R. POTTS,[**] J. TAUSCH, J. WARSHAW[‡]

Department of Anthropology, Hunter College, City University of New York, NY; [*]Department of Anthropology, Pennsylvania State University, University Park, Pennsylvania; [†]Department of Anthropology, Harvard University, Cambridge, Massachusetts; [‡]Department of Anthropology, NYCEP, City University of New York Graduate Center, New York; [§]Department of Anatomy and Developmental Biology, University College London, London, England; [¶]Department of Anthropology, Queens College, City University of New York, New York; [**]Department of Anthropology, Smithsonian Institution, Washington, DC, USA

The Analytical Microscopy and Imaging Center in Anthropology (AMICA) is a unique environment wherein faculty, students, and visiting researchers are able to perform multi-disciplinary microscopy research activities of particular significance to the anthropological sciences. Information about this Center may be found at: http://urban.hunter.cuny.edu/amica.

We provide here vignettes of AMICA work in progress, employing a variety of imaging systems important to this work: Leica-Leitz DMRX/E Universal Microscope, Leica MZ APO Stereo Zoom Microscope, Edge R400 and H160 Real-Time 3D Microscopes, Mitutoyo Video-Based 3-D Digitizer, Technical Instrument K2-S BIO Confocal Microscope, LEO Stereoscan 440 Scanning Electron Microscope, Leica Quantimet 600 High Resolution Image Analysis System, Syncroscopy Montage Explorer and Auto-Montage image systems, and image archiving and recording workstations.

Cocaine Binging and Bone Development (Chowdhury and Bromage)

While a number of studies have concentrated on the neurobiology of opioids, we wish to examine the effects of cocaine bingeing on bone development. The influence of cocaine on hard tissue development was considered in the femur and humerus of the growing laboratory rat. Scanning electron microscopy of whole bone surface remodeling and light microscopy of histological thin sections derived from midshaft are being studied. Preliminary results indicate that there is a perturbing effect on cells responsible for bone surface remodeling.

Craniofacial Muscular and Skeletal Postnatal Growth in Female *Erythrocebus patas* (Ellis, O'Higgins, and Bromage)

The facial skeleton and musculature of four female age-graded Erythrocebus patas were examined to determine and document patterns of postnatal growth. Scanning electron microscopy of the developing bone surfaces was performed to characterize the bone growth remodeling state of the facial skeleton. Facial muscles were dissected from the facial skeleton and fascia, carefully noting their origins and insertions. Three-dimensional (3-D) landmark coordinate data of the remodeling fields and muscle distributions were obtained and analyzed conjointly using the geometric morphometrics package Morphologika. The result is an animated three-dimensional ontogenetic sequence, representing both the cellular activity of the developing craniofacial skeleton, the resulting morphological changes, and the covariation between the muscles of facial expression and skeletal developmental proportioning.

Enamel Defects and Demographic Analysis (Ferrell)

Developmental defects within tooth enamel called accentuated striae (AS), which form during periods of physiological stress, have been used in previous studies of skeletons as a measure of a past population's nutrition and disease experience, since studies of living people have shown that tooth defects are associated with periods of nutritional stress and disease. However, the assumption that a higher number of AS in a skeletal sample indicates a population with poorer nutrition and a higher disease load has not been thoroughly tested and is always confounded by the selective skeletal sample that results from a population with heterogeneous levels of health. This study tests for a relationship between AS and age at death in skeletons from a medieval Danish village to determine whether those individuals with a higher risk of death (those dying at younger ages) had a higher incidence of AS. Individual AS chronologies are identified using light and scanning electron microscopy and survival analysis methods are then used to test for such a relationship.

Engraving Practice and Calendrical Notation in the Upper Palaeolithic (Marshack)

The beginnings of record keeping, or notation, apparently begin in the Upper Paleolithic some 20,000 or more years before formal writing and arithmetic appeared in the Holocene. The most important of the early notations is a small bone plaque from the Grotte du Taï, France, ca. 10,000 BC, which records a continuous serpentine sequence of sets and subsets of engraved marks for what appears to be a period of more than three years. The Taï plaque has raised significant interdisciplinary psychological and neuropsychological discussion. Since the plaque had been curated for three years, had it been marked with

a changing sequence of tools? Would one tool have been curated with the plaque for use during this time? Were different tools used at different locations during the group's seasonal movements? Could such notations have been read by anyone but the maker? There are a host of pragmatic and theoretical questions concerning the tradition and mode that can now be addressed by new and developing microscopy and software imaging technologies.

Comparative Primate Bone and Skeletal Structure (McFarlin and Warshaw)

Combined analyses of bone tissue composition, at both micro- and macro-structural levels, provide a holistic understanding of comparative primate skeletal morphology, functional adaptation, and growth and development. Such studies have important implications for understanding the biology of both living and extinct taxa. Utilizing broadly a comparative primate (and limited non-primate mammalian) sample, including focused primate samples (with individuals of known sex, age, body weight and provenience), our research has two major objectives: 1) to investigate the relationship between the micro-structure of developing bone and organismal life history in known primate populations; 2) to examine the nature of relationships among the structural-functional properties of bone tissues and skeletons, and their expression in specific lineages. We focus on a variety of properties of bone: Cross-sectional geometry; distribution of primary tissue types; intracortical remodeling, lamellar organization, osteocyte lacunar density, and preferred collagen fiber orientations.

Paleopathology of an Archaic Homo mandible (Nuger, Plummer, and Potts)

In 1932 an expedition led by L.S.B. Leakey discovered the anterior portion of a fossilized hominin mandible at Kanam, Kenya. While the taxonomic status of this specimen is uncertain, the Kanam mandible displays a pathological anomaly around the symphysis. This lesion is readily observed macroscopically as an irregularly shaped mass. Previous investigators have suggested four diagnoses: A subperiosteal ossifying sarcoma, a Burkitt's lymphoma, an osseous keloid following a fracture, and an osteomyelitis following a fracture. The lesion is currently being investigated using scanning electron and confocal light microscopy. Our presentation will review the preliminary results of this examination.

Three-dimensional Visualization of Bone Microanatomical Features (Pardi and Bromage)

We are presently experimenting with three dimensional (3-D) reconstruction and volume rendering of serial bone sections using two software packages; Analyze (Mayo Foundation, Rochester, Minnesota) and VoxBlast (VayTek, Inc., Fairfield, Iowa). Both are fully interactive with our light microscopy imaging. In addition to reconstructions of serial bone sections into 3-D volumes, one of the many features of Analyze and VoxBlast is their ability to detect and measure features within the bone volume, isolate regions of interest, and render other features transparent. For instance we will demonstrate how bone lamellae may be isolated from the surrounding bone matrix, manipulated in 3-D space, and virtually sectioned and measured. Serial 3D reconstruction of high resolution images may also be undertaken to measure such parameters such as osteocyte lacunae density.

The Muscle-Bone Interface of the Marmoset (*Callithrix jacchus*) Femur (Tausch and Bromage)

Understanding the morphologic and functional relationships between bone and muscle is important in studies of development and growth of the skeleton. Muscle insertions may include: 1) extrinsic collagenous bundles, 2) extrinsic fiber insertions into periosteum which, in turn, has its own collagenous insertions to the bone, and 3) insertions into joint capsule connective tissue. While the microanatomical characteristics of Sharpey fibers at the muscle-bone interface have been described, variation in both surface morphology and internal bone tissue organization is expected to vary according to muscle insertion types. To better realize their nature, surface and subsurface microstructural features of a subadult *Callithrix jacchus* femur are being mapped to delimit the relationship between muscle insertion type, action, and the spatial orientation and composition of the bone cortex underlying the muscle.

Acknowledgments: The Analytical Microscopy and Imaging Center in Anthropology is equipped entirely by grants from the National Science Foundation and the State of New York.

Nanotechnology and nanofabrication

Using Scanning probe lithography techniques and self-assembled monolayers to probe molecular electronics behaviors

C. GORMAN

Department of Chemistry, North Carolina State University, Raleigh, NC, USA

Electroactive self-assembled monolayers and multilayers and scanned probe lithography techniques have been used to construct prototype molecular electronics devices[1]. The self assembled monolayer may be used both as a de-

vice element and as a foundation for building up molecular devices. The investigation demonstrates that electroactive self-assembled monolayers such as those with ferrocenyl or galvinoyl groups can display substantial, negative differential resistance behavior in the current voltage curves. The relationship between electroactivity (e.g., redox behavior) and nonlinear electronic behaviors (e.g., those in tunneling diodes) has some parallels, but also some important differences.

Reference

1. Gorman CB, Carroll RL, He Y, Tian F, Fuierer R: Chemically well-defined lithography using self-assembled monolayers and scanning tunneling microscopy in non-polar organothiol solutions. *Langmuir* 16,15, 6312–6316 (2000)

The miniaturized multiple-tip scanning probe microscope–a useful tool for experiments in nanotechnology

M. HIETSCHOLD, F. MÜLLER, A.-D. MÜLLER, M. REUTER, J. WIBBELER,† B. LOEBNER,* TH. GESSNER*

Solid Surfaces Analysis Group, Institute of Physics; *Center for Microtechnologies, Chemnitz University of Technology, Chemnitz; †CAD-FEM GmbH, Grafing, Germany

Since the invention of the atomic force microscope[1] it has become increasingly clear that microminiaturized and microfabricated probes[2], probes with integrated functions for signal detection[3] or controlled movements[4], and finally parallel operated arrays of independent probes (for scanning tunneling microscopy (STM)[5] and scanning force microscopy (SFM)[6,7]) would be very well suited to the new scanning probe methods and, would also offer qualitatively new opportunities and prospects.

A recent spectacular publication from IBM[8] described an array of about 1,000 independent cantilevers. The aim of this very prestigious development (the "millipede") is the creation of a unique mass-storage device which overcomes the serious obstacle of all previous attempts at scanning probe lithography which has been limited by its slow, one-tip operation. Paralleling the tool-probes is the inherently new approach to making the step from academic research to real broad application.

Another concept brought forward by some of the authors[9] is to use a rather small array of versatile tools in a new type of a micro-nano-lab where several independent probes have access to overlapping areas on the sample surface. This allows different types of analysis and surface structure modification to be feasible by continuous and simultaneous operation of only one device.

A first step toward this goal was the development of a multiple-tip STM. This device consists of 4 independently

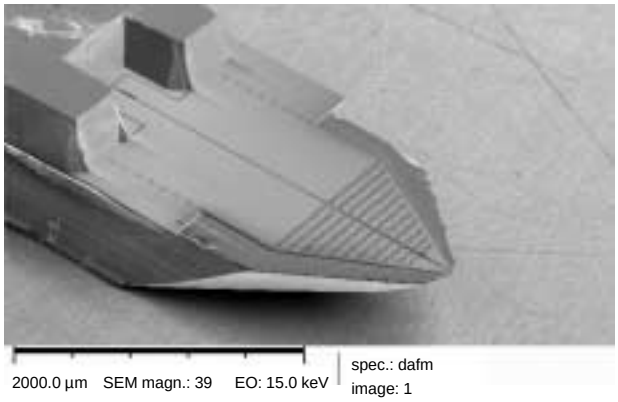

FIG. 1 Scanning electron microscope image of a microstructure with two scanning force microscopy tongues.

controllable Si tongues each of them equipped with a tunnel tip, The single tongues can be moved vertically by an applied electric field between the conductive tongue surface and a metal electrode in front of it. The whole system can be scanned over a sample surface. The mutual tip distances are of the order of 5 µm.[9]

A second step is a multiple-lever SFM. All single elements are force microscopes operated in the dynamic mode.[10] The single cantilevers are positioned at the outer edge of silicon tongues which can be excited to mechanical oscillations by electrical fields applied between the tongue surface and a metal electrode in front of them (deposited on a pyrex substrate bonded to the Si wafer). The figure shows a scanning electron microscope (SEM) image of a microstructure with two SFM tongues. The tongue surfaces are structured by a hole pattern to reduce damping of the excited vibrations during operation. The cantilever elongations are detected by the usual laser-beam deflection method. Images of sample surface topography with nm-resolution have been already obtained by this device. The microfabricated units can be inserted in the head of a home-built AFM.

The structures presented are characterized by typical eigenfrequencies f_i = 80 and 10 kHz (for cantilever and tongue, respectively), quality factors of the order of 10 and a sensitivity of 2 µm / 80 V (there is a quadratic dependence from the applied bias). Our present efforts are mainly directed to a further optimization of the design of the microstructures and suitable parallelization of the data acquisition process. The first task is accompanied by finite-element simulations of the microstructural design.

A possible future implementation will be parallel operation of several force microscopes at different positions of the sample surface with overlapping scan areas. Further extensions could be simultaneous profilometry and lithography or operation as scanning electrical force microscopes (SEFM).[11,12]

Acknowledgments: The authors are grateful for financial support by Deutsche Forschungsgemeinschaft in terms of Sonderforschungsbereich SFB 379.

References

1. Binnig G, Quate CF, Gerbe Ch: Atomic Force Microscopy. *Phys Rev Lett* 56, 930–933 (1986)
2. Albrecht TR, Quate CF: Atomic resolution with the atomic force microscope on conductors and nonconductors. *J Vac Sci Technol* A6, 271–274 (1988)
3. Tortonese M, Barrett RC, Quate CF: Atomic resolution with an atomic force microscope using piezoresistive detection *Appl Phys Lett* 62, 834–836 (1993)
4. Brugger J, Blanc N, Renaud Ph, deRooij NF: Microlever with combined intergated sensor/actuator functions for scanning force microscopy. *Sens Act* A43, 339–345 (1994)
5. Albrecht TR, Akamine S, Zdeblick MJ, Quate CF: Microfabrication of integrated scanning tunneling microscope. *J Vac Sci Technol* A8, 317–318 (1990)
6. Blanc N, Brugger J, deRooij NF: Electrostatically actuated silicon micromachined sensors for scanning force microscopy. *Forces in Scanning Probe Methods*. (Eds. H.J. Güntherodt *et al.*, IBM (1995) 79–84
7. Miller SA, Turner KL, MacDonald NC: Microelectromechanical Scanning Probe Instruments for Array Architectures. *Rec Sci Instrum* 68, 4155–4162 (1997)
8. Despont M, Brugger J, Drechsler U, Dürig U, Häberle W, Lutwyche M, Rothuizen H, Stutz R, Widmer R, Binnig G, Rohrer H, Vettiger P: VLSI-NEMS chip for parallel AFM data storage. *Sensors Actuators* 80, 100–107 (2000)
9. Müller F, Müller A-D, Hietschold M, Pfeifer G, Löbner B: Micromechanical Multi-Tip-Sensor Device for Overlapping Scan Ranges – First Steps Towards a Microfabricated Nanotechnology-Workstation. *Proc. Micro System Technologies 96*, (Eds. H. Reichl, A. Heuberger VDE) (1996) 615–619
10. Müller F, Müller A-D, Hietschold M, Kämmer S: Applications of scanning electrical force microscopy. *Microelectron Reliab* 37, 1631–1634 (1997)
11. Müller F, Müller A-D, Hietschold M, Kämmer S: Detecting electrical forces in non-contact atomic force microscopy. *Meas Sci Technol* 9, 732 (1998)
12. Martin Y, Williams CC, Wickramasinghe HK: Atomic force microscope–force mapping and profiling on a sub 100-Å scale. *J Appl Phys* 61, 4723–4729 (1987)

Chirality in self-assembled interfacial layers: The view from one billionth of an inch

G. FLYNN

Department of Chemistry and Columbia Radiation Laboratory, Columbia University, New York, NY, USA

Introduction

Since its invention nearly two decades ago, scanning tunneling microscopy (STM) and many of its scanning probe microscopy (SPM) variants have become essential tools for researchers working at the interface between various scientific disciplines including chemistry, physics, material science, and environmental studies. While initial studies probed bare metal and semiconductor surfaces under ultrahigh vacuum conditions, recently, STM has been used under ambient conditions and at liquid-solid interfaces to investigate the structure and dynamics of bare and adsorbate-covered surfaces in situ with molecular, submolecular, and even atomic resolution.

One of the principal focuses of our STM work has been concerned with the identification and use of STM "chemical marker groups" to interpret patterns of molecular ordering and conformations of individual molecules adsorbed at the liquid-solid interface. "Marker groups" are chemical functional groups that exhibit unusual contrast in STM images relative to the rest of the atoms in a molecule.[1,2]

High Resolution Scanning Tunneling Microscopy of Molecules at the Liquid-Solid Interface

Figure 1 shows an image of docosanol ($CH_3(CH_2)_{20}CH_2OH$) in phenyloctane solvent physisorbed on a graphite surface. Three of these molecules (in the middle of the image) are fully exposed. This topograph is just 3 nm on an edge and inspection of one of the fully exposed molecules shows individual spots that can be identified with each of the H atoms in the molecule protruding above the surface. The image is consistent with one where the carbon backbone of the adsorbed species is fully extended in an all trans configuration. Careful measurement of the apparent distance between H atoms suggests that the molecular backbone is almost parallel to the graphite surface. The position of the –OH functional group in this image can be identified by the dark trough at one end of the molecule.

Determination of Molecular Conformation and Chirality

Scanning tunneling microscopy has been used to determine the chirality of molecules chemisorbed on a silicon surface under ultra high vacuum conditions.[3,4] In addition the carboxylic acid and Br atom chemical marker groups, coupled with high resolution STM images similar to those

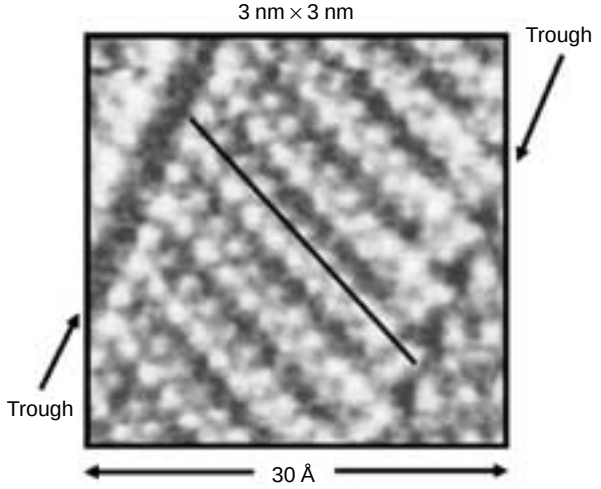

FIG. 1 A 3 × 3 nm image of docosanol taken at the liquid-solid interface on graphite. The black bar is superimposed over one molecular length, measured to be 3.0 + 0.2 nm.

in Fig 1, have been used to assign the absolute chirality for molecules of (R)/(S)-2-bromohexadecanoic acid physisorbed on a graphite substrate.[5] The separation of molecules into chiral domains for pure racemic R/S-2-bromohexadecanoic acid occurs at the liquid-solid interface and is likely driven by two significant energy dependent orientational effects.

Summary

Scanning tunneling microscopy provides remarkably detailed information that can be employed to analyze and hopefully tailor interfacial properties that touch issues at the heart of interfacial studies of self assembly, such as: (1) the nature of the forces governing molecular organization on the surface, (2) the roles of adsorbate-adsorbate versus adsorbate-substrate interactions in driving and stabilizing molecular order, (3) the relationship between two-dimensional structure observable by STM and three-dimensional crystalline ordering, and (4) the observation, design, and control of interfacial assemblies.

Acknowledgments: This work supported by grants from the NSF (CHE-97-27205, CHE-00-95649) and in part by the Columbia MRSEC (NSF DMR-98-09687).

References

1. Venkataraman B, Flynn GW, Wilbur J, Folkers JP, Whitesides GM: Differentiating Functional Groups with the Scanning Tunneling Microscope. *J Phys Chem*, 99, 8684–8689 (1995)
2. Cyr DM, Venkataraman B, Flynn GW, Black A, Whitesides GM: Functional group identification in scanning tunneling microscopy of molecular adsorbates. *J Phys Chem*, 100, 13747–13759 (1996)
3. Lopinski GP, Moffatt DJ, Wayner DDM, Wolkow RA: How stereoselective are alkene addition reactions on Si(100)? *J Am Chem Soc*, 122, 3548–3549 (2000)
4. Lopinski GP, Moffatt DJ, Wayner DDM, Zgierski MZ, Wolkow RA: Asymmetric induction at a silicon surface. *J Am Chem Soc*, 121, 4532–4533 (1999)
5. Fang H, Giancarlo LC, Flynn GW: Direct determination of the chirality of organic molecules by scanning tunneling microscopy. *J Phys Chem* B, 102, 7311–7315 (1998)

Nanoindentation and adhesion-force-mapping studies of polymer blend films: Factors influencing the measured force of adhesion

P. EATON, T.G. NEVELL, J.D. SMART, J.R. SMITH, J. TSIBOUKLIS

School of Pharmacy and Biomedical Sciences, University of Portsmouth, St. Michael's Building, Portsmouth, UK

Adhesion force mapping[1] and indentation mapping[2] using atomic force microscopy has been used to investigate a phase-separated blend of poly(methyl methacrylate) (PMMA) and poly(dodecyl methacrylate) (PDDMA). Comparison of the results from the blend with those from the pure constituent polymers showed that force mapping could identify PMMA- and PDDMA-rich areas in the blend. The adhesion and indentation maps produced were deconvoluted from sample topography and contrasted with data obtained from contact angle goniometry. The dependence of the measured adhesion forces on sample stiffness and topography provide further information concerning the contrast mechanism for adhesion force mapping of heterogeneous polymers.

References

1. Burnham NA, Colton HM, Pollock HM: Interpretation of force curves in atomic force microscopy. *Nature 4*, 64–80 (1993)
2. Raghavan D, Gu X, Nguyen T, Vanlandingham M, Karim A: Mapping polymer heterogeneity using atomic force microscopy phase imaging and nanoscale indentation. *Macromolecules 33*,7, 2573–2583 (2000)

Biological fibers as building blocks for nanosystems

R. GRÖGER,[*] P. VON BLANCKENHAGEN,[*] F. XIE,[*§] S. BEHRENS,[†] D. BARTON,[‡] H. SCHORLE[‡]

Forschungszentrum Karlsruhe, [*]Institut für Nanotechnology, [‡]Institut für Technische Chemie, [§]Institut für Toxikologie und Genetik, Germany; Institute of Physics, Chinese Academy of Sciences, China

Scanning probe microscopy (SPM) has allowed for the manipulation, modification, and characterization of organic molecules and fibers under ambient conditions with high resolution down to the atomic scale. It was shown that the components of cells prepared in solution could be depicted if they are deposited on appropriate substrates, such as single-crystal surfaces of mica or pyrolitic graphite. Nanometer scale organic constituents of cells, as realized in nature, may also become promising building blocks of artificial nanosystems, for example, as structure material, templates or functional components, such as conducting lines, molecular switches, or local catalysts.

Scanning probe microscopy measurements in this field were first performed to find suitable preparation methods and substrate surfaces with appropriate adhesion properties. As far as DNA molecules, as well as actin fibers and microtubulin fibers, are concerned, mica or highly oriented pyrolitic graphite (HOPG) are versatile substrate materials. These fibers have a diameter of about 7 and 25 nm, respectively, and a length of up to more than tens of micrometers.

We are studying the growth, self-organization, and thermal stability of the natural building blocks, as well as their modified derivatives, produced for example, by metalliza-

tion. For these studies, the sample temperature can be varied between room temperature and about 200 C° by means of an in situ heating stage adapted to the multimode atomic force microscope (AFM, Digital Instruments Nanoscope IIIa). For imaging the tapping and for manipulation, the contact mode of operation was applied in most part of the AFM studies. High-resolution experiments were performed with a scanning tunneling microscope (STM) operated in air.

By AFM experiments it was possible for the first time to observe directly the in-situ polymerization of a fiber, and quantitatively analyze the length growth of actin fibers. The growth started at freshly produced fiber ends after the native fiber was cut, using the AFM as a milling tool, and has been observed over a time period of 74 h. The growth rate in air with a humidity of 40% was 50 nm/h. The growth direction could be changed by bending the front end with the AFM tip. The fiber showed a periodic superstructure.

Natural as well as metallized microtubulin fibers have been prepared and imaged by AFM on mica substrates and by STM on HOPG substrates. The metallized samples are prepared for local conductivity measurements.

Guiding self-assembly with the tip of an atomic force microscopy

P. MESQUIDA, A. STEMMER

Nanotechnology Group, Swiss Federal Institute of Technology, Zurich, Switzerland

Nature successfully manufactures and assembles (sub)nanometer-sized components into larger structures within living cells, a working environment completely opposite to the cleanroom technology required for today's (sub)microfabrication processes. To gain speed and eliminate high-cost infrastructure, a sensible strategy for nanofabrication, therefore, will take advantage of production principles similar to nature's, that is, rely on specificity and self-assembly.

To create surfaces with defined geometry and functionality on the nanometer up to the micrometer scale, we apply voltage pulses to the conductive tip of an atomic force microscope (AFM) to deposit a pattern of localised electric charges on a suitable electret while the tip is drawn across the substrate. Subsequently, this latent image is "developed" by immersing the substrate into a solution carrying oppositely charged particles. The particles are driven to the charged pattern and attach there via Coulomb forces, similarly to the Xerox process on the macroscopic scale.[1]

For the charge writing process we currently achieve a resolution of 100 nm as determined by kelvin probe force microscopy.[2] The substrate is a Si-wafer coated with a 20 m thick Teflon-like fluorocarbon layer produced by plasma-enhanced chemical vapour deposition from hexafluoropropene precursor gas.[3] The voltage pulse height and length applied to the tip are +45 V and 5 µs, respectively. In teflon, deposited charges reside very closely to the surface and are quickly neutralised in water. Therefore, the latent charge image is "developed" in an insulating fluorocarbon liquid carrying colloidal particles. With commercial silica beads of 50 nm diameter, we currently achieve a resolution of about 800 nm.

The process described above is not restricted to insulating liquids. Electrets in which charges reside underneath the surface, open the way to aqueous solutions where the net charge carried by the solute can be easily adjusted. Local deposition of electric charges with an AFM tip provides direct control to guide the assembly of molecules and particles into larger structures in bottom-up nanofabrication.

References

1. Mort J: *The Anatomy of Xerography: Its Invention and Evolution.* McFarland, London (1989) 1–47
2. Jacobs HO, Stemmer A: Measuring and modifying the electric surface potential distribution on a nanometre scale: A powerful tool in science and technology. *Surf Interface Anal* 27, 361–367 (1999)
3. Knapp HF, Stemmer A: Preparation comparison and performance of hydrophobic AFM tips. *Surf Interface Anal* 27, 324–331 (1999)

Sunday, May 6

Probe microscopy for nanostructured materials

Scanning force microscopy of nanostructured materials

L. CHI

Physikalisches Institut, Westfaelische Wilhelm-Universtaet Muenster, Muenster, Germany

Lateral ordered nanoscopic structures over macroscopic regions can be obtained by adjusting the subtle balance of molecule-molecule interactions and molecule-substrate interactions when preparing thin organic films with Langmuir-Blodgett (LB) and self-assembly (SA) techniques. The origin of the structures is based on different mechanisms, such as 1) transfer process (from air/water interface to air/substrate interface) due to wetting instability; 2) interaction with substrate; 3) "mismatch" between hydrophilic group and hydrophobic regimes and 4) self-organization due to inter-molecular interactions. Besides the nanoscopic size and characteristic long-range order, the structures may be heterogeneous.

Scanning probe microscopy methods, especially scanning force microscopy (SFM), which turned out to be of great success for inspecting various organized organic molecular assembles, are used to characterize the structures obtained. The operation of SFM in dynamic mode, especially in the attractive regime by means of an active feedback controller, can minimize the damaging interaction between the tip and the sample, thus allowing the non-destructive imaging of weekly bound monolayers and soft molecular assemblies.

Modern optical microscopy, Part I

Biological confocal microscopy: Applications and quantitation

J.N. TURNER, D.H. SZAROWSKI,* S. LASEK, B.A. SIPPLE, W. SHAIN, A. CAN,* K. AL-KOFAHI,* B. ROYSAM*

Wadsworth Center, New York State Dept. of Health, Albany, NY; *Electrical, Computer and Systems Engineering, Rensselaer Polytechnic Institute, Troy, NY, USA

Most objects examined by light microscopy are three-dimensional (3-D). Imaging and analyzing the third dimension is essential. A 3-D object is one whose thickness, along the optic axis, is greater than the depth-of-field of the objective lens, which defines the z-axis resolution. If the object thickness is only a few times the depth-of-field, the image intensity is considered to be thickness invariant, that is, equivalent objects appear the same independent of their z-position. This is reasonable for " thin" objects such as single cells. However, image intensity decreases exponentially with depth in thick specimens, such as tissue slices 100× or thicker than the depth-of-field. When an extended object, a neuronal dendrite or large nucleus, is imaged at a large enough z-dimension, its signal in a single optical section will equal the image noise level. At this depth, the object is not detected and information is missing from the 3-D image. This is difficult to detect, as other brighter objects will be detected at the same depth. Unless a priori knowledge about the sample is available, the possibility of misinterpretation is high, especially the relative 3-D distributions of different objects such as large and small nuclei.[1] Approaches are being developed to predict the signal attenuation function and to correct for it. The most sophisticated approach is to image the specimen from both sides and register the two images creating a thicker combined 3-D image.[2]

Image interpretation can be further complicated by incomplete penetration of the labeling molecules into thick specimens, especially for immunocytochemical agents.[3] Figure 1 is a good example of this preparation artifact. The x,y projection appears to represent accurately the structure and distribution of astrocytes in brain, but the x,z projection shows incomplete penetration of the label. Penetration through the lumen of large vessels can further complicate the artifact.[3]

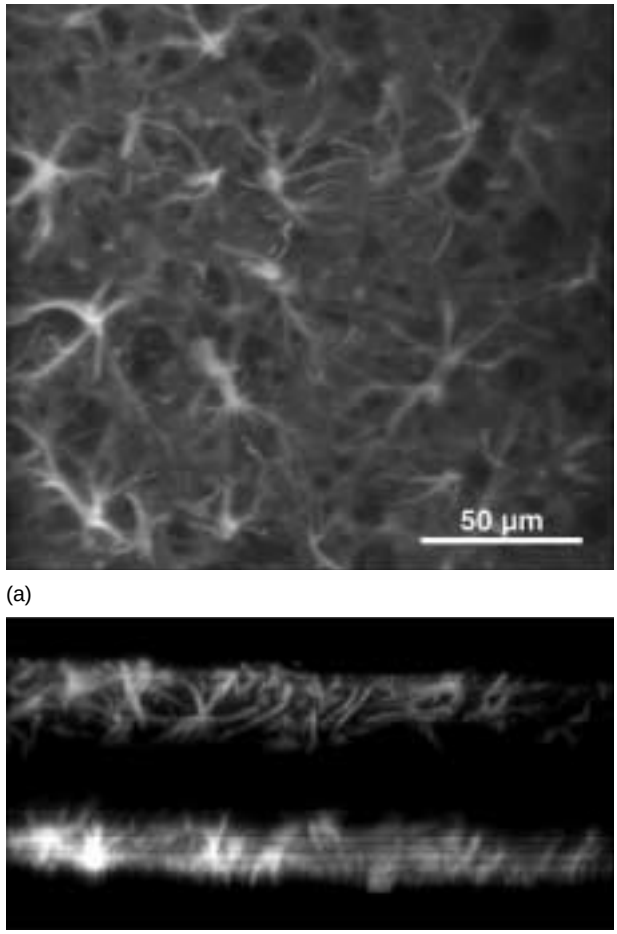

FIG. 1 An 80 µm brain slice immunocytochemically labeled for tenascin C. (a) An x,y projection shows what appears to be normal distribution of astrocytes; (b), An x,z projection shows incomplete penetration of the label.

Quantitative analysis is necessary for comparative studies, but is complicated by image variability. Adaptive segmentation delineate cells and nuclei[3–5] and vectorization methods trace branched structures, neurons[3,6] Total cells and nuclear types can be analyzed in volumes of tissue, and cells positive for immunochemical labels can be quantitated including their 3-D distributions.[3] Intensity-based analyses are difficult due to depth dependence signal levels, photobleaching, instrumental variations, spherical aberration, and label penetration and specificity. Deconvolution may also be essential for accurate analyses.

References

1. Shain W, Kayali S, Szarowski D, Davis-Cox M, Ancin H, Bhattacharjya AK, Roysam B, Turner JN: Application and quantita-

tive validation of computer-automated 3-D counting of cell nuclei. *Microsc Microanal*, 5, 106–119 (1999)
2. Can A, Lasek S, Szarowski DH, Turner JN, Roysam B: A Robust Two-View Method For Increasing The Imaging Depth And Correcting For Signal Attenuation In Confocal Microscope Images. *Proc Ann Meeting of the Microscopy Society of America*, 58th annual meeting, Philadelphia, (2000)
3. Turner JN, Shain W, Szarowski DH, Lasek S, Dowell N, Sipple B, Can A, Al-Kofahi K, Roysam B: Three-dimensional light microscopy: Observation of thick objects. *J Histotechnol (*2000)
4. Ancin H, Roysam B, Dufresne TE, Chestnut MM, Ridder GM, Szarowski DH, Turner JN: Advances in automated 3-D image analysis of cell populations imaged by confocal microscopy. *Cytometry*, 25, 221–234, (1996)
5. Roysam B, Ancin H, Bhattacharjya AK, Chisti A, Seegal RF, Turner JN: Algorithms for automated cell counting in thick specimens from 3-D confocal florescence microscopy data. *J Microsc* 173, 115–126, (1994)
6. Cohen AR, Roysam B, Turner JN: Automated tracing and volume measurements of neurons from 3-D confocal fluorescence microscopy data. *J Microsc* 173, 103–114 (1994)

Biological confocal microscopy: Automated three-dimensional image analysis

B. ROYSAM, A. CAN, K. AL-KOFAHI, S. LASEK,* D.H. SZAROWSKI,* J.N. TURNER*

Rensselaer Polytechnic Institute, Troy; *Wadsworth Center, New York State Dept. of Health, Albany, NY, USA

Three-dimensional (3-D) automated image analysis methods are used to quantitatively analyze confocal microscopic images of biological samples.[1] These methods are needed when making morphometric measurements, and when it is desired to detect and quantify changes in cells and tissue that result from a variety of stimuli including biochemicals, physiological changes, aging, learning, and thermal effects (Fig. 1). Fully-automated methods are needed when a large number of images must be analyzed. For small numbers of images, interactive methods are more useful.

Changes of interest range from the sub-cellular to the organ level. Examples include cell counts,[2] structural changes in extended structures such as blood vessels and neurons,[4] and the movements of tagged biochemicals.

It is common to study a large volume of tissue in sections, and perform extensive morphometric measurements. These measurements are analyzed to detect and quantify changes. The prerequisite step to all methods is image preprocessing. For example, adaptive smoothing to overcome noise artifacts, deconvolution[6] and signal attenuation correction[3] are sometimes warranted. It may also be necessary to resample the images to make them more isotropic.

Image segmentation is the next step. This separates the objects of interest (the foreground) from the background. This is hard, since biological images exhibit large variability, and suffer from a variety of artifacts. To date, a general purpose segmentation algorithm has not been developed. A collection of algorithms that are successful under different conditions are available instead. Increasingly, the settings for these algorithms can be computed from user-supplied examples and counter-examples.

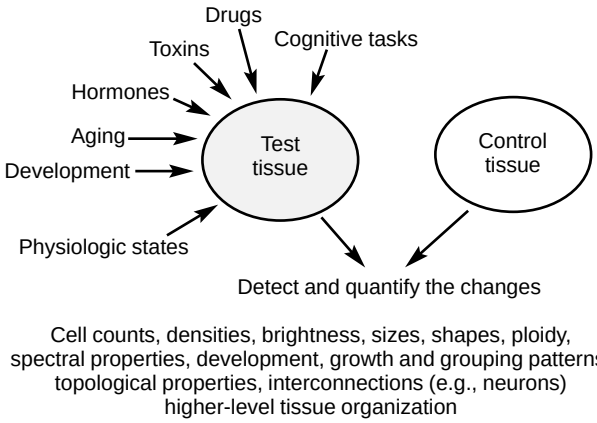

FIG. 1 Illustrating the types of problems of common interest.

The result of image segmentation is a set of labeled image regions representing connected objects such as nuclei that appear to be in contact. It is necessary to separate these regions into smaller regions that delineate objects, such as cell nuclei. Once this is done, morphometry can be accomplished. The segmentations can also be skeletonized to yield tracings of structures such as neurons and vasculature. It is straightforward to compute volumes, areas, lengths, diameters, eccentricities, and such other morphometric parameters. When changes over regions much larger than the field must be analyzed, it is necessary to perform non-overlapped sampling, or montage synthesis for consistent sampling.[5]

There are two approaches to change computation: Differential and automorphic. The former is relevant when the imaging is destructive (such as, fixed specimens). The latter is appropriate for live specimens that are imaged non-destructively.

Two important recent developments in 3-D image analysis are: 1) the emergence of fast exploratory image analysis algorithms, especially for the analysis of neurons and vasculature and 2) the birth of internet compute servers. It should be increasingly attractive for users to upload images to a server and download image analysis results.

References

1. Turner JN, Shain W, Szarowski DH, Lasek S, Sipple B, Pace C, Al-Kofahi K, Can A, Roysam B: Confocal light microscopy of brain cells and tissue: Image analysis and quantitation. *Acta Histochemica Cytochemica*, 32, 1, 5–11 (1999)
2. Ancin H, Roysam B, Dufresne TE, Chestnut MM, Ridder GM, Szarowski DH, Turner JN: Advances in automated 3-D Image analysis of cell populations imaged by confocal microscopy. *Cytometry*, 25, 221–234, (1996)
3. Can A, Lasek S, Szarowski DH, Turner JN, Roysam B: A robust two-view method for increasing the imaging depth and correct-

ing for signal attenuation in confocal microscope images. *Proc Microsc Soc Amer 58th Annual meeting*, Philadelphia, (2000)
4. Al-Kofahi K, Lasek S, Turner JN, Roysam B: Rapid automated 3-D tracing of neurons from confocal image stacks. *Proc Microsc Soc Amer 58th annual meeting*, Philadelphia, (2000)
5. Becker DE, Ancin H, Szarowski DH, Turner JN, Roysam B: Automated 3-D montage synthesis from laser-scanning confocal images: Application to quantitative tissue-level cytological analysis. *Cytometry*, 25, 3, 235–245 (1996)
6. Holmes TJ, Bhattacharyya S, Cooper JA, Hanzel D, Krishnamurthi V, Lin W, Roysam B, Szarowski DH, Turner JN: *Light Microscopic Images Reconstructed by Maximum Likelihood Deconvolution. Handbook of Confocal Microscopy*, (Ed. Pawley J). Plenum Press, New York, (1995)

Scanning oblique illumination for three-dimensional image representation in light microscopy

A. BOYDE, C.W. HEWITT,* G.L. GREENBERG†

Department of Anatomy and Developmental Biology, University College London, London, UK; *Department of Surgery, Robert Wood Johnson Medical School, Camden, NJ; †Edge 3D Imaging LLC, 441 N. 5th Street, Philadelphia, PA, USA

Real time 3-D images can be obtained from conventional (non-confocal, single objective) high-resolution transmission light microscopic systems by controlling the aperture of illumination, for example, by half-aperturing, such that each eye sees information deriving from opposite oblique ray bundles (1,2). Here we address the question of how much 3-D information can be obtained from temporal display sequences of images, that is, using motion rather than stereo-parallax.

Switching back and forth between the views obtained from the left, both, the right, both, and again the left off-axis illumination channels gives the impression of a tilting or rocking object, but backwards and forwards rocking displays of 3-D data sets are annoying. Motion parallax depth cues are best appreciated when the movement is continuous in one sense. Obviously we cannot keep looking at the same scene if we "fly past" it, so that continuous rotation of the real or apparent object is required. Since we cannot rotate other than very specially contrived samples on their own axes under a high numerical aperture light microscopic objective lens, we can exclude a real rotatory motion of a cylindrical sample as a realistic possibility.

We surmised that changing the direction of incidence of an oblique illuminating cone such that it spins whilst tilted with respect to the mean optic axis of the microscope system would create the illusion of the sample tilting continuously, or of the successive layers within the imaged volume moving past each other. We have made and evaluated several practical microscopic systems using this simple principle, and all worked. The simplest form of obscuring aperture is a pie-sector opening in an opaque disc placed at any of the relevant conjugate planes, the most accessible being in the illumination source and in the condensor lens assembly. For a live display, the open pie-wedge sector turns continuously at about one rotation per second. Now the light microscopic image can be transferred live via a video camera to a video display screen and many observers can view the same scene simultaneously. The effect is also obtained by recording and replaying a set of digital still images from a CCD camera, each taken with the illumination coming from a different off-axis direction. The new method has very important advantages in demonstrating and appreciating the 3-D context in supposedly "thin and flat" or "plane parallel" sections or cell smears.

References

1. Greenberg G, Boyde A: Novel method for stereo imaging in light microscopy at high magnifications. *NeuroImage* 1, 121–128 (1993)
2. Greenberg GL, Boyde A: Convenient and controllable direct-view 3D imaging in conventional optical microscopes: Approaches via illumination and inspection. *Proc Roy Microsc Soc* 32, 87–100 (1997)

Red laser video rate confocal reflection imaging for high spatial and temporal resolution study of intracellular motion

P. VESELY AND A. BOYDE*

Institute of Molecular Genetics, Academy of Sciences of the Czech Republic, Prague 6-Dejvice, Czech Republic; *Department of Anatomy and Developmental Biology, University College London, London, UK

Experience with confocal reflection imaging indicated that the original Noran Odyssey with composite video output (no longer in production) had apparently been the best system for backscattered light imaging of living cell internal dynamics. Rather than choose other systems, or the then-existent Noran upgrades (Odyssey XL, OZ), the betterment of the existing Odyssey appeared to be the right approach. The improvement included introduction of a 633 nm red HeNe laser and direct digital recording of the composite video signal in full PAL. Due to the lower dispersion of red light, we can obtain deeper penetration into the living cells, or small spheroids composed of up to 100 cells, or even into small fragments of normal or tumour tissues. The images have sharper contrast. Direct digital recording is achieved with a Sony DCR-TRV320E Camcorder with unblocked composite video input. The necessary movie editing and separation of images for further processing and animation is achieved in combination with a Pinnacle System Studio DV card (fire wire connection) and program. Such a system minimises information losses that previously occurred when the signal from VHS tapes was digitised. Direct computer grabbing is generally out of consideration because we do not know in advance of any

experiment of image series what information is worthwhile retaining.

The provision of the best physiologic conditions is an essential requirement for the investigation of living cells. This required the construction of a suitable housing for the microscope body that would ensure maintenance of the important survival parameters, including temperature and nutrition, as well as allowing for easy experimental procedures. After fulfilling these requirements, a plethora of motions inside living cells could be observed, and these motions could be tentatively linked to cellular activity subsequent to various experimental manipulations.

The relationships between fast intracellular motion (FIM) and Brownian motion were clarified by experimental treatments known to change biological processes reversibly or irreversibly. Rapid exposure to ice cold medium temporarily but reversibly slows the speed of FIM. Hypotonic medium raises the speed of FIM, whilst hypertonic media slow it. The FIM rate is largely unchanged by rapid cooling and warming. A degree of heating which will eventually cause cell shrinkage and detachment temporarily increases the speed of FIM. Fixation with glutaraldehyde initially reduces and then arrests FIM within about 3 min without changing the appearance of the structure under observation.

PowerPoint has revolutionised the chances for public demonstration of the range of phenomena of FIM in various primary normal and neoplastic cells and cell lines, and their changes under conditions threatening survival and their reactions during rescue.

Acknowledgments: Conversion of the Noran Odyssey VRCSLM to operation with a red laser was funded by a Royal Society Grant to AB. This work was also supported by grant No. 304/99/0368 from the Grant Agency of the Czech Republic and a Senior Visiting Fellowship from The Anatomical Society of Great Britain and Ireland for PV.

Red laser video-rate scanning confocal microscopy in vivo: experience in studies of renal tubular function

M. SIMEONI,*†‡ R.J. UNWIN,* D.G. SHIRLEY,*
G. CAPASSO,† A. BOYDE‡

*Centre for Nephrology, University College London, Middlesex Hospital, London, UK; †Second University of Naples, Naples, Italy; ‡Department of Anatomy and Developmental Biology, University College London, London, UK

Confocal microscopy is now in widespread use in biology to improve fluorescence imaging, mostly using slow scanning systems to document preserved cells and tissues in which motion in the subject and therefore the speed of image acquisition are no problems, but also at greatly reduced morphologic resolution to study fast ion fluxes in live cells in vitro. We attempted to create a system to improve structural and functional imaging at high temporal resolution in vivo, which is an absolute requirement where parts of the whole subject are changing very rapidly. We reconfigured a video rate laser scanning confocal microscope with the aim of making improvements in its performance in studying live tissues in vivo at a moderate scale of resolution (e.g., a field of view of 200 µm) and in examining the behaviour of intracellular organelles in living cells at extremely high resolution (e.g., a field of view of 5 µm obtained using a 100/1.4 objective and 10× zoom magnification). Our Noran Odyssey system was originally fitted with an argon ion laser with a dominant emission at 488 nm (blue-green), particularly suited for exciting green-yellow fluorescence, with additional lines at 458 and 514 nm. By fitting a 633 nm HeNe red laser, we reduce diffuse scatter and increase the depth at which we can image into tissues, at the same time reducing the tissue damage due to the laser radiation. Reflection mode confocal imaging at video rate is already remarkably impressive: by being able to use more power with less cellular damage, we achieve effectively noise-free imaging.

A particular aim of this study was to examine the application of video-rate scanning confocal microscopy to the nephron in vivo. This was done by direct visualisation of proximal and distal tubular segments following treatment with three classes of diuretics whose principal sites of action are established. Rats were anaesthetised and surgically prepared as for in vivo renal micropuncture, with the left kidney exposed, freed of fat, and placed on a supporting acrylic platform for imaging using a 40/1.0 oil immersion objective lens with glass coverslips sandwiched to 400 µm. We used optical sectioning at depths of 10 to 50 µm below the intact kidney capsule to observe superficial proximal and distal renal tubular segments and blood flow. Blood cells can easily be identified passing rapidly through peritubular capillaries.

Early and late proximal and segments can be distinguished on the basis of the reflectivity of the brush border, and this is absent in distal segments. Baseline measurements of tubule section diameter were made and analysed on image frames grabbed on-line, or from video recordings. After acute intravenous injection of mannitol (500 mg/kg), increases in both proximal and distal tubular diameters were observed. However, after frusemide (2 mg/kg) or hydrochlorothiazide (25 mg/kg), the increase in diameter was confined to the distal tubules.

We have also demonstrated ample fluorescence of Cy5 at 650–670 nm, both using the free dye and coupled peptides to study their uptake, but we require a greater range of affordable far-red fluorescing materials. However, in the interim, we are able to switch to the argon ion laser to study a larger series of shorter-wavelength labelled substances.

Studying the living tissues with video-rate scanning confocal microscopy abolishes the fixation, embedding, sec-

tioning, and staining artefacts of conventional histology. Making comparison with the use of the 488 nm laser light, the epithelial proximal cells are more sharply defined in video-rate confocal reflection scanning using the red laser, and this, therefore, represents a significant advance in physiologic imaging. The approach holds promise for future investigations of dynamic tubular morphology and function in vivo.

Acknowledgments: The authors thank The Royal Society, The National Kidney Research Fund and St Peter's Trust for Kidney, Bladder and Prostate Research for financial support.

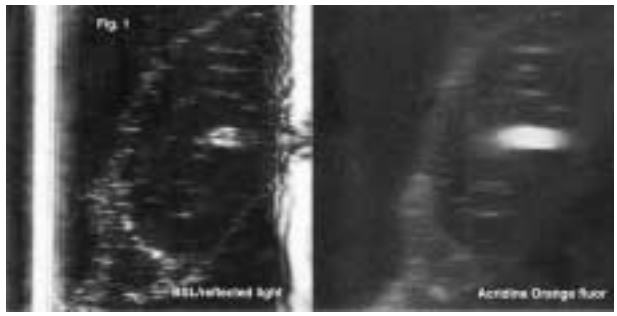

FIG. 1 Two XZ images of a fresh cheek cell made simultaneously using reflected light (left) and fluorescent light from Acridine Orange (right). In the left image, notice the difference in appearance between the refection image of the near and far glass/water interfaces. The image of the near side (left) approximates a straight line, that from the far side (right) shows distortion caused by the optical properties of the overlying nucleus, (the large blob in the fluorescence image).

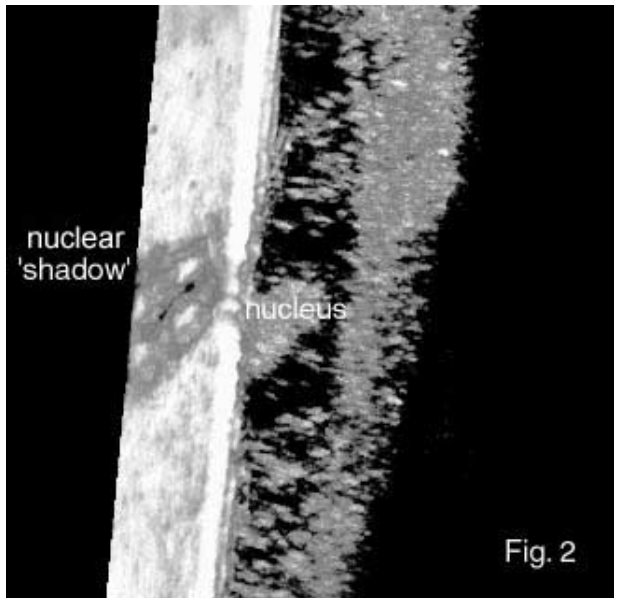

FIG. 2 A three-dimensional projection of a reflected light image of a sample similar to that shown in Fig. 1, but oriented to show the distortion of what should be a uniform representation of the lower glass/water interface in relation to the overlying cell nucleus causing it.

Limits to the precision of optical sectioning in live-cell confocal microscopy

J. PAWLEY

Zoology Department, University of Wisconsin-Madison, Madison, WI, USA

Confocal microscopy is inextricably linked to the concept of the optical section. Optical sectioning occurs because light originating from out-of-focus planes is excluded by the pinhole diaphragm in front of the photodetector. It is so firmly embedded in the psyche of modern biological microscopy that few stop to ask whether the "plane-of-focus" is an actual geometrical plane like a mechanical section, or merely "the surface described by the array of points at which the laser beam reaches best focus." In fact, this best focus plane will be something close to a geometrical plane only if the specimen is optically homogeneous (i.e., has the same refractive index: R.I.). For specimens such as embedded cells, this is a fair approximation. However, as more and more studies are performed on living cells, it is becoming clear that few living specimens are optically homogeneous. This should not come as a surprise: we have been viewing living cells using phase contrast and DIC for years. The contrast in these images reflects RI variations within cells.

The present work gives some indication of how serious this problem can be. Cheek cells were prepared fresh, stained with Acridine Orange and viewed in a 70 µm high chamber made of a coverslip separated from the slide by 4 dots of dried nail polish. This specimen was then viewed in the XZ plane using both fluorescent and reflected or backscattered light (BSL) (Fig 1). There is some loss of signal with depth, caused primarily by the increasing effects of spherical aberration, but general features of the cells can be seen in both fluorescent and reflected light: particularly nuclei and features in the cortex that outline the cell margin. However, the most noticeable feature of this image pair is the tremendous difference in appearance between the refection image of the near and far glass-water interfaces. The image of the near side at the left approximates a straight line. (The image is saturated because the surface signal is high compared to that from cellular components). The image of the far side is not a straight line. In some cases, deep "holes" in it can be correlated with the presence of overlying structures such as a nucleus (Fig. 2). Because we know that the surface of the side is essentially flat, the image of this surface should be uniformly bright. The fact that it isn't is an indication that the optical section is not flat, particularly under refractile features such as nuclei. Measurements from Fig. 1, suggest that the presence of the nucleus has displaced the "optical section" downward by about ~6 µm for all planes below it. Perhaps this explains the common observation that one seldom records fluorescent features on the far side of a nucleus.

As living cells necessarily have nuclei and other refractive organelles, it is not clear how we can avoid the sequellae of their optical properties. In some cells these features are naturally less optically disruptive: cornea and lens come to mind. For other tissues, it would be well to keep in mind that the visibility of peri-nuclear structures may depend strongly on whether or not they are located on the side nearest to the objective. When looking far below the surface of a tissue, it maybe worth the effort to try to arrange that the foreground contains as few nuclei as possible.

Applications of scanning microscopy in forensics science

Elemental analysis of various smokeless powders

C. N. BRUNO

Nassau County Police Department, Scientific Investigation Bureau, Mineola, NY, USA

The utilization of scanning electron microscopy/energy dispersive x-ray spectroscopy (SEM/EDS) for qualitative and quantitative nondestructive techniques in analysis of gunshot residue (GSR), metal alloys, powders, glasses, paints, etc., is made possible today with software that digitally captures images in SEM and qualitatively and quantitative analyzes x-rays in the EDS very rapidly. An Amray 1000 SEM and EDAX DX Prime EDS were utilized in this study. The conditions are: 20 kV accelerating voltage, 70 μ amp emission current, 30° sample tilt, 50–100× magnification, 40 μ s time constant, 12 mm working distance.

The analysis of GSR is comprised of both organic (smokeless powder) and inorganic (primer, etc.) components. The basis organic components (smokeless powder) are nitrocellulose for single base-smokeless powders and in addition nitroglycerin (up to 40%) for double-base powders. Some of the other commonly added components are dinitrotoluene isomers, potassium nitrate, and/or barium nitrate as oxidizers and/or muzzle flash suppressors; diphenylamine and/or ethyl centralite as stabilizers; potassium sulfate, sodium sulfate, tin, dinitrotoluene isomers, and/or ethyl centralite as burning rate modifiers; dibutyl phthalate as deterrent and/or plasticizer; and graphite as a coating. Some of these components are utilized for several different reasons. These organic components are often analyzed by GC/MS.

Olin Corporation manufacturers smokeless ball powder. The production starts with a nitrocellulose base and a stabilizer, such as ethyl centralite or diphenylamine, is added. The nitroglycerin and deterrent/plasticizer and/or burning rate modifier are then added. The grains are coated with graphite and, as a final step, additional inorganic ignition aids, flash suppressors, and fouling prevention agents are added.

The inorganic components are generally comprised of lead styphnate (mono or dibasic), as the primary explosive; barium nitrate, as the oxidizer; and antimony sulfide, as the fuel. All of these components are typically present in the primer (center fire) and would be analyzed by SEM/EDS for their characteristic elements (cations) of lead, barium, and antimony. Rimfire cartridges have various combinations of any of these components (one to three), depending on the manufacturer. In addition, in recent years, organic explosives have been substituted for lead free primers, as well as the presence of manganese, aluminum, titanium, zinc, etc. Other elements present in inorganic GSR analysis could be iron, from the gun; calcium and silicon, from the primer explosive composition; nickel, copper, and zinc, from the cartridge case or primer container; and sodium, potassium and sulfur, from the smokeless powder.

Elemental analysis of more than seventy different smokeless powders, from 1995 manufacture, was made by the author utilizing SEM/EDS and was both tabulated and recorded as spectra.[1–5]

References

1. Wallace JS: Chemical aspects of firearms ammunition. *AFTE Journal*, 22, 4, 370–374, 377–379 (1990)
2. Andrasko J: Characterization of smokeless powder flakes from fired cartridge cases and from discharge patterns on clothing. *J Forensic Sci* 37, 4, 1030–47 (1992)
3. Keto RO: Comparison of smokeless powders by pyrolysis capillary gas chromatography and pattern recognition. *J Forensic Sci*, 34, 1, 74–82 (1989)
4. Mach MH, Pallos A, Jones PF: Feasibility of gunshot residue detection via its organic constituents. Part 1: Analysis of smokeless powders by combined gas chromatography–chemical ionization mass spectrometry. *J Forensic Sci* 23, 3, 433–445(1978)
5. Olin Corporation: Smokeless powder production at St. Marks facility. (Detective Carl Bruno, Nassau County Police Department, Scientific Investigation Bureau, Mineola, New York, USA)

Lead: Lead us not astray

J. R. GIACALONE

West Virginia State Police Forensic Laboratory, South Charleston, WV, USA

During the course of gunshot residue (GSR) analysis via scanning electron microscopy/energy dispersive x-ray spectroscopy (SEM/EDS) in forensic laboratories, particles of lead are often encountered. These lead particles, which are collected and removed from a suspect or object by dabbing with a carbon-impregnated adhesive disc, may contain only lead or have a mixture of other detectable elements. In

an effort to establish the significance of these microtrace evidentiary particles with the discharge residue of a firearm, various non-firearm-related sources of lead are explored. Suppliers, occupations, and hobbies that utilize or require lead materials are targeted with special consideration to those which involve or evolve lead vapors.

Lead (Plumbum) is one metal that was known to the ancient world. It is a bluish-white silvery grey metal, which is highly lustrous when freshly cut. It is soft and ductile. Lead tarnishes upon exposure to air, it melts at 327° C, boils at 1740° C, and has a density of 11.34 g/cc. Lead is one of the four most largely produced and utilized metals. Considerable lead scrap is recovered and recycled. It is used in construction,as an alloy constituent, for storage batteries, in shot and bullets, and in protective coatings for iron and steel. At one time, its primary use was in paint pigments and leaded gasoline. The addition of up to 12% antimony improves its casting properties and increases its hardness. Tin and lead in various proportions form a highly useful series of alloys known as soft solders, which are used to join objects made of copper, iron, nickel, lead, zinc, and glass. Lead with combinations of bismuth, cadmium, and antimony are used in low-melting point alloys for safety devices. Type font metal in the printing industry is composed of lead, tin, and antimony.[1]

When a lead projectile is discharged from a firearm, the elevated temperatures and pressures it experiences during its flight down the barrel permit its exterior to vaporize. The resulting hot gas cloud expanding and condensing around the firearm contains the products of propellant oxidation, partially reacted and unreacted molecules of nitroglycerin and nitrocellulose, primer residue (GSR), and projectile vapors. A large portion of the inorganic vapors is composed of lead. Exceptions to this occur when the projectile is nonplumbumous or encased in a full metal jacket. The incidence of these exceptions is minimal in case work samples, therefore the presence and identification of lead particles on collected evidence specimens warrants the need to assess their probative value.

Items containing lead were collected from various sources. These included hobby shops, hardware stores, plumbing suppliers, home supply stores, automotive repair shops, sporting good stores, and roofing material distributors. One item studied, which is used at elevated temperatures, was solder. The particle residue morphology of solder is spheroidal. The majority of lead materials studied are not intended to be heated therefore the microtrace particles associated with them are suspected to be nonspheroidal.

The specimens were prepared by dabbing the item with a carbon adhesive tape stub. The particles were analyzed using the SEM/EDS parameters employed for GSR. This included a conventional high vacuum system with 25 keV accelerating voltage. The EDS spectra and images of interesting particles encountered were obtained.

The GSR produced by some imported ammunition analyzed by the West Virginia State Police Forensic Laboratory is composed of lead/tin/antimony particles. The occurrence of these particles, which are atypical of those usually encountered, from nonfirearm-related materials has not been explored. Therefore this study attempts to locate potential sources that might mimic such imported ammunition GSR.

The gathering, cataloging, and analysis of several dozen objects that contain lead has been accomplished. Some of the specimens were found to contain spheroidal particles of lead as well as lead/antimony and a select number of other elements. This work establishes that there are activities, hobbies, and occupations that involve micotrace particles containing lead. Though a firearms discharge has never been held as an exclusive source of spheroidal lead particles, their existence has now been identified in non-gunshot related activities.

References

1. *Van Norstrand's Scientific Encyclopedia: Lead*. Litton Educational Publishing Inc. (1976) 1449–1451

Forensic analysis of glass fragments using quantitative elemental analysis: Comparison of the techniques scanning electron microscopy/energy dispersive x-ray/wavelength dispersive x-ray and EDX-µ-RFA

G. Gorzawski, M. Franke, M. Gilberg, B. Reisse
R. Fischer

Bundeskriminalamt, Forensic Science Institute,
Wiesbaden, Germany

Glass is one of the major types of evidence in crimes such as traffic accidents, burglary, and vandalism. Besides measurement of refractive index, one of the common methods of examination is elemental analysis of polished glass samples. However, in real forensic investigations it is often necessary to get information from glass fragments. Two non-destructive techniques are available to analyse small regions of glass in view of elemental composition. Both the µ-x-ray fluorescence (µ-XRF) analysis equipped with an energy dispersive x-ray (EDX) detector as well as the scanning electron microscope (SEM) combined with energy dispersive or wavelength dispersive (WDX) x-ray analysis were tested and compared. As narrow limits are set for the main components used in the glass manufacturing process, in many cases pure qualitative results are not sufficient. Therefore, a quantitative determination of elemental composition is necessary to discriminate between different glass samples.

Efficiency of both methods especially concerning quantitative element analysis in forensic investigations was as-

sessed and limiting factors for the analysis of smallest fragments of glass were determined by our results.

Scanning electron microscopes and forensic science

J.P. KRÜSEMANN

FEI Company - Electron Optics Division, Eindhoven, The Netherlands

Over the last few years, scanning electron microscopy has become an indispensable tool for forensic investigation, allowing a focus on poorly visible or invisible microscopic traces of evidence by imaging, image comparison, and x-ray microanalysis. Since crime is a part of everyday's world, the samples for a forensic lab come from a very wide range of micromaterials. Recently, environmental scanning electron microscopic (ESEM) techniques have been improved to allow a far better match to the wide range of samples.

Key in the forensic investigation is the validity of the proof (accuracy), the nondestructiveness of the measurement method, and the speed of the analysis. Because of the nature of forensic samples, any changes are undesirable because of their value as evidence in the proceedings, as well as complexity and reproducibility of examination. Here, the forensic (E)SEM is a good solution, since one of the key technologies for this instrument is ESEM: samples require no preparation, and can be examined in their natural state. Traditional techniques such as secondary and backscattered electron imaging and x-ray analysis can also be used on all available modes of operation. Even nonconducting, outgassing, dirty, oily, or wet samples can be examined nondestructively: no coating, no cutting, no drying, no cleaning, no manipulation.

One of the most attractive features is the wide variety of forensic applications for a single instrument. The forensic ESEM can help detect forgeries and identify the force or instrument that caused textile damage. It can also analyze pollen left on peoples' clothes, as well as paint chips at the scene of a crime, and even tell whether a car's headlights were on at the time of an accident. Special software can add major functions like highly automated GSR (Gunshot Residue Analysis). Here, the SEM can give detailed information of the explosive and primer batch to match residues found on the clothes and skin of people who have fired guns.

(E)SEM has a much greater depth of field than optical microscopy, and can hence provide much clearer images of fibres, hairs, bullets, cartridge cases, and other items that do not have a flat surface. Similarly, it is much more suitable than optical microscopes for studying shoeprints and similar clues.

Report on the 2nd International Proficiency Test on identification of gun shot residue by scanning electron microscopy/energy-dispersive x-ray

L. NIEWÖHNER,[*] H. W. WENZ, J. ANDRASKO,[*] R. BEIJER,[†] L. GUNARATNAM[‡]

Federal Criminal Agency, KT23, Wiesbaden, Germany; [*]National Laboratory of Forensic Science, SKL, Linköping, Sweden; [†]Netherlands Forensic Institute, NFI, Rijswijk, The Netherlands; [‡]National Bureau of Investigation, NBI, Vantaa, Finland

Introduction

The 2nd European Proficiency Test on Identification of GSR by SEM/EDX was organised by the working group "Firearms" of the European Network of Forensic Science Institutes (ENFSI). This test is part of the quality assurance program of ENFSI. The aim of this program is to promote quality in forensic science and to provide and share information and advice on quality matters among the participants. Altogether 49 laboratories from Europe and North America participated in this test.

The task of organising and evaluating the proficiency test was performed by the Bundeskriminalamt (BKA) (Federal Criminal Agency) in Germany together with the National Laboratory of Forensic Science (SKL) in Sweden, the Netherlands Forensic Institute (NFI) in the Netherlands, and the National Bureau of Investigation (NBI) in Finland.

Sample Description

The test items for the proficiency test consisted of a set of completely identical samples as it is demanded in the ISO 5725 standard for the performance of proficiency tests. Therefore, the samples were produced using a special, patent pending method. Synthetic "GSR particles" of a known composition of lead and antimony were precipitated onto a silicon substrate of a size of 6×6 mmx. The total number of these synthetic GSR particles as well as their size and location on the sample have been well defined (Fig. 1).

Particle parameters concerning number and size were:

- 20 PbSb particles of 1.2 µm in diameter,
- 20 PbSb particles of 2.5 µm in diameter, and
- 3 PbSb particles of 6 µm in diameter.

Finally, the samples were provided with a thin photoresist layer containing environmental particles of Pb, Fe and Cu, and fixed on a standard 1/2″ SEM stub.

Before dispatch each sample was pre-examined by the organizer in order to guarantee an identical sample set for the test.

Although the test stubs do not represent "real case" GSR samples, this kind of sample material was chosen because it is considered to be the only way to facilitate the manufacture of really identical samples as demanded for proficiency testing.

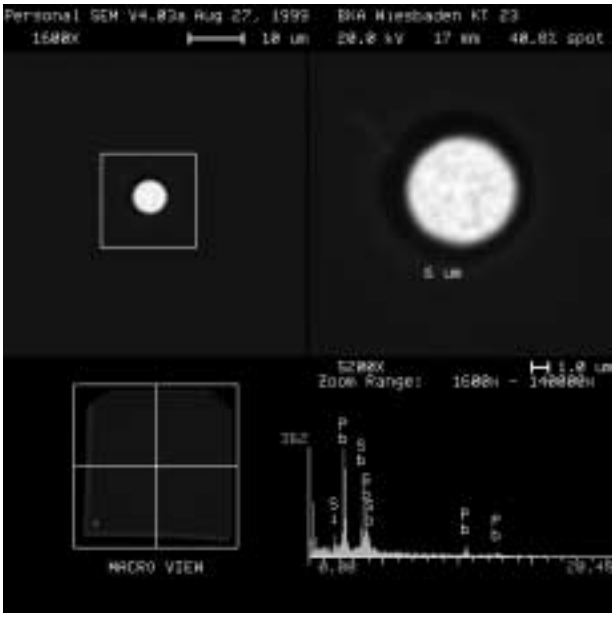

FIG. 1 Backscattered electron image and affiliated EDX spectrum of a precipitated 6 µm PbSb particle.

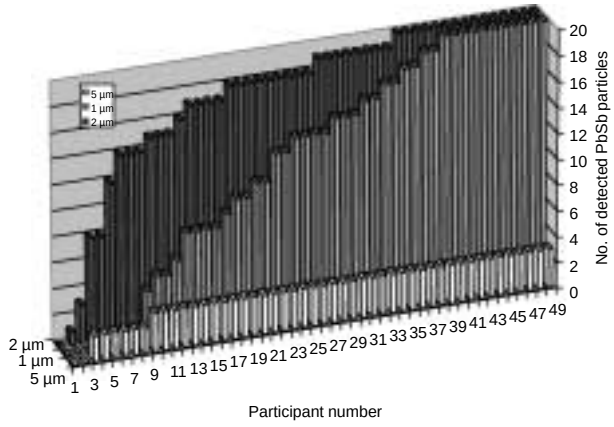

FIG. 2 Number of detected PbSb particles per sample as a function of the particle size; in total 43 PbSb particles were distributed on each sample.

Evaluation of Data

All participants were asked to analyse the received sample using their standard GSR examination routines on their SEM/EDX systems, and to report the results within 4 weeks to the organisation committee. Among other analytical parameters, all reports had to include the number of detected PbSb particles, their size, and their exact position on the sample.

Sample evaluation was performed by comparing the received data with the original dataset of the sample production. Figure 2 shows the number of detected PbSb particles with respect to particle sizes.

From all participating laboratories

- 84% detected all 6 µm particles,
- 47% dectected 95% of the 2.5 µm particles, and
- 27% dectected 95% of the 1.2 µm particles.

A comprehensive report on the results of the proficiency test was prepared and sent to all participants.[1]

Reference

1. *Report on the 2nd European Proficiency Test on Identification of GSR by SEM/EDX*; private communication to all proficiency test participants; organisation committee of the proficiency test; Jan. 2001

Electron/instrument modeling in the SEM

Shape-sensitive linewidth measurement with the scanning electron microscope using a model-based library

J. S. VILLARRUBIA, A. E. VLADÁR, J. R. LOWNEY, M. T. POSTEK

National Institute of Standards and Technology, Gaithersburg, MD, USA

In semiconductor electronics manufacturing, device performance often depends upon size. For example, microprocessor speed is linked to the width of transistor gates. Accurate measurement of feature width is an important but challenging problem. When a scanning electron microscope (SEM) forms an image of a silicon line, areas within a few tens of nanometers of the line edges are characteristically brighter than the rest of the top-down secondary electron image. In general, the shape of the secondary electron signal within such edge regions depends upon the energy and spatial distribution of the electron beam and the sample composition, and it is sensitive to small variations in sample geometry. Image formation can be modeled using Monte Carlo techniques that model the electron/sample interaction to follow representative electrons through the process of scattering inside of the material before being captured or escaping and being counted. In practice it is the inverse of this process (determination of sample shape given the image) that is required. There is presently no straightforward way to calculate this inverse. Indeed, in a strict mathematical sense, the inverse usually does not exist because many sample geometries produce the same image. Accordingly, assigning edge locations is done by finding a model sample for which the forward calculation produces an image equal to the one actually observed. Edge locations, and consequently linewidths, are assigned based upon this model sample. Compared to the preferen-

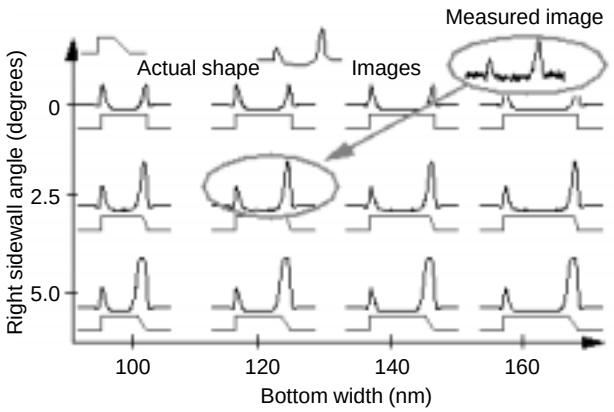

FIG. 1 Concept of metrology based upon a model library. Images are precomputed for many line shapes, resulting in a library of shape/image pairs. Given an image of a sample with unknown shape (upper right) one finds the closest match in the library and identifies the corresponding shape with the unknown.

tially etched single crystal silicon samples we studied in previous years[1,2] polysilicon line shapes are less constrained a priori, a larger set of possible shapes must be modeled and tested for a match to the observed image profile, and the possibility of encountering multiple acceptable matches is increased. We address this by the use of a precomputed library of modeled shapes in a further development of a method first employed for the SEM by Davidson and Vladár.[3] The concept is shown in Fig. 1. Matching to the library is performed using a least squares method. We introduce interpolation of the library and the "independent edges" approximation to improve accuracy and speed. We have tested this procedure on polysilicon test patterns on a thin gate oxide. For the library we varied sidewall angle and radius of the upper corner. The procedure produced good fits to the measured data. Scatter in the measured edge shape and line width parameters was about as expected based upon the observed image noise level. Uncertainties are greater for parameters (such as, corner radius) which have only subtle effects on the observed image than for parameters (such as, edge locations and corresponding overall linewidth) that have more dramatic effects.

References

1. Villarrubia JS *et al.*: Intercomparison of SEM, AFM, and electrical linewidths. *Proc SPIE*, 3998, 84–95 (2000)
2. Villarrubia JS *et al.*: Linewidth measurement intercomparison on a BESOI sample. *Proc SPIE*, 3677, 587–598 (1999)
3. Davidson MP, Vladár AE: An inverse scattering approach to SEM line width measurements. *Proc SPIE*, 3677, 640–649 (1999)

An application of image retrieval technology to sidewall structure estimation from top-down scanning electron microscopy imagery

K.W. TOBIN, P.R. BINGHAM, J.R. PRICE, M.H. BENNETT*

Oak Ridge National Laboratory, Oak Ridge, TN;
*International SEMATECH, Austin, TX, USA

Critical dimension (CD) metrology for lithographic linewidth control is a critical technology in semiconductor device manufacturing. For line-width measurements scanning electron microscopy (SEM) tools are used almost exclusively in the industry due to resolution requirements that are well below the resolving capability of optical microscopes. For example, the international technology roadmap for semiconductors[1] describes line widths of approximately 130 nm today moving towards 70 nm by 2008. As line widths continue to shrink, the need to accurately characterize printed structures by cross-section profile, not just line-width, becomes increasingly important for effective control of the lithographic process. Structural characterization typically requires a destructive analysis of the device under test by physical cross-sectioning and subsequent SEM review.[2] The need to cross-section test structures and product wafers either limits throughput or sampling and ignores the body of historical cross-section data and imagery that has been collected over time. To address this apparent conflict between shrinking line widths and the increasing need to physically cross-section wafers, researchers at the Oak Ridge National Laboratory (ORNL) have been developing a method for effectively re-using historical top-down and cross-section CD SEM metrology imagery and process data to estimate cross-section structure. This method uses content-based image retrieval (CBIR) to describe top-down device structures in imagery and provide an image-based correlation to cross-section data.

The ability to manage large image databases has been a topic of growing research. Imagery is being generated and maintained for a large variety of applications including remote sensing, architectural and engineering design, geographic information systems, and weather forecasting. CBIR is a technology that is being developed to address these needs.[3] CBIR refers to techniques used to index and retrieve images from databases based on their pictorial content. Pictorial content is typically defined by a set of features extracted from an image that describe the color, texture and/or shape of the entire image or of specific image regions. This feature description is used in CBIR to index a database through various means such as distance-based techniques, approximate nearest-neighbor searching, rule-based decision-making, and fuzzy inferencing.[3,4] CBIR addresses a problem created by the growing proliferation of automated semiconductor review technologies, i.e., the management and re-use of the large amounts of image data collected during review. Current semiconductor yield man-

agement databases contain on the order of 30% of their data in the form of defect, CD, and overlay images from optical, confocal, SEM, and other imaging modalities.[5] For semiconductor yield management applications we have denoted CBIR technology as Automated Image Retrieval (AIR).[6] For cross-section estimation and image data management we have developed a unique feature description and AIR approach that uses top-down and CD SEM image pairs. These pairs are used to estimate the structural cross-section without destructive testing while making use of the historical data record. The ability to predict device cross-section from top-down imagery is made possible by comparing the top-down feature description between a query and a database to retrieve imagery containing similar top-down morphology. Cross-section data that has been maintained from historical measurements are used to infer the cross-section structure of the query therefore reducing the manufacturers dependency on physical cross-sectioning.

Early feasibility studies of this approach have verified three critical assumptions on a limited set of focus/exposure (F/E) data provided by International SEMATECH (ISMT): (1) Top down SEM images encapsulate three-dimensional (3D) structural information similar to that which is made apparent through physical cross-sectioning; (2) The unique AIR feature description developed for our feasibility study effectively captures and describes this 3D structure, and; (3) An image retrieval-based approach can be used to bound the problem of sidewall structural estimation and prediction by making use of a historical data repository. Data used to date for this initial study has been limited to a single CD SEM metrology tool and an extensive set of F/E data. Continued work in this area will address the inclusion of F/E data collected across several CD SEM tools to investigate the cross-tool and cross-product extensibility of the AIR-based method. It is anticipated that this technique will reduce the semiconductor manufacturer's dependency on physical cross-sectioning of test and product wafers while providing an effective CD SEM metrology image management and re-use capability.

Acknowledgments: Prepared by the Oak Ridge National Laboratory, Oak Ridge, Tennessee, 37831-6285, operated by UT-Battelle, LLC for the U.S. Department of Energy under contract DE-AC05-00OR22725.

References

1. Semiconductor Industry Association, International Technology Roadmap for Semiconductors, 269–293, (1999)
2. Rai-Choudhury P: *Handbook of Microlithography, Micromachining, and Microfabrication*. (Ed.) SPIE Optical Engineering Press, Bellingham, Washington, 1, 477–584 (1997)
3. Gudivada VN, Raghavan VV: *Content-Based Image Retrieval Systems*. IEEE Computer Magazine, 0018-9162, September 18 (1995)
4. De Marsicoi M, Cinque L, Levialdi S: Indexing documents by their Content: A Survey of Current Techniques. *Imaging and Vision Computing*, 15, 119–141 (1997)
5. Tobin KW, Karnowski TP, Lakhani F: *The Use of Historical Defect Imagery for Yield Learning*, The 11th Annual IEEE/ SEMI Advanced Semiconductor Manufacturing Conference and Workshop, Fairmont Copley Plaza Hotel, Boston, Mass., September 12–14 (2000)
6. Karnowski TP, Tobin KW, Ferrell RK, Lakhani F: *Content Based Image Retrieval for Semiconductor Manufacturing*, IS&T/ SPIE's 12th International Symposium on Electronic Imaging: Science and Technology, San Jose Convention Center, January (2000)

Studies of backscattered electrons in scanning electron microscopy using Monte Carlo simulations

E. NAPCHAN

DLM Enterprises, London, UK

The electron backscattering coefficient (BSC) is the fraction of primary beam electrons which emerge from the sample's top surface after a series of elastic and inelastic collisions with the specimen's atoms. The elastic reflection coefficient (ERC) consists of those electrons that underwent only elastic scattering. The BSC is important when working with signals that depend on the energy loss and deposition in the specimen, such as x-ray microanalysis and EBIC (electron beam induced current) in semiconducting devices. The ERC is used in surface analysis techniques, such as EPES (elastic-peak electron spectroscopy).

The BSC for a bulk material is usually given as an integrated value, at times, as function of the incident beam energy. The ERC shows in addition an angular distribution. Further parameters that affect measured and calculated values of these parameters are the beam tilt angle, specimen composition, surface condition, and the characteristics of reflected electrons detectors.

Monte Carlo simulation (MCS) of electron trajectories has become a common method for calculating electron scattering parameters. The basic idea in the simulation is to calculate trajectories for a large number of electrons, using a combination of physical models and fits to experimental data that can be derived from the simulations. Aspects of the simulation process include specimen definition based on its composition and geometry, elastic scattering and inelastic scattering considerations, and detector properties. In many cases, such as in multilayer specimens, this type of simulation is the only method available.

The composition of multicomponent specimens can be dealt in MCS either by assuming some form of averaged values for the material parameters, or by tabulating scattering parameters for the range of electron energies of interest. Dapor and Miotello[1] tabulate the inelastic and elastic cross sections for various oxides for beam energies <10 keV. They find that calculated BSC values were close to experimental within 5–15% in the above energy range, and that the values and their beam energy dependence are similar to that of a compound material whose average atomic

number is ~ 10. Berger and Niedrig[2] report that the BSC angular distribution and the integrated BSC from W-Cu were similar to that of a single component with a mean atomic value calculated using a quadratic weighted (using atomic concentration) average of the atomic numbers.

Detector characteristics effects in the calculation of BSC have been studied by Rosenberg *et al.*[3] It is clear from this work that these play a major role in values obtained for the BSCs, and therefore the wide spread in reported experimental reports for this parameter, as given in the tabulations by Joy,[4] and the graphical presentation of these by Napchan[5] is not surprising.

With increased detection sensitivity and definition, and the selection of suitable elastic and inelastic scattering, it might be possible to increase the quality of available backscattered electron data and perhaps increase the experimental resolution to a few atomic layers range, as calculated by Kwei *et al.*[6] for reflected electrons from Cu at 400 eV primary beam voltage.

References

1. Dapor M, Miotello A: Backscattering of electrons from selected oxides: MgO, SiO/sub 2/, and Al/sub 2/O/sub 3/. *Eur Physi J Appl Physics* 5, 143–148 (1999)
2. Berger D, Niedrig H: Complete angular distribution of electrons backscattered from tilted multicomponent specimens. *Scanning* 21, 187–190 (1999)
3. Rosenberg N, Jiang CZ, Morin P: Monte Carlo simulations of coaxial backscattered electrons in SEM. *Ultramicroscopy* 76, 97–105 (1999)
4. Joy DC: A database of electron-solid interactions (search the web for most recent version of the data http://web.utk.edu/ ~sr-cutk/htm/interact.htm). *Scanning* 17, 270–275 (1995)
5. Napchan E: Graphical presentation of the backscattering coefficients for materials in the Joy 1995 database. http://www.napchan.com/bse/bse.htm (1999)
6. Kwei CM, Hung CJ, Su P, Tung CJ: Spatial distributions of elastically backscattered electrons from copper and silver. *J Phys D(Appl Phys)* 32, 3122–3127 (1999)

CASINO V2.0: A fast and easy-to-use tool for scanning electron microscope users

D. DROUIN, A.R. COUTURE, R. GAUVIN,* P. HORNY*

Département de génie électrique et génie informatique; *Département de génie mécanique, Université de Sherbrooke, Sherbrooke, Québec, Canada

Monte Carlo simulation has been widely used by microscopists for the last few decades. It used to be a slow process that also required a high level of computer skill from users. Recent outstanding progress in the microelectronics industry allows customers to obtain affordable desktop computers with clock rate greater than 1.5 GHz. With this type of computing power Monte Carlo simulation is no longer a long overnight process. The topic of this paper is to present a new Windows™ environment version of the CASINO[1] Monte Carlo simulation program. The goal of this program is to assist scanning electron microscope users in their routine analysis and also in more advanced topics such as electron beam lithography for example. The new version uses a new architecture, which provides results twice as fast.

Based on a single scattering algorithm, this software is specifically designed for low beam interaction in a bulk and thin foil. This program uses tabulated Mott elastic cross-sections,[2] which have the benefit of both fast calculation and accurate interaction at low beam energy. At the moment, CASINO can either be used to generate x-rays or backscattered electron signals. The program uses simple two-dimension geometry to represent real samples. The new version includes a new, free 2-dimension environment in addition to the standard vertical and horizontal planes. Figure 1 shows the possibility of such an environment by representing a cross-section of a MOSFET device with the electron beam in a fixed position. The beam can then be scanned across different regions to produce x-ray linescans or bascattered electron profiles.

Many new, convenient characteristics have been added to the version 2.0 of CASINO. The new interface lets the users consult the results as the simulation while still in progress. The parameters setup for a new simulation is performed through a step by step wizard and easy-to-use dialogs such has inline typing to enter the chemical composition of the sample regions. All the simulation data are stored in a single file to ease the consulting and handling of the results. The results can be directly printed, exported as a bitmap (BMP) or transferred to a spreadsheet such as Microsoft Excel™ for further analysis or formatting. A backup file is automatically created, which avoids data loss and allows resuming of an uncompleted simulations.

Finally, new outputs have been included in this version such has the lateral intensity of x-ray. This distribution allows the user to estimate the spatial resolution of an x-ray mapping from a heterogeneous sample. Also, a 3-dimen-

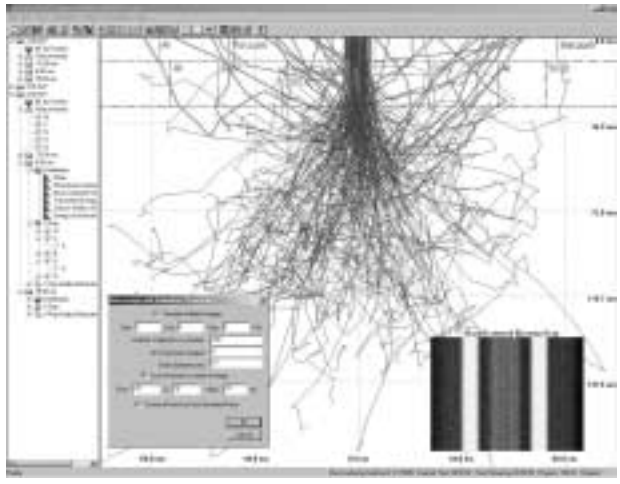

FIG. 1 Simulation of a backscattered electron line profile across a MOSFET device.

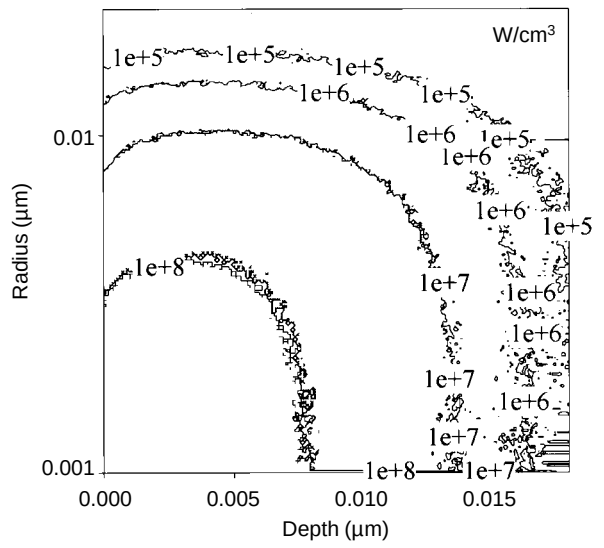

FIG. 2 Calculated energy density line as a function of depth and radius in a Ni sample for a 1.4 keV electron beam.

sion energy density distribution can be calculated. This feature provides information on the spatial distribution of the absorbed energy in the sample. Figure 2 presents an example of this by showing the energy density line as a function of depth and radius in a Ni sample. This type of output has many applications for sample characterization using advanced techniques such as electron beam-induced conductivity (EBIC) or cathodoluminescence.

This program is a shareware that is available for download through this website: www.gme.usherb.ca/casino. The details related to the used of this program are also found at this address.

References

1. Hovington P, Drouin D, Gauvin R: CASINO a new era of Monte Carlo code in C language for the electron beam interaction — Part I: Description of the program. *Scanning* 19, 1–14, (1997)
2. Hovington P, Drouin D, Gauvin R: CASINO — a new era of Monte Carlo code in C language for the electron beam interaction–Part II: Tabulated values of mott cross section. *Scanning* 19, 20–28, (1997)

Practical aspects of microanalysis using secondary electrons in scanning electron microscopy

S. MIL'SHTEIN, B. KIMBALL,* R. KNOWLES,* K. NOVARIS,† P. ERSLAND†

Advanced Electronic Technology Center, ECE Dept. UMass, Lowell; *FEI Co, Peabody; †MA/COM, Lowell, MA, USA

Recently, a theoretical model and methodology[1] of microanalysis using secondary electrons (MuSE) in the scanning electron microscope (SEM) was developed. It was suggested that a sample scanned by the beam in SEM be used as an electron spectrometer for secondary electrons (SE) by providing a bias across the tested material. The amount of voltage applied to a sample defined the energy range (in eV) for SE distribution. The method consists of taking an SE intensity scan along unbiased samples, then repeating the scan of the same area when the sample is biased. Digital subtraction of the two scans produces so-called S-curves. The first derivative of the S curve in a range of applied voltages results in a bell-shape SE distribution. The model predicted that the shape of SE distribution would be unique for each material.

Current study focused on obtaining experimental proof for the theory and a new method for performing microanalysis in SEM. Some practical aspects of the new method that need to be defined include sample preparation, geometry of SEM chamber, type of SE detector, regime of SEM operation, and type of data processing.

Test structures containing doped Si and GaAs resistors were fabricated on semiconductor wafers. Long and short resistors made from tested materials were wired by ball-bonder. GaAs samples were also prepared as wide stripes between ohmic contacts. Sample preparation is a key for successful microanalysis. Presence of thick oxide on Si samples or passivation layers on GaAs resistors made MuSE almost impossible due to strong charging effects. Geometry of a resistor (long or wide) creates certain art effects in SE images, but does not impact the result of line scans which is taken away from the edges of a resistor.

We performed the experiments on scanning microscopes Hitachi-S570, LEO-1982, and environmental microscope XL30 ECEM-FEG at high vacuum and 0.3 torr. Acceleration voltages were used in a range of 4–5 keV, working distances varied from 9 to 2mm. Hitachi-S570 was equipped by LaB_6 gun, where LEO-1982 and XL30 ECEM-FEG operated field emitters. Among the SEM parameters of the used microscopes, stability of beam current and stability of the signal of SE detector are most important. All the microscopes produced S-curves. However, the results from LEO-1982 and Hitachi-S570 required binominal smoothing of the S-curves before taking the derivatives. The most stable were the results from the environmental microscope XL30 ECEM-FEG and, what is more important, the operation at 0.3 torr and at high vacuum produced similar results. Unbiased resistors, being tested at 0.3 torr, generated nonsmooth curves. This phenomenon needs further study.

Processing of the data was performed using the differential voltage contrast (DVC) software, which is developed at UMass, and the intensity profile (IP) software developed by FEI Co. Both softwares were serving the purpose of MuSE well. The described study should be seen as a first experimental proof of the concept and as initial step in establishing MuSE in SEM as a legitimate methodology.

References

1. Mil'shtein S: *Microanalysis Using SE in SEM*. (patent application)

Influence of dynamic angular deviation of primary beam during scanning on image contrast of surface analytical scanning electron microscopy by Monte Carlo simulation

H. YAN, L. SUN*

Veracel Inc. Toronto, Ontario, CANADA; *Surface Science Western, University of Western Ontario, London, Ontario, Canada

A miniature of the scanning electron microscope system[1,2] provides opportunity to apply its principle into an analytical scanning electron microscope, such as the scanning auger microscope (SAM) and loss electron signal. The factor of dynamic angular deviation has been simulated for the loss electron signal[3]. In the current work, Monte Carlo simulation has been applied to Auger microanalysis on embedded Au and Cu strips in Si substrate. The main parameters altered in the simulations are (1) distance between primary beam source and the main surface of the specimen, (2) Auger transitions, and (3) length of Au and Cu-embedded strips.

Besides the signal intensity difference due to dynamic angular deviation during scanning, the simulated results show that (1) backscattering coefficients of the constituent affect the signal intensity difference between regions on each side of the strip, and (2) higher kinetic energy of Auger transition results in a relatively larger intensity gap.

References

1. Khursheed A, Phang JC, Thong JTL. A portable scanning electron microscope column design based on the use of permanent magnets. *Scanning* 20, 87–91 (1998)
2. Caltech JL: Miniature Scanning Electron Microscope for in-situ Application. 1999 NASA/JPL workshop on miniature vacuum pump technology. http://www.nasatech.com/Briefs/Nov99/NPO20499.html.
3. Yan H, Gomati MM E1, Prutton M, Wilkinson DK, Chu DP, Dowsett MG: Mc3D: A three-dimensional Monte Carlo system simulating image contrast in surface analytical scanning electron microscopy I—object-oriented software design and tests. *Scanning* 20, 465–484 (1998)

Advances in biological and biomedical scanning microscopy and microanalysis, Part I

Bone structure in transgenic mice overexpressing tartrate-resistant acid phosphatase (AcP5, TRAP)

S.J. JONES, A. BOYDE, A.R. HAYMAN,* T.M. COX†

Dept. of Anatomy, University College London; *Division of Molecular and Cellular Biology, School of Clinical Veterinary Science, Bristol; †Dept. of Medicine, University of Cambridge, UK

Introduction

The generation of transgenic mice overexpressing tartrate-resistant acid phosphatase (AcP5) threefold and eightfold has been described previously.[1] Using histomorphometric techniques, the mice were found to have less trabecular bone than their wildtype, suggesting a mild osteoporosis. This was thought to have resulted from an increase in bone resorption that was partly compensated for by a twofold increase in the rate of bone formation. However, the mice were examined only as neonates and therefore in a phase of adjustment and rapid growth. If the rate limiting step in bone resorption is the demineralisation of the bone prior to the degradation of the organic matrix by enzymes released by the osteoclast into the resorptive vacuole abutting the bone,[3] then increased resorption should be minimal or, indeed, non-existent. Although access to the mineral might be enhanced by more efficient removal of the organic phase, the mineralized matrix could not be removed unless more H+ ions were available to uncover more of the organic phase. It therefore seemed necessary to examine the transgenic mice when older to discover whether there was any evidence for increased bone resorption.

Materials and Methods

Mice were generated as described previously. Wildtype and transgenic mice with either threefold or eightfold overexpression of AcP5 were culled as young adults at 10–11 weeks, or as older adults at 18 months or 22–23 months. The animals were fixed in 70% ethanol, and limb bones defleshed and cleaned using Tergazyme or peroxide. Some bones were then opened longitudinally using a bur to expose the marrow cavity and then recleaned using Tergazyme or peroxide. Other long bones were embedded in PMMA. The embedded specimens were cut and micromilled, and all specimens were coated with carbon for scanning electron microscopy and imaged using backscattered electrons.

Results: Mice aged 10–11 weeks

(Figure 1) The right tibiae-fibulae and femurs of six mice were examined: a male and a female of each of the three genotypes. There was less than 2% difference in the lengths of their femurs and the thicknesses of the bone shafts were similar. The internal and external diameters of the bones were also similar in all six mice. In the females, the trabeculae in the distal ends of the femurs extended an equal distance towards the midshaft; in the males, the trabeculae did not extend as far as in the transgenics but may have suffered damage in preparation. There was no evidence for increased bone turnover in the transgenic compared with the wildtype mice, such as more active resorption or more incompletely mineralized, recently deposited bone.

Results: Mice aged 18 or 22/23 months

The right and left femurs and tibiae-fibulae of seven mice were examined: a male and a female of each of the three genotypes, and another male overexpressing AcP5 threefold. Two mice were aged 22/23 months: the male overexpressing AcP5 eightfold and one of the males overexpressing AcP5 threefold. No trabeculae remained in the marrow cavity at either 18 or 22/23 months. The sizes of the bones of all the males and females aged 18 months were similar; the bones of the two oldest animals were larger than the ones from the 18 month mice, but otherwise similar and of equal size. Endosteal resorptive areas were observed in all these mice. The resorption pits in the bones from mice overexpressing AcP5 did not differ from those in the wildtypes in appearance or distribution, nor were the internal or external diameters of the bones larger. If turnover was increased, one would expect to find evidence of more new patches of bone repairing resorbed regions: this was not observed.

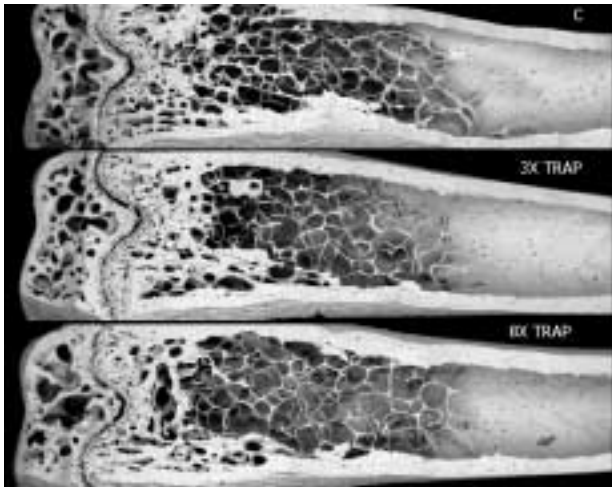

FIG. 1 Control, 3× and 8× TRAP overpression mouse distal femurs. 20 kV BSE SEM. Field width = 5.94 mm.

Discussion

There are no differences between the wild type, the 3× and the 8× overexpression phenotypes at the ages examined. The present findings can be explained by assuming that the rate limiting step in osteoclastic bone resorption of mature lamellar bone tissue is that of the acid induced demineralisation prior to organic matrix degradation employing proteolytic enzymes.[3] Although lack of AcP5 results in disruption of endochondral ossification and some impairment of resorption leading to a mild osteopetrosis,[2] having more AcP5 does not increase bone resorption, because enough is enough. How can these findings be brought into line with the earlier conclusion of compensatory exuberant bone replacement in the presence of excess resorption? Firstly, that conclusion was reliant upon methodologies classed as 'bone histomorphometry', which were devised for big samples of adult lamellar bone, not neonate mice. Secondly, we have previously noted that immature bone contains a built-in self-destruct mechanism, and that its osteoid, which constitutes a much higher proportion of the bone tissue, may be destroyed by any protease which can activate latent enzyme or enzyme-inhibitor complexes. This in turn favours osteoclastic resorption, since bone salt may act to stimulate osteoclastogenesis and activate osteoclasts. Bone turnover is necessarily rapid in the foetus and neonate during modelling. The osteoid of mature bone is differently constituted, the microdistribution of the mineral within the bone dissimilar, and remodelling in the older subadult and adult is a much slower process.

Acknowledgments: The authors thank AI Cassady and DA Hume for providing the mouse lines, and the Arthritis Research Campaign and the HBLB for financial support.

References

1. Angel NZ, Walsh N, Forwood MR, Ostrowski MC, Cassady AI, Hume DA: Transgenic mice overexpressing tartrate-resistant acid phosphatase exhibit an increased rate of bone turnover. *J Bone Min Res* 15, 103–110 (2000)
2. Hayman AR, Jones SJ, Boyde A, Foster D, Colledge WH, Carlton MB, Evans MJ, Cox TM: Mice lacking tartrate-resistant acid phosphatase (AcP5) have disrupted endochondral ossification and mild osteopetrosis. *Development,* 122, 3151–3162 (1996)
3. Jones SJ, Arora M, Boyde A: The rate of osteoclastic destruction of mineralized tissues is inversely proportional to mineral density. *Calcif Tiss Int,* 56, 554–558 (1995)

Multiple oblique backscattered electron detectors to simulate multiple oblique illumination in scanning electron microscopy

A. BOYDE

Dept. of Anatomy and Developmental Biology, University College London, London, UK

The present work originated through attempts to improve microscopic imaging of porous bone. For work with bone, we use unembedded thick, plane-parallel slices. For unembedded bone, we remove all cells to expose osteoid or mineralised bone, or remove any osteoid to expose the mineralising front. The superficially deproteinised preparation is the simplest to produce and hugely productive of data regarding bone surface activity states. To image cancellous bone requires an optical system with a great 3-D depth of field and SEM is therefore the preferred imaging box, but SEM contains many more tools than are generally recognised.

Here, I report on the enhancement of information content from separate recordings from multiple fast electron (backscattered electron, BSE) detectors, the image series being recombined (1) to simulate dynamic motion of illumination sources, (2) through colour encoding, and (3) by combinations of these two approaches.

Each image field is documented with at least four scans with as many separate detectors. (Sometimes I have used nine, four above for BSE, four below for forward scattered electrons, and one to intercept the direct unscattered primary beam.) The number of BSE images in a circle or cycle is increased by interpolation to emulate acceptance angles into 8, 16, or 32 etc. virtual detectors. Playing the images in sequence continuously sweeps the apparent angle of illumination and powerfully increases depth interpretation.

In addition to moving the direction of apparent illumination, the sample may be moved systematically such that replayed image sequences emulate linear motion parallax from "flying past" or "flying into and out of" the surface.

Further enhancement is achieved through spectral colour coding of the apparent direction of illumination, when much wider sectors of the total data set are used simultaneously. Here, also, we can exploit the advantages in single, still images. The procedure involves the acquisition of (usually and most desirably and at least) three images which are used to provide the red, green, and blue components of a combined image. The combined coloured BSE images code surface slope via brightness and direction via hue. Surfaces normal to the electron beam appear grey.

The methods I describe will have extremely wide fields of applicability in all branches of science and technology where SEM imaging is used today. This will be obvious for solid samples with topographic relief in the applications fields of metallurgy, materials science, geology, and forensics. However, the methods also prove to be extremely well suited to the study of the types of sample used by all biological users of SEMs. These were, originally, mostly water, being on the order of 10 to 15% of solids with a density on average just greater than 1; water is removed in most sample preparation protocols, so that the net sample density is around 0.15. Compare this with values which are a factor of 10 to 100 greater in all other branches of SEM usage. The dried sample is also nonconductive. To be able to study such very low density insulators, 99% of all such samples are sputter coated with gold or another heavy metal. The enhanced signal from the sample surface actually derives from the gold coating. The gold coating is the right thickness to return the higher spatial resolution component of the BSE signal, uncontaminated by the lower resolution component resulting from the sideways scatter of electrons passing through it. Compared with gold, the sample itself returns essentially to zero signal.

Cryogenic micro-computed tomography scanning

S.M. JORGENSEN, E.L. RITMAN

Department of Physiology and Biophysics, Mayo Foundation and Clinic, Rochester, MN, USA

Basic functional units of the organs (e.g., nephrons, hepatic lobules, terminal bronchiole) are of the order of 0.1 mm^3 so that they fall below the spatial resolution of whole-body imaging methods (e.g., clinical CT or MRI) and exceed the size of the intact volume that needs to be imaged (at the desired resolution) by methods such as confocal and other microscopies. To adequately image those structures in isolated, intact, fixed rodent organs or biopsies of organs from large animals or humans, we developed a bench-top micro-CT scanner.[1]

Our micro-CT scanner generates 3-D image volumes consisting of up to a billion cubic voxels, each 5 to 25 μm on a side, with isotropic spatial resolution. Its main components are a spectroscopic x-ray source that produces selectable primary emission peaks at 17 or 23 keV (anode material dependent) and a fluorescing, thin, (CsI(Tl)) crystal plate that converts the x-ray transmission image to a light image that is, in turn, imaged at selectable magnification with a lens onto a cooled 2.5×2.5-cm, charge-coupled device (CCD) detector array. The specimen is positioned as close as practical to the crystal and is rotated in 361-1441 equiangular steps around 360° between each x-ray image acquisition. Tomographic reconstruction algorithms, applied to these recorded images, are used to generate 3D images of the specimens.

Specimens are fixed with formalin and embedded in paraffin or bioplastic. If the blood vessels or ducts are of interest, they are injected with contrast medium. Display and analysis of the 3D image are used to examine the internal structure-to-function interrelationships between the basic functional units.

Micro-CT scanning often spans many hours per specimen. The relatively long duration of the scan has two consequences. One is that specimens must be "fixed" (e.g., in formalin) and potted in wax to prevent progressive distortion and degradation of the specimen during the scanning process. This greatly limits options for subsequent analysis of the specimen, such as serial-section histoimmunological imaging. The second consequence is that even relatively slow dynamic processes, such as diffusion of x-ray contrast media across vessel endothelium (into vessel wall or into organ parenchyma), cannot be imaged because the diffusion process either continues during the scan or is completed before the specimen is fully fixed.

We overcame these limitations by developing a cryogenic micro-CT scanning method so "flash frozen" biopsies can be scanned in the frozen state. This method maintains both the "fresh" state of the specimen and literally freezes the dynamic (usually diffusion) process at the selected time-point. The method involves rapid removal of an entire rodent organ (or biopsy from a large animal or human) and cooling it down by, for instance, immersion in a slurry of dry ice and acetone. The scanning vessel consists of a double-walled copper container with a vacuum space between the walls. Beryllium "windows" in the vessel walls minimize x-ray attenuation of the 17 or 23 keV x-ray photons used in the micro-CT scanner. The frozen specimen is placed inside the vessel and maintained at a selected, subfreezing, temperature ($\pm 0.5\ C^{\circ}$) without frost buildup on the vessel walls or specimen for at least 20 h during the scan. Progressive build-up of frost, or thawing, during the scan is achieved by passing a flow-controlled jet of cold nitrogen gas continuously over the specimen during the scan to keep it at the desired cold temperature and then heating the vented gas which is then passed over the outer Beryllium windows to ensure frost-free operation. The specimen is mounted on a thin vertical rod, which traverses the vessel wall through a small opening, so that the specimen can be rotated (within the special vessel) in the small angular steps required in the CT scanning process. From time-to-time during the scanning process the entire vessel and its specimen can be moved out of the x-ray beam to provide a direct measure of the x-ray beam intensity, data needed for the tomographic reconstruction computation. Initial application to iliac crest biopsies demonstrate the feasibility of this approach.

References

1. Jorgensen SM, Demirkaya O, Ritman EL: Three-dimensional imaging of vasculature and parenchyma in intact rodent organs with x-ray micro-CT. *Am J Physiol* 275, H1103–H1114 (1998)

Three-dimensional reconstruction of *Zea mays* stem by magnetic resonance imaging (MRI) technology

P. C. CHENG, J. H. CHEN,* S. C. HWANG,* C. K. SUN,* D. B. WALDEN,† W. Y. CHENG‡

Dept. Electrical Engineering, University at Buffalo, Buffalo, NY, USA; *Dept. Electrical Engineering, National Taiwan University, Taipei, Taiwan, Rep. of China; †Dept. Plant Sciences, University of Western Ontario, London, Ontario, Canada; ‡Williamsville East High School, Williamsville, NY, USA

The three-dimensional (3-D) arrangement of vascular bundles in plants is an interesting subject in the study of mechanical properties of stem. However, one of the difficulties frequently encountered is the availability of 3-D imaging tools needed for obtaining physical dimensions of various components in a stem. Recent development in confocal and multiphoton microscopy allows 3-D imaging of plant tissue in high resolution. However, other than physical sectioning[1], macroscopical study of plant organs in 3-D remains a difficult task. Among various available technologies for macroscopical imaging (e.g., x-ray macrotomography, optical coherent tomography (OCT), and MRI), MRI is an ideal choice for its contrasting modality in volumetric imaging of soft tissues.

To test the idea of imaging stem in 3-D, a 3T Biospect MRI system (Brucker, Germany) (Fig.1 a), equipped with a 6 cm inner diameter microquadrature coil (Fig.1 b), for radio frequency (RF) transmission and reception of MRI signals, was used in this study. Spin echo based RARE sequence was used to obtain T2 weighted images with TR/TE = 3160.5/58.5 ms and field-of-view of 1.67×1.67cm (256×256 pixels) at a slice thickness of 0.8 mm. This corresponds to a voxel size of $65 \times 65 \times 800\ \mu m$. Data were obtained within 1/2 h with number-of-excitations (nex) set at 16. Figure 1 (c-n) shows a series of MRI sections through a stem node (the node below the main ear insertion) from field-grown maize (*Zea mays* L., var. Odyssey sweet corn). The specimen was obtained from 2000 summer crop grown in the field station of University of Western Ontario (London, Ontario, Canada); the stem was fixed in 1:3 EtOH/acetic acid, washed thoroughly in water prior to imaging. Air bubbles trapped in the tissue were removed by vacuuming to avoid imaging artifact due to low magnetic susceptibility of air. Three-dimensional reconstruction was performed by using Vaytek VoxBlast™ and AutoQuant's AutoVisulize 3D™ software (Fig. 1 (o, p, and q).

In combination with image segmentation and tracing tools, the MRI will greatly enhance our capability in the understanding of vascular architecture and its development in plants. Using the material properties of the stem tissue and the information on dimension, orientation, and connection of the vascular bundles, it is possible to ana-

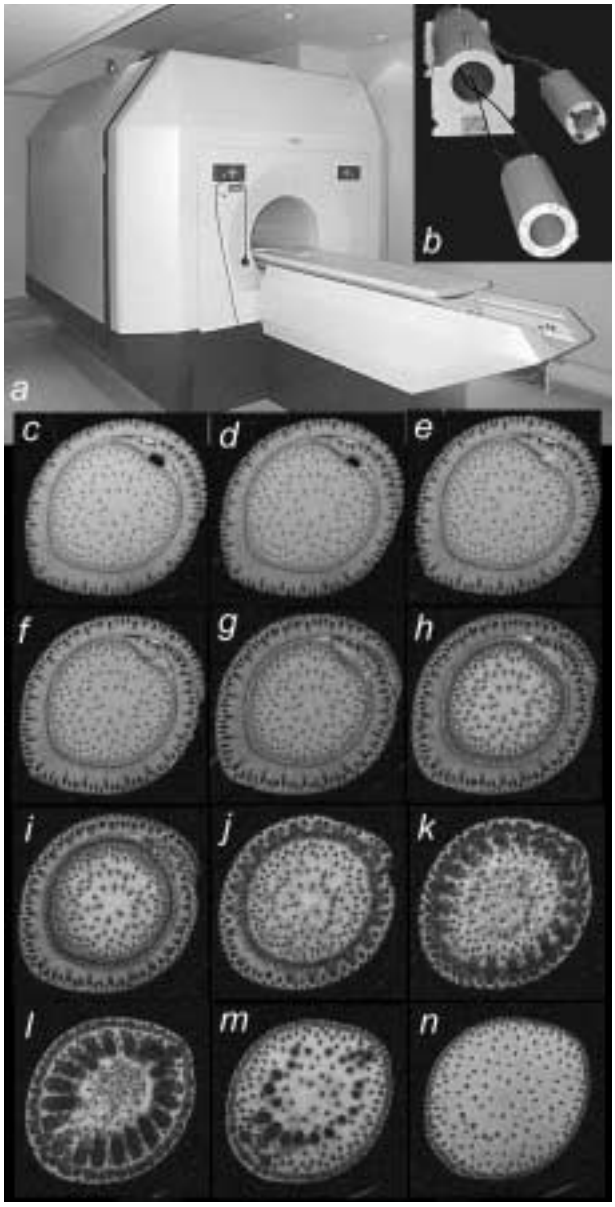

FIG. 1 (a and b) 3T Biospect MRI system (a) equipped with a 6 cm inner diameter microquadrature coil (b). (c–n) Series of MRI slices through a maize node. (o–q) Three-dimensional reconstruction of maize stem around a node from the original MRI sections (c-n).

lyze the mechanical properties of the stem. The maize stem and leave insertions can be approximated to a composite material structure to resemble a reinforced concrete (RC) pillar with long-arm street lights attached, and can be analyzed by conventional civil engineering tools. Results from the analysis will be published elsewhere. This information would be useful in a breeding program to determine varieties resistant to a high-wind environment.

Acknowledgments: Supported by the National Science Council (NSC), Rep. of China: NSC-88-2811-B-001-0023(PCC), NSC-89-2811-E-002-0058(PCC), NSC-89-2215-E-002-064(CKS). The MRI facility is a national user facility funded by the NSC and operated by the Precision Instrument Center, National Taiwan University. The authors are grateful to Vaytek and AutoQuant for providing their software. Maize plants were grown at the University of Western Ontario nursery.

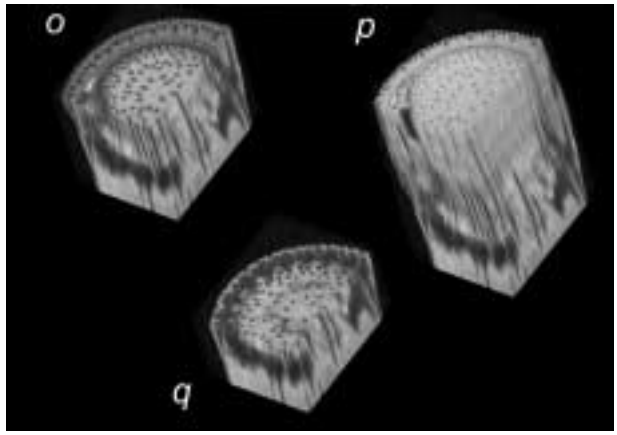

FIG. 2 Reconstructed longitudinal section of a stem revealing complex node vasculature.

References

1. Cheng WY, Cheng PC, Cheng MI, Walden DB: The use of modified flatbed and film scanners for large specimen imaging, *Scanning*, (2001) (this volume)

Subcellular isotopic imaging by dynamic secondary ion mass spectrometry ion microscopy in biology and medicine: Studies of calcium stores and localization of therapeutic drugs

S. CHANDRA

Department of Chemistry and Chemical Biology, Cornell University, Ithaca, NY, USA

For understanding the role of elements and therapeutic drugs under physiological and pathological conditions it is important to identify their intracellular locations. Conventional approaches rely on cell fractionation and gross measurements in subcellular fractions. However, these approaches can redistribute the analyte from its native physiological location to intracellular sites with high chemical affinity. Direct measurements with microscopic techniques provide the most effective approach for these studies. Ion microscopy, based on secondary ion mass spectrometry (SIMS), provides a powerful technique for subcellular studies of elements, ion transport, and drug localization.[1,2] The Cameca IMS-3f ion microscope is capable of producing visual images of isotopic gradients in relation to cell morphology with 0.5 micrometer spatial

resolution. The high elemental (isotopic) sensitivity of the technique in the parts-per-billion range makes it a versatile tool in biological research. Since SIMS analysis involves the gradual eroding of the cell surface for isotopic detection, a sequential three-dimensional (3-D) recording of images within a few minutes of analysis provides the distribution of many desired elements (Ca, Na, K) from the same cell. Strict cryogenic sample preparations are required for these studies so that the subcellular analysis reflects the native chemical composition of the living state of the cell.

It is feasible to directly inject a stable isotope or a therapeutic drug that carries a characteristic elemental tag (boronated anticancer drugs, fluorinated drugs) into the animal's blood supply and then to study their intracellular distributions in the target organ with ion microscopy. Indeed, such studies have provided novel information on hormonally-induced calcium transport[3] and the targeting of individual cancer cells in normal brain with boronated drugs.[4] A few unique SIMS applications in biology and medicine are discussed here.

Quantitative subcellular imaging of calcium stores by SIMS revealed a two-fold higher thapsigargin-releaseable calcium pool in MCF-10A normal breast epithelial cells as compared to MCF-7 tumorigenic breast cancer cells. The nuclear calcium store was not significantly different in these cell lines. As the endoplasmic reticulum (ER) releases its stored calcium in response to thapsigargin, these observations indicate that the calcium pool of the ER is compromised in tumorigenic MCF-7 cells.

The 3-D imaging of calcium distribution in mitotic cells from a normal cell line (LLC-PK) revealed the highest local concentrations of calcium in the spindle region of metaphase and early anaphase cells. Similar analyses of transformed mitotic T98G human glioblastoma cells showed no such calcium gradients. Pathological implications of these initial observations are yet to be understood and may have significance in affecting equal partitioning of mitotic chromosomes in cancer cells.

Secondary ion mass spectrometry has now become an important tool for drug localization studies. The imaging of fluorine in primary hepatocytes revealed the intracellular location of anti-hepatitis B fluorinated drugs. In another study the efficacy of boronated drugs, synthesized for the treatment of brain cancer (glioblastoma multiforme), was checked for their ability to accumulate only in the S phase cells. The pulsing of boronated drugs in question along with bromodeoxyuridine provided a novel approach for testing the drug-targeting of S phase cells. SIMS imaging of bromine and boron from the same cells identified the S phase cells with intranuclear bromine signals and a direct comparison of boron concentrations in S phase and non S phase cells.

References

1. Chandra S, Morrison GH: Imaging elemental distribution and ion transport in cultured cells with ion microscopy. *Science* 228, 1543–1544 (1985)
2. Chandra S, Smith DR, Morrison GH: Subcellular imaging by dynamic SIMS ion microscopy. *Anal Chem* 72, 104A–114A (2000)
3. Chandra S, Fullmer CS, Smith CA, Wasserman RH, Morrison GH: Ion microscopic imaging of calcium transport in the intestinal tissue of vitamin D-deficient and vitamin D-replete chickens: A 44Ca stable isotope study. *Proc Natl Acad Sci*, USA 87, 5715–5719 (1990)
4. Smith DR, Chandra S, Coderre JA, Morrison GH: Ion microscopy imaging of ^{10}B from p-boronophenylalanine in a brain tumor model for boron neutron capture therapy. *Cancer Res* 56, 4302–4306 (1996)

The role of the terminal arterial supply of the rat liver lobule. A corrosion cast and EDX study

U.M. SPORNITZ, I. BARTUSKOVA, G. MORSON

Institute of Anatomy, University of Basel, Basel, Switzerland

Because of the dual vascular supply of the liver lobules, the exact role of the arterial and portal terminal vessels has so far been discussed rather controversially.[1] With the aid of a newly developed method,[2] such as the combination of corrosion casts and detection of marker substances with energy dispersive x-ray analysis (EDX), the terminal afferent vessels could not only be perfectly told apart, but also the nature of the terminal arterial vessels and their mode of entry into the liver lobules has been elucidated. The arterial and portal sides of the blood supply were injected under controlled pressure with Mercox containing two different marker substances, both of which can readily be detected with EDX. The outflow of both injected substances was monitored at the inferior vena cava. Extraportal venous inflow into the liver was cut off with ligatures. To produce corrosion casts which showed either the arterial or the portal part of the vessel only, some preparations were made where through one of the vessels either water or Mercox without hardener was injected. The best results were obtained with water. From these experiments it became clear that the majority of terminal afferent vessels drain individually into the liver lobules. However, the low-pressure terminal portal system is drained with the assistance of two high-pressure pathways: 1. A "high-pressure wall" of sinusoids at the periphery of the lobules which is almost exclusively supplied through terminal arterial branches. 2. Intralobular arteries reaching deep into the lobules. The "high pressure wall" at the lobular periphery originates from the terminal arteries running along the lobular circumference, while the deep intralobular arterial branches originate directly from the interlobular arteries of the periportal fields. The subcapsular region of the liver does not show the well known hexagonal pattern of the classic liver lobules. It is supplied largely through arterial branches. These branches drain into the superficial layer of sinusoids from underneath. The majority of larger vessels present in the imme-

diate subcapsular region are veins draining the outermost layer of the subcapsular sinusoids.

References

1. Saxena R, Theise ND, Crawford JM: Microanatomy of the human liver–exploring the hidden surfaces (Review). *Hepatology* 30 (6), 1339–1346 (1999)
2. Spornitz UM, Bartuskova I, Morson G: Exact detection of arterial and portal branches of the terminal afferent vessels in the rat liver by means of corrosion casts and EDX . *Microsc Microanal*, 5 (Suppl 2), 1204–1205 (1999)

Monday, May 7

Museum applications of SEM

Dinosaur eggshell microstructure visualized by scanning electron microscopy

F.D. JACKSON

Museum of the Rockies and Department of Earth Science, Montana State University, Bozeman, Montana, USA

Dinosaur eggs were first reported in France in 1859. However, they attracted little interest until the discovery of fossil eggs in the Gobi Desert of Mongolia by an American Museum of Natural History expedition in 1923. Since that time, fossil eggs have been found on nearly every continent.[1] Most localities consist of only unidentified hatched eggs or fragmented eggshell. Currently, only eight dinosaur species are definitively identified from eggs containing embryonic bone.

In the absence of embryonic remains, however, fossil eggshell structure provides clues to egg identity. A genetically controlled biomineralized tissue, eggshell exhibits distinct internal structure that distinguishes systematic groups of animals such as turtles, geckos, crocodilians, birds, and dinosaurs.[2] The study of dinosaur reproductive biology, therefore, relies on identification of eggs by structural characteristics, the study of egg and clutch distribution, and comparison of fossil eggs and nests with those of living animals.

Eggshell structure also provides information about reproductive biology and dinosaur physiology. For example, the type of eggshell pore system, which provides embryonic gas exchange, allows inferences about nest construction based on comparison with living animals.[3] The pitted interior of extant bird eggshell results from calcium mobilization for embryonic bone development.[4] The same features in dinosaur eggs suggest a similar physiological process. Eggshell characteristics also support evolutionary relationships: Identical eggshell structure found exclusively in small carnivorous dinosaurs and living birds indicates similarities of reproductive anatomy and augments anatomical studies indicating that birds represent the only surviving dinosaurs.[3]

The study of fossil eggshell, however, requires differentiation of primary structural features resulting from egg formation from secondary features originating from geologic processes (diagenesis). An expanding range of scanning electron microscopy (SEM) techniques provide the analytical tools necessary for interpreting the physical, chemical, and biological changes that affect eggs during burial history.

Scanning Electron Microscopy

High magnification and three-dimensional imaging allows identification of features not visible under lower magnification. For example, permineralized organic tissue such as eggshell membrane may appear as opaque laminations under a petrographic microscope, while high magnification SEM reveals delicate, branching structure and insertion points into the eggshell calcite. These structural details help differentiate the organic shell matrix from ancient or modern fungal or bacterial contaminants of similar morphology.

Backscatter Imaging and Electrodiagnosis

Backscatter imaging often enhances visualization of eggshell structure. Replacement of eggshell calcite by a mineral of higher atomic weight during diagenesis is readily apparent. Electrodiagnosis allows identification of the mineral, which provides valuable information in assessment of paleoenvironmental conditions. For example, barite and gypsum identified in eggs and sandstones from an extensive nesting horizon in Argentina indicate arid conditions, providing a possible mechanism for destruction of the eggs.

Problems and Solutions

Some SEM techniques, however, are destructive to the specimen. Conductive materials (gold or carbon) applied to the fossil specimens improve imaging, but may permanently alter the specimen. Imaging with an environmental SEM eliminates the necessity of specimen coating but results in charging and poorer resolution. With rare specimens, creating a mold from dental putty or silicone and producing an exact epoxy replica of the specimen provides an alternative. The replica can then be gold-coated and imaged. Although fossil eggshell is generally less susceptible to damage from the high voltage electron beam than modern eggshell, structural features in both may sustain significant alteration.

References

1. Carpenter K, Alf K: Global distribution of dinosaur eggs, nests, and babies in Dinosaur eggs and Babies, Carpenter (Eds. KK Hirsch, J. Horner) 16–30 (1994)
2. Mikhailov KE: Fossil and Recent eggshell in amniotic vertebrates: Fine structure, comparative morphology and classification. Special papers in Palaeontology No. 56, Palaeontological Association, London, UK 1–80 (1997)
3. Coombs WP: Modern analogs for dinosaur nesting and parental behavior in Paleobiology of the Dinosaurs, (Ed. JO Farlow) 21–53 (1989)
4. Solomon SE: *Egg and eggshell quality*. Iowa State University Press. Ames, Iowa 1–149 (1997)
5. Gauthier J: Saurischian monophyly and the origin of birds. Memoirs of the California Academy of Science, 8, 1–55 (1986)

Ultrastructure of antennae of tortoise beetles and leaf-mining beetles (*Insecta: Coleoptera: chrysomelidae*)

C. S. CHABOO, T. NGUYEN

Department of Invertebrates, American Museum of Natural, New York, NY, USA

In a search for novel characters for elucidating evolutionary relationships and identifying species of tortoise beetles (subfamily *Cassidinae*) and leaf-mining beetles (subfamily *Hispinae*) (*Insecta: Coleoptera*: Family *Chrysomelidae*), antennae of adult beetles were examined by scanning electron microscopy (SEM). SEM has been applied very little to morphological study in these beetles and has never been used to investigate antennae, an important sensory structure.

Specimens were selected from multiple tribes to reflect taxonomic diversity. These were relaxed and the antenna was removed, cleaned by sonication in soapy water, dehydrated through a graded series of ethanol, critical point dried in carbon dioxide, mounted on tape, and sputter-coated with gold-palladium.

Scanning electron microscopy analysis revealed structures not previously known for cassidine and hispine beetles. Microtrichia, pores, and five types of sensilla were discovered and characterized. The sensilla varied in size, cuticular sculpturing, basal attachment, numbers and arrangement on the antenna. These features have taxonomic implications.

Cold field emission scanning electron microscopy at the American Museum of Natural History: A diversity of applications

A. V. KLAUS

Core Imaging Facility, American Museum of Natural History, New York, NY, USA

The American Museum of Natural History (AMNH) is well known for its public displays of specimens and objects representing the diversity of the natural world and human culture. However, what may not be apparent to most visitors, and indeed to many scientists, is that AMNH also supports a large academic research community. Curators and their associated graduate students, assistants, and post-doctoral fellows are engaged in a wide range of research activities, many of which depend upon the use of scanning electron microscopy (SEM) and x-ray microanalysis.

The core imaging facility at AMNH maintains a state-of-the-art, cold field emission (FE) SEM. The decision to purchase a cold FE-SEM was based upon the instrument's unique ability to accommodate the diverse imaging and x-ray microanalysis projects encountered by a core facility in a natural history research setting. The high brightness/low current probe produced at low accelerating voltages (i.e., 1 kV) allows for the imaging of uncoated specimens with the absence of charging artifacts.[1] This is particularly important for visualizing many of the rare specimens in the AMNH collections. The instrument produces adequate beam current under analytical operating conditions for carrying out energy-dispersive spectroscopy (EDS) analyses. The user interfaces that control SEM and EDS operation are intuitive enough so that casual users with a minimum of prior training can be taught to operate the instrument unsupervised. The narrow probe produced by an FE gun usually negates the need for changing condenser lens settings at higher magnifications, thus allowing the casual user to produce publication quality images without undue assistance from an experienced microscopist.

Applications for SEM at AMNH can be divided into three broad categories: biological, geological, and anthropological. The AMNH biological scientists use SEM imaging with one major application in mind—the analysis of anatomical features (characters). Character analysis is crucial to the sciences of systematics (taxonomy) and evolutionary biology.[2] Entomologists and arachnologists are heavily dependent upon SEM imaging technology. Other biologists who use SEM at AMNH include paleontologists, mammalogists, ichthyologists, and invertebrate zoologists. Geologists generally use the FE-SEM for its analytical capabilities. Backscattered electron (BSE) imaging, qualitative EDS analysis, x-ray mapping, and line scanning are all important to these researchers. A particular advantage of FE-SEM to geologists at AMNH is the ability to do high spatial resolution EDS analysis. Anthropologists rely on both the imaging and analytical capabilities of SEM.

Specimen morphology and elemental composition can help determine the temporal origin of an artifact or object as well as pinpoint its origin in terms of geographical location.

References

1. Goldstein JI, Newbury DE, Echlin P, Joy DC, Romig AD, Lyman CE, Fiori C, Lifshin E: *Scanning Electron Microscopy and X-ray Microanalysis*. Plenum Press (1992), 8
2. Schuh RT: *Biological Systematics: Principles and Applications.* Cornell University Press (2000) 3–28

Metallurgical examinations of medieval sword blades

J. KINDER, M. KLEIN,* C. SEGEBADE

Federal Institute of Materials Research and Testing (BAM), Berlin; *VisiTec™ Microtechnik GmbH, Grevesmühlen, Germany

Two medieval sword blades have been investigated by very different but almost nondestructive methods in order to reveal sufficient information about the ancient sword manufacturing technique. Both blades exhibit approximately the same age because they show almost the same appearance and because they were excavated around 1920 from one site on the river bank of the Rhine by a British officer. The appearance of the blades is typical for Viking swords showing normal shape (length below a meter, relatively wide if compared with younger swords). They are showing a well-developed damascene pattern which is typical for pattern-welded Viking swords. One of these blades is owned by a British museum and the other is privately owned by a British collector. The latter one is slightly wider and exhibits the stronger patterns than the first one and is referred to as "the wider one" which has been investigated much more intensively than the first one.

Obviously, old objects, especially in such good condition, are rather precious in all aspects of their cultural or historical value or their present value. This means that any examination that is conducted over a span of several years had to be as nondestructive as possible. Most nondestructive methods with regard to the question of the sword's manufacturing technique are less evident from the metallurgical point of view than the classical methods that are more or less destroying. To accomplish these requirements on the one hand and to receive as much information as possible from the material itself on the other hand, a federal institute for materials research and testing (BAM)-unique combination of several advanced and nondestructive methods was combined with very little metallographic examinations on the surface and on some tiny cuttings of the blades. The cuttings originated from the edges of the blades tips, and because of the interior of the central part of the wider blade.

The methods used were x-ray fluorescence-, x-ray diffraction-, and gamma-photon radiation-induced activation analysis for receiving compositional information. The internal stresses of the blades were also revealed by x-ray diffraction. The surface of the blades was investigated by conventional metallography using an inverted light microscope, including microhardness testing. These investigations were strongly sustained by metallographic and microprobe examinations of the tiny cuttings from the blades. In addition, a very unique scanning electron microscope that is being developed and produced exclusively by VisiTec¨ Microtechnik, combined with an x-ray energy dispersive spectroscopy device could be used for the examination of the wider blade. This special microscope provides an evacuated specimen chamber which is indeed big enough to accommodate a whole Viking sword without any destruction by cutting the blade into pieces. Furthermore, conventional x-ray microradiography combined with digital image processing and x-ray computer tomography was used to collect as much information as possible from the interior of that blade. Due to a rather big corrosion hole in the surface of the wider blade, which was filled with polymeric resin by its owner, a cutting could be prepared, thereby resembling an almost total crosssection of the blade. This special cutting was also investigated by metallography and microprobe analysis and will be compared with the results of the nondestructive testing methods.

The results may be summarised as follows: The technique of surface hardening by mechanical dressing could be proven by x-raying in both cases. The most obvious difference between the blades lies in the manufacturing process, that is, the several forging steps which caused the differences in the appearance of their patterns. Obviously, the temperature and/or the process times during the complex forging of the blades could not be kept as constant as, for example, with modern industrial production techniques. Both blades may have been manufactured by the same blade smith, but of course it was impossible to keep each step of production reproducible. Surprisingly, the damascening technique needed a rather narrow time-temperature gap for all the different forging steps because the patterns are quite sensitive to forging temperatures as they are too high or to forging times as they are too long. Because the appearance of the patterns of the blades investigated is determined by the distribution of phosphorous which diffuses from high P-regions to low P-regions during forging, a technological step-by-step approach is presented, thereby proving the high skill of the ancient blade smith.

Food microstructure and functionality

Molecular manipulation of milk by biotechnology for commercial benefits

N.C. GANGULI

Malviya Nagar, New Delhi, India

The ubiquity of milk in our diet is based on its nutritional virtues. Apart from the major nutrients like fat, proteins, lactose, vitamins, and minerals, milk is a depository of myriad bioactive proteins and "protein-derived molecular relatives", which are of paramount importance offering both health value and commercial benefits.

The application of biotechnology can transform milk to have new molecules serving as biopharmacy, designer milk, or low lactose milk by cloning the B-galactosidase enzyme. Another group of scientists engaged in new milk product development are contributing monumental products like humanized milk, bioactive molecules, and probiotic milk products, and are exploiting the microorganisms by profitable management.

Molecular manipulation of the existing biomolecules in milk has enabled the food scientists to incorporate new molecules in milk and milk products with prohealth virtues. The birth of new protein families in milk can now be more profitably utilized for the manufacture of a new brand of products with "therapeutic assurance" and is likely to surpass the "subordinate status" in the food industry.

Scanning probe microscopy applications in the food sciences

J.T. THORNTON

Digital Instruments/Veeco Metrology Group, Chadds Ford, PA, USA

Surface microstructure is an important parameter in the appearance, texture, and processing of many foods. Microscopy provides the ability to investigate food structure, and promotes the understanding of the structural role of individual components and their effect on the properties of the final product. Scanning probe microscopy (SPM) characterizes a food substance in three dimensions nondestructively from the angstrom/nanometer scale up to 100 microns, providing the ability to study single molecules as well as complex composite structures. Atomic force microscopy (AFM), the most common form of SPM, is conducted in ambient and fluid environments and requires minimal sample preparation. Studies in solution provide the ability to image a specimen in its hydrated state and under a controlled environment.

Over the past 15 years, SPM has been used extensively to investigate biological and polymeric structures, and has been found to be just as useful in the study of food biopolymers. Carbohydrates, polysaccharides, proteins, gels, colloids, bacteria, and cells are common samples for food-related SPM investigations. Scanning probe microscopy has also found utility in investigating food packaging, the study of bacterial interactions, the formation of biofilms, and determining how parameters in the processing of food affect the microstructure and other properties. Dynamic studies of processes in situ as well as temperature studies have also been conducted.

There are also a wide range of SPM techniques that can be used to investigate the physical and material properties of structures. Phase Imaging has been used to determine the distribution of components in a composite food system by detecting differences in adhesion and/or viscoelasticity during imaging. Differences in compliance and hardness have also been investigated by conducting nanoindentation with the AFM.

Area-scale analysis of food surfaces

T. S. BERGSTROM, C. A. BROWN

Surface Metrology Laboratory, Worcester Polytechnic Institute, Worcester, MA, USA

Area-scale fractal analyses are applied to cornflake surfaces measured by scanning laser microscopy (SLM), demonstrating scale-dependent interactions with milk.

Understanding surface functionalities can improve product and process design, as well as quality assurance. Many aspects of behavior and processing are suspected to be influenced by the roughness or influence the roughness of foods, for example, wetability, flavor, adhesiveness, appearance, coating volume, rheology, and biological growth; however, the interaction with roughness is often poorly understood.

Average roughness, Ra,[1] has been found inadequate for understanding functionality.[2] Fractal methods may be better [4–6] and have been applied to food[6–8] And, scale-sensitive fractal analysis can be used to determine scales of interaction.[7]

Methods

Four Kellogg's cornflakes were inserted in whole milk, two for 5 min and two for 10 min. Excess liquid was absorbed from the surfaces prior to the measurements by slow dabbing with a paper towel. Six regions, 5×5 mm, almost entirely overlapping, were measured on each flake before insertion and again after removal. The SLM measures a series of profiles with laser triangulation to produce a topographic map and has lateral and vertical resolutions of 25 and 12.5 μm, respectively. Each of the six measurements contains 200×200 elevations and took 3.8 min.

Area-scale fractal analysis,[8] with a series of virtual tiling

exercises with triangular patches to determine the relative areas (the apparent area divided by the nominal area), was applied from scales of 0.001 to 10 mm″.

Results and Discussion

Log-log plots of relative areas versus scales of measurements for successive measurements on one cornflake are shown in Figure 1. The plots of the measurements made on the other cornflake inserted for 5 min are similar, and those inserted for 10 min have relative greater areas.

The increases in relative area both with scale and time are dramatic. For the dry cornflakes, the relative area increases from 1 to 1.6 from scales 1 to 0.001 mm″, indicating 60% more area available for interaction at the finer scales. After inserting in milk for 5 min, the relative areas at the fine scales are around 2, indicating twice the surface available for interaction, and 20 min later the relative areas at the fine scales exceed three. The intensity of interactions sharing these scales should increase with the relative areas.

Figure 2 shows the relative areas at 0.0189 mm″ versus the time after insertion in milk. The high R″ indicates that the relative area is an excellent indicator of the time since insertion in milk. Similar results, with R″s consistently greater than 0.8, are observed for relative areas at scales between 0.001 and 0.1 mm″. This establishes functionality and indicates that phenomena are occurring over these scales as the milk interacts with the cornflakes.[3]

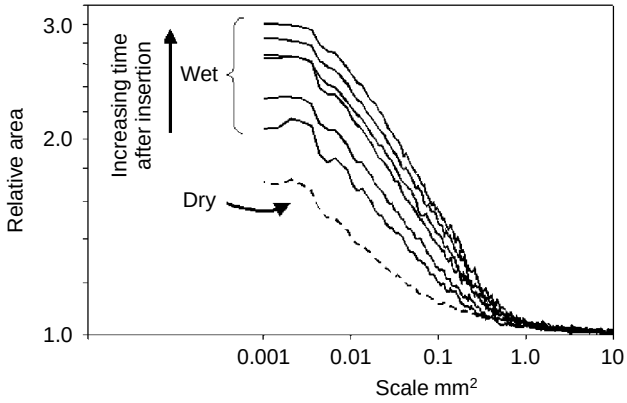

FIG. 1 Log-log plots of relative areas versus scales of measurements for successive measurements on one cornflake.

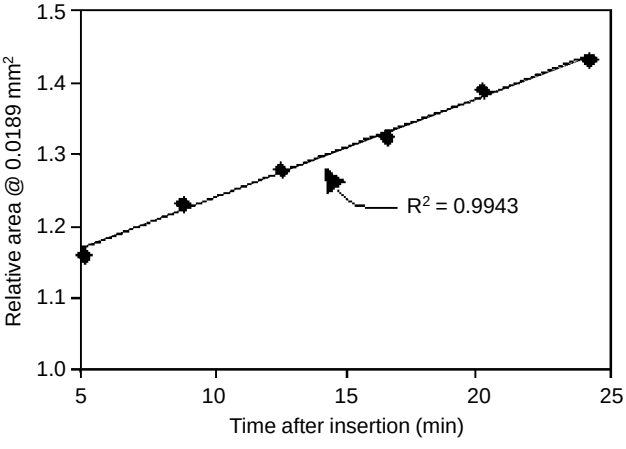

FIG. 2 Relative areas at 0.0189 mm" versus the time after insertion in milk.

Conclusions

Relative areas increase dramatically with time after the flakes are removed from the milk.

Relative areas and time of exposure to milk correlated highly over scales from 0.1–0.001 mm² indicating that these scales are characteristic of the milk–cornflake interaction.

References

1. ASME*: Surface Texture (Surface Roughness, Waviness, and Lay).* ASME B46.1-1995, American Society of Mechanical Engineers, New York (1969)
2. Hershko V, Weisman D, Nussinovitch A: Method for studying surface topography and roughness of onion and garlic skins for coating purposes. *J Food Sci*, 63, 2, (1998)
3. Russ JC: *Fractal Surfaces*, Plenum Press, New York (1994)
4. Pedreschi F: Characterization of the changes in the structure of potato during frying. Ph.D. dissertation, Pontificia Universidad Catolica de Chile, Santigo (2000)
5. Pedreschi F, Aguilera J-M, Brown CA: Characterization of food surfaces using scale-sensitive, fractal analysis. *J Food Process Engin*, 127–143 (1999)
6. Peleg M: Fractals and food. *Criti Rev Food Sci Nutr* 33/2 149–165 (1993)
7. Brown CA, Seigmann S: A method for determining the characteristic scale for adhesion for a discrete bonding model on a rough substrate. *Proc 10th International Colloquium of Surfaces Chemnitz* (Eds. Dietzsch M, Trumpold H) Shaker Verlag, Aachen (2000) 196–204
8. Brown CA: A method for concurrent engineering design of chaotic surface topographies. *J Mater Process Technol* 44 337–344 (1994)

Pharmaceuticals

Computer-assisted correlative microscopy and analysis: Thinking beyond the box for characterization of change in biological tissues

K.W. BAKER, I. PISCOPO*

Ken Baker and Associates, Acton, Ontario, Canada;
*EM Consultant, Norwalk, CT, USA

In the context of pharmaceutical toxicology and safety assessment in an FDA-regulated environment, it is frequently the case that structural and analytical assessment of unexpected or anomalous results must occur under rapidly changing circumstances and frequently with little option for altering the larger experimental protocol. The

goal, for reasons of safety and cost, is to provide a rapid, simple, and informative answer; to do so in a closely documented fashion; to correlate results with those acquired using other methodologies; and finally, to be able to link and communicate those results expeditiously.

The following describes a typical, in situ, correlative microscopy and analysis initiative undertaken for rapid identification of a sulfated metabolite as the source of renal crystals occurring in high-dose animals in a regulated study. Unlike such initiatives occurring in less rigorously regulated circumstances, this analysis had to consider, document, and precisely communicate the nature of acquired digital images and related data, especially considering that most data were not acquired in house using standard operating procedures.

Representative samples of renal cortex from high-dose and control animals of each gender were extracted from tissue archives and prepared for light (LM), scanning electron (SEM), and transmission electron microscopy (TEM), including energy dispersive x-ray microanalysis (EDX).

A specialized SEM/EDX technique was devised using microscope slides sputtercoated with 60/40 Au/Pd, both as an elemental reference background and as an adhesive for sections. Renal sections were cut at 7 μm, mounted, deparaffinized with xylene, cleared with 100% EtOH, and air-dried. Sections were left uncoated for LM and EDX analysis and sputtercoated for SEM morphology. Slides were mounted directly in the specimen chamber of a Hitachi S-570 SEM equipped with a Noran thin window x-ray system. X-ray microanalysis was performed from 3 to 20 kV to encompass elements from the entire periodic table and to determine the optimum penetration depth. If Au or Pd appeared in the spectrum, it was assumed that the beam had exceeded the specimen's thickness and that x-rays were being elicited from the underlying support film. Subtle differences were shown to occur within 1–2 kV. The EDX results, reported as Net Counts per second, identified elevated concentrations of C, O, Si, and S, with S showing the highest peak to background.

Samples were additionally processed for TEM and 120 nm epon sections were analyzed using a Hitachi 7110 scanning transmission electron microscope (STEM) equipped with a Noran Voyager II x-ray system and digital image acquisition. The electron probe was maintained at a fixed diameter for EDX analysis of all structures, and elemental Net Counts for C, O, Si, and S were recalculated and displayed as a counts per unit time ratio to the Formvar background.

Paraffin sections on Au/Pd-coated glass slides facilitated rapid correlation of LM and SEM morphology and EDX analysis. We were able to compare spectra from separate samples with some assurance that probe depth (and x-ray source) was comparable. Crystal morphology was more apparent because of the airdrying-induced shrinkage of surrounding renal tissue.

Correlative TEM/EDX analysis also identified elevated concentrations of C, O, Si, and S, with S again having the highest peak to background. Crystal morphology and composition correlated with that described previously using LM and SEM/EDX. Transmission electron microscopy morphology also revealed the extent to which crystals were closely invested with a subcellular organic component and suggested that a noncrystalline component must also be contributing to the x-ray spectra.

In summary, SEM/EDX analysis provided a fast, preliminary answer, while TEM/EDX results, acquired independently and at a later time, confirmed the early findings. The documentation, archiving, and communication of these electronic data, though challenging, were necessarily precedent setting in establishing paths for comparable initiatives. Advanced correlative microscopies, imaging and analysis as such, though underutilized, remain extraordinarily well suited for providing the kind of specialized solutions described in this account. Used effectively, they can rapidly provide important and definitive answers, not only to questions of safety but also for understanding therapeutic mechanisms of pharmacologic action.

Particle analysis of tablets

R. ANDERHALT

EDAX Inc., Mahwah, NJ, USA

Automated particle analysis is a general procedure that is useful for particle sizing and energy dispersive spectroscopy (EDS) analysis of grains or phases that can be isolated by their gray-level values from their surrounding area. Typically, the backscattered electron (BSE) detector is used, and we are able to separate phases with higher average atomic numbers (i.e., brighter areas in the image) from a matrix having a lower average atomic number. Although it would also be possible to detect automatically the phases with a lower average atomic number, this rarely works efficiently in pharmaceutical materials because of the predominantly organic matrix and confusion of dark areas with pores and areas with a depressed topography. Quite often phases representing active ingredients, pigmenting agents, other fillers, and contaminants can be detected, sized, and chemically analyzed with a speed and efficiency that is not possible by more manual analyses. The consistency and distribution can be analyzed as a check in certifying the quality of production.

Tablets can be prepared by fracturing the tablet or by crushing the tablet to produce a powder. The fractured tablet offers the advantage of being able to examine a consistent area in which a particle's location is meaningful with respect to its location within the tablet, but has the difficulty that a nonoptimal topography can prevent the collection of reliable EDS data. Careful fracturing or "shaving" of the surface can minimize this problem. The number of particles per field or per square millimeter can be used to address the consistency of the application of the phase. Powdered materials can be useful for searching for contaminants, but the

number of particles per field or per area unit of the sample is not meaningful because the particle density is determined by the technique used to apply the particles to the substrate. However, this may still be a useful technique if more than one chemical phase is being detected and analyzed. The ratio of one phase to a second phase is a parameter that may be used to determine the tablet quality.

The EDS particle spectra can be quantified as a measure of composition that can ultimately be of use in the classification of the particles. Particle size and topography will alter the analysis results and can cause a departure from the ideal composition of the phase. A threshold can be adjusted to permit classification when the analysis does not perfectly match the analysis used in the classification library. As such, the quantitative analysis is used only to group the data qualitatively even though the numbers may not be accurate.

A spreadsheet may be used to summarize the data analysis. These data may also be sorted to segment the class, size range, or range of chemistries. Bivariate plots are useful to display the relationship between size, shape, or chemistry parameters. Trivariate plots can be used to display three normalized elements or to display three groups of elements. In the trivariate plot, each apex of the triangle is color coded (red, green, and blue) to make a composite color used in this plot, and the same color will be displayed on top of the particle in the BSE image.

Developing a new chemical entity (NCE) — Why does it take so long?

B.D. HARTMAN

Department of Pathology, Schering-Plough Research Institute, Lafayette, NJ, USA

There are many hurdles in the development process before a new chemical entity (NCE) can make it to the drug store shelf. The development process for a new drug in the United States usually takes in excess of 10 years and costs over 500 million dollars. There are three main phases in the development of an NCE. The first phase is drug discovery, which is the process of identifying an NCE that has therapeutic value and is driven by medical need and the biological/chemical programs available. During this phase of development, NCEs are screened for activity in animals and cellular models predictive of efficacy for the selected disease.

Once an NCE has been identified, the second phase, preclinical, begins. At this time, toxicology and pathology work together to assess the safety of the NCE. Depending on the nature of the NCE and its intended use, preclinical studies in two mammalian species, a rodent and a non-rodent, are required before the NCE can be administered to humans. At this stage, the sponsor may begin clinical trials while further preclinical studies are conducted. The doses used and duration of treatment in these early clinical trials is determined by the results from the animal studies.

Genetic toxicology and preliminary reproductive toxicology studies are also required. Since the NCEs come into the safety assessment phase with undefined toxicity, studies are designed to determine adverse side effects and possible target organs as well as the dosage, route of administration, etc. An NCE may spend 4 to 6 years in the preclinical safety assessment phase. It is critical that the sponsor provide enough data to assure the NCE is safe for testing in humans.

In an attempt to harmonize technical requirements for drug products around the world, the International Conference on Harmonization (ICH) provides regulatory guidance documents. These documents provide guidelines on the extent and timing of preclinical testing. The studies are designed based upon the nature of the drug, the route of administration, and the targeted population.

The investigational new drug application (IND) is required by the FDA prior to the initiation of clinical studies. This IND must include preclinical data to permit an assessment as to whether the NCE is safe for testing in humans. The IND must also include manufacturing information and detailed protocols for proposed clinical studies. Sponsors are permitted to initiate the clinical trials proposed in the IND 30 days after the FDA receives the application, provided the agency has not contacted the sponsor during the 30-day period.

Clinical trials represent the third phase in the drug development process and are complex, time consuming, and costly. Most clinical development programs have three phases. Phase 1 studies are done in a small number of patients to gain basic pharmacologic information. Phase 2 studies are designed to obtain preliminary safety and efficacy data in patients who suffer from the clinical condition. Phase 3 studies are done on a large population of patients, are designed to gather extensive safety data, and must prove the NCE's effectiveness.

The new drug application (NDA) is the vehicle through which the sponsor of a NCE formally requests that the FDA approve an NCE for sale and marketing in the US. An NDA comprises thousands of pages of nonclinical and clinical data along with information about the drug's formulation and manufacturing. The NDA is used by the FDA to determine whether the NCE is safe and effective in the target indication and whether the proposed labeling is appropriate. The FDA has one year from the sponsor's submission date to respond to the NDA. Once the FDA is satisfied that the NCE is safe and effective, the sponsor will be notified and the NCE can be marketed.

The pharmaceutical community and the FDA are working together to make NCEs as safe as possible and to get them to the public sooner. In 1982, the Orphan Drug Act (ODA) was created to provide incentives for sponsors to develop NCEs for rare diseases. With cooperation between the FDA and the pharmaceutical community, NCE will be developed faster and approved more quickly, while ensuring the safety of the public.

Application of correlative microscopy to genetic therapy of various human diseases

K.C. MOORE

University of Iowa, Iowa City, IA, USA

Light and Electron Microscopy are essential tools for developing strategies to use genetic therapy in the treatment of diseases. Negative staining and cryo-electron microscopy are critical in understanding the structure of native and hybrid vectors to be used as transfer agents. Enzyme cytochemistry is widely used for the detection of markers that aid in determining the rate of gene transfer to cells and tissues. Immunocytochemistry is necessary to identify new gene products. Light, confocal and electron microscopy are used to evaluate pathogenesis, inflammation and cellular changes. For much of the past decade, we have been working to identify the specific gene and cell structure (chloride channel) that is compromised in Cystic Fibrosis patients. Subsequently, appropriate vectors have to be developed for treatment. A significant amount of time and effort has been expended to identify effective viral and other vectors to be used in the transfer of the normal gene construct. In addition to Cystic Fibrosis, specific strategies for gene therapy approaches to Muscular Dystrophy, Hemophilia, neurological problems, and various skin disorders will be introduced.

Atypical applications of scanning electron microscopy within the pharmaceutical industry

R.L. MÜLLER

GlaxoSmithKline, King of Prussia, PA, USA

We have applied the scanning electron microscope (SEM), in conjunction with other various analytical techniques, within the pharmaceutical industry. Scanning electron microscopy is commonly used to study the particle/surface morphology of pharmaceutical materials, elemental composition and particle size distributions. An environmental SEM can also be used to study pharmaceutical materials under dynamic conditions.

Information obtained from environmental scanning electron microscopy (ESEM) images is somewhat limited because it is visual and subjectively descriptive. However, when the ESEM is used in conjunction with other techniques, it becomes a powerful characterization tool for pharmaceutical materials, as seen in three case studies. First, during early development of an active pharmaceutical ingredient (API), the water content of this hydrated material became critical to control. During the drying process of this hydrated material, generation of an anhydrous material was observed. By using multi-technique assays, including hot stage ESEM, this anhydrous material was characterized and the relationship between the hydrated and anhydrous materials was understood. Second, by using energy dispersive x-ray spectroscopy, it was demonstrated why some core tablets manufactured from newer API batches failed content uniformity, whereas core tablets produced from older API batches or re-worked newer API batches passed content uniformity. Third, we have used videos of dynamic ESEM experiments to document hydration and/or recrystallization experiments and solid-liquid phase changes.

Comparison of healing effects of estrogen and bombesin in gastric and colonic inflammation

Ö. GÜNAL,[*] E. ÖZÇINAR,[‡] S. ARBAK,[‡] B.K. OKTAR,[†] B.Ç. YEĞEN[†]

[*]Department Of Surgery, Medical Faculty, I. Baysal Un. Bolu; [†]Department. Of Physiology; [‡]Department of Histology-Embryology, Medical Faculty, Marmara Un. Istanbul, Turkey

Several experimental and clinical studies suggest that pregnancy and lactation markedly reduced the incidence of gastroduodenal ulcers.[1,2] Meanwhile, the gastroprotective effect of bombesin, a tetradecapeptide, by means of increasing gastrin secretion in gastric ulcer was investigated n many studies.[3,4]

To investigate the effects of these two agents in gastric inflammation, Wistar albino rats of both sexes were used. Gastric ulcers in Ulcer Group were produced by applying 75 μl of acetic acid (80%) onto the serosal surface of anterior wall of the stomach for 25 seconds under ketamine anesthesia. In another group of rats (Colitis Group), either vehicle or acetic acid (1 ml, 5%) was inserted through a polyethylene tubing at 7 cm from the anus under light ether anesthesia. The Ulcer Group was subdivided into 2 subgroups: One group was treated with 17 β estradiol benzoate (10 mg/kg/day; sc) or oil (Ulcer-Estrogen Group) and the other group was administered Bombesin (30 mg/kg/ day; sc) or BSA (Ulcer-Bombesin Group) for 7 days. For the Colitis Group, the same dose of 17 β estradiol benzoate was administered for 4 days until they were decapitated. In both gastric and colonic tissues, macroscopic and scanning electron microscopy (SEM) evaluations of damages, along with the determination of tissue myeloperoxidase (MPO) activities, an index of neutrophil infiltration were done to demonstrate the extent of the injuries. Estradiol and bombesin reduced the gastric ulcer index ($p< 0.05$ and $p < 0.01$) and colonic damage score ($p< 0.05$) when compared to with oil- and BSA- treated rats. Elevated tissue MPO levels were significantly reduced in both the gastric and colonic tissues as compared with corresponding vehicle groups. In oil- and BSA-treated groups, SEM demonstrated extensive disruption in the glandular architecture in both gastric and colonic surface epithelium with extreme

epithelial desquamation, significant hemorrhage, prominent vasocongestion, and eosinophilic infiltration. In the estrogen and bombesin treated groups, glandular architecture of both tissue were moderately disrupted, with mild eosinophilia, moderate hemorrhage, and vasocongestion.

The results of the present study indicate that both exogeneous estrogen and bombesin accelerates the healing of the gastric inflammatory process. Regarding the results of the microscopical scoring and values of MPO activity, the bombesin group was concluded as the less affected group from the harmful effects of acetic acid. On the other hand, exogeneous estrogen inhibits neutrophil-derived inflammatory mediators in the colon and has an effective healing effect in case of colonic inflammation. Both of these agents are thought to ameliorate microvascular disturbances.

References

1. Chen TS, Doong ML, Chang FY, Lee SD, Wang PS: Effects of sex steroid hormones on gastric emptying and gastrointestinal transit in rats. *Am J Physiol*, 268, G171–G176 (1995)
2. Coskun T, Sevinç A, Tevetoglu I, Alican I, Kurtel H, Yeğen BÇ: Delayed gastric emtying in concious male rats following chronic estrogen and progesterone treatment. *Res Exp Med*, 195, 49–54 (1995)
3. Hernandez DE, Burke JD, Orlando RC, Pragne AJ: Differential effects of intracisternal neurotensin and bombesin on stress- and ethanol-induced gastric ulcers. *Pharmacol Res Commun*, 18, 7, 617–627 (1986)
4. Mercer DW, Cross JM, Chang L, Lichtenberger LM: Bombesin prevents gastric injury in the rat: Role of gastrin. *Dig Dis Sci*, 4, 826–833 (1998)

Modern optical microscopy, Part II

Biological multi-modality nonlinear spectro-microscopy: Multiphoton fluorescence, second- and third-harmonic generation

P.-C. CHENG, C.-K SUN,* B. L. LIN,† F.-J. KAO,‡ S-W CHU*

AMIL, Department of Electrical Engineering, University at Buffalo, Buffalo, NY, USA; *Department of Electrical Engineering, National Taiwan University, Taipei and; †Institute of Molecular Biology, Academia Sinica, Taipei, Taiwan; ‡Department of Physics, National Sun Yat-sen University, Kaohsiung, Taiwan, Republic of China

The intrinsic optical sectioning properties in nonlinear optical microscopy have drawn much interest in biological sciences; in conjunction with numerous fluorescence bioprobes, multiphoton fluorescence microscopy has become a powerful tool for deep tissue imaging and microspectroscopy at high spatial resolution.[1] In addition to the fluorescence signals generated by multiphoton excitation process, nonlinear phenomena such as harmonic generation can also provide useful information about the structure and optical properties of a specimen.[3]

Two-photon fluorescence and harmonic generating microscopy were performed on a modified Olympus Fluoview confocal unit equipped with a mode-locked Ti-sapphire laser (780 nm, 100 fs pulse, 82 mHz) or a Cr-forsterite laser (1230 nm, 110 mHz, 130 fs). For spectromicroscopy, a SpectraPro-500 spectrometer (Acton Research) equipped with a LN-cooled CCD detector or a TE-cooled CCD equipped SpectraPro-150 spectrometer was added to the microscope. Spectromicroscopy was performed in transmission mode by using a computer-controlled scanning stage.

Plant cells produce strong autofluorescence due to the presence of large amounts of photosynthetic pigments. The predominate fluorescent emission is in the green and red.[2] Using two-photon microspectroscopy, the fluorescence emission of a single cellular organelle can be studied. Figure 1b shows the time-lapse study of the fluorescence emission from a single chloroplast in the protoplast of *Zea mays* (Fig. 1a). Similar to the two-photon fluorescence process, second-harmonic generation (SHG) process, which is a $\chi^{(2)}$ second-order nonlinear process, provides strong nonlinear signals but occurs only in non-centro-symmetric media. The SHG process can thus be used to image biointerfaces and orderly arranged structures, where centro-symmetry is broken. In SHG, only virtual state transition was involved, thus no photo-damage and bleaching from the process are expected. With a square dependence on the incident illumination intensity, the SHG process provides the same optical sectioning resolution as the two-photon fluorescence process if the same excitation wavelengths are used.

Unlike SHG, third-harmonic generation (THG) is a $\chi^{(3)}$ third-order, nonlinear process; however, different from the two-photon absorption process, only virtual state was involved. The marked advantage of this virtual state transition of the THG process makes no energy deposition during the conversion process, thus no photo damage from the process is expected. Due to the large refractive index difference between the fundamental and THG light and the positive dispersion in biological specimens, effective THG generation occurs only in thin layer or on the interfaces. This coherent length effect provides to the THG process an excellent axial resolution in detecting the surface of cellular organelles and membranes.

Simultaneously detecting the multiphoton fluorescence, SHG and THG provide a new way of studying biological specimens. This multimodality microscopy allows colocalization of the biosignificant fluorescence signal with structural information corresponding to the generation of SHG and THG signals. Figure 1c–e shows a set of images [THG (c), SHG (d), and red fluorescence (FL; e)] and a selected spectrum obtained from the parenchyma cells of maize stem (fixed in 3:1 EtOH/ acetic acid). Recording the

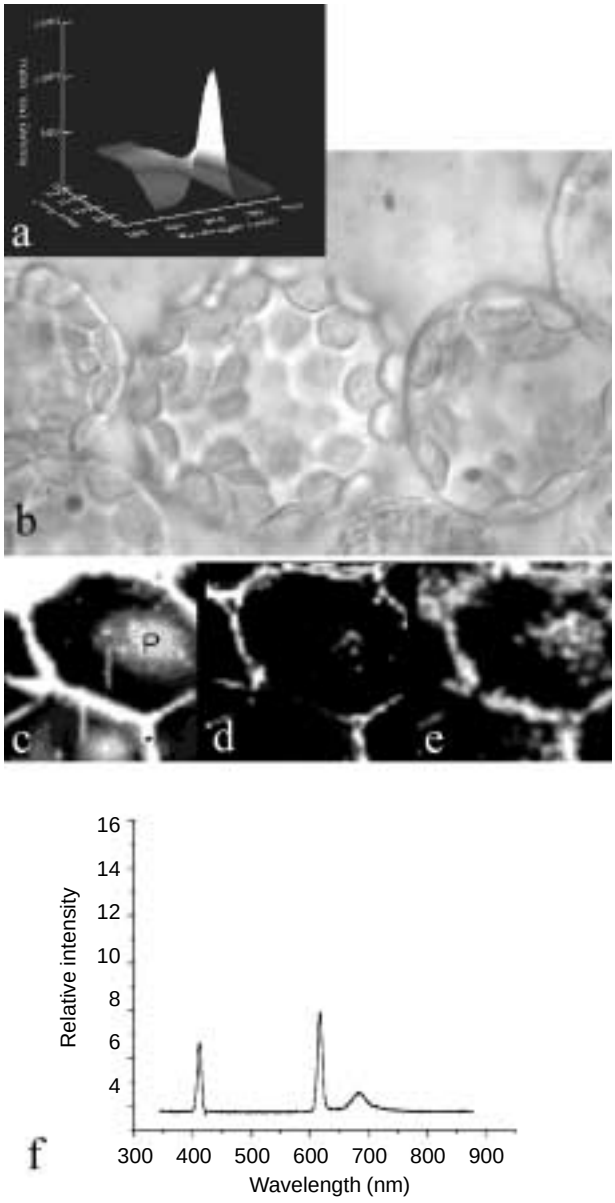

FIG. 1 (a) Transilluminated micrograph of maize protoplasts showing numerous chloroplasts. (b) Time-recording of the red fluorescence intensity variation of a single chloroplast under intense NIR illumination. Excitation: 780 nm, 100 fs. (c-e) Multimodality microscopy of maize parenchyma cell showing (c) THG, (d) SHG and (e) fluorescence (FL). The bright patch (P) in (c) is the transverse wall of parenchyma cell. Illumination: 1230 nm. (f) Spectrum taken from selected point in a parenchyma cell.

spectrum of each pixel in an image ensures positive identification of the origins of signals (Fig. f).

Acknowledgments: Supported by NSC-ROC under grant numbers: NSC-88-2811-B-001-0023(PCC), NSC-89-2811-E-002-0058(PCC), NSC-89-2311-B-001-032(BLL), NSC-89-2112-M-110-016, NSC-89-2216-E-110-003 (FJK), NSC-89-2215-E-002-064(CKS) and Academia Sinica(BLL).

References

1. Kao FJ, Lin BL, Cheng PC: Two-photon micro-spectroscopy of chloroplasts from *Arabidopsis thaliana*. *Scanning*, 22, 91–92 (2000)
2. Cheng PC, Lin BL, Kao FJ, Xu MG, Gan XS, Huang MK, Wang YS: Multi-photon fluorescence microscopy–the response of plant cells to high intensity illumination. *Micron* (in press) (2001)
3. Muller M, Squier J, Wilson KR, Brakenhoff GJ: 3D microscopy of transparent objects using third-harmonic generation. *J Microsc*, 191, 266–270 (1998)

The virtual transmitted light interference microscope: Reconstruction of optical path length distribution from differential interface contrast microscopy images

D. S.C. BIGGS, S. INOUÉ, * T. J. HOLMES

AutoQuant Imaging, Inc., Watervliet, NY; *Marine Biological Laboratory, Woodshole, MA; AutoQuant Imaging, Inc. and Rensselaer Polytechnic Institute, Troy, NY, USA

Differential interference contrast (DIC) microscopy is a popular modality for observing live transparent biological specimens without toxic staining. Differential interface contrast microscopy detects changes in the optical path length distribution of a specimen along a certain orientation. The optical path length is dependent on the thickness of a specimen and the distribution of refractive index within the specimen. However, since DIC microscopy is a differential technique, it does not directly provide quantitative information about the optical path length distribution.

The aim of this research is to reconstruct a map of optical path length distribution from a single DIC image. The technique is a software-based image processing algorithm that enables a standard DIC microscope to operate as a "virtual" transmitted light interference microscope. The transmitted light interference microscope was once popular in the 1950s and 1960s; however, DIC is now a more prevalent modality.

The reconstruction is currently performed in two stages; first to invert the differential nature of the DIC image, and second to improve the resolution of the reconstructed optical path length distribution using a deconvolution algorithm. The processing algorithms are both iterative in nature and can process a typical 256×256 image in under 1 min on a standard Pentium computer. The reconstruction includes a regularization filter to prevent streaking artifacts that would otherwise appear parallel to the shear direction, and a penalty on negative values. The image data is also preprocessed to correct for the effect of the sinusoidal transfer function that characterizes the interference of the sheared beams, which converts the difference in phase to image intensity.

The reconstructed data exhibits bright features against a dark background, and is now in a form that is suitable for

use with standard image programs for segmentation, object analysis, cell counting, and cell tracking. The improved resolution also enables features to be seen beyond the diffraction limit of the microscope. In addition, three-dimensional (3-D) specimens optically sectioned using DIC optics can now be volume rendered and visualized. Image registration can be used to correct for specimen movement that may occur between sections.

The transmitted light interference microscope can determine the optical path length, for a single point on a specimen, which is a capability that DIC microscopy does not directly provide. The technology developed from this research enables the optical path length distribution over an entire specimen to be derived from a single DIC image. The optical path length information can then be used to measure the "dry mass" of a specimen. Tracking the dry mass of a cell, or cell parts, over time allows changes in growth to be observed. Analysis of cell growth and behavior will allow the effects of manipulating a cell's genome to be determined, which could play a major role in characterizing the phenotypic results of genetic engineering.[1]

Results will be presented for a number of biological specimens, including the reconstruction of DIC images of yeast cells, which reveal that the nucleus has a lower optical path length (and presumably lower relative refractive index) with respect to the surrounding cytoplasm. The 3-D reconstruction of a dandelion pollen grain, optically sectioned using DIC will also be presented. This specimen was captured using Dr Inoué's optical-bench inverted universal light microscope, using Nikon DIC optics and a Hamamatsu Orca-1 cooled CCD camera.

This project has shown the feasibility of reconstructing the distribution of optical path length from DIC imagery of a specimen, thus enabling the function of a transmitted light interference microscope to be emulated in software.

Acknowledgments: This research is supported by funding from the NIH under SBIR grant number 1R43GM60833-01.

References

1. Dunn GA: Transmitted-light interference microscopy: A technique born before its time, *Proc Royal Microsc Soc*, 33, 189–196 (1998)

Effects of apodization and wavefront functions on the point spread functions

S. SAMN, S. COHEN,* AND G. LI†

Air Force Research Laboratory, Brooks Air Force Base, TX; *US Army Natick Soldier System Center, Natick, MA; †University of Texas at San Antonio, San Antonio, TX, USA

The point spread function (PSF) is a function of optical aberrations, apodization functions, and wavefront functions. For an aberration-free optical system, and a variety of wavefront functions such as spherical and parabolic wavefront function the PSFs in the focal plane and meridional plane were calculated. For an aberration-free optical system and a variety of apodization functions such as linear, parabolic, and the Bessel functions the PSHs in the focal and meridional planes were also calculated. We defined the lateral and axial half width of the PSFs as a criterion to evaluate the lateral and axial resolution of an optical system. Thus, we quantitatively calculated and compared the lateral and axial resolution of an aberration-free optical system for a variety of apodization and wavefront functions. Our results showed that for an aberration-free optical system and spherical wavefront if the amplitude or apodization functions at the entrance pupil of an optical system increases from the center to the edge their lateral effective half width (EHW) is smaller than that from uniform illumination. Thus, an optimal apodization and/or wavefront function may be found by numerical analysis and the resolution of a confocal system may be greatly improved.

This study provides useful information to design high resolution confocal microscopes using spatial light modulators (SLM) and deformable mirrors (DM). An SLM is available to generate any kind of apodization functions, in principle. A DM may also generate any kind of wavefront functions. Based on the above numerical analysis a confocal microscope using SLM and DM to achieve high lateral and axial resolution was designed.

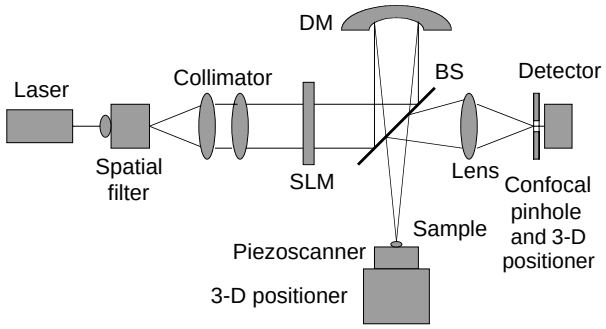

FIG. 1 The optical system of a new confocal scanning microscope.

3-D images of the HgBrI compound obtained by using confocal scanning microscopy

G. A. STANCIU, S. G. STANCIU

Department of Physics, University "Politehnica" of Bucharest, Bucharest, Romania

The ternary compounds $HgBr_xI_{2-x}$ ($0<x<2$) are solid solutions of the HgI_2-$HgBr_2$ system.[1] They have large molecular weight, high-energy gap value ranging from 2.1 eV

for HgI_2 to 3.5 eV for $HgBr_2$, and high electrical resistivity, which are properties required in a material suitable for the fabrication of x- and gamma-ray detectors that operate at room temperature. The leading material for these applications is HgI_2, which has the disadvantage of a solid-solid phase transformation around 130°C, which limits the growing of single crystals to vapour phase methods. The ternary compounds, for x>0.4, do not exhibit any phase transformation, so crystal growth is possible with most of the available methods, even with the common ones from the melt.

Lately we have reported some results obtained on the similar compund $HgBr_2$.[2–3] The first results obtained by us on the HgBrI were also published.[4]

In the present paper, the growth of $HgBr_xI_{2-x}$ crystals with several compositions (x=0.4, 0.6, ..., 2.0) is given, by two different techniques, the Bridgman-Stockbarger from the melt and the moving vapour growth method.

$HgBr_xI_{2-x}$ ($0.4<x<2$) crystals were grown by two abovementioned methods. For the Bridgman-Stockbarger method, a vertical furnace arrangement was employed. The starting materials were HgI_2 and $HgBr_2$ powders, in amounts corresponding to the desired crystal composition.[5] The ampoule was placed in the high-temperature area of the furnace, and then it was lowered towards the cooler part of the furnace. The cooling rates employed at the solidification point that were were 0.25, 0.50, 0.75, and 1.0°C/h. For the moving vapour growth method, the growth followed two stages. In the first stage, the starting material in the desired composition was prepared in polycrystalline form by melting together HgI_2 and $HgBr_2$ powders and then cooling them to room temperature. In the second stage, the ampoule loaded with the starting material was placed in the lower part of a vertical transparent furnace (warmer area), until the material melted, and then it was raised towards the upper part of the furnace (cooler area). When the upper tip of the ampoule reached a temperature lower than the solidification point of each composition, the material condensed there formed a small crystal which grew in size during the movement of the ampoule until the whole amount of the starting material was deposited. The cooling rates employed were in the 0.1–1.0°C/h range.

The atomic compositions were determined by EDAX with the Philips model 505- EDAX scanning microprobe. Finally, a new finding from the EDAX analysis is the deficiency in iodine of all examined crystals, independent of the growth method.

Using a confocal scanning laser microscope Biorad MRC 600 equipped with an Ar-ion laser, accorded on 488 nm, we obtained a compound volume image by photoluminescence as well as by reflection. In this way we had the possibility to localize the region with inhomogeneities in a very precise way. We had the possibility to establish the types of impurities kind in a few situations.

References

1. Turyanitsa ID,.Khiminets VV: Phase diagram of the system $(HgI_2)_x x(HgBr_2)_{1-x}$ and some optical properties of its single single crystal. *Sov Phys Cryst* 18, 688–689 (1974)
2. Stanciu GA, Oprica MH, Oud JL, Daviti M, Anagnostopoulos AN, Paraskevopoulos KM, Polychroniadis EK: Growth and characterisation of $HgBr_2$ crystals using confocal laser scanning microscopy, optical spectroscopy and DC conductivity measurements. *J Phys D Appl Phys* 32, 1928–1933 (1999)
3. Stanciu GA, Polychroniadis EK: Surface investigations on $HgBr_2$ single crystals by using confocal scanning laser microscopy. *Scanning* 22 182–186 (2000)
4. Stanciu GA, Oud JL, Polychroniadis EK, Daviti M, Stanciu A, Miu C: Investigations on HgBrI using laser scanning microscopy and x-ray diffraction. *Proc SPIE* I, 241–245, 3405, (1998)
5. Toubektsis SN, Polychroniadis EK, Economou NA: A new technique for growing single HgI_2crystals. *J Crystal Growth* 79, 427–431 (1986)

Advances in SEM microscopy

Sharpness search algorithms for automatic focusing in the scanning electron microscope

C.F. BATTEN, D.M. HOLBURN, B.C. BRETON, N.H.M. CALDWELL

Department of Engineering, Cambridge University, Cambridge, UK

The scanning electron microscope's transition from a research device to a common industrial tool has increased the need for instrument automation, both in conventional and remote microscopy.[1] Traditionally, autofocusing research has concentrated on finding an optimal sharpness measure, which is then applied over a range of focal lengths and the focal length with the maximum sharpness is chosen as the best focus.[2] The present work investigates the use of more sophisticated sharpness search algorithms that decrease search time without sacrificing the sharpness of the final image.

Four sharpness measures were evaluated based on their robustness to noise, applicability to different specimens, implementation cost, and adherence to the strict unimodality property. A strictly unimodal sharpness measure has a single peak at the best focus and is strictly decreasing away from this peak. Strict unimodality is particularly important to the success of more sophisticated search algorithms. The sharpness measures considered were based on the image gradient, sum of specific frequency domain components, image autocorrelation, and image variance.

The gradient measure was found to be the most susceptible to noise, while the variance method was largely insensitive to noise. The auto-correlation measure was usually strictly unimodal but had poor reproducibility, and while the frequency domain measures performed well, the implementation cost of performing frequency domain transforms in software was significant. The variance measure was chosen as the primary sharpness measure for this work because of its strict unimodality regardless of noise, as well as its simple implementation.

Signal-to-noise (SNR) ratio and objective lens hysteresis effects are important concerns when developing sharpness search

algorithms. In this work, SNR issues were addressed by choosing a moderate level of hardware noise reduction and using a robust sharpness measure. Hysteresis was compensated for by resetting the focal length between iterative sweeps and by direct calculation of a hysteresis offset when returning to the best focus following a focus sweep. This hysteresis offset was calculated using a new technique based on the relative sharpness of images obtained during and after the sweep.

The fixed step-size search required the most images for a given accuracy. Stopping the search after detecting a sharpness peak improved performance but is applicable only under high SNR conditions. The iterative search (using multiple sweeps at decreasing step-sizes) required fewer image captures but additional hysteresis corrections. Following these searches, interpolation can be used to further improve the estimated best focus. A new interpolation technique was developed which uses a model of the image variance as a function of defocus and was found to be reasonably successful under most test conditions, but adds significant overhead to the search.

The variable step-size search attempts to decrease the step-size during the sweep as the sharpness increases. This technique requires careful initial step-size choice, and is less effective in low SNR conditions. The Fibonacci search partitions the search space into segments and iteratively reduces the search space using additional, carefully placed sharpness measurements. This technique requires the fewest images, but like the variable step-size search, it relies heavily on the strict unimodality property.

The search algorithms were tested on various standard and non-biological samples, using both stored focus series and live images on a LEO 440. Their results were verified against maximal sharpness and human assessments of "best focus".

This work has investigated the potential of more sophisticated sharpness search algorithms which require slightly higher SNR requirements but significantly fewer image captures, and introduced novel hysteresis correction and interpolation techniques.[3] The Fibonacci search using a variance sharpness measure is robust and efficient for rapid fine focusing, and combined with the other methods could create a complete full focusing solution.

Acknowledgments: The authors would like to thank the Winston Churchill Scholarship Foundation, LEO Electron Microscopy Ltd., and the Isaac Newton Trust for their support of this research.

References

1. Caldwell NHM, Breton BC, Holburn DM: WebXpertEze: Intelligent instruments via the internet. In *12th European Congress on Electron Microscopy*, Czechoslovak Society for Electron Microscopy, (Brno) 3, 411–412 (2000)
2. Tee WJ, Smith KCA, Holburn DM: An automatic focusing and stigmating system for the SEM. *Journal of Physics E: Scientific Instrumentation*, 12, 35–38 (1979)
3. Batten CF: *Autofocusing and Astigmatism Correction in the Scanning Electron Microscope*, Master's Thesis, University of Cambridge (2000) (unpublished)

Effect of pseudo-random scan parameters on negative specimen charging and beam landing errors in the scanning electron microscope

J.T.L. THONG, W.K. WONG, A. ZAINAL

Centre for IC Failure Analysis and Reliability (CICFAR), Faculty of Engineering, National University of Singapore

The use of a pseudo-random scanning algorithm[1] has previously been shown to reduce image degradation due to negative charging effects when specimens with insulating areas are viewed at high-beam energies in the scanning electron microscopy (SEM). On insulating specimens with slight conductivity, random scanning reduces the occurrence of surface breakdown and Malter discharge. Beam deflection errors and contrast artefacts can also be effectively reduced. The principle underlying the reduction of surface charging is to spread out deposition of charge by the beam over the scan field in a manner that consecutive pixels are well separated.[2] On a slightly conductive specimen, this allows surface charge to leak away at any point in the scan field before the beam revisits its vicinity again. With a conventional raster scan, consecutive pixels are adjacent to one another, which results in a rapid build-up of charge that can lead to dielectric breakdown and other severe charging artefacts.

The pseudo-random algorithm is based on a pixel interlace factor (IF) which is the number of pixels to increment on a one-dimensional raster scan pixel map, and remapped onto a two-dimensional scan map. A judicious choice of IF is found to be important as it affects the beam landing error due to the charge pattern that has been already been established on the specimen surface by the time sequence of charge deposition. Assuming an initially uncharged surface for a conventional raster scan, the total charge build-up increases monotonically in the frame scan direction, and this results in a wider scan field towards the end of the frame. This effect is acceptable especially if the rate of charge build-up is relatively small. On the other hand, with random scanning, the beam vectors all over the scan field, and depending on the extant surface charge, may result in periodic beam landing errors that manifest as "jagged" images. It was observed experimentally that certain IF give images that are practically free of jagged edges.

To understand this phenomenon, computer simulation was carried out to model the effect of evolving surface charge on the beam landing error. In the model, the primary beam is scanned over a dielectric surface according to the pseudo-random scan algorithm. At any irradiated point, the surface charge is assumed to redistribute uniformly by electron beam-induced conductivity (EBIC) within the backscattering radius of the beam. The trajectory of the primary beam is then traced through the electric field resulting from the surface charge, and this determines the landing position of the next point to be irradiated. In the present model, charge decay is assumed to occur through the sub-

strate but does not otherwise redistribute laterally on the surface when the beam is not positioned at the area concerned. The charging state of the surface and the surface potential can be visualised as a three-dimensional surface plot as scanning progresses.

The beam landing error for a raster scan is as expected, with the scan field expanding towards the end of the frame. However, at higher charge doses (higher beam currents), the beam landing error interacts with the charge deposition and results in ripples appearing in the charge distribution. For random scanning, the IF affects the distribution of charge, but for sensible values of IF the difference in the maximum charge is marginal and is invariably lower than that of a raster scan. However, the beam landing error can take on very different forms as the IF is changed. Certain scan sequences result in monotonic distortion of the scan field, while others give rise to seemingly erratic beam positioning errors, supporting the experimental observations of random-scan images. A truly random scan, where the scan coordinates are generated by a pseudo-random number generator, gives the worst possible scenario with unpredictable beam landing error and an irregular surface charge distribution. On the other hand, IF-based pseudo-random scanning with a proper choice of IF can yield the benefits of the technique without the effects of erratic beam positioning errors.

References

1. Lee KW, Thong JTL, Wong WK: Reduction of charging effects using pseudo-random scanning In the scanning electron microscope, *Scanning* 22, 112–113 (2000)
2. Postek MT: Low accelerating voltage inspection and linewidth measurement in the scanning electron microscope, scanning electron microscopy Part III. 1065–1074 (1984)

Acknowledgments: Supported by the Horserace Betting Levy Board.

Specimen charging characterization using computer-based image contrast-emission processing for the scanning electron microscope

W.K. WONG, Y.Z. WEI, J.C.H. PHANG, J.T.L. THONG

Centre for Integrated Circuit Failure Analysis and Reliability (CICFAR), Faculty of Engineering, National University of Singapore, Singapore

Specimen charging problems are frequently encountered in imaging with the scanning electron microscope (SEM). Such problems are especially common during the observation of poorly conducting specimens using high-beam energies and at high-current densities associated with high magnifications.[1] Therefore, in situ imaging analysis in the form of charging detection and quantification to derive additional information on the sample charge state is needed if consistent performance from the SEM is desired. One useful way of representing the information on the charging attributes of the sample is in the form of a 2-dimensional charging map of the sample that can be derived from a combination of both physical and image-based measurements.

The basis for an image-based charging detection technique can be constructed based on the fundamental emission behavior of insulators under an electron-beam probe as described by the electron emission coefficient, σ which represents the ratio of the total emission current over the primary beam current. For most typical semiconducting and insulating materials but excluding metals, σ can span ranges both within and in excess of unity depending on the effective electron landing energy.[2] This property allows different charging-characteristic zones to be investigated at different beam energies. For example, in the $\sigma > 1$ region, in which more electrons are emitted than injected into the sample, the resultant net positive charging situation results in a relatively darker image intensity of the final secondary electron (SE) image of the sample due to suppression of electron emission from the now positively charged surface.[3] Conversely, operation in regions where $\sigma < 1$ results in a net higher image intensity due to negative charging. It is assumed that all primary electron-optical parameters remain constant and charge proximity or neighborhood effects[4] are negligible. A means of mapping out regions that exhibit this contrast fluctuation with beam voltage can then be constructed to form a charging map technique for charging detection.

In the first case of moderate charging in which the charging artifact is manifested as relatively subtle contrast aberrations in the resultant image without gross image distortions or drifts in the image field-of-view, a method employing voltage-by-voltage differential beam energy analysis (BEA) has been developed. Using beam energy alteration as the primary stimuli, the charging condition changes according to the total yield curve behavior of the regions of interest. In the subsequent processing of the image data obtained, two methods, the maximum distance distribution (MDD) and the least misclassified distribution (LMD) techniques, have been implemented. Comparing the contrast on each combination of image frames obtained under different beam energies, the combination that gives maximum discrimination of the feature-of-interest from the noncharging background is selected. It was found that the MDD method generally requires less computation at the expense of the higher charging region misclassification error rate. The LMD algorithm, on the other hand, requires larger amounts of computation and hence results in longer charging detection turnaround times, but with better charging detection accuracy.

A secondary algorithm has also been developed to detect relatively severe charging, where charging artifacts are attributed to beam deflection effects on the primary electron beam by strong surface electric field build-up.[5] In this case, an image drift detection technique is implemented as the primary detection parameter. Using a combination of

frame-by-frame comparison, drift detection, and thresholding techniques, a charging map is also generated to describe the zones of severe charging.

The charging map generation techniques described above provide the critical information required for the detection and eventual compensation of specimen charging. The above-mentioned modules are part of an overall charge control architecture for the SEM which is presently under development at CICFAR. The successful development of charge control techniques would ultimately result in self-optimising SEMs where the accuracy of analysis in the face of charging can be more reliably ascertained compared with present conventional SEMs.

References

1. Wong WK, Phang JCH, Thong JTL: Charging control using pulsed scanning electron microscopy. *Scanning* 17, 312–315 (1995)
2. Joy DC: A model for calculating secondary and backscattered electron yields. *J Microsc* 147, 51–64 (1987)
3. Joy DC: Control of charging in low-voltage SEM. *Scanning* 11,1–4 (1989)
4. Postek MT: Low accelerating voltage inspection and linewidth measurement in the scanning electron microscope. *Scan Electron Microsc* 1984, Part III, 1065–1074
5. Shaffner TJ, Hearle JWS: *Recent Advances in Understanding Specimen Charging*. Proc Ninth Annual Scan Electron Microsc Symposium. IIT Research Institute, Chicago (Ed. Johari O). I, 61–70 (1976)

Visualization of the energy band contrast in SEM scanning electron microscopy through low-energy electron reflectance

I. MÜLLEROVÁ, L. FRANK, O. HUTAR

Institute of Scientific Instruments AS CR, Brno, Czech Republic

The trend towards lowering the primary beam energy in the scanning electron microscope (SEM), motivated by the aim of observing non-conductors with suppressed charging-up, and at of improving the surface relief visualization, reaches its limits (in conventional instruments) slightly below 1 keV, as a result of growing aberrations and decreasing current. Further energy lowering is possible when non-constant beam energy along the column is employed and the final deceleration is performed close to the specimen surface. In cases in which the decelerating field is applied directly to the specimen, i.e.that is, when a "cathode lens" is introduced, the beam energy can be decreased to units of eV without any significant sacrifice to the resolution.[1] The specimen is then exposed to a strong electric field of, say, 2 to 3 kV/mm. This does not, however, create a gradient exceeding 10 volts per micrometer in the silicon oxide, so most semiconductor devices should not be endangered.

Technological development and detection of defects for modern large integration semiconductor devices require the use of high-resolution visualization of topology of differently doped areasdoping profiles. In order toTo restrict the radiation damaged area to the shallowest surface, and also to decrease the energy delivered, low- energy electrons should be used for this purpose. Successful imaging of both p- and n-type doping within a broad energy range [2] has been explained on the basis of the surface band bending creating a variable height barrier for the secondary electrons (SE), causing the p-type areas to be brighter in the image. Some recent results [3] regarding the low- energy range and contrast between p^+ and n^+ areas with respect to n-type substrate are also interpreted with the help of the surface barriers connected with the carbonaceous contaminants.

True observation of the electronic structure is, nevertheless, possible when employing very low- energy electron reflectance, as can be seen from the I-V curves for the I_{00} spot of the low energy electron diffraction (LEED) pattern. At energies below approx. 20 to 30 eV, where all mechanisms of inelastic electron scattering settle enough so that both the energy and wave vector of the impacting electron conserve over the electron penetration depth, the reflection rate is inversely proportional to the density of states coupled to the incident wave.[4, 5] . More simply, electrons hitting the forbidden gaps above the vacuum level are reflected significantly more than when their energy corresponds to allowed states. This phenomenon has been demonstrated in LEED[5] and also in the low- energy electron microscope (LEEM).[4] . Implementation into SEM is likely to bring a novel diagnostic method for semiconductor technology.

Distribution of the energy band features within semiconductor devices, caused by local doping, can be visualized when tuning the (very low) landing electron energy so that it fits forbidden gaps only in a part of the variously doped areas, while in the remaining areas electrons penetrate inside as hot electrons.[6]. Note that SE emission does not play a role here, and that the contrast is due to reflected electrons only. Fine energy tuning could even reveal, at least at higher doping levels, penetration into donor or acceptor bands, depending on the shape and height of the band bending. Demonstration experiments are best performed on a partly processed substrate with the first doping operation performed, but with no further layers grown.

References

1. Frank FL, Müllerová I: Strategies for low- and very-low-energy SEM. *J. Electron Microsc*. 48, No. 3, 205–219 (1999)
2. Perovic DD, Castell MR, Howie A, Lavoie C, Tiedje T, Cole JSW: Field-emission SEM imaging of compositional and doping layer semiconductor superlattices. *Ultramicroscopy* 58, 104–113 (1995)
3. El-Gomati M, Wells TCR, Frank L, Müllerová I: On the imaging of semiconductor doping using low energy electron microscopy. *Proc. 12th Eur. Congr. El. Microsc*. (edEd. Frank FL, Ciampor F),). CSEM, Brno 2000, Vol . II, 2000, 635–636
4. Bauer E: Low energy electron microscopy. *Repts Progr. Phys.* 57, 895–938 (1994)

5. Bartos I, van Hove MA, Altman MS: Cu(111) electron band structure and channelling by VLEED. *Surface Sci,* 352, 660–664 (1996)
6. Howie A: Electron microscopy of electronic structure and behaviour. *Proc. Internat. Centennial Symp. on the Electron* (edEd. A Kirkland, PD A, Brown PD), Cambridge (1997), 135–145

Imaging of unstained and uncoated specimens in the scanning electron microscope at optimum electron energy

L. FRANK, I. MÜLLEROVÁ, J. KÁNOVÁ

Institute of Scientific Instruments AS CR, Brno, Czech Republic

The conventional way of suppressing charging in nonconductive specimens due to electron bombardment in the scanning electron microscope (SEM), consisting of staining by metallic salts and conductive coatings, causes alteration to the acquired data, and much effort is being made to avoid these steps of preparation. One currently popular alternative is the environmental SEM with a gas pressure sufficient for surface discharging by impacting ions.

Another routine method of observation relies upon observation at electron energies below a certain critical value, at which the total electron yield crosses the unit level. The specimen acquires a positive surface charge, the field of which reattracts a portion of the slowest secondary electrons, which leads to the establishment of the charge balance at only moderate surface potential. Because of the presence of other electrostatic fields in the vicinity (such as that of the Everhart-Thornley detector), the final potential can reach tens of volts. This value can sometimes cause problems, so it is worth aiming for a reduction.

In order to diminish "residual" positive charging, one has to approach, as close as possible, the critical energy, preferably from the lower energy side. A successful method of for determining the critical energy can be based on monitoring the image signal in time immediately after the first illumination of a pixel.[1] The resulting energy value, found as that at which the overall signal change is minimal, secures the least charging in exactly the desired sense, that is, as regards the impact on the signal electrons. The critical energy established in this way depends both on the specimen material and the local impact angle of the electrons, that is, the surface relief. It is anticipated that typical energy values will work for certain classes of specimens, such as families of microorganisms, soft tissue specimens, etc.

The procedure for acquiring a sufficient assembly of the signal vs. time data from points suitably distributed over a view field not illuminated before, and its processing, can be well automated provided the beam energy is "easily" adjustable. This is the case for an SEM fitted with a cathode lens, where the fully shaped and positioned beam is decelerated just in front of the specimen surface.[2] The landing energy of electrons can be varied here via negative specimen bias with minimum readjustment in the column, restricted to moderate corrections in focusing and magnification according to preselected figures.

Important examples of structures suitable for this method of observation include those of a powder, porous or fibrous nature, which are difficult to make sufficiently conductive by conventional methods. Demonstration experiments were performed with some aerial and other mycelia, intestinal protozoan cells, dried milk specimens, etc.

References

1. Frank L, Zadrazil M, Müllerová I: Scanning electron microscopy of nonconductive specimens at critical energies in a cathode lens system. *Scanning* 23, 36–50 (2001)
2. Frank L, Müllerová I: Strategies for low- and very-low-energy SEM. *J Electron Microsc* 48, No. 3, 205–219 (1999)

Image management for a multi-instrument, multi-platform microscopy facility

J.A. MURPHY

Microscopy Technology Center, San Joaquin Delta College, Stockton, CA, USA

In the digital age, the management of images can be very time consuming when there are several digital image acquisition systems involved. The choice of which database to use depends on the number of image acquisition systems as well as how the images are to be used. In our facility, the same images often have to be accessed by several users for group projects. We needed the ability to track the images not only with other data (e.g. spectra) and reports but also by several criteria such as sample number, type, client number, etc. Our image acquisition systems are operating on Macintosh, PC, and Unix®, platforms. Our digital imaging systems include transmission electron microscopes (TEMs), scanning electron microscopes (SEMs), light microscopes (LMs), focused ion beam (FIB), atomic force microscope (AFM), flat bed scanners (FBS), negative scanners (NS), video cameras (VC), and digital cameras (DC). Because we look at a great variety of sample types with all types of microscopy, we want to make images available for teaching purposes inside as well as outside our institution. For that purpose, we wanted the images to be available in a compressed format, but available to researchers in the original high-resolution format. At the same time, we needed to have security with respect to who can access research images. To minimize staff time, it was also necessary that image categorization be done during acquisition.

We examined a myriad of databases. The database that met all of our needs and that was tailored to microscopy

was Quartz PCI TM by Quartz Imaging Corp.[1] We required the capabilities of the client/server Enterprise Database version.

We chose to use Microsoft® SQL ServerTM as the underlying database engine. If Oracle® is used, the database server's operating system can be either Windows NT® or Unix®. We chose Microsoft® SQL ServerTM, which only runs on NT, because it is about one-fifth the cost of Oracle® and would be easier to manage in our lab. Adding images to the database and searching for images is done either through platform-independent, web-based software, or through PCI Client software that requires either Windows® 95, 98, or NT. In PCI, the actual images can reside separate from the database on a file server. We chose NT as the operating system for both the database and the file server.

The PCI database software consists of 3 parts: The PCI Intranet Image Server (which gives web access to the database), the PCI Acquisition Software which goes on each image acquisition system; and the PCI Client Workstation software (which is used to change or modify the database). For internet use, one also requires a web browser such as Netscape Communicator® or Microsoft® Internet Explorer. Thus minimally, one needs 1-PCI Intranet Image Server, 1 PCI Acquisition Software for each image acquisition system, at least one Client Workstation software, and a web browser. For security, passwords are added to the system.

For a server we are using a Dual Pentium-III 500MHz LANServer, with one TB of hard drive arrays with built-in RAID 5. Automatic back up is provided with a Cybernetics Tape system and Seagate software. A CD/DVD server/jukebox will be added to the server. The hardware system thus consists of a main server, a CD/DVD jukebox, CD/DVD archives and a back-up tape system. Many microscopy-oriented fields already exist on the initial "off the shelf" database version, but others can be added and made mandatory or non-mandatory. Each user, thus, actively "makes the database" without having to first save images to the hard drive and then put them into the appropriate folders and then route them to a server at a later time. The images are then easily accessed from the server either via the PCI software or through any web browser from the Internet.

Image management with the use of the Quartz PCI Database has thus made possible easily categorizing and finding images, but also tracking samples, compiling reports from a variety of information including multimedia files and will make almost painless, the supplying of images to a variety of internal and external programs.

References

1. Quartz Imaging Corporation, Vancouver, BC, Canada; http://www.quartzimaging.com. Distributed in the US by Hitachi, Nissei Sangyo America, Ltd., Mountain View, CA, USA; http://www.nissei.com

Advances in materials science—microscopy, microanalysis and theory

The backscattered electron (BSE) signal from an iodinated polymer series: Use for standardising BSE images for bone mineralisation density bone

P.G.T. HOWELL,[*†] L.H. KOOLE,[‡] G.M.R. WETZELS,[‡] Y.B.J. ALDENHOFF,[‡] A. BOYDE[†]

[*]Department of Prosthetic Dentistry, Eastman Dental Institute, and [†]Dept. of Anatomy and Developmental Biology, University College London, London; [‡]Center for Biomaterials Research, University of Maastricht, Maastricht, The Netherlands

Bone is neither a uniform nor a permanent material. Mature lamellar bone matrix undergoes a long-term increase in mineralisation after its initial mineralisation. Thus, it changes its properties with time, since the elastic modulus increases with the degree of mineralisation. The degree of mineralisation of bone should be measured in volume elements, which exclude cell occupied space. Currently, backscattered electron (BSE) imaging in a scanning electron microscope (SEM) is the only method to give the required resolving power. It has the additional advantage that entire plastic (e.g., PMMA) embedded blocks are used, and they only need to be cut once. No physical section is required, so that the interface may remain intact during a trimming and micromilling operation to generate the very flat surface required to ensure that BSE signal variations are due to changes in composition (principally changes in the volume occupancy by bone mineral), excluding topography as a confounding factor. The BSE signal is then a measure of mineralisation, but there is a problem in standardising such measurements.

Halogenated polymers may be very suitable for acting as standards against which to measure the relative electron backscattering properties of bone and other calcified tissues. These materials are a prime choice because they are solid, uniform, easily fabricated to have very flat surfaces, and have no long-range structural order to generate electron-channelling contrast. Metals, alloys, and ionic crystalline materials give rise to backscattering contrast dependent upon grain orientation and are therefore unsatisfactory in this regard. For the last few years at UCL, we have routinely used two of the several halogenated polymers originated by the late K.M.W. Davy, chosen because they provide markers located conveniently at each end of the range of backscattering given by bone embedded in PMMA. We have also used and tested other polymers made by Davy in attempts to improve our understanding of the physics of electron backscattering per se. Progress in this field has enabled us to reject the oversimplified theories that will be found in all standard texts in this field.[1]

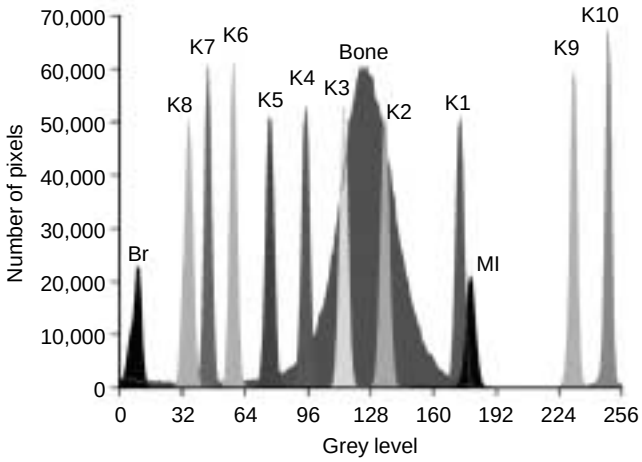

FIG. 1 These backscattering electron values include a typical field on bone, as well as the monobromo and monoiodo compounds.

We report here on a novel series of 10 methacrylate type copolymers that contain an increasing amount of iodine covalently linked to their backbone structure. The new standard materials were prepared from methylmethacrylate (MMA) and 2-[4'-iodobenzoyl]-oxo-ethylmethacrylate (4-IEMA) through polymerization in bulk.[2] The materials are optically transparent and closely resemble poly (MMA). The materials were machined into circular discs with diameter 10 mm, and thickness 2 mm. These discs were cemented to a block PMMA and micromilled to a common surface so that all regions of all the discs would lie at the identical distance from the BSE detector in the SEM and carbon coated by evaporation. Digital BSE images were recorded using a Zeiss DSM962 SEM (20 kV, 0.5 nA, annular detector at 17 mm working distance, 1 mm detector-sample distance) under external computer control, addressing the selected fields on each material in sequence. The values in Figure 1 include a typical field on bone, as well as the monobromo and monoiodo compounds which we have previously employed.[1]

This extended series of iodinated polymers covers the range of backscattering found from normal PMMA embedded bone. Thus, they will be suitable as standards for intraspecimen, interspecimen, interstudy, and interlaboratory comparisons of bone quality.

Wide-field imaging is frequently needed in surveying bone, but low-magnification images may show significant signal loss in the peripheral field. These new materials can be used to generate exact shading correction images to compensate for such effects.

Acknowledgments: AB was supported by the Horserace Betting Levy Board.

References

1. Howell PGT, Davy KMW, Boyde A: Mean atomic number and backscattered electron coefficient calculations for some materials with low mean atomic number. *Scanning* 20, 35–40 (1998)

2. Kruft MA, Benzina A, Bar F, van derVeen FH, Bastiaansen CW, Blezer R, Lindhout T, Koole LH: Studies on two new radiopaque polymeric biomaterials. *J Biomed Mater Res* 28, 1259–1266 (1994)

Direct assessment of recombination noise in semiconductors using electron beam-induced conductivity

S. MIL'SHTEIN

Advanced Electronic Technology Center, ECE Dept.
UMass, Lowell, MA, USA

The level of internal noise of the transistors, diodes, and other semiconductor components limits successful design of any low-noise electronic system. All types of noise, namely, Johnson, 1/f, etc., are generated due to activity of crystalline defects such as vacancies, dislocations, and others. Intensity of the electron scattering and recombination processes, inflicted by defects (traps), controls the level of noise. Dependent on dynamic operation condition of semiconductor devices, such as external biases and level of current injection, the traps will generate a certain type and level of noise.

Material growth or device processing technologies could introduce the defects. Therefore characterization of semiconductor wafer in the early stages of processing (at least before packaging) could help to predict the level of noise due to the type and density of defects present on the wafer. Sorting out bad semiconductor chips could save money and effort in the RF design of low-noise circuits.

Current study focuses on most powerful generators of noise, linear defects, named dislocations. These defects could be found in the bulk as well as the epitaxial interfaces of a semiconductor device. Nanoscale size of these defects makes the scanning electron beam an instrument of choice for proposed study. Conventional electron beam-induced conductivity (EBIC) produces images of the defects, where contrast is proportional to the recombination rate at the site of a defect. Since contrast is measured as fraction of a percent, the relative nature of contract value precludes quantitative measurements of the recombination rate, thus making quantitative assessment of 1/f noise impossible. In our model, using the Boltzman continuity equation, the recombination-generation processes per unit of length of a dislocation was defined for two operational conditions of EBIC, namely, for low and high intensity of an electron beam. The experimental technique of the quantitative measurement of carrier recombination[1] consists of taking two EBIC scans along the selected defect at two different beam intensities, digitally subtracting the first scan from the second one, and normalizing the result to the size of the electron range. The value of the recombination rate,

extracted from the model, is then used to predict the level of 1/f noise in tested semiconductor sample.

Reference

1. S. Mil'shtein: *Quantitative EBIC Measurements* (patent application)

Secondary electron contrast of a 319 aluminum alloy

W. T. DONLON, A. CHEN, J. HANGAS

Ford Motor Company, Scientific Research Laboratory, Dearborn, MI, USA

Cast aluminum alloys are used in the automotive industry for many applications including engine blocks and cylinder heads. Their microstructure consists of aluminum dendrites and eutectic regions containing aluminum, silicon, and various intermetallic particles. Examination of polished sections of these alloys using a conventional Everhart-Thornley detector in a JEOL 840A scanning electron microscope shows that the silicon particles appear dark, while iron and copper intermetallic particles are white (Fig. 1a). The pronounced lower secondary electron (SE) yield (δ) of the silicon compared with the aluminum matrix is unexpected since introductory texts to scanning electron microscopy state that the SE yield is insensitive to composition.[1,2] In addition, one might suspect that the silicon phase should appear brighter than the aluminum matrix since silicon has a higher backscattered electron coefficient (η). The higher η also increases the number of type II and type III SEs.

Since SE generation is due to the interaction of the primary beam electrons with conduction band electrons, the lower δ of silicon is presumably due its covalent bonding.[2–4] The possibility of surface oxide films causing the observed contrast is ruled out because the same contrast has been observed in the scanning Auger microprobe after sputtering away all surface films.

The observed contrast is quite different when the sample has been carbon coated with 10 nm of carbon (Fig. 1b). The silicon particles can only be identified when the contrast is increased to a level much higher than that used for normal imaging. In this case the silicon phase appears brighter than the matrix. This observed contrast arises because most of the Type I SE are generated in the conductive carbon layer while the backscattered electrons are produced in the sample. Similar contrast is observed when the solid-state backscattered electron detector is utilized (Fig. 1c).

The SE contrast of these samples (noncoated condition) was also observed using a Cameca SX50 microprobe. The Cameca secondary detector is comprised of three pairs of plates mounted parallel to the sample surface and placed in front of the scintillator. Three positive bias conditions exist

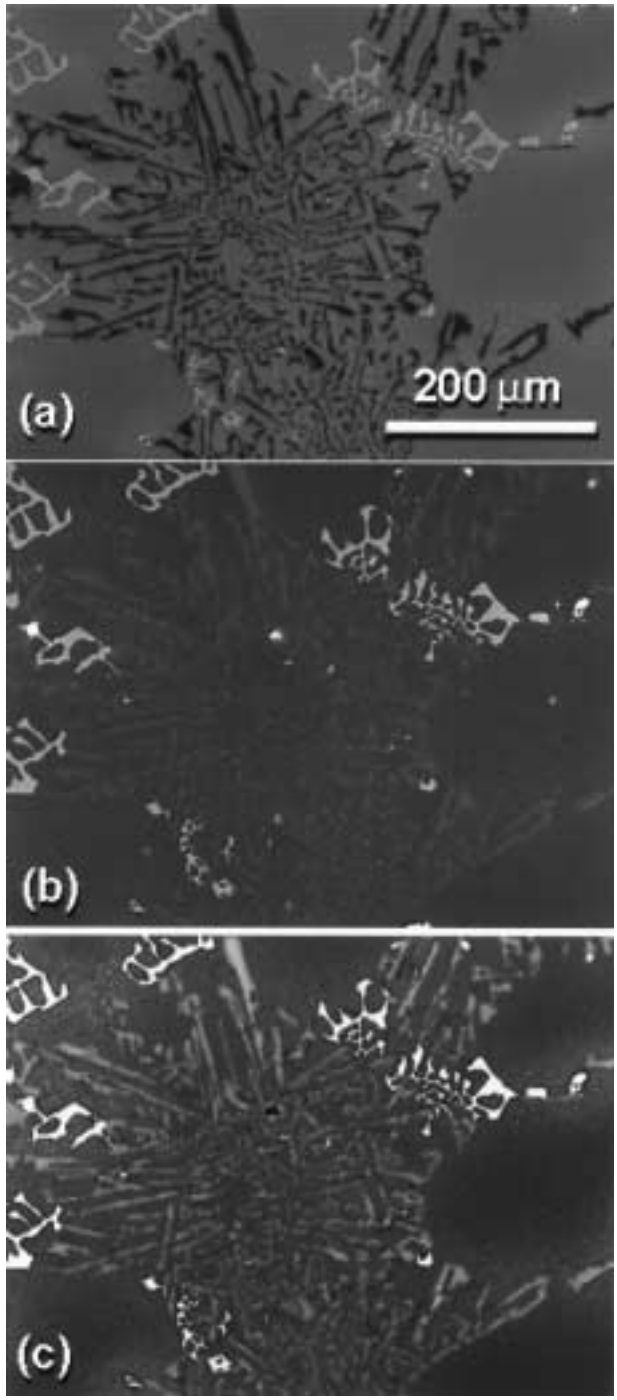

FIG. 1 Secondary electron images (a and b) of a 319 aluminum alloy showing the aluminum-silicon eutectic (E_o = 15 keV). (a) shows the polished surface, while (b) is the same area after carbon coating. (c) is a backscattered image obtained with a solid-state detector.

(the biases progressively increase as one approaches the scintillator) and are set either automatically based on the beam current or manually by the operator. Using bias condition 3 (highest plate biases) with this detector, the silicon particles are observed as dark particles when a higher than normal contrast setting was utilized. No contrast was ob-

served between the silicon and aluminum when bias condition 1 (lowest plate biases) was utilized.

Secondary electron images of a highly irregular fracture surface showed subtle differences when different plates were energized. More directional illumination of the sample was evident when bias condition 1 was utilized. Although the quality of this image was consistent with a typical SE image, it was evident that the backscattered electrons were more dominant. The larger component of backscattered electrons in this image is also consistent with the lack of contrast between the silicon and aluminum on polished samples of this material, where the contrast between these two phases arises because of differences in their SE yields.

References

1. Joy DC: *Scanning Reflection Electron Microscopy, Handbook of Microscopy II,* (EDS. Amelinckx S, van Dyck D, van Landuyt J, van Tendeloo G. VCH Press (1997), 539–548
2. Goldstein JI, Newbury DE, Echlin P, Joy DC, Romig AD, Lyman CE, Fiori C, Lifshin E: *Scanning Electron Microscopy and X-Ray Microanalysis 2nd edition.* Plenum Press, (1992) 106–116, 176–181
3. Dubbeldam L: *Advances in Voltage Contrast Detectors in Scanning Electron Microscopes, Advances in Optical and Electron Microscopy* 12, (Eds. Mulvey T,. Sheppard CJR). Academic Press, (1991), 155–165
4. Hachenberg O, Brauer W: *Secondary Electron Emission from Solids, Advances in Electronics and Electron Physics,* (Eds. Marton L) Academic Press, (1959), 413–499

Synthesis and characterisation of in-situ Al-TiB_2 metal matrix composites

M. CHAKRABORTY, N.K. JONNALAGADDA, R. MAITI, B.S. MURTY

Department of Metallurgical and Materials Engineering, Indian Institute of Technology, Kharagpur, India

The cast metal matrix composites (MMCs) prepared by the addition of ceramic reinforcing particles into the vortex of a stirred molten alloy normally suffer from poor cohesion at the particle-matrix (P-M) interface.[1] The P-M interface in case of in-situ MMC is, however, very clean and continuous as the reinforcing ceramic particles are formed by a chemical reaction within the molten alloy. In the recent years some researchers have reported on the synthesis of in-situ Al-TiB_2 MMC by the reaction of molten aluminium with K_2TiF_6 and KBF_4 salts and the present work is yet another effort in that direction.[2,3]

The present work confines itself to the synthesis of an in-situ Al-5%TiB_2 MMC and its characterization by Scanning Electron Microscopy (SEM), EDS x-ray microanalysis and x-ray diffraction (XRD). Initially, the MMC was synthesized by the reaction of molten aluminium with the K_2TiF_6 and KBF_4 salts under different conditions of reaction temperature (750-800°C), reaction time (30-120 minutes) and sequence of salt addition. The SEM and EDS x-ray microanalysis of the microstructure of the MMCs so prepared supplemented by the XRD revealed the presence of very fine (0.5-2 μm) TiB_2 particles together with a large number of fine $TiAl_3$ particles (~ 1 μm). Presence of AlB_2 or (Al,Ti)B_2 particles, if any, could not be detected. The large fraction of $TiAl_3$ particles results from intense reaction of K_2TiF_6 salt with the molten aluminium due to the emulsification of the former in the latter. The sluggish nature of the reaction of molten aluminium with KBF_4 salts or the possible loss of B as BF_3 gas at 1000°C[4] resulted in low B pick that explains the formation of only a small fraction of TiB_2 particles.

The in-situ Al-5%TiB_2 MMC was then synthesized by melting together the Al-3.45%Ti and Al-1.55%B master alloys. The Al-3.45%Ti and Al-1.55%B master alloys were first prepared separately by the reaction of molten aluminium with K_2TiF_6 and KBF_4 salts respectively at a reaction temperature of 800°C for a reaction time of 60 minutes. A mixture of these master alloys was then studied by differential thermal analysis (DTA), which revealed an exothermic peak at 895°C suggesting a reaction between Ti and B leading to the formation of TiB_2 particles. These master alloys were then melted together at 1000°C for 20, 30 and 60 minutes in an electric resistance furnace to synthesize the in-situ Al-TiB_2 MMC.

Microstructural analysis revealed that remelting of the binary master alloys together in the resistance furnace resulted in the disappearance of $TiAl_3$ particles gradually with the increase in reaction time and the appearance of a large number of hexagonal shaped particles of size 2-5 μm. The EDS x-ray microanalysis supplemented by XRD confirmed these to be TiB_2 particles. The particles were also extracted from the matrix by chemical leaching and studied by SEM and EDS x-ray microanalysis. These studies confirmed that the particles contain Ti and B only. X-ray diffraction of the extracted particles also confirmed these to be TiB_2 particles.

It is thus clear that the reaction of molten aluminium with the mixed salts cannot yield the desired Al-TiB_2 MMC as a large fraction of the Ti remains locked in the form of $TiAl_3$. Moreover, the B is either lost or the reaction of molten aluminium with KBF_4 is too sluggish resulting in the formation of a small fraction of fine TiB_2 particles. The in-situ Al-TiB_2 MMC can, however, be synthesized by melting of the Al-Ti and Al-B master alloys together in a resistance furnace.

References

1. Svendsen L, Jarfors AEW: In-situ formed aluminium composites. *Adv Light Alloys Composites*, 65–70 (1998)
2. Lakshmi S , Lu L, Gupta M: Microstructure and mechanical properties characterization of Al-TiB_2 metal matrix composites processed using in-situ technique. *Proc Fabric Adv Materials, VI*,1, 465–474 (1998)

3. Yang B, Wang YQ, Zhou BL: The mechanism of formation of TiB_2 particulates prepared by in-situ reaction ion molten aluminium. *Metallurg Materials Trans* 29B, 635–641 (1998)
4. Prasad KVS, Murthy BS, Pramanik P, Mukunda PG, Chakraborty M: Reaction of fluoride salts with molten aluminium. *Materials Sci Technol*, 12, 766–780 (1996)

Scanning electron microscopy/energy-dispersive x-ray spectroscopy spectral artifacts/SUM peaks and auto ID: A reminder

S.S. HURBAN

IBM Corporation, Materials/Failure Analysis Laboratory, Endicott, NY, USA

Difficulties were encountered in determining the presence of tin (Sn) in a silicon dioxide (SiO2) environment. In an attempt to stimulate more x-ray information, count rate was increased (larger spot size) in areas of analyses. This resulted in the formation of a small peak in the 3.4 keV range; using an auto peak identification program, the peak was labelled as Sn La. Manually identifying this peak at the full spectral scale could also lead to the misidentification of the peak as Sn La. However, under closer examination, it is fairly obvious that the acquired peak is at a slightly higher energy than that of the calibrated Sn La peak marker; in addition, no secondary peaking for Sn was observed. The calibrated peak reference markers show an exact alignment of the peak with the Si Kα SUM marker.

Increasing the count rate to >15,000 counts per second (cps) resulted in approximately 60% dead time, not optimum energy dispersive spectroscopy (EDS) acquisition parameters.[2] These instrument parameters can not be overlooked when collecting spectral data. Analyzing the same SiO2 rich areas using different instrument parameters (<3000 cps and approximately 20% dead time), the peak was no longer observed at this location. This was supportive proof that the peak was indeed a Si Kα SUM peak.

This analysis served as a reminder that there are specific instrument/specimen conditions that will enhance the occurrence of spectral artifacts. Knowledge of both the sample and the instrumentation capabilities/limitations play an integral role in accurate and complete elemental analysis. Even today's systems, that incorporate an efficient pulse pileup rejector, may not separate two pulses closely spaced in time. Overloading the EDS detector limits it's capability to separate pulses in nearly exact coincidence, and results in the formation of a small pulse pileup peak in the EDS spectrum. [1,3]

These findings led to the investigation of Auto ID routines on various instruments to examine the accuracy of the systems in practice. The two classic cases of Si Kα and Al Kα SUM peaks were used as examples. The results revealed a range of peak ID accuracy from absolutely unacceptable (mislabelling of the major Si Kα, Al Kα peaks and total disregard of the SUM peaks) to very impressive (accurate and complete labelling of all peaks including the SUM peaks).

References

1. Fiori CE, Newbury DE, Myklebust RL: *Artifacts Observed in Energy Dispersive X-ray Spectrometry in Electron Beam Instruments— A Cautionary Guide.* NBS Special Publication 604 (1981), 315–333
2. Goldstein JI, Newbury DE, Echlin P, Joy DC, Fiori C, Lifshin E*: Scanning Electron Microscopy and X-ray Microanalysis*. New York, Plenum Press (1992) 275–292
3. Goldstein JI, Newbury DE, Echlin P, Joy DC, Fiori C, Lifshin E*: Scanning Electron Microscopy and X-ray Microanalysis*. New York, Plenum Press (1992) 226–241

The morphology and microstructure of SiO_2/Al_2O_3 composite inorganic membrane

S. LIN, Y. HU, W. HE,* J.LI*

Instrumental Analysis and Research Center; *School of Chemistry and Chemical Engineering, Zhongshan University, Guangzhou, People's Republic of China

For many of their advantages, such as low energy consumption, high selectivity, resistance to high temperature and chemical corrosion, and biological degradation,[1,2] inorganic membranes have been proven to be of bright future in many fields, such as high temperature gas separation and membrane catalytic reactor.

In this work, a silicon/aluminum (SiO_2/Al_2O_3) composite inorganic membrane was prepared according to the processes described previously.[3] The morphology and microstructure of this membrane were investigated by scanning electron microscopy (SEM) and energy dispersion x-ray (EDX) analysis. The performance of this membrane for the treatment of industrial wastewater was discussed as well.

Preparation of the SiO_2/Al_2O_3 Composite Membranes

The silicon contented poly-aluminum solutions with different ratios of Si/Al were prepared. The surface of the substrate pre-treated with kaolin was carefully touched to the above Si/Al solution for 4 s. This substrate was picked up and treated with aqueous ammonia at ambient temperatures for 3 h. Then, it was put into an oven and heated slowly to 110°C, and kept at this temperature for 30 min. The temperature was thereafter increased up to 550°C in 20 min, and the sample was roasted at this temperature for 3 h. After cooling down to ambient temperature, a SiO_2/Al_2O_3 composite membrane was obtained.

Characterization of the SiO_2/Al_2O_3 Composite Membranes

Detail for the characterization of the SiO_2/Al_2O_3 membrane's performance, including measurement of liquid permeate rate, and maximum pore radius of the membrane, as well as retention rate of the membrane for poly-(ethylene glycol) were described in reference.[3]

The maximum pore radius of the membranes, r, is calculated as $r = 2\sigma/\Delta P$, where σ is surface tension of the liquid, and ΔP is bubble-point pressure.

The maximum pore radius r_{max} of the SiO_2/Al_2O_3 membranes with different ratio of Si/Al was measured. The maximum pore radius difference, Δr_{max}, and the maximum pore radius contraction were calculated and listed in Table 1. The results obviously show that, the pore radius contraction rate of the membranes was increased along with the ratio of Si/Al. This means that the presence of silicon is very helpful in improving the surface structure of the membranes, and is mainly referred to as the formation of Si-Al com-crystallites during the roasting process.

TABLE I Some data of the SiO_2/Al_2O_3 membranes.

Sample	Si/Al	Δr_{max}	Contraction (%)
A	0	0.046	6.01
B	0.05	0.063	7.30
C	0.07	0.123	13.9
D	0.10	0.139	15.2

Morphology and Microstructure Analysis of the SiO_2/Al_2O_3 Membranes

The morphology and microstructure of the SiO_2/Al_2O_3 membranes, as well as the distribution of silicon in the composite layer of the matrix were examined with a Hitachi S-520 SEM coupled with an Oxford ISIS300 EDX.

The EDX examination results of the SiO_2/Al_2O_3 membranes were listed in Table 2. One finds from the results that when the matrix was treated with a higher silicon content solution, the resulting membrane has higher silicon content in the skin layer. Meanwhile, the morphologies of the membranes showed that the micro-particles in this layer were piled up more densely. The results obtained from the SEM were in agreement with those of the EDX and retention rate.

TABLE II Silicon content in SiO_2/Al_2O_3 membranes treated with different Si/Al solutions.

	Si/Al ratio in the composite membranes	
Si/Al ratio in the solutions	In skin layer	In matrix
0	1.26	1.67
0.05	2.15	1.69
0.07	2.23	1.59
0.10	2.39	1.75

Acknowledgments: The authors gratefully acknowledge the China National Natural Science Foundation for the financial support.

References

1. Yongqian H, Changqiong Z: Inorganic separating membranes and environment protection. *Environ Eng* 16, 2, 27–29 (1998)
2. Shengcheng L, Linlin G: Porous ceramics membrane and sol-gel methods. *University Chem* 8, 6, 5–10 (1993)
3. Weiguang H, Shaokun L, Kangcheng Z, Xiaogang L, Senshu L: The effect of basicity of polyaluminum macromolecule solution on the properties of Al_2O_3 ceramic membrane. *J Membr Sci* 155, 2, 185–191 (1999)

Advances in biological and biomedical scanning microscopy and micro-analysis, Part II

Geothermal and pathogenic clostridial and bacillus endospore ultrastructural attachment mechanisms

B. PANESSA-WARREN, G. TORTORA* J. WARREN†

Biology Department and †Instrumentation Division, Brookhaven National Laboratory, Upton; *Clinical Microbiology Laboratory and School of Health, Technology, and Management, SUNY, Stony Brook, NY, USA

Although it is known that bacteria attach in disease and in ecological environments, we found that bacterial spores, called endospores, also have a ability to attach to substrates.[1,2] Endospores are small (0.3–1.0 um), dehydrated, dormant structures that exhibit high resistance to heat, cold, ultraviolet radiation, acids, bases, solvents, and many sporocides.[3] These ubiquitous spores are carried by the wind, found everywhere in the environment, and normally exist in the mammalian digestive and urogenital tracts. Unlike bacterial vegetative cells, clostridial and bacillus endospores can remain dormant for many years, breaking dormancy and germinating when conditions for growth are favorable.

Bacterial colonization and the infective process have been traditionally thought to begin when mature bacterial cells attach to a surface. The data from this study suggest that this process begins much earlier, with the activated endospore attaching to a site by means of a responsive outer "exosporial" membrane. The purpose of this investigation was to determine whether this attachment capability, reported in pathogenic species (*C. sporogenes* and *C. difficile*) in our laboratory,[1, 2] was also characteristic of other clostridial and bacillus endospores isolated from patients and environmental hot springs (Terrace Hot Spring and Firehole Cascades at Yellowstone National Park,

Wyoming). The geothermal hot springs chosen had turbulent water movement (geysers, outflow channels, cascades), bacterial mats, water temperatures of 40–80ºC, and were rich in Ca++,Mg++ and silicon. All spores were examined using light microscopy histochemistry, transmission (TEM) and scanning electron microscopy (SEM), with an LaB6 gun, field emission SEM (FESEM), and atomic force microscopy (AFM). Endospores were harvested and grown on trypticase soy agar with 0.5% glucose (TSA), CDC blood agar, or on human tissue culture monolayers (MRC-5 embryonic fibroblast, colon carcinoma Caco-2 cells). Both aerobic and anaerobic species were grown at 37° and 56°C. Spores examined by AFM (no fixation) were allowed to attach to etched Si substrates and examined in sterile water. Analyses revealed that endospores isolated clinically as pathogens had the same responsive outer exosporial membrane (and same histochemistry) as environmental species. The predominately bacillus species isolated from the geothermal sites had additional ruthenium red-positive exosporial membrane surface structures, both delicate hair-like appendages at the beginning of germination (TEM, FESEM), followed by a heavier uniformly thick ruthenium red outer layer (TEM). The most elaborate ultrastructural attachment systems were found in the geothermal organisms (isolated from sediment of highly turbulent outflow channels), with one specie having vesicular material stored within the endospore cortex that was released prior to outgrowth of the newly developed bacterial cell, thereby preventing the immature vegetative cell from being swept away. Atomic force microscopy revealed that in intact, viable spores, the exosporial attachment appendages were not mucilaginous, nor deformable. In conclusion, the endospores studied showed the same exosporial membrane responsiveness, spore staining, and similarity of exosporial membrane structure as the clinical endospores. This strongly suggests that spore attachment via the exosporium may be common to spores of these genera, indicating that colonization and invasion may begin far earlier than was generally believed. With the advances of high-resolution scanning microscopies (SEM, FESEM, AFM), it was possible to clearly image the delicate attachments of intact attached (and even viable) spores.

References

1. Panessa-Warren B, Tortora G, Warren J: Electron microscopy of *C.sporogenes* endospore attachment and germination. *Scanning* 16, 227–240 (1994)
2. Panessa-Warren B, Tortora G, Warren J: Exosporial membrane plasticity of *C.sporogenes* and *C.difficile. Tissue Cell* 29, 441–461(1997)
3. Russell A: Bacterial spores and chemical sporicidal agents, *Clin Microbiol Rev* 3, 99–119(1990)

Examination of the surface attachment in-vitro of *Escherichia coli* clones using scanning electron microscopy

W.A. COOLEY, R.M. LA RAGIONE, A. BEST, M.P. DIBB-FULLER

Veterinary Laboratories Agency, Central Veterinary Laboratory, New Haw, Addlestone, Surrey, UK

Escherichia coli (E.coli) is a major bacterial cause of intestinal and extraintestinal infections in both humans[1] and animals[2]. A main area of research focuses on the mechanisms of bacterial pathogenesis. *E.coli* usually follow the requisite approach of infection: colonisation of mucosal sites, evasion of host defences, multiplication, and host damage. The adhesion, particularly of diarrheagenic *E. coli* to the mucosa, is recognised as an important early event in colonisation and development of disease. To study the means bacteria employ in the infection process, the development of in vitro and in vivo models and assays is essential. These enable an understanding to be gained of the mechanisms utilised by the bacteria for colonisation, invasion, survival, and persistence within the host. However, with animal models it is often very difficult to interpret why bacteria localise in a particular area and how this is achieved. Because of this, in vitro models have been developed in an attempt to determine the specific factors involved in bacteria-cell interactions. One invaluable tool for investigating this interaction of bacteria with cells has been the scanning electron microscope (SEM).

In this SEM study we present some preliminary findings on the adherence characteristics of three different zoonotic *E. coli* isolates, to HEp-2 cells. The isolates used were an enterohaemorrhagic *E. coli* (EHEC) serotype O157:H7, an enteropathogenic *E. coli* (EPEC) serotype O111: NM and an avian pathogenic *E. coli* (APEC) serotype O78: K80. Confluent monolayers of HEp-2 cells on 13mm round coverslips were infected with inoculum of viable bacteria for each isolate of *E.coli* and incubated for up to 6 hours at 37ºC (5% CO_2). The infected monolayers were gently washed three times with Hanks Balanced Salt Solution to remove non-adherent bacteria and fixed overnight in 3% gluteraldehyde in a 0.1 M phosphate buffer. The coverslips were carefully washed with phosphate buffer and post fixed using 1% osmium tetroxide. After dehydration and treatment with hexamethyldisilazane for 5 minutes the air-dried coverslips were fixed to aluminium stubs, sputter-coated with gold, and examined in a stereoscan S250 MarkIII SEM at 10–20 kV.

Examination of the cells by SEM showed that for the APEC isolate a diffuse adherence pattern was observed (Fig. 1). Single bacteria or occasional small groups were seen at the attachment sites on the apical cell surface. The dense network of microvilli on the cell surface was not affected by this isolate. The close association of the bacteria with the cell surface indicated that some invasion might be

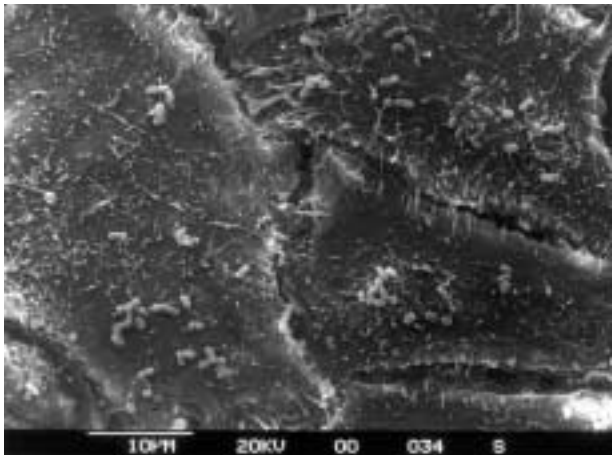

FIG. 1 A diffuse adherence pattern of an avian pathogenic E. coli (APEC) serotype O78:K80 to Hep-2 cells.

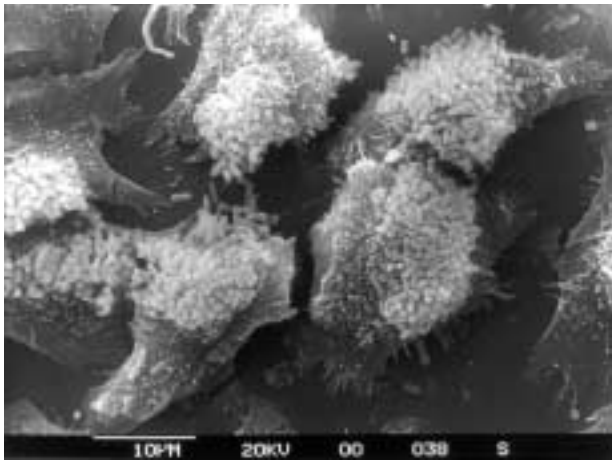

FIG. 2 Formation of microcolonies by an enteropathogenic E. coli (EPEC) serotype O111:NM to Hep-2 cells.

occurring, although attaching and effacing lesions were not observed. Transmission electron microscopy (TEM) confirmed invasion had taken place. A different pattern of adhesion was seen for the EHEC and EPEC isolates. EHEC showed isolated, localised adherence, as well as large numbers of bacteria grouped together in close association to the apical cell surface on virtually all cells. There was also microcolony formation on many of the cells. Signs of cellular damage and possible cell lysis were visible, even though this was not a verotoxigenic *E.coli*. The EPEC isolate was similar in its attachment profile to the EHEC strain. The major differences were in the size and number of microcolonies present (Fig. 2). They were numerous and very pronounced, often 20-30 bacteria deep. There was evidence of intimate attachment of the bacteria to the cell surface and the appearance of bacteria located on a pedestal of cell membrane. This was confirmed by TEM, as was the presence of attaching and effacing lesions.

Electron microscopic approaches to this kind of investigation are one of the most powerful methods available to follow interactions of bacteria with the host cell. In this study SEM has given vital information and widened our understanding on initial stages of adherence and bacterial clumping as well as the formation of microcolonies. This work will continue and will be hopefully be complemented by other techniques including confocal laser scanning microscopy.

References

1. MI Garcia, C Le Bouguenec: Role of adhesion in pathogenecity of human uropathogenic and diarrhoeogenic *Escherichia coli*. *Bull Inst Pasteur* 94, 201–236 (1996)
2. CC Gay, TE Besser: *Escherichia coli septicemia in calves. In: Escherichia coli in domestic animals and humans*. (Ed CL Gyles) (1994) 75–90

From preparation to presentation: Developing the perfect microbiological image

T. S. SCHWACH

Microscopy Consulting Services Inc., Mendota Heights, MN, USA

The preparation of biological materials for scanning electron microscopy (SEM) is straightforward: fix, dehydrate, CPD, coat, mount, scan, and shoot. Yet within these steps are a myriad of details contributing to the final outcome. When that outcome is an image specifically destined for presentation, some details become more important than others.

Of utmost importance are how the microorganisms are grown and the substrate is used for support. Silicon, glass, and brass supports should be autoclaved, smooth, free of artifacts, and coated with a 1% poly-L-lysine solution to promote adherence. Glass chips, 5×11 mm, are easily made from microscope slides and can be numbered using a diamond scribe. Supports are added directly to freshly inoculated liquid cultures, incubated either in a rack or on a shaker, and removed after18–48 h depending on the organism. When only an agar plate containing bacterial colonies is available, a heavy suspension is made in buffer (0.1 M cacodylate containing 3% sucrose, pH 7.2), to which the support is added, and removed 2–6 h later. Supports taken from heavy bacterial suspensions are rinsed thoroughly in buffer to remove cellular debris and larger bacterial colonies and dried slightly prior to fixation.

Supports are immersed in the primary fixative consisting of 2.5% glutaraldehyde, 0.5% paraformaldehyde, and 0.1% Ruthenium Red in 0.1 M cacodylate buffer (3% sucrose and pH 7.2). Ruthenium Red fixes acidic mucopolysaccharides, a common capsular component, but necessitates the use of cacodylate buffer over phosphate buffer.[1,2] Fixation is done at 4°C for at least 18–24 h. Samples are rinsed once in buffer and postfixed in 1% osmium tetroxide in 0.1 M cacodylate buffer (no sucrose, pH 7.2)

at room temperature for at least 1 h. After rinsing twice in buffer (no sucrose), the supports are placed in mesh CPD baskets to facilitate transfer between dehydration solutions. Dehydration is done for 15 min in each solution of a graded ethanol series of 25, 50, 75, 95%, and twice in dry 100% proceeds, followed by critical point drying.

At this point, the samples are further evaluated as to what magnifications, which microscope, and how the final images will be used. Larger samples, such as fungi and insects, which are examined at lower magnifications, are generally coated with Au-Pd in a vacuum evaporator. Bacteria, viral and parasite samples, examined at higher magnifications, are coated in an argon ion-beam coater with platinum. Supports are mounted on to SEM stubs using carbon conductive tabs.

The Hitachi S-900 (in-the-lens) or the S4700 (below-the-lens) field-emission SEM is used to view samples. The advantage of the 4700 is that larger image files can be acquired, which translates into more pixels for enlargement. However, superior resolution and the added use of the backscatter detector of the S900 make this instrument more desirable for smaller organisms or when surface detail enhancement is required. Generally, a series of images are acquired over a variety of magnifications, showing the organisms singly, in small clusters, and in larger, more complex groupings. Microscope conditions are set to enhance surface detail: a small aperture size, accelerating voltages between 1.0 and 2.0 keV, and extremely short working distances (6–8 mm). Images are acquired using a slow capture speed and the largest image file size available, generally limited by the line-scan generator and/or the image acquisition software. Typical files are 2560×1920 pixels, about 4.6 Mb. Of lesser importance are contrast and brightness, both of which can be later adjusted in Photoshop.

As electron microscopists, we accept black and white images. However, colored images have a greater visual impact and more easily convey important information to the viewer. For example (Fig. 1), like-organisms, when presented in the same color, make it easier to recognize species predominance. In other cases, backgrounds can be made less conspicuous and bland, thereby bringing out details of greater importance. Finally, the choice of colors is limitless, although microbiologists often tend toward blues and purples for gram-positive species and pinks and reds for the gram-negatives, reminiscent of the gram stain used in LM.

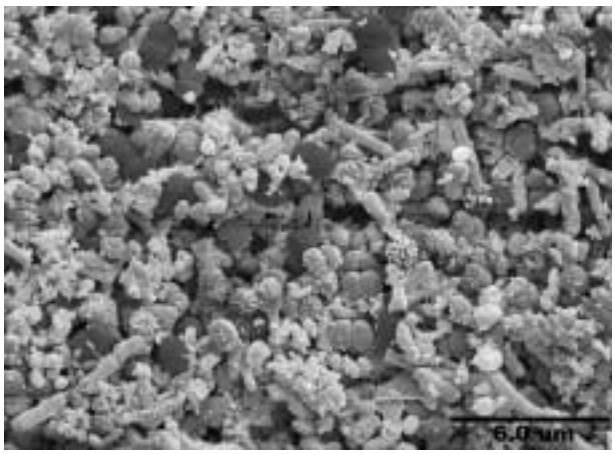

FIG.1 SEM micrograph of fecal flora. Image acquired on a Hitachi S4700 FESEM at 4.0 keV.

References

1. Schwach TS, Zottda EA: Use of scanning electron microscopy to demonstrate microbial attachment to beef and beef contact surfaces. *J Food Sci* 47,1401–1405 (1982)
2. Vandevivere R, Baveye P: Improved preservation of bacterial exopolymers for scanning electron microscopy. *J Microsc* 167, 323–330 (1992)

Scanning electron microscopy on in vitro culture of two leguminous species

N. GHOSH, A. CHATTERJEE,* D. W. SMITH†

Department of Life, Earth and Environmental Sciences, West Texas A & M University, Canyon, TX, USA; *CAS, Department of Botany, University of Calcutta, India; †Department of Biological Sciences, University of North Texas, Denton, TX, USA

A publication by the American National Academy of Sciences on tropical legumes[6] outlined some of the research needs for a great variety of economically important woody species whose remaining genetic resources need urgently to be collected and conserved. Most of these serious issues remain unaddressed or unsolved. Plant regeneration has been quite difficult among the legumes. Twenty-five leguminous species have been regenerated in vitro, but in most cases regeneration is at low frequency or limited by the source of explants and isolation of regenerative callus in vitro.

We established a viable regeneration system via tissue and cell suspension culture for *Albizia lebbeck* Benth. and *Albizia falcataria* Roxb., two important wood-yielding leguminous tree species. We standardized the culture medium after several trials and modifications by adding different growth regulators and growth supplements to obtain callus from the leaflet explants of the tree species. We found that the optimum use of casein hydrolysate (w/v) and coconut milk (v/v) in addition to 6-BAP and IBA could induce morphogenesis and somatic embryogenesis in the cultured tissue. This reports the first observation of somatic embryogenesis of *A. lebbeck* using leaflets as the explants. The leaf explants responded differently to combinations and concentrations of growth hormones and growth factors. On MS[5] media modified with 6-BAP (6 mg/l), NAA (0.02 mg/l), PVP (0.5%) and coconut milk (5% v/v), the explants produced proembryoids, other hormonal combinations produced various callus forms. We found that the modification of the culture medium by the addition of 0.5%

PVP (polyvinyl- pyrrolidone) could solubilize the phenolic compound secreted from the cut end of the explant within the culture vessel and increase considerable survivability.[1–4,7] In the third week, multicellular structures developed with various forms, fibrillar, ovoid, heart-shaped. The heart-shaped structures formed embryos. The embryos were observed at different magnifications with dissecting scope, compound microscope, and scanning electron microscope (SEM). We prepared proembryoids, the regenerative and nonregenerative calli for SEM study following standard techniques: fixation, dehydration, critical point drying (CPD) and gold-coating. The embryos were fixed in 4% gluteraldehyde in 0.1M phosphate buffer, postfixed in osmium-tetroxide (OsO_4), and dehydrated in ascending concentrations of ethanol and finally in isoamyl acetate. The tissues from the suspension culture were dried following CPD, coated with gold, and scanned with SEM. We recorded the different stages of embryogenesis and plant development.

The developing embryos were transferred to fresh liquid Gamborg's medium supplied with adenine sulfate (120 mg/l) and NAA (2 mg/l). On subculturing on fresh media the proembryoids developed cotyledons, shoots above the surface of the medium and roots below. Increased concentration of IAA induced profuse rooting. A pre-exposure of the rooted plantlets in sterile Knop's medium (10%) for 5 to 6 days yielded a better survival rate (55–60% in the greenhouse than is the case with sterile distilled water. The survival rate was less (30–40%) when plants were not hardened in Knop's medium. After hardening in the greenhouse we transferred the regenerated plants to the greenhouse. Some of the trees grew more than 25 feet tall within a few months outside the greenhouse.

References

1. Ghosh N, Chatterjee A: Cytological study on the effect of aging on callus cultures of *Dalbergia sissoo* Roxb. *Plant Sci in the Nineties*, 440–447 (1992)
2. Ghosh N: Cytogenetical and tissue cultural investigations on some tree species. Ph.D. thesis in Botany, University of Calcutta, India, 1–240 (1993)
3. Ghosh N, Smith DW, Chatterjee A: Cytological effects of gamma-radiation on in vitro culture of *Albizia falcataria*. (Eds. Manna GK, Roy SC). *Perspectives in Cytology and Genetics* 8, 97–107 (1995)
4. Ghosh N, Chatterjee A, Sinha A, Smith DW: Somaclonal variation in in vitro culture of *Dalbergia sissoo* Roxb- a leguminous tree. *Perspectives in Cytology and Genetics* (Eds. Manna GK, Roy SC) 9, 685–696 (1998)
5. Murashige T, Skoog F: A revised medium for rapid growth and bioassays with tobacco tissue cultures. *Physiol Plant* 15, 473–497 (1962)
6. NAS: *Report on Tropical Legumes: Resources for the Future, Nat Acad Sci Pub*, Washington D.C. (1978)
7. Ghosh N, Smith DW, Chatterjee A: From leaf to plant: Scanning electron microscopic studies on the in vitro regenerator of *Albizia falcararia* (L.) Fosberg — a leguminous tree species. *Am J Bot* 84,6,42 (1997)

Mitochondrial lifespan dynamic morphology in human skeletal muscle

C. BERTONI-FREDDARI,* J. VECCHIET,* G. FELZANI , P. FATTORETTI, M. SOLAZZI

Neurobiology of Aging Centre "N Masera" Research Department INRCA, Ancona; *Department of Internal Medicine and Aging, University "G. D'Annunzio", Chieti, Italy

A progressive time-related impairment in muscle energy metabolism has been reported to play an important role in the marked decrease of muscle functional performances occurring in aging.[1] To investigate the effect of age on the morphofunctional metabolic competence of muscle mitochondria, we carried out a morphometric investigation on subsarcolemmal and intermyofibrillar organelles in human bioptic samples from healthy volunteers of different ages ranging from 17 to 81 years.

Thirty-nine patients who underwent surgical interventions were enrolled in our study. They were divided into three age groups: 17-39 (12 patients), 40-60 (14 patients) and 60-83 (13 patients) years of age. The tissue pieces were collected according to the surgical intervention to be performed and this yielded different types of muscle samples to be analysed (vastus lateralis, anterior tibialis and vastus medialis). Fresh, glutaraldehyde-fixed samples were processed according to conventional electron microscopic procedures. In subsarcolemmal and intermyofibrillar regions: the mitochondrial area, perimeter, diameter, and axial ratio (Feretratio) were measured by conventional, semiautomatic, computer-assisted morphometry. Systematic random sampling was adopted as criterion to select the organelles to be analysed by our computer program. Namely, starting from a fixed position of the electron microscope specimen holder, a random programmed path was run and mitochondrial scoring was stopped at 100 intermyofibrillar as well as subsarcolemmal organelles/ patient. Mitochondrial images, acquired by a TV camera from the electron microscope, were recorded and the organelle perimeter was drawn by the computer mouse. The measurements were stored on different files according to the patient's code.

We found a significant decrease of the area, perimeter, and diameter of intermyofibrillar as well as subsarcolemmal mitochondria in the middle-aged group (40-60 years) versus the young one. A significantly lower mitochondrial area of the subsarcolemmal organelles was found also in the oldest group versus the young one. These reductions are counteracted by consistent, but not significant, increases in the length of the cristae/mitochondrial area in the subsarcolemmal region. SDH activity did not show age-related changes. Higher percentages of rounded (Feretratio close to 1) intermyofibrillar organelles, supporting mitochondrial splitting, were found in mature and old groups versus the young one, while a similar increase in

subsarcolemmal mitochondria was observed only in the old group.

On the basis of the marked frailty of their DNA, mitochondria are proposed to play a central role in aging and age-related pathologies.[2–4] Namely, the progressive accumulation of somatic mutations is supposed to lead to a mosaic of cells with metabolic potentials ranging from normal to severely impaired.[2] As a consequence, the oxidative phosphorylation efficiency decreases with time,[3] but physiological compensations to this decline occur in all systems including skeletal muscles which can be maintained in adequate efficiency by physical activity. In this context, the balanced changes we observed among the age-groups analysed account for an age-related morphofunctional remodelling of the muscle hardware for energy provision. Interpreting the lifespan constancy of mitochondrial ultrastructural dynamics according to "the bioenergetic mosaic hypothesis,"[2] we propose that an excessive mitochondrial impairment may result in apoptosis of the energy-defective cells[5] and this physiological selection, while leading to the marked sarcopenia reported in aging, preserves the ones still capable of proper metabolic competence.

References

1. Trounce I, Byrne E, Marzuki S: Decline in skeletal muscle mitochondrial respiratory chain function: Possible factor in aging. *Lancet* 1, 637–639 (1989)
2. Linnane AW, Marzuki S, Ozawa T, Tanaka M: Mitochondrial DNA mutations as an important contributor to aging and degenerative diseases. *Lancet* 1, 642–645 (1989)
3. Wallace DC: Mitochondrial genetics: A paradigm for aging and degenerative disease. *Science* 256, 628–632 (1992)
4. Miquel J: An update on the oxygen stress-mitochondrial mutation theory of aging: Genetic and evolutionary implications. *Exp Ger* 33, 113–126 (1998)
5. Nagley P, Zhang C, Martinus RD, Vaillant F, Linnane AW: Mitochondrial DNA mutation and human aging: molecular biology, bioenergetics, and redox therapy. In *Mitochondrial DNA in human pathology* (Eds. S Di Mauro, DC Wallace). Raven Press (1993) 137–157

Oversized junctions in physiological and pathological (Alzheimer's Disease) brain aging provide clues to a novel interpretation of perforated synapses

C. Bertoni-Freddari, P. Fattoretti, T. Casoli, G. Di Stefano, M. Solazzi, N. Gracciotti

Neurobiology of Aging Centre "N Masera" Research Department INRCA, Ancona, Italy

Aging of the human brain can be considered a condition in which pathologic changes can be found without clinically evident manifestations. Deterioration of function occurs when the numeric densities of neurons and of their connections decrease below a critical reserve level and coping with environmental stimulations becomes difficult.[1] In such a situation, degenerative phenomena and compensatory reactions continuously remodel synaptic connectivity. In the senile brain of rats, human beings as well as old patients affected by Alzheimer disease (AD), we reported that the decrease of synaptic numeric density (Nv) is associated with a significant enlargement of the average area (S) of the persisting contacts.[2] To better understand the size composition of the age-related patterns of synaptic connectivity, we performed a percent distribution of the S values measured in adulthood and aging.

As anatomical models, we chose two discrete areas of the central nervous system (CNS): the cerebellar cortex and the hippocampal dentate gyrus. Freshly excised samples were used for studies on adult and old rats (12 and 28–30 months of age, respectively) while human material was obtained at autopsy from adult, old and AD patients (mean age: 55.8, 81.4 and 83.6 years, respectively). Synaptic junctional areas were stained by the ethanol phosphotungstic acid preferential technique according to.[2] S of each contact zone was calculated by computer-assisted, semiautomatic measurements of the length of postsynaptic density in systematically and randomly sampled sections. Both in rat and human aging, as well as in old AD patients, we found an increased complement of enlarged contact zones (Fig. 1). The percentage of oversized junctional areas resulted markedly higher in the hippocampus than in the cerebellum.

Enlargement of synaptic junctional areas is supported to be an intermediate step in synaptic remodelling processes. Namely, it has been hypothesised that, as a consequence of stimulation, synaptic contact zones increase in size (I), perforate (II) and split (III) to yield an increased number of smaller contacts which can be reinforced or reabsorbed according to their use. On the basis of these concepts, the higher percent of larger synapses found in physiological aging and AD has been proposed to represent: I) the final outcome of the selective elimination of smaller and scarcely used contacts; II) the result of unaccomplished cycles of synaptic remodelling.[2,3] An alternative interpretation of our findings can be suggested if perforated (PSs) and non perforated contact zones are considered populations of junctions each representing different forms of synaptic rearrangements. In physiological aging, and at a higher extent in AD, synaptic ultrastructural dynamics are consistently reported to be markedly impaired,[1,2] thus an increased complement of enlarged contacts may result from a progressive pruning of PSs purported to reinforce the most frequently used contacts. Stimulation-tuned synaptic networks are structurally accomplished by high synaptic densities which require adequate metabolic provisions: the physiological PSs pruning process, proposed by us in normal aging and AD, would allow to spare energy for the proper functional maintenance of reduced synaptic connectivities. Despite the speculative character of the above assumptions, the presence of abundant PSs, while increasing synaptic efficacy, implies high metabolic rates, a condition which is difficult to meet in the old CNS.[1,2]

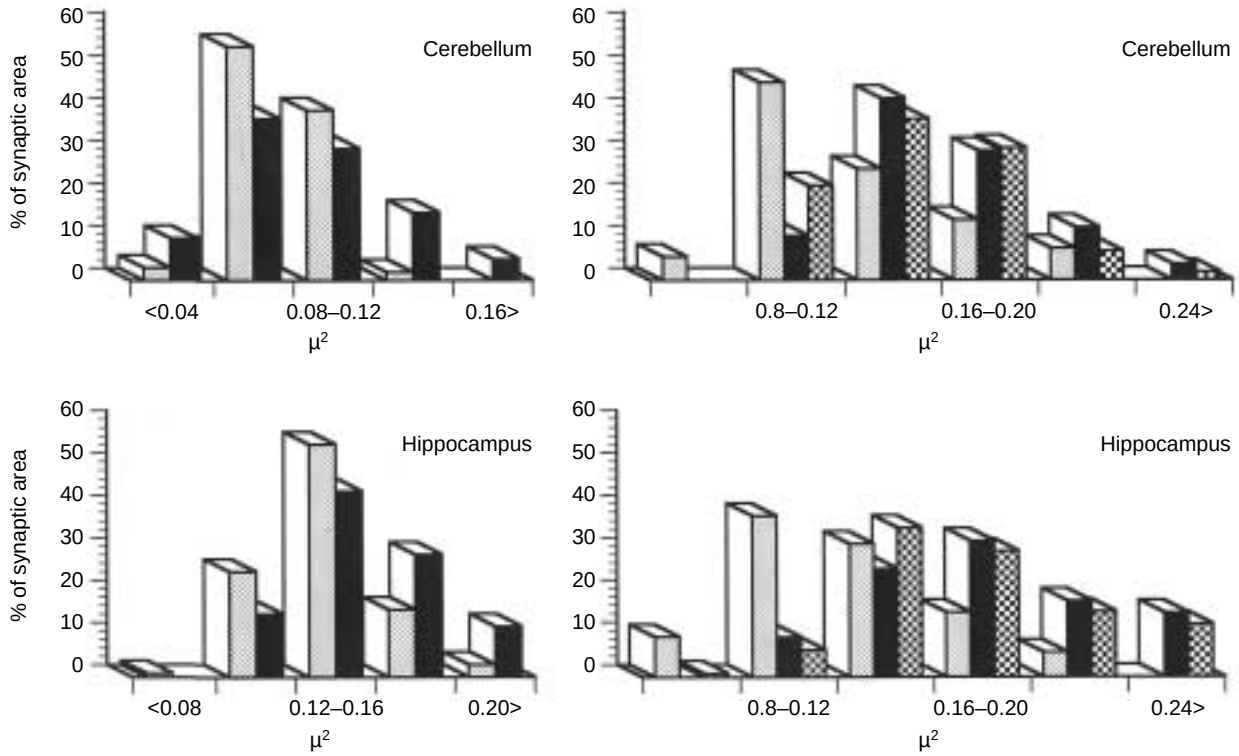

FIG. 1 Percentage distribution of the synaptic average size in the cerebellar glomerulus and hippocampal dentate gyrus from rat and human beings in adulthood, physiological aging and Alzheimer disease (AD). An increased percent of oversized synapses is present in the senile and demented nervous system.

References

1. W Meier-Ruge, O Hunziker, P Iwangoff: Senile dementia: a threshold phenomenon of normal aging? A contribution to the functional reserve hypothesis of the brain. Ann N.Y. *Acad Sci*, 621, 104–118 (1991)
2. C Bertoni-Freddari, P Fattoretti, R Paoloni, U Caselli, L Galeazzi, W Meier-Ruge: Synaptic structural dynamics and aging. *Gerontology* 42, 170–180 (1996)
3. RK Carlin, P Siekevitz: Plasticity in the central nervous system. Do synapses divide? *Proc Natl Acad Sci* (USA) 80, 3517–352 (1983)

Applications of scanning probe microscopy in biotechnology: Imaging, sensing and manipulation

Biological sensing using scanning force microscopy

T. L. PORTER, M. P. EASTMAN, D. L. PACE

Northern Arizona University, Deptartments of Physics and Chemistry, Flagstaff, AZ, USA

Microsensor systems capable of providing unambiguous identification of chemical and biological agents have wide applicability. Such systems must be robust, inexpensive, miniaturized and capable of being interfaced to low cost telemetry hardware. We have developed a new and very promising type of sensor based upon piezoresistive microcantilevers that is robust, inexpensive, miniaturized and capable of being interfaced to low cost telemetry hardware. This type of sensor can be adapted to a wide range of sensing applications including the sensing of biological materials.

Using a simple mechanical approach mechanism, a piezoresistive cantilever is brought into contact with the sensor film (active material). These cantilevers are only 100-200 microns long, and about 50 microns wide. These cantilevers contain an internal channel of piezoresistive material, connected to two tiny external electrodes. The non-stressed resistance of these cantilevers is on the order of 2 k ohms, but changes rapidly and measurably in response to any bending of the cantilever. In fact, these cantilevers are sensitive enough to measure bending strains of only a few Å. Any swelling of the active material in contact with the cantilever tip (organic polymer, bio-layer, etc.) will result in an immediate, easily measurable change in the cantilever channel resistance. This change will be in exact proportion to the amount of the vertical swelling, a simple ohmmeter is thus sufficient to record the sensing activity.

We fabricated an active biological sensing layer by depositing a gold layer atop a mica substrate. This layer was functionalized by exposing it to thiol-derivatized single-

strand DNA. The DNA chosen was consisted of 25 base units with a thiol group attached to the 5' end. The thiol group tethers the DNA molecule to the gold substrate, producing a layer of single strand DNA on the substrate. The piezoresistive cantilever is then brought into gentle contact with this "sensing layer". All tests of this piezoresistive biological sensor were performed in aqueous solution. In order to test this sensor configuration, three sets of single-strand DNA in aqueous solution were used as analytes. The concentration of the analyte solutions was 5 mM. The three sets of analyte DNA consisted of the exact compliment to the DNA layer on the gold substrate, the exact compliment with one base substitution, and the exact compliment with 5 base substitutions. Separate areas on the active sensing layer were used for each test.

Upon exposure to the analyte solution consisting of the exact complimentary DNA strand, an immediate response of 0.5 ohms (resulting from cantilever bending) was recorded. This change in cantilever resistance was stable for 15 minutes, at which time the sample began to dry, and the cantilever was retracted. The measured resistance changes due to cantilever bending are the direct result of the binding of the complimentary DNA (analyte) strand to the DNA layer tethered to the gold substrate. For the analyte consisting of the complimentary strand with 5 base substitutions, a resistance response change of 0.02 ohms was measured. In the case of the complimentary strand with only a single base substitution, a resistance change of 0.2–0.3 ohms was measured. These preliminary results indicate that for a sensing layer consisting of 25 base strands, the sensing of the exact complimentary strand is easily achieved, with good differentiation on analyte DNA strands differing by several bases. Only moderate to poor differentiation occurs for analyte strands differing by a single base.

Microcantilever biosensors

T. THUNDAT

Life Science Division, Oak Ridge National Laboratory, Oak Ridge TN, USA

The advent of inexpensive, mass-produced microcantilevers, such as those used in atomic force microscopy, promises to bring about a revolution in the field of chemical, physical, and biological sensor development. The microcantilever resonance response such as resonance frequency, deflection, and Q-factor undergo variation due to external stimuli. The resonance response variation can be due to mass loading, surface stress, or damping. When molecules adsorb on surfaces they can also produce a surface stress due to forces involved in the adsorption process. These surface stresses can be observed as changes in deflections of a thin microcantilever. Microcantilever biosensors have been made by coating the cantilevers with selective layers, such as antibodies, DNA, enzymes, etc. These bio-coated cantilevers have been used to detect analytes by either stress or heat-induced bending of the microcantilever. The arraying of bio-molecules on microcantilevers have great potential in high throughput screening applications.

High-sensitivity mechanical resonant mass sensor

H. G. CRAIGHEAD, B. ILIC, D. CZAPLEWSKI, M. ZALALUTDINOV

School of Applied and Engineering Physics, Cornell University, Ithaca, NY, USA

Engineered micro- and nano-mechanical systems[1,4,5] can provide multi-functional, highly-sensitive mass sensors. We present a resonant frequency-based chemical and biological mass sensor, comprising nanofabricated silicon or low-stress silicon nitride cantilever beams. We have demonstrated these devices to detect, for example, molecular monolayers and single *Escherichia coli* (E. coli) cell-antibody binding events.

The highly-sensitive sensors considered here are a resonating cantilever beam made of thin silicon or low-stress silicon nitride, using nanofabrication methods previously reported.[1,2,3] Because the mass of the resonant devices can be made extremely small, significant resonant frequency shifts can be obtained by remarkably small added masses. Signal transduction was achieved by employing an optical deflection system, similar to that used in atomic force microscopes, to observe the mechanical resonance and to measure the resonant frequency shift resulting from added mass. For bacteria detection cantilevers were coated with antibodies reactive to *E. coli* serotype O157:H7 and then immersed into solutions containing *E. coli* cells.[2] In order to remove loosely bound cells, devices were rinsed in deionized water and blown dry with nitrogen after each immersion. The resonant frequency spectra of the cantilever, in air, before and after antibody and cell attachment, were measured. The binding of a single cell with mass on the order of 0.5 picogram was easily detectable.

To further enhance the sensitivity of our devices we employed vacuum encapsulation. Because the air damping is eliminated the quality factor increases and resonant frequency linewidth decreases. This allows detection of much smaller frequency shifts in vacuum than in air. In this case the binding of a monolayer of Aminopropyltriethoxysilane (APTS) is readily detectable.

Resonant Si wires as small as 20 nm can be fabricated by electron beam lithography. With the combination of ultra-low mass devices, driven resonance, and optical detection, arrays of high sensitivity mass detectors can be formed. With selective coatings these devices can become highly sensitive chemical or biological sensors.

References

1. Carr DW, Evoy S, Sekaric L, Craighead HG, Parpia JM: Measurement of mechanical resonance and lossesin nanometer scale silicon wires. *Appl Phys Lett* 75, 920–922 (1999)
2. Craighead HG: Nano Electromechanical Systems. *Science*, 290, 1532–1536 (2000)
3. Ilic B, Czaplewski D, Craighead HG, Campagnolo C, Batt C, Neuzil P: Mechanical resonant immunospecific biological detector. *Appl Phys Lett* 77, 450–452 (2000)
4. Newell WE, *Science* 161, 1320, (1964)
5. Peterson KE, *Proc. IEEE* 70, 420 (1982)

Electrostatic potentials measurement of single photosynthetic reaction center by kelvin force microscopy

I. LEE,[*†] J.W. LEE,[*] E. GREENBAUM[*]

[*]Chemical Technology Division, Oak Ridge National Laboratory, Oak Ridge; [†]Department of Electrical and Computer Engineering, The University of Tennessee, Knoxville, TN, USA

Photosystem I (PS I) reaction centers are nanometer-size robust supramolecular structures that can be isolated and purified from green plants. The PS I reaction center is a molecular diode[1] and photovoltaic device[2] made by nature. We have demonstrated that PS I can be selectively oriented by chemical modification of a surface without denatured.[3] Using the technique of Kelvin force probe microscopy, we report here the first measurement of exogenous photovoltages generated from single PS I reaction centers in a heterostructure comprised of PS I, organosulfur molecules, and atomically flat gold. Illumination of the reaction centers was achieved with a diode laser at λ= 670 nm. Data sets were obtained consisting of 22 individual PS Is measured entirely under laser illumination, 12 PS Is measured entirely in darkness, and four PS Is in which the light-dark transition occurred in mid-scan of a single PS I. The average values of the light minus dark voltages relative to the substrate for the four PS Is were –1.13 ± 0.14 V and –1.20 ± 0.19 V at diametrical peripheries, and –0.97 ± 0.04 V at the center. Under illumination, the potentials of the central region of the PS Is were typically more positive than the periphery by 6-9 *kT*, where *kT* is the Boltzmann energy at room temperature. These energies suggest a possible mechanism whereby negatively charged ferredoxin, the soluble electron carrier from PS I to the Calvin-Benson Cycle, is anchored and positioned at the reducing end of PS I for electron transfer. From our measurements, we found that the polarity and magnitude of the light-induced voltage are consistent with the known structure and energetic features of PS I but with the ability to measure PS I in air and bounded with various manmade structures.

References

1. Lee I, Lee JW, Warmack RJ, Allison DP, Greenbaum E: Molecular electronics of a single photosystem I reaction center: Studies with scanning tunneling microscopy and spectroscopy. *Proc Natl Acad Sci* USA, 92,1965–1969 (1995)
2. Lee I, Lee JW, Stubna A, Greenbaum E: Measurement of electrostatic potentials above oriented single photosynthetic reaction centers. *J PhyS Chem* B, 104, 2439–2443 (2000)
3. Lee I, Lee JW, Greenbaum E: Biomolecular electronics: Vectorial arrays of photosynthetic reaction centers. *Phys Rev Lett*, 79, 3294–3297 (1997)

The structure and chemistry of a hydrogen cyanide polymer: Implications for chemical evolution and the origin of life

M. P. EASTMAN, F. S. E. HELFRICH, T. L. PORTER

Departments of Chemistry and Physics and Astronomy, Northern Arizona University, Flagstaff, AZ, USA

Hydrogen cyanide in basic aqueous solution reacts to form a heterogeneous cyanide polymer, containing paramagnetic sites, capable of releasing biologically significant molecules such as adenine.[1–2] Since radio astronomy shows that H_2O, HCN and NH_3 are among the most abundant molecules in the universe, the nature of this reaction has implications in the areas of chemical evolution and the origin of life. For a synthesis carried out at room temperature, under aerobic conditions, with no agitation of the reaction medium, the polymer forms a variety of structures reminiscent of those formed by ice. The polymeric material appears to coalesce in water and disperse in dimethyl sulfoxide and dimethyl formamide. The material produced in this reaction contains a substantial concentration of paramagnetic sites whose magnetic parameters have been determined by x-band and w-band paramagnetic resonance. Microscopy of the polymeric material shows dendritic structures, often with a hexagonal core, about 10 μ in diameter. Scanning force microscopy (SFM) of fine structure emanating from the dendrites shows hollow tubules approximately 0.5 μm in width; other SFM images show ellipsoidal structures reminiscent of the Arime or graupel@ formed by ice. Evidence for Mullins-Sekerka instabilities during the growth phase can be seen in the polymeric structures observed by microscopy and SFM.[3] The polymer systems studied have structures with large surface areas; the tubules may include solutions and enable the transportation of dissolved species from one region of the structure to another. It is possible that the varied structural features of the dendrites produce an array of microenvironments for subsequent reactions and that the structures and chemistry of the polymer can undergo evolutionary processes if left for extended periods. At present, it is unknown to what extent the tubule walls are permeable to solvent, ions, or dissolved organic species.

References

1. Volker T: *Angew Chemie* 72, 379 (1960)
2. Oro J: *Biochem Biophys Res Commun*, 2, 407 (1960)
3. Mullins WW, Sekerka RF: *J Applied Phys* 35, 444 (1964)

Scanning tunneling microscopy spectroscopy of biomolecules

J. STEIN, F.R. ZYPMAN

Yeshiva University, Department of Physics, New York, NY, USA

Introduction

It has been found that tip-sample, current-voltage (I-V) curves are related to global and local density of states (DOS). Although there have been various attempts to find general concrete rules relating these quantities, and extensive advances have been made, the problem remains an open one. Here, we study scanning tunneling microscopy (STM) spectroscopy of carbon chains. In the next sections, we present the theory, and show results for alkane and alkene macromolecules. This method is an extension of that developed to study scanning tunneling spectroscopy (STS) on Si samples.

Theory

Consider the system under study to be the union of three regions. Two conducting tip regions, and an organic chain, the sample under study, which serves as the channel for current between the conductors.

The energy states are obtained within the tight binding (TB) approach. TB has been used in the past to study chemisorption on surfaces and density of states (DOS) of surface electrons. Within TB, the wave function has the following expression.

$$\Psi_{\vec{k}} = \sum_{\vec{m}=atomic\ \ sites} C_{\vec{m},\vec{k}}\ \ \Phi_{\vec{m}} \tag{1}$$

where k is the electron crystal momentum, ϕ_m are atomic orbitals, and $C_{k,m}$ are the expansion coefficients. The vector m labels both tip and sample atomic sites. We impose, as a boundary condition, that the wave function, far away from the interfaces, be a Bloch wave:

$$C_{\vec{\theta},\vec{m}} \propto e^{+\_i\vec{m}\bullet\vec{\theta}}\ \ for\ \ |\vec{m}_z| \geq m_0 \tag{2}$$

where m_0 gives an idea of the extension of the tunneling region and z is perpendicular to the interfaces. M_0 is a single-digit number, because bulk properties are recovered a few atoms away from a perturbation to the perfect crystal. ϕ is defined as k times the tip lattice constant.

At the positively biased conductor, we consider the sum of spherically scattered electrons that move away from the tunneling region, with amplitude $f(\phi_m)$. To obtain the current, we evaluate $f(\phi_m)$, together with C_m. The amplitude of the spherical waves is[4]

$$f(\Omega_{\vec{m}}) = m\ a\ \ e^{-im\ \theta^+}\ \ C_{\vec{m},\vec{\theta}^-} \tag{3}$$

where ϕ^+ is a function of ϕ^- correspond to the positive and negative region respectively, and a is the lattice parameter of the tip. The current for state ϕ^- is,

$$I_{\vec{\theta}^-} = \frac{e\hbar\theta^+}{a\ m_e}\int_{Plane}\frac{1}{r^2}\,|\,f_{\vec{\theta}^-}\,|^2\ r^2 d\Omega \tag{4}$$

The total current is the sum of all the contributions from states ϕ^- with energies below the Fermi energy:

$$I = \sum_{\vec{\theta}_T/E(\vec{\theta}_-)<E_F} I_{\vec{\theta}_-} \tag{5}$$

This expression has an implicit dependence on the voltage, since the energies and states depend on the applied voltage.

Application to Organic Macromolecules

We applied the general theory outlined in the previous section, to detect DOS variations due to changes in molecular bonds. For that purpose, we considered two 100-atom long hydrocarbon chains: a simple alkane, and an alkene with alternating double bonds. Within TB, the two molecules are characterized by different Coulomb and Resonant integrals. These TB parameters are readily available in the published literature. We take the tip to be made of Tungsten and, accordingly, used the TB parameters and Fermi energy from Zypman at al. The curves dI/dV vs V show sharp peaks at the positions of the energy levels. The presence of more hydrogen atoms in the alkane, induces typical “hydrogen spikes”, less frequently present in the alkene molecule. Thus, our method serves to differentiate between hydrocarbons with different bonds. Currently we are investigating whether this method can be used to identify alkene isomers with only one double bond.

Acknowledgments: This work is supported by the National Cancer Institute through Grant # CA77796-02 and Yeshiva University.

Posters

Ultrastructural features of axonal cytoskeleton in aging: A quantitative study at internodal regions of rat sciatic nerve

C. BERTONI-FREDDARI, U. CASELLI, P. FATTORETTI, T. CASOLI, G. DI STEFANO, M. SOLAZZI

Neurobiology of Aging Centre "N Masera" Research Department INRCA, Ancona, Italy

Synthesis and assembling of constitutive molecules of nerve terminals are in charge of activities occurring in neuronal perikaryon, however the axonal cytoskeleton also participates in the renewal and maintenance of peripheral synaptic regions.[1] Neurofilaments, microtubules, microfilaments, and their relationships are major determinants of the functional transportation along the axon and represent a very dynamic system, actively supporting nerve cell adaptive responses to environmental stimulations.

To test whether slow axoplasm flow between nerve cell body and synaptic regions is affected by structural alterations due to age, we performed a morphometric evaluation of the axonal cytoskeleton ultrastructural features at the internodal regions of the sciatic nerve of 3, 12, and 30 month-old rats.

Nerve segments (3 mm) were processed according to conventional electron microscopic procedures. Axons sectioned perpendicularly to their longitudinal axis at the internodal region (axoplasm area: 18.25–26.5 μm^2) were analysed (Fig. 1). As inclusion criteria, we considered those sections showing a compact myelin sheath, while Schwann cell nuclei, Schmidt-Lanterman clefts or expanded Schwann cell myelin were not present. The axoplasm areas, acquired from the electron microscope by a TV camera, were enlarged up to 200,000× at the image analyser video. In each axon, measurements were carried out on six fields to yield a total sampled area of 4.8 μm^2. These fields were systematically and randomly chosen by superimposing a square template on low magnification images. The overall number of neurofilaments (No.Nfs) and microtubules (No.Mts) per axoplasm area, the numeric density (number/μm^2 of axoplasm area) of neurofilaments (NaNfs) and microtubules (NaMts), the myelin thickness, the number of myelin lamellae, and the R-proportion (No.Nfs/No.Nfs + No.Mts) were the parameters measured by computer-assisted semiautomatic procedures.

No.Nfs and NaNfs as well as myelin thickness and number of myelin lamellae were the same between 12 and 30 months of age, while a significant increase of these parameters was found in a comparison with young rats. No.Mts and NaMts were significantly increased at 12 versus 3 as well as at 30 versus 12 months of age, respectively. R-proportion did not show any difference due to age. The present findings support that the dynamic condition of the axonal cytoskeleton is substantially preserved between adulthood and aging. As a speculative explanation of the apparent discrepancy between constancy of cytoskeletal elements from 12 to 24 months of age and the reported retardation in their slow axonal transport along the axon,[2] we suggest that an unaccomplished and/or defective neurofilament protein phosphorylation may constitute a critical determinant for the age-related axonal flow decay. An ordered process of phosphorylation is reported to be essential for a proper set up of neurofilaments both in the perikaryon and in the axoplasm,[3] conceivably, irregular assembly may result from aberrant phosphorylation patterns at selected sites as has been documented in age-related neuropathological conditions, such as Alzheimer's disease and in chemical intoxication.[3] Abnormal neurofilament phosphorylation has been supported to occur also in physiological aging.[3] As a consequence, interactions may take place among proximal cytoskeletal elements which may be responsible for changes in their packing density leading to a decrease in the rate of transport. Conceivably, intra-axonal spacing constraints of cytoskeletal elements (e.g. neurofilaments), rather than

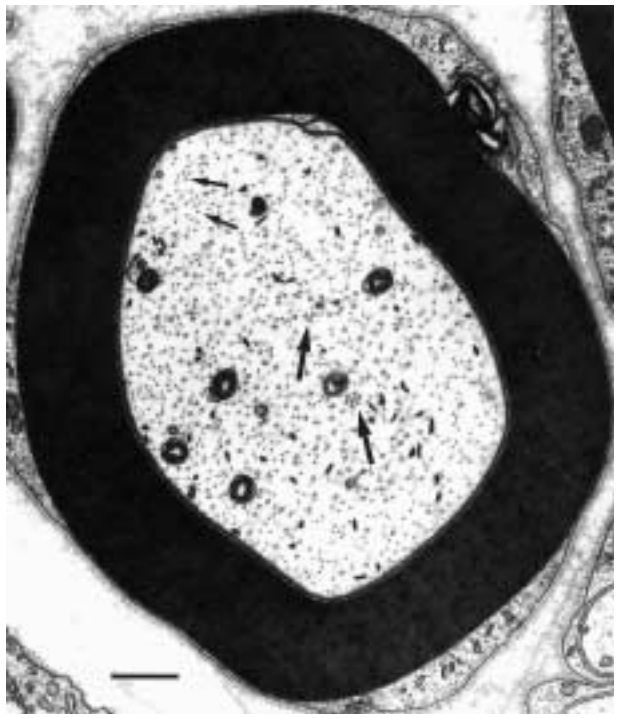

FIG. 1 Electron microscopic picture of a rat sciatic nerve axon sectioned perpendicularly to its longitudinal axis. The regularly ordered myelin lamellae and the sharp bleb (upper top of the axoplasm) clearly document the good fixation of the sample. Big arrows: microtubules. Small arrows: neurofilaments. Bar = 0.25 μm.

their numeric density, may be supported to contribute to the decline of the slow axonal transport of organelles and molecules reported in aging.

References

1. Bartlett-Bunge M: The axonal cytoskeleton: its role in generating and maintaining cell form.Trends in Neurological Sciences, 9, 477-482 (1986)
2. McQuarrie IG,Brady ST, Lasek RJ: Retardation in the slow axonal transport of cytoskeletal elements during maturation and aging. Neurobiology of Aging, 10, 359-365 (1989)
3. Sternberger LA, Sternberger J, Ulrich J: Aberrant neurofilament phosphorylation in Alzheimer disease. PNAS USA, 82, 4274-4276 (1985)

An ultrastructural study of platelet activation in Alzheimer's disease

T. CASOLI, G. DI STEFANO, N. GRACCIOTTI, P. FATTORETTI, M. SOLAZZI, C. BERTONI-FREDDARI

Neurobiology of Aging Centre, "N. Masera" Research Department, INRCA, Ancona, Italy

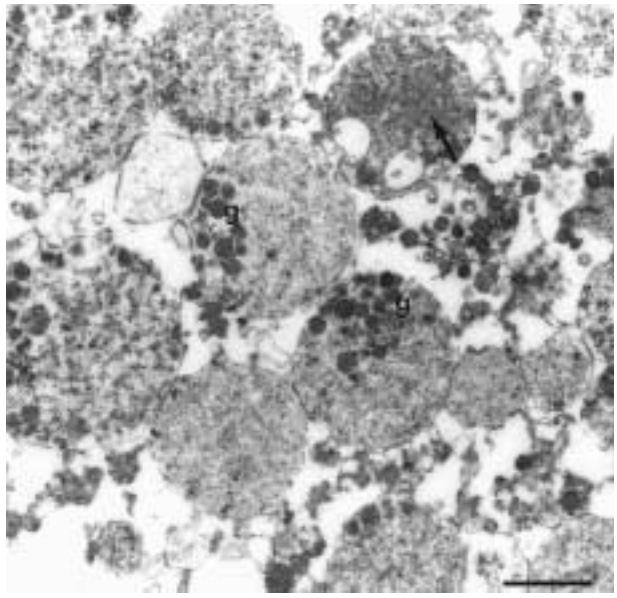

FIG.1 Platelet ultrastructure from an Alzheimer disease (AD) patient. Cells are swollen and the cytoplasm appears diluted. Internal contraction was apparent in some of the cells (≠). Granules are localized mostly beneath the plasma membrane (g). Bar = 1 μm.

Although principally a disease of the brain, Alzheimer's disease (AD) has also been associated with peripheral manifestations. Platelets have received particular attention in this regard, with reported abnormalities including increased membrane fluidity,[1] reduced cytochrome c oxidase activity,[2] and reduced phospholipase C activity.[3] Platelets have also recently been shown to exhibit greater unstimulated activation than those of controls.[4] To test whether platelets from AD patients displayed an increased platelet activation in the resting state, we carried out an ultrastructural study of platelets from healthy adult donors (n=4; mean age: 38±7), Alzheimer's patients (n=5; mean age: 67±5), and age-matched controls (n=5; mean age 70±3). The diagnosis of probable AD was made according to the National Institute of Neurological Disorders and Stroke-Alzheimer's Disease and Related Disorders Association criteria.

Platelets were separated from citrated blood by a centrifugation at 200× g to obtain platelet-rich-plasma (PRP). Platelets were separated from PRP by centrifugation at 2000× g for 20 min and washed twice in Hepes buffer containing 145 mM NaCl, 5 mM KCl, 1 mM $CaCl_2$, 1 mM $MgCl_2$, 10 mM Hepes, 10 mM glucose, adjusted to pH 7.4. 10 μm prostaglandin E_1 (PGE_1) was added to prevent aggregation. Platelet pellets were fixed overnight in 2.5% glutaraldehyde in 0.1 M sodium cacodylate buffer, postfixed in 1% buffered osmium tetroxide, dehydrated in a graded series of ethanol, and embedded in Durcupan resin. Ultrathin sections were stained with uranyl acetate and lead citrate.

Healthy adult donors' platelets had a characteristic discoid shape with some extending pseudopods. Their morphology reflects that of fresh platelets. Several types of organelles were randomly dispersed in the matrix of the cytoplasm like mitochondria, dense bodies, granules and small particles of glycogen. Platelets from old healthy subjects appeared spherical in form, demonstrated granule swelling, vacuole formation and cytoplasmic dilution. Internal contraction was apparent in some of the cells. Platelets from AD patients were similar to those from age-matched controls. Physical alterations suggestive of cell destruction were present in most of the cells (Fig.1). The alterations were consistent with loss of surface membrane integrity.

The present findings support the fact that platelet unstimulated activation is not considerably different in AD as compared to age-matched controls. Both groups display a wide variety of structural alterations observed in fresh platelets after stimulation by potent aggregating agents. Thus platelet activation in the resting state seems to be related to aging rather than to AD. It has been demonstrated that in aging there is a significantly higher amount of circulating platelet aggregates and a decrease in ADP threshold for irreversible aggregation.[5] In addition, atherosclerosis may contribute to platelet hyperactivation. All these processes might result in the observed increased platelet activation in the resting state during aging.

References

1. Piletz JE, Sarasua M, Whitehouse P, Chotani M.: Intracellular membranes are more fluid in platelets of Alzheimer's disease patients. *Neurobiol Aging* 12, 401–406 (1991)
2. Parker WD, Mahr NJ, Filley CM, Parks JK, Hughes D, Young DA, Cullum CM: Reduced platelet cytochrome c oxidase activity in Alzheimer's disease. *Neurology* 44, 1086–1090 (1994)

3. Matsushima H, Shimohama S, Fujimoto S, Takenawa T, Kimura J.: Reduction of platelet phospholipase C activity in patients with Alzheimer disease. *Alzheimer Dis Assoc Disord* 9, 213–217 (1995)
4. Sevush S, Jy W, Horstman LL, Mao WW, Kolodny L, Ahn YS: Platelet activation in Alzheimer disease. *Arch Neurol* 55, 530–536 (1998)
5. Gleerup G, Winther K: The effect of ageing on platelet function and fibrinolitic activity. *Angiology* 46, 715–718 (1995)

Transmission and scanning electron microscopic study of vertebrate oligodendroglial cells

O.J. CASTEJÓN, H.V. CASTEJÓN

Laboratorio de Microscopía Electrónica, Instituto de Investigaciones Biológicas, Universidad del Zulia, Maracaibo, Venezuela

Oligodendroglial cells have been extensively studied in normal and pathological conditions by means of light, confocal, transmission electron microscopy and molecular biology techniques.[1–3] However, very few studies have been devoted to analyzing their three-dimensional outer and inner surface morphology. In the present communication we have used thin sectioning transmission electron microscopy and the cryofracture methods for scanning electron microscopy to analyze the cytoplasmic and nuclear compartments of fractured oligodendroglial cells.

Specimens of two teleost fish: Arius Spixii and Salmo trout were fixed by vascular perfusion with Karnovsky fixative. Cerebellar slices, 2-3 mm thick, were cut with a razor blade and fixed by immersion in the same fixative for 4-5 h. After washing in buffered saline, they were postfixed in 1% osmium tetroxide in 0.1M phosphate buffer solution, pH 7.4 for 1 h. After rinsing in a similar buffer, tissue blocks were dehydrated through graded concentrations of ethanol, rapidly frozen by plunging into Freon 22, cooled by liquid nitrogen and fractured with a precooled razor blade. The fractured fragments were returned to fresh absolute ethanol for thawing. The cytoplasmic and nuclear soluble proteins were washed out, presumably during the thawing step, leaving anfractuous cavities surrounding the cytomembranes and allowing visualization of the surface details of cytoplasmic and nuclear structures. The tissues were then dried by the critical point method with liquid CO_2 and coated with gold-palladium. Specimens were examined with a JEOL 100 B Electron Microscope with ASID scanning attachment at 80 kV.

In human cerebral cortex processed for transmission electron microscopy, perineuronal or satellite oligodendrocites were observed ensheathing pyramidal and nonpyramidal nerve cells and establishing a neuron-glia unit from the structural point of view. Oligodendrocyte plasma membrane appeared closely apposed to neuronal plasma membrane, being separated by an extracellular space 20 nm in width. The nucleus showed a condensed aggregation pattern of chromatin substance. Perivascular oligodendrocytes were also found associated to the perivascular astrocytic end-feet, at the level of the capillary wall.

In the mouse cerebellar cortex, interfascicular oligodendrocytes were observed intimately applied to myelinated axons, revealing their myelin forming cell role. At higher magnifiction, the oligodendroglial plasma membrane was observed surrounding the outer myeling lamellae.

In samples of teleost fish cerebellar cortex processed by the freeze-fracture SEM method, the cryofracture oligodendrocytes exhibited the inner surface details of nucleus and cytoplasm. The freezing process preserved the compact heterochromatin masses at the nuclear periphery and the vacuolated appearance of subjacent euchromatin substance. The washing out process of cytosol permitted to observe the outer surface of endoplasmic reticulum and cytoskeletal structure. The organelle region and the stereospatial arrangement of endoplasmic reticulum were better appreciated at the nuclear poles of interfascicular oligodendrocytes. In addition, the high mass density heterochromatin masses exhibited a continous interconnected trabecular system, the dark spaces corresponding to the euchromatin substance localization, which was also extracted during the freeze-fracture preparation procedure.

The freeze-fracture method for SEM offered new information on the three-dimensional structure of cytoplasmic and nuclear details of fractured oligodendrocytes. The transmission electron microscopy images of perineuronal, interfascicular, and perivascular oligodendroglial cells provide supporting evidence, by their localization, for the nursing role of oligodendrocytes on neuronal soma, myelinated axons and blood-brain barrier.

Acknowledgment: This research has been partially supported by a CONDES-LUZ subvention.

References

1. Castejón OJ: Low resolution scanning electron microscopy of cerebellar neurons and neuroglial cells of the granular layer. *Scan Electr Microsc* III, 1391–1400 (1984)
2. Bjartmar C, Hildebrand C, Loinder K: Morphological heterogeneity of rat oligodendrocytes: electron microscopic studies on serial sections. *Glia* 11, 235–244 (1994)
3. Castejón OJ, Castejón HV: Oligodendroglial cell behaviour in traumatic oedematous human cerebral cortex: a light and electron microscopic study. *Brain Injury* 14, 303–317 (2000)

The use of modified flatbed and film scanners for large specimen imaging

W. Y. CHENG, P.-C. CHENG*, M.-I. CHENG,†
D. B. WALDEN‡

Williamsville East High School, Williamsville; *Department of Electrical Engineering, University at Buffalo, Buffalo; †AMIL Technologies, Williamsville, NY 14221 USA; ‡Department of Plant Sciences, University of Western Ontario, London, Ontario, Canada

The limited field-of-view of the conventional compound microscope restricts the observation of organs and large pieces of tissue sections. This becomes a difficult task when both overall view and high-resolution study are required simultaneously. In the course of studying the development of maize stem, we encountered the need for digitizing large hand sections and mounted tissue slices on microscope slides for three-dimensional (3-D) reconstruction. Splicing a series of images that are taken at different positions to form a montage is not acceptable, because the jointed image suffers from mismatch due to lens distortion. Considering the resolution needed in our study, one alternative is to use consumer flatbed and film scanners designed for a personal computer. To adopt the conventional scanner for wet tissue scanning, an Acer 620T PC flatbed scanner (Taiwan, ROC), equipped with a trans-illuminator, was modified (Fig. 1a). This is because scanning wet specimens are placed in a glass tray; the additional thickness contributed from the bottom of the glass tray raised the sample, preventing proper focusing by the scanner. Therefore, the glass window of the scanner should be lowered accordingly to the thickness of the glass tray used. To do this modification, the glass window of the flat-bed scanner was first carefully removed, then a spacer (with the same thickness as the bottom glass of the specimen tray) was glued between the glass plate and the scanner body with silicon adhesive. It is important to use silicon adhesive to prevent spilled water from leaking into the scanner body. This modification placed the sample to the original focus of the scanner. A LEGO™ fence was added to prevent the transilluminator surface from being scratched by the tray. We have found it is much more convenient and productive to use a film scanner to image tissue slices mounted on standard microscope slides. We have employed a film scanner (Minolta DImage Scan Dual) for this job; the film cartage was modified to allow slide mounting and to ensure proper focusing of the tissue section (Fig. 1 b).

The modified Acer 620T PC scanner allowed us to scan an area (up to 18×13 cm) at a resolution of 21 μm/pixel (44 pixels/mm or 1200 dpi). Figure 1c shows an image of maize stem (*Zea mays, inbred Ohio 43*) obtained at 21 μm/pixel (44 pixels/mm) resolution. Individual cells can be easily identified. In contrast, the Minolta film scanner allowed us to scan an area (up to 24×36

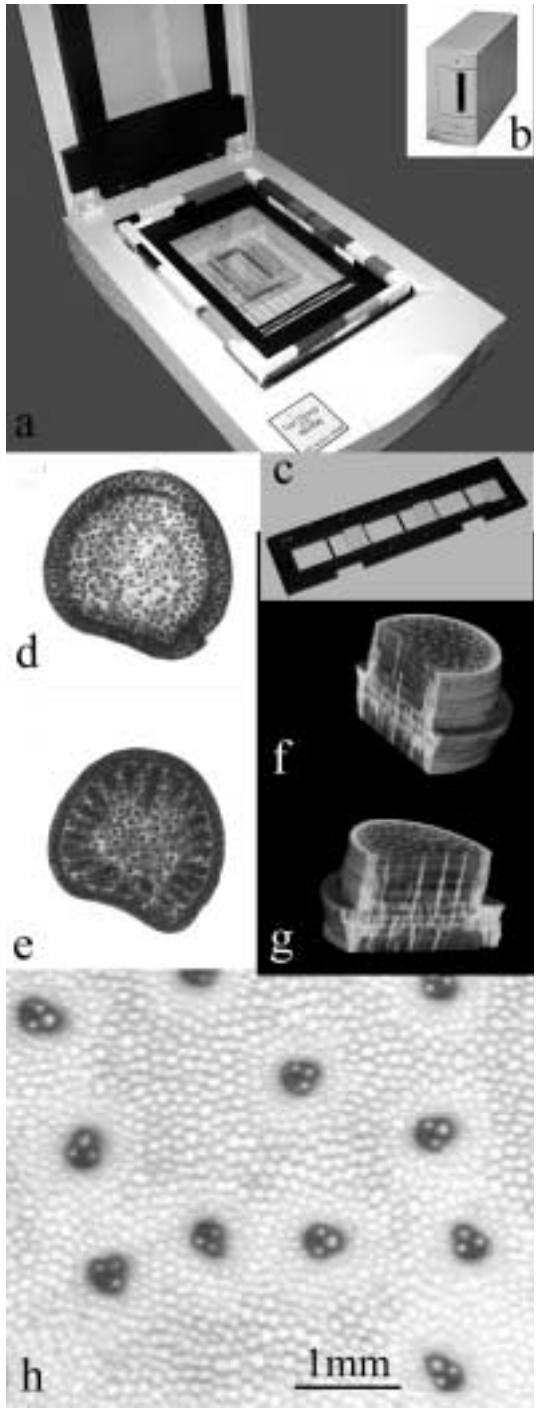

FIG. 1 (a) Modified Acer 620T PC flat bed scanner showing the LEGO fence and the wet specimen chamber. The glass window of the flat bed scanner is lowered to take up the additional thickness from the bottom of the specimen. (b and c): Minolta DImage film scanner. No modification to the scanner itself is required, however, the film holder should be modified to accommodate the microscope slide and ensure proper focus. (d and e): Hand sections of maize stem imaged by the flatbed scanner. (f and g): Three-dimensional reconstruction of the node region of maize stem from the data set obtained from flatbed scanner. (h): Zoom-in view of a maize stem showing vascular bundles and ground tissue. The image was obtained at 1200 dpi resolution on a flatbed scanner.

mm) at a resolution of 10 μm/pixel (95 pixels/mm or 2438 dpi). This resolution is high enough to hand most of the needs in macroscopy.

In conclusion, this article demonstrates the use of a low-cost flatbed and film scanner to achieve large area digitization for tissue and organ study. This technique can also be used in the imaging of electrophoresis gel commonly used in molecular biology.

Acknowledgments: This report is a portion of a summer research project of WYC from the Williamsville East High School.

The stem vasculature of *na1/na1* and *na2/na2* in *Zea mays*

W. Y. CHENG, P.-C. CHENG,* M. GU, X. GAN,†
D. B. WALDEN‡

Williamsville East High School, Williamsville, New York, USA; *M AMIL, Dept. of Electrical Engineering, University of Buffalo, NY USA; †Centre for Nano-Photonics, Swinburne University of Technology, Melbourne, Australia; ‡Dept. of Plant Sciences, Univ. of Western Ontario, London, Ontario, Canada

The stem development of two recessive dwarf mutants, nana-1 (*na1)* (Fig. 1) and nana-2 (*na2)* (Fig. 1b) of maize (*Zea mays* L.) were studied. All the plants used in this study were grown at the field station of University of Western Ontario, London, Ontario, Canada, in the summer of 2000. The specimens were harvested and fixed in methanol and/or EtOH/acetic acid (3:1), serially sectioned with a razor blade using a specially made jig. The hand sections were decolored in 70% iso-propanol for at least a month, then dehydrated in acetone and cleared in xylene. Digital images of individual hand sections were obtained before/after dehydration and clearing processes. Digital images were obtained by using a modified Acer 620T PC flatbed scanner in liquid (water or xylene).[1] The digital images obtained from hand sections were aligned by using a special issue of ImageAcquire™ software (Williamsville, N.Y.). After digitization, the hand-sections were infiltrated and embedded in JB-4 medium (Polysciences) for future reference. To achieve deep tissue imaging, optical sections were obtained by two-photon florescence microscopy using an Olympus Fluorview FL300 confocal microscope equipped with a Spectra-Physics Mai-Tai tunable ultra-fast Ti-sapphire laser. Excitation wavelengths was set at 780 nm NIR with a pulse width of 100 fs, <550 nm autofluorescence was detected. Extended focus views were generated by using AutoQuant's AutoVisualize-3D™ software.

Different from the parallel arranged longitudinal vascular bundles commonly found in the internodes of wild type[2] *na1/na1* has a complex stem vasculature (Fig. 1a).[3,4] However, cross-sectional view reveals that the vascular

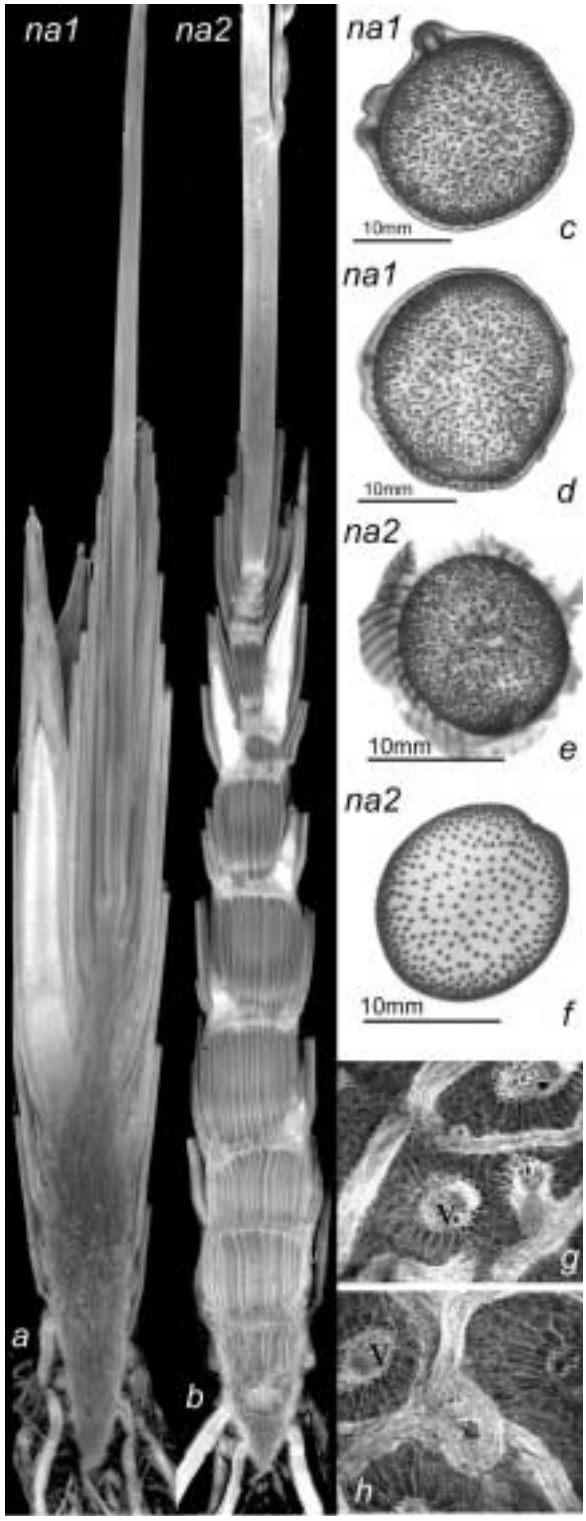

FIG. 1 (a) *Na1/na1* plant. The entire stem resembles to a single node. Note the lack of node-internode structure in the ear branch and the elongation of tassel nodes. (b) *Na2/na2* plant. Note the elongation of tassel nodes and insertion of ears. (c, d) Cross-sectional views of *na1/na1* stem. (e) Cross-sectional views of *na2/na2* node. (f) Cross-sectional views of *na2/na2* internode. (g, h) Extended focus views of *na1/na1* stem obtained by two-photon fluorescence microscopy. Note the branching of vertically arranged vascular bundle (v).

arrangements of the entire *na1/na1* stem (Fig. 1 c, d) resemble those found in the nodal region of normal plant. Therefore, one may consider that the entire *na1/na1* stem is made up of a single node. Similar to the main stem, the ear branch of *na1/na1* also lacks well-defined node-internode structure. It is important to point out that the *na1/na1* stem is composed of many interlinked vascular bundles. The branching of vertically arranged vascular bundle (v) is evident in the extended focus view (Fig. 1 g, h) obtained by multiphoton fluorescence microcopy. The complexity of the vascular bundle suggests that it may be impossible for elongation to occur because of the interlocking of the vascular bundle. The tassel internode, however, does elongate and consists of wild-type vasculature. Heterozygous *na1/+* develops stem vasculature similar to that of the wild type.

In contrast, *na2/na2* stem (Fig. 1 b) has a "normal" stem appearance, but the internode length is significantly shortened compared with that found in the wild type. The cross-sectional views of *na2/na2* stem (Fig. 1 e, f) reveal similar nodal (Fig. 1 e) and internodal (Fig. 1 f) vascular arrangements as found in the wild type. The elongation of tassel internodes occurs in *na2/na2* (Fig. 1 b). However, *na2/na2* has an interesting point in that the stem is frequently composed of slanted nodes instead of the normally found horizontal nodes in wild type. Heterozygous *na2/+* develops stem vasculature resembling that of the wild type.

References

1. Cheng WY, Cheng PC, Cheng MI, Walden DB: The use of modified flatbed and film scanners for large specimen imaging. *Scanning* (this Volume) (2001)
2. Cheng PC, Chen JH, Hwang SC, C Sun CK, Walden DB, Cheng WY: 3D reconstruction of *Zea mays* stem by MRI technology. *Scanning* (this volume) (2001b)
3. Cheng WY, Cheng PC, Walden DB: Abnormal node development in maize na1/na1 mutant – A confocal microscopy study. *Microsc Microanal* 6, 692–693 (2000)
4. Cheng WY, Cheng PC, Walden DB: The study of vascular development in the stem of *na1* mutant in maize by confocal microscopy. *Scanning*, 22 189–190 (2000)

Cosmetic assessment of the human hair by confocal microscopy

P. CORCUFF, G. DATY, G. MADRY, C. HADJUR

L' Oréal Recherche, Laboratoires de Recherche Avancée, Aulnay-sous-bois, France

Introduction

Confocal microscopy provides high resolution images with no out-of-focus areas and fits very well with non-planar surfaces like the cylinder shape of hair. For the past ten years, this technique has been successfully applied for non-invasive imaging of the surface as well as the internal structures of the hair.[1] Consequently it has been proposed as an alternative mode to the classic scanning electron microscopy observation. Preserving the integrity of the sample opens up a wide range of applications in cosmetic research including almost any kind of surface deposits and repeated chemical or physical treatments.

Materials and Methods

The confocal laser scanning microscope LSM 310 from Zeiss was equipped with two laser sources: He-Ne 540 nm and Ar-Kr 488/568/647 nm. Objective lenses were selected according to their performance in hair imaging: x20 and x50 dry, x40, and x63 oil immersion. The motorised stage (X,Y) was computer controlled for repositioning the sample automatically with a precision of 0.05 µm. A direct current motor having a run of 20 mm and a Z resolution of 50 nm assured fast focusing. Z-series of 80 optical sections separated by 1 µm steps provided either one in-focus projection image of the surface or a stack for volume rendering of the internal structures of the hair. Using the OTIP3D software (LISA labs, CPE Lyon), 3D reconstruction was possible. The confocal scanner had a two-channel configuration that permitted simultaneous imaging of reflected light and fluorescence contrast. Hair samples were simply attached to microscopic slides coated with double-sided adhesive tape. Internal structures of the hair shaft were imaged using oil immersion in order to attenuate the strong reflection generated by the index mismatch at the hair surface.

Results

Reflection images of the surface showed that untreated hair exhibited smooth borders of the cuticle cells whereas crenelated cuticle borders characterized hair fatigue. In advanced hair degradation, local absence of the cuticle revealed the cortex.

Reflection images with repositioning allowed to compare polymer deposits on the hair and the remanence of the polymer before and after shampooing.

The internal exploration of the hair structures can be performed on white hair labeled with Octadecyl Rhodamin. The reflection image revealed the medulla and nuclear remnants of the cortical cells. The fluorescence image showed the location of the probe into the medulla, in the cortex and delineating the border of cuticle cells.

Fluorescence images of hair treated with a polymer labeled with Rhodamin B showed that the polymer infiltrated the borders of the cuticle cells while the reflection signal demonstrated the absence of polymer on the surface of the cuticle.

Transversal optical sections allow follow-up of the penetration of fluorescent probes. Rhodamin B in water was absorbed by the cuticle and did not penetrate into the cortex. Octadecyl Rhodamin in EtOH/H2O (9:1) penetrated into the medulla.

The OTIP3D software allowed volume rendering of cuticle envelope and medulla channel on hair labeled with Octadecyl Rhodamin.

Summary of the Results

Confocal microscopy provides rapid, easy, elegant, and nondestructive observation of the hair in its natural environment.

Both the surface and the internal structures can be imaged without invasion providing longitudinal and transversal optical sections for volume rendering.

The condition of the hair surface can be evaluated according to the chemical or physical injuries sustained.

Surface deposits can be observed in terms of thickness, homogeneity, and brilliancy as well as their resistance to cosmetic treatments.

The routes of penetration of fluorochromes into the hair structures can be dynamically investigated.

Reference

1. Corcuff P, Gremillet P, Jourlin M, Duvault Y, Leroy F, Lévèque JL: 3D reconstruction of human hair by confocal microscopy. *J Soc Cosmet Chem* 44, 1–12 (1993)

Preparation of cultured cells for study of intracellular element concentrations by x-ray microanalysis using a scanning electron microscope

P.V. CRESPO, F. ARREBOLA,* S. ZABITI, F.J. CANIZARES, M.A. CUBERO, A. WARLEY,† E. FERNANDEZ-SEGURA, A. CAMPOS

Department of Cell Biology, School of Medicine, and *Institute of Neurosciences, University of Granada, Granada, Spain; †EM Unit, The Rayne Institute, St. Thomas' Hospital, London, UK

Cultured cells provide a model to study the composition, distribution, and transport of ions in defined physiologic states by electron probe x-ray microanalysis with electron microscopy. Different methods have been developed and various conditions have been used to grow and prepare cultured cells for x-ray microanalysis.[1-3] Two methods have predominantly been used to prepare cultured cells for x-ray microanalysis: (1) analysis at the subcellular level of freeze-dried ultrathin cryosections with scanning transmission electron microscopy (STEM) and (2) analysis at the cellular level of whole freeze-dried preparations with STEM and scanning electron microscopy (SEM). However, despite the usefulness of these methods, preparation of the cells for x-ray microanalsyis with SEM has some methodological problems. In spite of these limitations, it is evident that x-ray microanalysis of whole cultured cells with SEM provides a simple and very useful technique to determine total cell element levels. We present here two simple methods to prepare cultured cells for growth in monolayers and in suspension to analyze the elemental composition by x-ray microanalysis using SEM.

The MCF-7 (human breast cancer), LLC-PK_1 (pig kidney), U937 (human monoblastoid), and PC12 (rat pheochromocytoma) cell lines were used throughout this study. The cultures were maintained in DMEM and RPMI1640 supplemented with 10% fetal bovine serum (FBS) at 37ºC in a humid atmosphere containing 5% CO_2. To prepare MCF-7, LLC-PK_1, and PC12 cell lines, cells were subcultured at a density of 2.5×10^4 cells/ml in 12 mm polycarbonate tissue culture plate well inserts of 0.4 μm pore size (Millicell, Millipore, Bedford, Mass., USA) placed in 24-well tissue culture plates. Cells were cultured in DMEM supplemented with 10% FBS at 37ºC in 5% CO_2. After 24 to 48 h, polycarbonate membrane filters were cut from their cylindrical polystyrene holders. To prepare U937 cells grown in suspension, cells were transferred to polycarbonate tissue culture plate inserts placed in 15 ml conical centrifuge tubes, and the cells were centrifuged at 170 g for 3–5 min at room temperature. After centrifugation, the polycarbonate membranes were cut out as described above. Cells were then washed with ice-cold washing solutions for 5 s to remove the culture medium. After washing, cells were plunge frozen in liquid nitrogen and placed in a pre-cooled aluminum specimen holder at liquid nitrogen temperature. The specimen holder was then transferred to an Emitech K775 temperature-controlled freeze-drier (Emitech, Ashford, UK) and cells were freeze-dried under vacuum (<10 mbar) using a fast drying schedule. X-ray microanalysis was carried out using a Philips XL30 scanning electron microscope (Philips, Eindhoven, The Netherlands) equipped with an EDAX energy-dispersive detector. To optimize the x-ray signal collection, we used a range of accelerating voltages between 10 and 20 kV. All spectra were collected in the spot mode at 10,000× magnification for 200 s live time, and only one spectrum was acquired from each cell. Spectra were processed, and quantitative data were derived by the peak-to-local-background (P/B) ratio method.[4] The system was calibrated against standards made from known amounts of inorganic salts dissolved in 20% dextran.

We report two simple methods for cultured cells growing in monolayers or in suspension for measurement of elemental composition by x-ray microanalysis with SEM. These methods have several advantages over previously published methods: the substrates are available commercially, no special equipment needs to be built, the samples can be handled easily, and parallel experiments can be done under identical conditions. In addition, these methods make it possible to prepare cryosections of samples simultaneously for STEM.

Acknowledgments: Supported by Fundación San Francisco Javier y Santa Candida 98/1P02.

References

1. James-Kracke MR, Sloane BF, Shuman H, Karp R, Somlyo AP: Electron probe analysis of cultured vascular smooth muscle. *J Cell Physiol*, 103, 313–322 (1980)
2. Abraham EH, Brewslow JL, Epstein J, Chang-Sing, P, Lechene C: Preparation of individual human diploid fibroblats and study of ion transport. *Am J Physiol*, 248, C154–C164 (1985)
3. Warley A, Cracknell KPB, Cammish HB, Twort CHC, Ward JPT, Hirst SJ: Preparation of cultured airway smooth muscle for study of intracellular element concentrations by X-ray microanalysis: comparisons of whole cells with cryosections. *J Microsc*, 175, 143–153 (1994)
4. Boekestein A, Thiel F, Stols ALH, Bouw E, Stadhouders AM: Surface roughness and the use of a peak to background ratio in the x-ray microanalysis of bio-organic bulk specimens. *J Microsc*, 134, 327–333 (1984)

Candy anatomy: A microstructural survey of aerated confections

N. R. DECKER AND G. R. ZIEGLER

Penn State University, University Park, PA, USA

Many of the confectionery products we consume on a daily basis include an ingredient not listed on the label—air. Air has long been recognized as an essential component of foods such as beer, bread, and ice cream,[1] and considerable microstructural analysis has been carried out to characterize air cell size, bubble size distribution, and extent of aeration in these products. While there are a few published examinations of the microstructure of such confections as toffee, hard candies, chocolate, and caramel, very little work has been conducted on aerated products. Kaletunc *et al.*[2] investigated marshmallow compressibility and elasticity, but did not include microstructural analysis. Air cell size, shape, and size distribution are all important parameters when producing quality aerated confections.

To better understand the structure of aerated confections, an examination of a wide variety of commercial products was undertaken. Six aerated confectionery products were purchased from a local supermarket. These included starlight mints, butter cream mints, circus peanuts, jet-puffed marshmallows, taffy, and a chocolate-covered nougat bar. The samples were frozen, fractured, and freeze-dried to stabilize the internal structure. They were then examined using scanning electron microscopy (SEM). A seventh sample, an ungrained flavored nougat stick, was obtained from industry and viewed using cryostage SEM. Images obtained were subjected to analysis by eye and by an image analysis program. Differences in air cell size, shape, and distribution were observed. Grained and ungrained products were easily distinguishable by the presence of sugar crystals in the matrix. From this survey, a general understanding of the microstructure of aerated confections as well as sample preparation methods was obtained.

References

1. Campbell GM, Mougeot E: Creation and characterization of aerated food products. *Trends Food Sci Technol* 10, 283–296 (1999)
2. Kaletunc G, Normand MD, Johnson EA, Peleg M: Instrumental determination of elasticity of marshmallow. *J Texture Studies* 23, 47–56 (1991)

Cytochemical assessment of succinic dehydrogenase activity by computer-assisted stereology in nerve and muscle cells during aging

P. FATTORETTI, C. BERTONI-FREDDARI, N. GRACCIOTTI, T. CASOLI, G. DI STEFANO, M. SOLAZZI, G. FELZANI,* J. VECCHIET*

Neurobiology of Aging Centre, "N Masera" Research Department, Ancona; and *Department of Internal Medicine and Aging, University "G. D'Annunzio," Chieti, Italy

An impaired mitochondrial capacity to provide adequate amounts of adenosine triphosphate in due time has been reported to constitute an adverse condition predisposing to organ and system dysfunction.[1] With advancing age, this metabolic decay may be particularly critical in nerve and muscle cells which are characterised by frequent bursts of high energy requests. As a constitutive molecule of the respiratory chain (complex II), succinic dehydrogenase (SDH) plays a key role in cellular bioenergetics at maximum respiration rates and is reported to be a sensitive indicator of mitochondrial oxidative metabolic capacity.[1] To test the effect of age on cellular bioenergetics, we carried out a computer-assisted morphometric study on mitochondria cytochemically stained for SDH activity in Purkinje cells of 3, 12, and 24 month-old rats and in bioptic muscle samples from young (25.0 ± 4.4 years), middle-aged (50.4 ± 7.5 years), and old (75.5 ± 3.9 years) human beings.

SDH activity was preferentially evidenced by the copper-ferrocyanide method.[2] Freshly excised rat cerebellar slices and human bioptic muscle samples were incubated for 45 min. at 37°C.[3] Control samples were processed as above in a substrate-free incubation solution. In rat Purkinje cells, SDH-positive mitochondria were systematically and randomly sampled: 1 slice was chosen with a fixed periodicity of 10 (currently denoted as section separation = 10). The ultrastructural features of the positive mitochondria (Fig. 1) were acquired by a TV camera and analysed by a computer-assisted image analyser. The number of organelles/mm^3 of Purkinje cell cytoplasm (Numeric density: Nv), the average mitochondrial volume (V) and the mitochondrial volume fraction (Volume density: Vv) were measured. Nv was significantly higher at 12 than at 3 and 24 months of age. V was significantly decreased in adult and old rats, but was the same at 12 and 24 months of age. Vv was significantly decreased in old animals versus the other groups. In bioptic samples from human muscles, to get information on

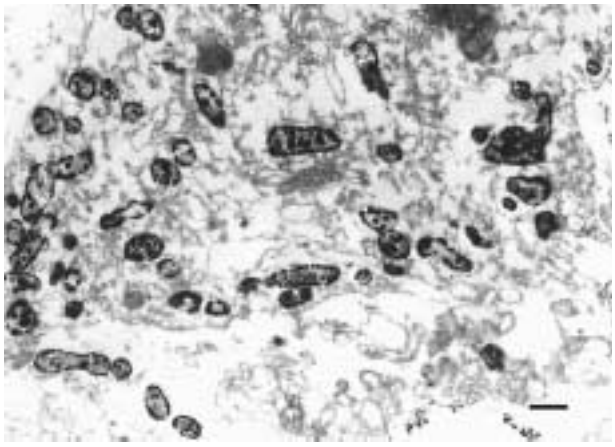

FIG. 1 SDH-positive mitochondria in a rat Purkinje cell: the electron opaque, insoluble copper ferrocyanide precipitates are trapped within the mitochondria at the inner membrane of the organelles. Bar= 0.5 μm.

the mitochondrial metabolic competence versus the organelle's size, we calculated the ratio (R): overall area of the SDH precipitates/area of each mitochondrion. Despite an 8% increase of R in adult versus young and old groups, no significant difference was found among the three groups of age.

These data document that SDH activity can be cytochemically shown and morphometrically evaluated as sharp copper-ferrocyanide precipitates both in nerve and muscle cells. The ferricyanide used to visualise SDH activity readily accepts electrons from the respiratory chain and is reduced to ferrocyanide which is captured by copper at the site of enzyme activity. In addition to these reactions, SDH is a flavoprotein able to react directly with ferricyanide. Conceivably, the copper-ferrocyanide procedure can be regarded as a reliable method for quantitative studies of both SDH activity and the efficiency in energy production by the Krebs cycle. Morphometric quantitation of the precipitates as a results of SDH activity is of reliable scientific relevance since the molecules of this enzyme are located at the inner mitochondrial membrane, thus offering the possibility to map the metabolic competence of discrete populations of organelles in different experimental models. With specific reference to the present study, we interpret our findings to denote age-related rearrangements of the mitochondrial morphofunctional features.

References

1. Beal MF, Hyman BT, Koroshetz W: Do defects in mitochondrial energy metabolism underlie the pathology of neurodegenerative diseases? *Trends Neurosci*. 16, 125–131 (1993)
2. Kerpel-Fronius S, Hajos F: The use of ferricyanide for the light and electron microscopic demonstration of succinic dehydrogenase activity. *Histochemie* 14, 343–351 (1968)
3. Fattoretti P, Bertoni-Freddari C, Caselli U, Paoloni R, Casoli T: Quantitative cytochemistry of succinic dehydrogenase activity in rat mitochondria. *Analytical Quantitative Cytology and Histology* 6 (20), 521–525 (1998)

X-Ray microanalysis of frustules from edaphic diatoms

M. GANGER, S.J. KOEPP, J. M. MCCORMICK

Montclair State University, Montclair, NJ, USA

Silicon dioxide (SiO.nH20) contained within diatom frustules (skeleta) forms an intricate structural framework that allows the cell to become stronger but allows the continued exchange of gases, nutrients and metabolites between the cell and its surrounding environment. A number of authors have previously reported a variety of elemental contaminants contained within the frustule of diatoms. On that premise, diatoms were collected from three distinctly different aquatic habitats in Northern New Jersey, USA. These three locations were Sandy Hook Bay near the mouth of the Hudson-Raritan estuary, an intertidal beach in Bayonne, New Jersey on Newark Bay representing an estuarine environment, and from small submerged rocks in a creek confluent to the Passaic River representing a fresh water habitat.

The samples from each area were collected, cleaned with hot HCl to which a small amount of potassium dichromate was added, subsequently dried onto millipore filter paper (.45 μm) and mounted on carbon SEM stubs. Each sample was first coated with gold/palladium to accentuate signal production for high resolution photography and related identification of species. X-ray microanalysis was carried out on each of the samples using a Hitachi 2460N SEM coupled with a Princeton Gamma Tech (PGT) IMIX analysis system (software version 8.12B). Since detection of trace elements was the goal of this detection sequence, reference spectra were obtained for the following: a carbon stub with clean filter paper, coated with gold/palladium and a separate spectrum for silicon dioxide collected from a silica reference. These particular spectra were obtained and classified as known constituents of the frustules and therefore not required for spectral analysis. Subsequently a fresh reference spectra was obtained and the two above mentioned spectra overlaid and subtracted out to produce a final spectrum that contained the elements contained within the frustule, ruling out the possibility of masking elements that could possibly have energy overlaps to known contaminants (i.e. silica dioxide).

Analysis of frustules revealed significant contamination of some of the siliceous frustules with strontium and other elements such as rubidium, tungsten, and aluminum. The non-siliceous elements observed appear to be incorporated as an integral part of the frustule, but it is possible that they are adhering to the frustule surface. The source and form of the contamination, however, was not determined and was not a subsequent focal point of this study.

The overplus phenomenon of *Gloeocapsa alpicola* and heavy metal uptake

J.J. GOLDBERG, T.E. JENSEN, M.J. BAXTER

Department of Biological Sciences, Lehman College, Bronx, and The CUNY Graduate Center, New York, New York, USA

It has been previously shown by Jensen *et al.*[1], and others that microbial polyphosphate bodies are the main sites for metal sequestration. In our present study we have exposed cells of *Gloeocapsa alpicola*, grown to log phase and to overplus phase, to 20 PPM of seven different heavy metals. Cells of *Gloeocapsa alpicola* were grown in modified Fitzgerald's media and harvested after a logarithmic growth phase of 14 days. The overplus cells were grown, as has been previously described.[2] The heavy metals included Al, Cu, Mn, Ni, Pb, Zn, Cd (5PPM), and a control. Cells were either placed on formvar coated grids or embedded in Epon according to Luft's procedure. Cells were analyzed using the scanning transmission electron microscopy mode of a transmission electron microscope in conjunction with a PGT IMIX energy dispersive x-ray spectrometer. The data were then analyzed using the bulk sample analysis program (ZAF method) in standardless mode (w/w) based on the Hall continuum theory.[3] Approximately 60 cells were analyzed; we looked at the capsule, cell wall, cytoplasm, and PPB, and the averages of the elements were calculated. The volume of the cell was then determined by using the formula for calculating the volume of a cylinder, that is, $V=\pi r^2 h$, and the volume was obtained using $V=4/3\pi r^3$ for a spherical body. All calculations were done at the same magnification of 40,000×.[2] The volumes of the various components were calculated. The quantitative analysis of the cells revealed that cells exposed to Al showed a capsule containing 0%, the wall contained 3.04%, the cytoplasm contained 2.89%, and the PPB contained 6.24%. Cells exposed to Cu showed a capsule containing 0.23%, the wall contained 2.33% the cytoplasm contained 4.65%, and the PPB contained 7.40%. Mn showed up as 0.053% in the capsule, the wall contained 2.00%, the cytoplasm contained 3.65%, and the PPB contained 5.78%. Upon analyzing Ni we found a capsule containing 0%, wall 2.30%, cytoplasm 4.89%, and the PPB contained 5.53%. Cells that were exposed to Pb showed a capsule containing 1.69%, a wall containing 2.84%, the cytoplasm had 6.00% and the PPB contained 8.93%. The Zn exposed cells had 0.66% in the capsule, the wall 6.62%, the cytoplasm 8.99% and the PPB contained 19.04%. The cells exposed to 5 PPM of Cd, contained 6.00% in the capsule, the wall had 8.56%, the cytoplasm had 5.51%, and the PPB had 18.40%. These results brought us to the conclusion that even though the cell on a whole has more volume than the polyphosphate bodies the polyphosphate bodies, will bio concentrate more of the metal then a rest of the cell.[2] The analysis of the overplus cells further supports this; since the PPBs are larger and more numerous, they occupy a greater volume of the cell. These data would indicate that *Gloeocapsa alpicola* sequester metals differentially, and that different metals are also sequestered differentially in the different cell components.

References:

1. Jensen T, Baxter M, Rachlin JW, Jani V: Uptake of heavy metals by *Plectonema boryanum* (*Cyanophyceae*) into cellular components, especially polyphosphate bodies: An x-ray energy dispersive study. *Environ Pollutants (series A),* 27, 119–127 (1982)
2. Baxter MJ, Jensen TE: Cell volume occupied by polyphosphate bodies during the polyphosphate overplus phenemenon in *Plectonema boryanum*. *Cytobios* 45, 147–159 (1986)
3. Hall TA: Quantitative electron probe x-ray microanalysis in biology. *Scanning Microsc* 3,461–466 (1986)

Examination of nonwoven textiles using scanning electron microscopy

W. R. GOYNES, D.V. PARIKH

USDA, ARS, Southern Regional Research Center, New Orleans, LA, USA

Typical commercial textile fabrics are produced from yarns using either weaving or knitting processes. Other types of textiles known as "nonwovens" are mats formed by processes such as needle punching, hydro-entanglement, chemical bonding, or heat-setting. These products are becoming commercially important for use in disposable products such as hygiene and medical supplies, as well as in furniture and carpet backings. Development of these products requires better understanding of production processes, and of the interaction of different kinds of fibers within the product.

Evaluation of effects of variations in processing and of fiber content on structures of these materials can be accomplished using microscopic procedures. Scanning electron microscopy (SEM) allows study of fiber interactions and bonding processes to show changes on fabric surfaces as well as on internal regions. Fabrics in this microscopic study included (1) a high-loft perpendicular-laid fabric made of cotton, polyester, and bicomponent bonding fibers, (2) fabrics incorporating short cotton linters, (3) insulating fabrics blended of recycled polyester fibers and cotton.

Cotton fibers can contribute desirable properties of softness and absorbency to these products. However, incorporating cotton into nonwovens can require novel approaches. The nonwovens market is highly oriented to synthetic fibers and some current methods for producing nonwovens depend on fiber fusibility and require fiber lengths that can only be provided by synthetic or high quality cotton fibers. Because most nonwoven materials are intended for markets of low-cost products, use of premium cotton fibers should be avoided where possible. Lower quality cotton fibers or linters can provide many of the same property benefits to

nonwoven goods as do premium fibers. Devising ways to incorporate low-grade, waste cotton fibers or linters into blended cotton/synthetic products is a challenge. Linters are short fuzz fibers that undercoat the lint on the cotton seed surface and remain on the seed after ginning lint fibers. The average length of these sheared fibers is 5 mm. They are difficult to separate into individual units and usually remain clumped in small bundles. Blending with longer fibers is difficult. Use of fusible synthetic fibers is one means of incorporating cotton linters into nonwovens. Fused fibers can attach to the short linter bundles, immobilizing them within the fabric structure. Webs of fused synthetic fibers can also be used to form networks that entrap the linter bundles to prevent movement. The added body provided to the material by the linter bundles produces nonwoven sheets usable as padding or fillers. Novel methods of folding and heat-setting the nonwoven sheets can provide thick, resilient cushioning materials. Examination of these blended products by SEM shows extent of blending of component fibers. The nature and number of the bonds formed by the fused fibers are also evident.

Cotton fibers can also be blended with recycled polyester fibers to form nonwoven products that are thermally insulative. Waste polyester fibers and cotton fibers that required no chemical processing were used to produce a low-cost, semidurable nonwoven product. Materials used were 60% reprocessed polyester and 40% greige cotton. These products were tested for use as thermal blankets, intended for short-term uses as in medical or military facilities, and in disaster relief centers. They were structured to be durable through limited launderings. Fabrics were given a carboxylic acid finish to improve structural stability during use and laundering. The finish greatly reduced surface matting of loose fibers. These blanket material were light-weight, had a good hand, and exhibited excellent thermal and comfort qualities. Scanning electron microscopy showed that fiber tangles formed during laundering of unfinished materials were not formed when chemically finished fabrics were laundered.

Light and scanning electron microscopy of these novel nonwoven materials indicated the necessity of incorporating short fiber bundles within the fiber networks in order to obtain maximum utility of properties of the blended fibers. Dyeing techniques also showed locations and functions of various types of fibers within the products.

Spatial distribution of acidulants and humectants in model food by confocal laser scanning microscope fluorescent detection

LINNEA M. HALLBERG, IRWIN A. TAUB

U.S. Army, Soldier and Biological Chemical Command, Natick, MA, USA

Our previous study used a confocal laser scanning microscope (CLSM) to track moisture migration to map distributions in a mixed moisture bilayered system. This study extends that capability to pH distributions in the matrix. In food, it is crucial to ensure that regions of high water activity (A_w) and neutral pH are avoided in order to achieve microbiological stability. The resulting pH and mositure maps are relevant to future efforts to model pathogen growth potential. The main objective of this study is to map the non-homogeneous distribution of pH and moisture in model food matrices by monitoring the fluorescence of dyes with a CLSM, and to determine the factors that promote or prevent the dispersion of the associated acidulants and humectants. Model matrices os whey gels were formulated with varying amounts of acidulants (glucono delta lactone) and huectants (glycerol), and measured globally and locally for pH, and A_w. Model matrices were made in ways that create a dispersion in the distribution of components so that there will be microscopic regions in which their concentrations differ, thus affecting localized chemical and microbial stability. An apporpriate dye with selected pK values near 5.5 was added. The dye distributes among these regions until thermodynamic equilibrium is achieved and they dissociate to a lesser or greater extent depending on pH.

The scanning was performed with a real-time, slit-scanning, upright confocal microscope using an air-coooled Argon laser to excite a rhodol dye (DM-NERF Moleculare Probes) at 488 nm. A charge-coupled device, and band pass filters (530/30 and 580/30 nm) were used to detect the emission from either the basic or acid form of the dye. A series of optical sections (25 μ apart) were auto-collected by a computer controlled z-drive. These sections provided two-dimensional and constructed three-dimensional images. The ratio of basic-to-acid emission intensities were converted into a local pH value, and the total emission intensity from a local region was associated with the local moisture level. The maps of the intensities obtained were drawn to represent microscopic regions of differeing pH and/or moisture content. These maps, and the influence of level of added components on them, can be used to determine if all regions conform in A_w and pH for the conditions of "no growth" that have been established for food safety.

A scanning electron microscopy study of needle-shaped processes of Japanese rice hulls and microscopic crystal-like substances in the lung

T. HOJO

Institute of Anatomy & Anthropology, Kitakynshu City, Japan

Needle-shaped processes of Japanese rice hulls are scattered and floating in the air of the rice farmers' houses. These needle-shaped processes may be mixed in the dust, and may have some effects on their lungs, eyes, and other organs of their bodies. The features of the needle-shaped

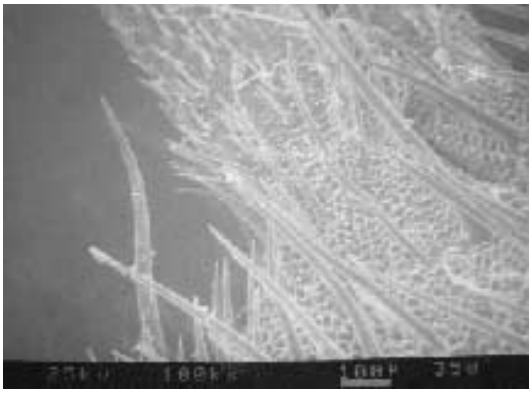

FIG. 1 An SEM micrograph of the needle-shaped processes of Japanese unhulled rice. Bar = 100 microns.

FIG. 2 Some crystal-like substances in the human alveoli. Bar = 3.3 microns.

processes of two kinds of Japanese unhulled rice, Oryza sativa, were examined using an SEM[1] (Fig. 1).

The figures were taken using an SEM with a digital camera, and analysed.

The basal parts of the hulls showed fewer needle-shaped processes than those of the upper part of the hulls. These processes were cylindrical in the shafts and had needle-shaped points. The shapes of the processes were compared with those of fibers and crystals in the alveoli of the lungs. The results of the SEM probe showed the shapes of the needle-shaped processes were different from those of the fibers and the crystals in the alveoli.

The SEM of the alveoli made from the lung cast showed some kinds of fibers and other artificial substances[2] (Fig. 2). The crystal-like substances were different from the processes of the rice hulls. These results show that SEM studies are useful for probing fine substances.

References

1. Hojo T: Scanning electron microscopic study of the needle-shaped processes on two kinds of Japanese unhulled rice. *Igaku Kenkyu* 61, 63–65 (1991)
2. Hojo T: Scanning electron microscopy of styrene-methylethylketone casts of the airway and the arterial system of the lung. *Scan Microsc*, 7, 287–293 (1993)

New observations of human chromosome scanning electron microscopy and transmission electron microscopy

E.C. JENKINS, JR., G.Y. WEN, M. GENOVESE, E.C JENKINS, W.T. BROWN

New York State Institute for Basic Research in Developmental Disabilities, Staten Island, NY, USA

Introduction

Two new observations have been made on human chromosome ultrastructure using both Chromosome Scanning Electron Microscopy (SEM) and Transmission Electron Microscopy (TEM). A bipartite, apparently half-chromatid-like structure was observed when whole human chromosomes were studied with SEM and when longitudinally sectioned chromosomes were analyzed with TEM. In addition, we also observed a zipper-like configuration as the parallel sister chromatids separated likely due to the supercoiled structure of the chromosome and chromatid.

Methods

Human chromosomes in metaphase were obtained from short-term whole blood cultures from an anonymous individual previously determined to have an apparently normal male karyotype of 46 XY. Cell cultures were processed according to standard methodology for chromosome preparation including hypotonic solution and colcemid treatment. However, the cells were not allowed to air-dry[1] but were mounted with a coverslip in pH 7.0 phosphate buffer.

Chromosome preparations were prepared for SEM by post-fixation according to a modification of a previously published protocol[2]. Our modification calls for prefiltering all solutions with a 0.22 :m Millipore filter. The chromosome preparations were then gold-coated and studied with an ISI-SS40 SEM. For TEM, the chromosomes were prepared as already described except they had to be removed from the glass slides using our "repeat chill" protocol[3] so that whole chromosomes could be serially sectioned longitudinally, including the entire metaphase, and examined by an Hitachi 7,000 TEM.

Half-Chromatid Structure

Scanning electron microscopy studies revealed that the chromatid is bipartite longitudinally. We have been calling that structure a "half-chromatid." In an analysis of 12 cells in metaphase, all exhibited a majority of chromosomes with half-chromatids. Since all the cells were not complete due to protocol-related limitations, such as unseen chromosomes blocked by the grid window bars in TEM, the total number of chromosomes were analyzed such that 268 of 290 or 92.4% of the chromosomes exhibited this half-chromatid structure. For TEM, this half-chromatid structure

was also visible. Among 5 cells analyzed, all exhibited chromosomes with this half-chromatid structure. Of 75 chromosomes studied, 39 or 52% showed the half-chromatid structure.

Zipper-Like Configuration of Sister Chromatid Borders

Additional studies revealed that sister chromatids separated from each other symmetrically indicated by the configuration of their parallel inner borders. That is, the sister chromatids would separate similar to coming apart like pieces of a puzzle or a zipper opening. This was observed in all of nine cells studied with SEM. Among 91 chromosomes studied 48 or 52.7% exhibited this observation, while five cells examined by TEM also had this configuration among 49 of 74 or 66.2% of chromosomes analyzed.

Conclusions / Discussion

We have demonstrated ultrastructurally that chromatids exhibit a longitudinal bipartite structure that we are terming "half-chromatid." And, we have also shown that symmetrical sister chromatid separation is indicated by parallel configurations that resemble a puzzle separating or a zipper opening. Our images show this and also show a coil-like structure, as expected, along the longitudinal axes of both SEM and TEM chromatid preparations that likely account for the configuration along the inner longitudinal borders of the chromatids. This study was funded in part by a grant from the Aluminum Association, and in-part by the New York State Office of Mental Retardation and Developmental Disabilities.

References

1. Wen GY, Jenkins EC, Goldberg EM, Genovese M, Brown WT, Wisniewski HM: Ultrastructure of the fragile X chromosome: New observations on the fragile site. *Am J Med Genet* 1999, 83, 4, 331–33 (1999)
2. Sanchez-Sweatman OH, de Harven EP, Dube ID: Human chromosomes: Evaluation of processing techniques for scanning electron microscopy. *Scan Microsc* 1993, 7, 97–106 (1999)
3. Wen GY, Jenkins EC, Yao X-L, Yoon D, Brown WT, Wisniewski HM: Transmission electron microscopy of chromosomes by longitudinal section preparation: Application to fragile X chromosome analysis. *Am J Med Genet*, 68, 445–449 (1997)

A complex method for reconstruction of specimen image using a backscattered electron signal

D. KACZMAREK, A. MULAK, J. DOMARADZKI

Institute of Microsystem Technology, Wroclaw University of Technology, Poland

Introduction

The methods of shape forming shading, shaped from stereo[1] and Monte Carlo[2] are the most frequently applied for reconstruction of three-dimensional (3-D) image of real surface topography in scanning electron microscopy (SEM).

The development of multiple detector systems for backscattered electron (BSE) signal detection and the methods of digital processing of the signals have enabled reconstruction of the third dimension on the basis of two-dimensional SEM images.

The method shape from shading consists of application of at least two pairs of detectors situated perpendicularly to each other (detectors D1, D2 and D3, D4). The third dimension is calculated either by iteration or by Monte Carlo[2] method. Simultaneous presentation of 3D sample topography and composition is also possible.[3]

Method

The proposed method of 3D reconstruction of surface image in SEM is based on the measurements of BSE currents sensed by four detectors (D1÷D4) versus the inclination angle δ of Au sample with specially prepared smooth surface ($I_{BSE}=f(\delta)$characteristic).The measurements were done after accurate alignment of electron beam at every point of the surface. Semiconductor detectors were placed at medium angles (~60°) with respect to the specimen surface. The normalised signals (Tx, Ty) versus the angle of δ, where: Tx=(D2-D1)/(D1+D2) and Ty=(D4–D3)/(D3+D4), were strictly connected to the inclination of the elementary section of the surface in the x and y direction, respectively. The experimental characteristics $T=F(\delta)$ were then transformed into the characteristics $tg\delta=f(T)$ and approximated with 8-th order polynomial (Fig. 1).

The knowledge of tangent δ value enables us to reconstruct the inclination of the surface in relation to D1 and D2 detectors in x-z plane and D3 and D4 detectors with relation to the y-z one. The reconstruction of specimen surface is made for each of the detector pairs separately, starting from point x=0 (y=0); z=0. Fig. 2 presents the microscopic image of a specimen in TOPO mode and the image after 3-D reconstruction.

The simultaneous presentation of TOPO and COMPO modes has been named as a complex method. It consists of an application of colour simulations for indicating particular values of atomic numbers Z of the elements occurring on the specimen surface. The digital simulation of the

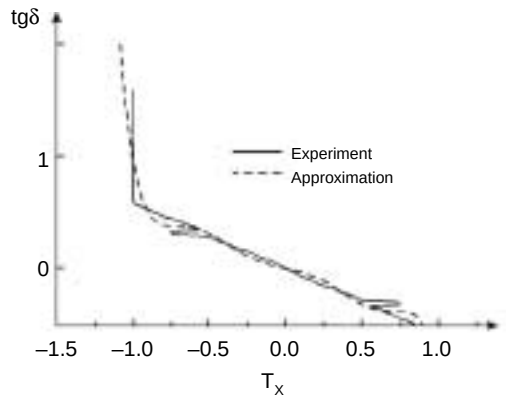

FIG. 1 Experimental and theoretical dependencies tgδ=f(T) (in the case of D1, D2 detector pair aligned along y axis).

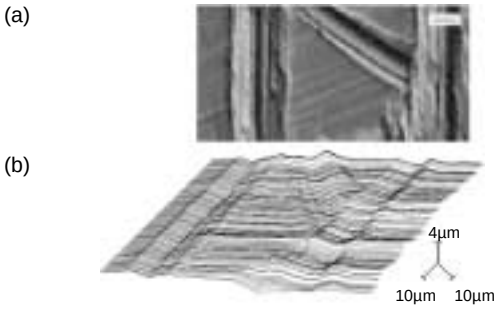

FIG. 2 The image of scratched tantalum surface. (a) microscopic in TOPO mode (bar = 23 μm). (b) Three-dimensional reconstruction.

colours was done after application of the method of linearization of backscattered electron characteristics versus Z^2. Below, the single stages of the complex method have been presented:

1. Recording of microscopic images in the form of digital bitmap[4]
2. Typical separation of TOPO and COMPO modes[3]
3. Correction of TOPO and COMPO modes based on theoretical analysis[5]
4. Linearization of backscattered electron characteristics[2]
5. Simulation of colours for specimen composition analysis
6. Three-dimensional reconstruction of surface topography image
7. Setting up a colour bitmap showing material composition and profile of 3-D surface

Conclusions

The proposed method can be used both for correct 3D reconstruction of surface topography and evaluation of its composition. The method is competitive to the other ones because it enables the reconstruction of 3D surface within the angles of inclination of a surface section of up to 60°.

References

1. Beil W, Carlsen IC: Surface reconstruction from stereoscopy and "shape from shading" in SEM images, *Machine Vision and Applications*, 4, 271– 285 (1991)
2. Radzimski ZJ, BSE image simulation in scanning electron microscopy, *J Computer–Assisted Microscopy*, 6, 4, 149–165 (1994)
3. Wassink DA, Raski JZ, Levitt JA, Hildreth D, Ludema KC, Surface topographical and compositional characterisation using backscattered electron methods, Scanning Microscopy, 5, 4, 919–926 (1991)
4. Kaczmarek D, The method of increasing COMPO contrast by linearization of backscattering characteristic $\eta = f(Z)$, *Scanning*, 19, No. 4, 310–315 (1997)
5. Kaczmarek D, Theoretical analysis of SE and BSE signals applied to SEM multiple detector systems, *Opt Appl*, 27, 3, 161–171 (1997)

Secondary electron image profiles using the bias voltage technique in deep contact hole

Y.-U. KO,[*] D.C. JOY,[*†] N. SULLIVAN[‡]

[*]EM Facility, University of Tennessee, Knoxville, TN; [†]Div. HTML, Oak Ridge National Laboratory, Oak Ridge, TN; [‡]Schlumberger, Concord, MA, USA

As the size of semiconductor devices shrinks the cost of wafer fabrication increase and it becomes more important to use non-destructive techniques to monitor all aspects of production. Though current critical dimension (CD) metrology tools can give reliable, in-line measurement of lines, spaces, pitches, and contact holes, information on side-wall angle or resist profile is needed for quality control, which is a time consuming and tedious process. It is also important to determine if the deep contact hole is open or closed by analyzing the scanning electron microscopy (SEM) signal collected from the bottom of the contact. To enhance this bottom image, the technique of applying high bias voltage between objective lens and sample ground has been developed. But the mechanism of the extraction of secondary electrons (SEs) from the bottom is not clear and it is necessary to know the degree of improvement quantitatively using this technique. In this work, we have used Monte Carlo simulations for modeling the charging phenomena and for calculation of the resultant SE beam profile in contact hole. Firstly we calculate the spatial distribution of charges when e-beams are incident onto the sample. A potential results because positive and negative charges are placed in different areas and currents flow as a result of EBIC and therefore the potential is decreased. We can then calculate the ejected SE trajectories from this potential distribution. We quantitatively compute image

profiles errors in various operating conditions and dimensions of contact hole. We have used etched oxide/Si and UV5/AR/Si as pattern material and the substrate. We have calculated and observed brightness of deep contact hole for the changing of operating conditions such as landing energy and current and also time sensitivity. To enhance the brightness of the bottom we have used pre-dose processing under low magnification. The positive charging around the hole makes high extracted fields that can escape the emitted SE from the bottom without collision against the wall. The results show that the brightness of bottom image is higher as current and yield are increased. As time has passed the brightness is increased until saturated and then decreased because of dominant positive charging around the hole and finally fades out. But this result shows we can observe the bottom of contact hole within certain limit of time. The effect from high yield is most influential and the time is shortest to reach the saturation point.

AFM studies of fracture surfaces of composition B energetic materials

Y. D. LANZEROTTI

U. S. Army ARDEC, Picatinny Arsenal, NJ, USA

Scanning electron microscopy (SEM) studies of the fracture surface of Composition B (59% cyclotrimethylene (RDX), 40% TNT, and 1% wax) has revealed the characteristics of the RDX fracture surfaces.[3] However, attempts using SEM to view the fine surface detail of TNT were unsuccessful.[3] Although the original work was carried out some time ago, the characteristics of TNT crystals remain a subject of investigation in melt-cast TNT formulations that are filled with a large percentage of RDX. In this paper, the characteristics of TNT crystals in Composition B at the fracture surface using atomic force microscopy (AFM) are presented.

The size of the TNT crystals has been determined by analyzing the surface structure that is exhibited after mechanical failure of the Composition B. The sample of melt-cast Composition B used for the AFM studies fractured[2] at 46 K*g* in an ultracentrifuge at 25°C. Atomic force microscopy examination of the topography of the fracture surface of the Composition B reveals fracture across columnar grains of the TNT. The AFM scan sizes were increased in steps from 2 to 13.6 μm with the maximum scan size ultimately limited by the curvature of the fracture surface.

The measured width and height of the TNT columnar grains are given as a function of the AFM scan sizes in table I. The compiled data in table I show that the width of the columnar TNT grains range from ~ 1 to ~ 2 μm. The height of the columnar TNT grains range in size from ~ 50 to ~ 300 nm. To the best of our knowledge, values of these quantities for TNT in Composition B have not been reported before (and were said to be unsuccessful).[3]

The microstructure of the matrix of TNT is normally one of highly oriented columnar grains.[1] Therefore, the results of table I suggest that the fracture of the Composition B is occuring within the TNT of the Composition B.

TABLE I TNT columnar grains in Composition B atomic force microscopy scans

Scan size (μm)	TNT columnar grains	Width (μm)	Height (nm)
2.0	2	1	60–300
4.0	4	1	50–300
8.0	5	1–2	100–300
13.6	7	1–2	100–300

Ultimately such knowledge can lead to better formulations of these materials that might result in less sensitive energetic materials.

We have introduced AFM techniques to characterize the fracture surface topography of Composition B obtained at high acceleration. Using AFM we have measured the size of the columnar TNT grains of Composition B and have determined that the fracture of the Composition B occurs within the TNT.

Acknowledgments: We thank Dr. S.A. Mogren, Columbia, MD for assistance in obtaining the AFM scans.

References

1. Chick MC, Connick W, Thorpe BW: Microscope observations of TNT crystallisation. *J Crystal Growth*, 7, 317–326 (1970)
2. Lanzerotti YD, Sharma J: Brittle behavior of explosives during high acceleration. *App Phys Lett*, 39, 455–457 (1981)
3. Smith DL, Thorpe RW: Fracture in the high explosive RDX/TNT, *J Mat Sci*, 8, 757–759 (1973)

Interactions between cells and the extracellular matrix: The role of chemical versus topographical signals in muscle development

M.A. LAWSON, S. MOSLER, * S. ARNESEN,
N. GADEGAARD,* N.B. LARSEN,* P.P. PURSLOW

Department of Dairy and Food Science, Royal Veterinary and Agricultural University, Frederiksberg; *Condensed Matter Physics and Chemistry Department, Risø National Laboratory, Roskilde, Denmark.

Background and Objectives

Cells respond to a variety of cues from their environment, which can include chemical, mechanical, and topographical signals. The differentiation of myoblasts requires a combination of signals. It is well documented that myoblast fusion is strongly influenced by the chemical nature of the surrounding matrix and can be affected by mechanical stimulation. Studies have additionally shown that a

large variety of cell types are also influenced by surface topography of a substrate.[1] There is evidence[2] that cells can recognize and interact with surface topographies as small as 30 nm.

Cells grown on a collagen-coated surface differentiate more readily than those grown in the absence of the extracellular matrix protein.[3] It is not known whether the effects of myoblast interaction with collagen are due solely to chemical interactions. The 67 nm periodicity of collagen fibers may also provide topographical signals that affect the growth and differentiation of myoblasts during the development process.

The purpose of this study was to investigate the behavior of myoblasts on biologically relevant collagenous surfaces with identical chemical characteristics but varying topography.

Materials and Methods

C2C12 murine myoblasts (ATCC, Gaithersburg, MD) were cultured on surfaces coated with 100 µm molecular collagen I or 20 ng/mm″ fibrous collagen I. Cells were stained with rhodamine phalloidin and DAPI for adhesion spreading and proliferation assays. Images were obtained using a Leica DmiRB inverted microscope (Leica, Herlev, DK) coupled with an Image Pro Plus digital image analysis system (Image House, Copenhagen, DK). For further morphological analysis, AFM images were obtained using a Digital Instruments Dimension 3000 operating in tapping mode. Images were recorded using super sharp silicon cantilevers (Nanosensors, Wetzlar, Germany). Scanning proceeded at a rate of 0.5 lines/s with a sampling density of 512 × 512 points/image. Height image is supplemented with 20% artificial illumination. For detection of adhesion plaques, cells were immunostained using an anti-talin primary antibody (Sigma, ST. Louis, MO) followed by a fluorescently labeled secondary antibody. Images were obtained using a Leica TCS scanning confocal microscope. All micrographs were prepared using Adobe Photoshop (San Jose, CA). Differentiation of myoblasts was determined using a creatine phosphokinase activity assay, as per manufacturers instructions (Sigma, St Louis, MO).

Results

Our results indicate that myoblasts can recognize and react to the specific topography of collagen fibres. As seen by atomic force microscopy and scanning confocal microscopy, myoblasts spread more quickly and completely on fibrous collagen-coated surfaces. Numerous cellular processes can be seen attaching and extending along collagen fibers and the ends of these processes attaching directly to individual fibers using integrin-containing focal adhesion complexes. This increased spreading leads to both stronger adhesion to the fibrous surface and an increase in cellular proliferation. These differences do not lead to an increase in myoblast differentiation however. Our data indicates that topographical signals play a role in early muscle development, but that other signaling pathways regulate myoblast differentiation.

Conclusions

Our results show that cells plated on fibrous collagen surfaces exhibit a more spread morphology with numerous small surface filopodia. Cells adhere to, and spread on, fibrous collagen surfaces more readily than molecular collagen surfaces. Interactions of cells with fibrous collagen lead to higher proliferation rates than interactions with molecular collagen. The differences seen in the interactions of cells with fibrous collagen do not lead to significant differences in cell differentiation rates. Therefore, cells recognize and react to the surface topography of collagen fibers, but these topographical signals do not lead to large differences in cell differentiation.

References

1. Clark P, Connolly P, Curtis AS, Dow JA, Wilkinson CD: Cell guidance by ultrafine topography in vitro. *J Cell Sci* 99, 73–77, (1991)
2. Wojciak-Stothard B, Curtis A, Monaghan W, MacDonald K, Wilkinson C: Guidance and activation of murine macrophages by nanometric scale topography. *Exp Cell Res* 223, 426–435, (1996)
3. Swandison S, Mayne R: In vitro attachment of skeletal muscle fibers to a collagen gel duplicates the structure of the myotendenous junction. *Exp Cell Res* 193, 227–231, (1991)

Endothelial transport in fast and slow twitch muscles

T.G. MANFREDI, A.C. COMAS*

University of Rhode Island, Kingston, RI; *University of Connecticut, Allied Health Professions, Storrs, CT , USA

Endothelial permeability is modulated by the fusion of vesicles into clusters, which may act as transendothelial channels. Vesicle numbers are tissue-specific and are controlled by acute environmental changes[1]. Ultrastructural alterations associated with vesicle fusion leading to transendothelial channels can increase the capillary endothelial surface by a factor of 0.5 to 2.0. We reported that diet and exercise alter myocardial capillary ultrastructure in rats, in particular in the vesicle profiles[2].

It is well established that the oxidative capacity of fast and slow twitch muscle differs, however, no information exists regarding the capillary ultrastructure of these fiber types. The purpose of this study was to compare morpohometric profiles in capillary endothelium in response to anesthesia and electrical stimulation in two muscles of the rat hindlimb, the capillary enriched slow-twitch soleus as compared to the low oxidative fast-twitch plantaris. Twelve

Sprague-Dawley rats were divided into 3 groups: 1) rats programmed to 45 minutes of electrical stimulation, 2) rats under anesthesia for 45 minutes, and 3) a control group. Electron microscopic analysis of capillaries from anesthetized animals was slightly larger with thinner endothelium which occupied a larger percent of the total capillary area ($p < 0.01$). The size distributions of vesicles across and within treatments differed. Treatments had no effect on vesicle concentrations (vesicle numbers/unit of capillary area) or size. Vesicle concentrations were greater in soleus capillaries ($p<0.01$). Anesthesia and stimulation posed opposite effects on vesicle numbers/capillary in soleus and plantaris muscle ($p < 0.05$), suggesting that changes in vesicle concentrations within treatments reflect alterations in vesicle numbers and not size. We suggest that fast and slow twitch muscle synergists display unique capillary endothelial morphometric profiles and that vesicle fusion, diffusion distance, and endothelial surface area are postulated mechanisms associated with acute cell environmental changes.

References

1. Simionescu M, Simionescu N, Palade GE: Morphometric data on the endothelium of blood capillaries. *J Cell Bio*, 60:128–152 (1974)
2. Cosmas AC, Kernan K, Buck E, Fernhall B, Manfredi TG: Exercise and dietary cholesterol alter rat myocardial capillary ultrastructure. *Eur J Appl Physiol.* 75:62–67, (1997)

The effect of ingredients and process parameters on the microstructure and stability of starch-meat extrudates

C.I. Moraru, T.-C. Lee, M.V. Karwe, J.L.Kokini

Department of Food Science and Center for Advanced Food Technology, Rutgers University, New Brunswick, NJ, USA

The influence of meat type and preliminary thermal treatment on the microstructure, texture, and stability of intermediate extruded starch-meat extrudates was studied.

Food extrusion involves applying thermal and mechanical energy to food ingredients in a process of mixing and cooking. The idea of combining carbohydrates and meat proteins and producing nutritionally balanced snacks using extrusion recently gained a lot of interest, since it can provide the consumer with the necessary nutrients "in one bite." One of the challenging aspects of this application is obtaining a homogeneous matrix with acceptable and stable structure and texture, since proteins and carbohydrates are thermodynamically incompatible biopolymers, which both undergo detrimental changes during storage.

During extrusion, starch undergoes gelatinization (at m.c.>28–29%) and dextrinization (at m.c.<20%).[1] Application of heat and mechanical treatment to meat can lead to tissue disruption, protein extraction, and gelation, and consequently a heat set matrix forms, which entraps components like starch or fat.[2] During gelation, the salt soluble muscle proteins first suffer partial denaturation and then undergo aggregation, forming a gel network stabilized by disulfide bonds.[3–5] Several studies showed that denaturation of muscle protein prior to gelation results in weak gels, while Prabhu and Sebranek[6] found that, if myosin is gelled before being heated in the presence of starch, it prevents the uniform distribution of starch in the matrix.

In this study, intermediate moisture extrudates (moisture content of 28–30%w/w) were obtained by extruding mixtures of 55% potato granules, 40% ground beef (low fat and high fat), 2% salt, 1.5% sugar, and 1.5% spices. The mixtures were extruded using a ZSK-30 twin-screw extruder (Werner & Pfleiderer, Ramsey, NJ). The microstructure of the extrudates was analyzed using a scanning electron microscope (SEM) (JEOL, JSM 35C, Tokyo, Japan) at 15 kV. The textural changes of the extrudates during storage were monitored by small amplitude mechanical measurements using RSA II and ARES (Rheometrics Scientific) and large

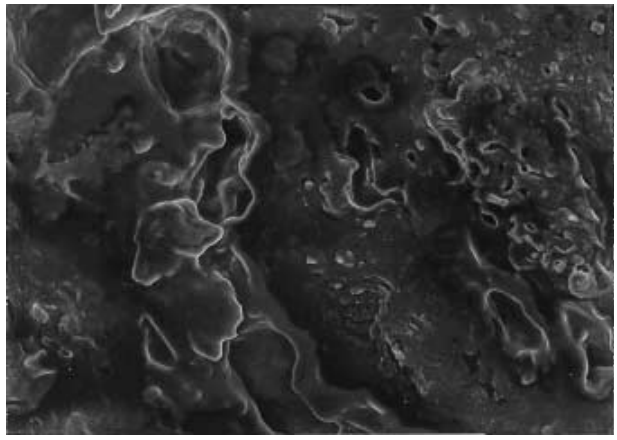

Fig. 1 Cross-section of extrudate obtained from starch-low fat raw meat mixtures.

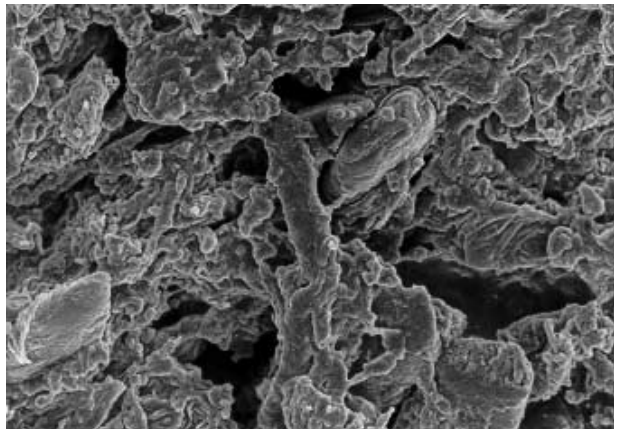

Fig. 2 Cross-section of extrudate obtained from starch-low fat precooked meat mixtures.

amplitude measurements with a TAXT2 texture analyzer (Texture Technologies Corp., Scarsdale, NY).

The use of raw meat led to meat-like extrudates with a homogeneous microstructure (Fig.1), less prone to toughening during storage. This uniform matrix resulted from the interaction of the denatured, gelated meat proteins with the gelatinized starch. Using precooked meat in the formulation led to a heterogeneous microstructure, where myofibrils, fat inclusions, and other components were entrapped in a disrupted protein matrix (Fig.2).

Sample toughening during storage, caused mainly by starch retrogradation, was more pronounced for the precooked than for the raw meat extrudates. Structural changes that occurred during storage were observed by SEM. A high fat content of meat led to discontinuities during extrusion and fat separation. When 1% glycerol was added to the matrix obtained with precooked meat, the microstructure became homogeneous and samples became softer due to the plasticizing effect of glycerol.

In conclusion, intermediate moisture extrudates obtained from potato granules-raw meat mixtures have better sensory characteristics, microstructure, and more stable texture than extrudates obtained from potato granules-precooked meat mixtures. High fat content can result in problems during extrusion and in fat separation, which is detrimental for the product quality and stability.

References

1. Gomez MH, Aguilera JM. A physicochemical model for extrusion of corn starch. *J Food Sci* 49, 1, 40–43,63 (1984)
2. Alvarez VB, Smith DM, Flegler S: Effect of extruder die temperature on texture and microstructure of restructured mechanically deboned chicken and corn starch. *Food Struct* 10, 153–160 (1991)
3. Smith DM: Meat proteins: Functional properties in comminuted meat products. *Food Technol* 42, 4, 116 (1988)
4. Fennema O: *Food Chemistry.* Marcel Dekker, Inc., New York (1996) 191–204
5. Matsumura Y, Mori T: Gelation. In *Methods of Testing Protein Functionality,* (Ed. GM Hall). Blackie Academic Professional, London (1996 **)** 76–109
6. Prabhu GA, Sebranek JG: Quality characteristics of ham formulated with modified corn starch and kappa-carageenan. *J Food Sci* 62, 1, 198 (1997)

Colour cathodoluminescence of europium-and terbium-activated calcium tungstate phosphors

T.A. NAZAROVA, M.V. NAZAROV, G.V. SAPARIN*, S.K. OBYDEN, * P.V. IVANNIKOV,* E.J. POPOVICI,† F. FORGACIU

Institute of Applied Physics, Moldova; *Moscow State University, Russia; †Institute of Chemistry, Cluj-Napoca, Romania

Colour cathodoluminescence (CCL) mode that is incorporated into scanning electron microscopy (SEM) obviously gives both spectral and spatial information with high resolution and is a very informative SEM-mode of operation[1]. It has been shown that the use of colour contrast increases the amount information on the colour image in comparison with its black-and-white counterpart by about two orders of magnitude. Earlier we have used the CCL-SEM for a complex characterisation of different organic, dielectric, and semiconductor luminescent materials. Here we describe some applications of the CCL-SEM examination of calcium tungstate phosphors in powder form. We investigated samples, activated with different rare earth (RE) elements: $CaWO_4$:Eu^{3+}, $CaWO_4$:Tb^{3+} and self-activated $CaWO_4$:W. The line dimension of each particle (~50 μm) prevailed over an electron beam diameter as well as electron scattering volume.

To reveal the spectral composition and its variations with an RE activator, the photoluminescence (PL) spectra were taken from the above-mentioned self-activated calcium tungstate phosphors. Depending on the activator ion nature, RE concentration, and incorporation degree, various partial emission bands were observed in the total spectra. The characteristic blue emission observed at 400 nm is related to some tetrahedral WO_4 groups of the scheelite host lattice.[2] The specific green emission band at 545 nm can be attributed to the electronic transition inside the Tb-centre. Comparison of the spectra taken from different samples shows that efficiency of the gree PL emission increases with the Tb-activator concentration. The PL spectrum taken from $CaWO_4$: Eu^{3+} exhibits a specific red emission band at 615 nm, which can be attributed to charge transfer in the Eu^{3+} -O centre. However, because of the great generation volume of PL, the PL spectrum could not be correlated with a definite point on the surface under study. PL-spectra give, therefore, only spectral information about the role of activators in the PL and do not reveal any spatial distribution of the activator on the surface of the samples.

Spatial distributions of the blue, green, and red luminescence, attributed, respectively, to WO_4,-group, Tb-, and Eu^{3+}-O centres, were recorded in a form of the CCL-SEM maps. The panchromatic CCL-SEM map represents a spatial distribution of all the luminescent centers responsible for luminescence in visible spectral range (400–800 nm). Spatial distributions of the blue, green, and red luminescence partial bands of the total spectrum were mapped by using the monochromatic CCL maps taken at 480, 540, and 600 nm. An image analysis of the CCL-SEM maps taken from the powders must account the peculiarities of CL contrast, which have not been observed in the maps for solid specimens. In the case of powders, the main artifacts are topographic contrast (aureoles) and the mixed CL spectrum displayed by particles in contact. Some of the powders were pressed into tablets. In tablets, distances between particles of powder are minimal and the main artifacts, therefore, are aureoles at the perimeters of tablets. The CL from the central region of each tablet may be considered as a true CL. It has been shown that the spectral compositions of the true CL depend on the type of activators. For exam-

ple, the tablets activated with Tb^{3+} emit mainly blue and green light that corresponds to the intensive partial peaks in the short-wavelength spectral range. But the CCL-map of the Eu-activated calcium tungstate phosphors is multicolour that can be attributed to several partial peaks at both the short-wavelength and long-wavelength spectral ranges. Hence, incorporation of the Eu^{3+} ion into the $CaWO_4$ host lattice creates more defect states than incorporation of the Tb^{3+} ion. The monochromatic maps reveal that the surface of the Eu-activated calcium tungstate phosphors gives intensive CL emission at three partial bands: blue, green, and red. This wide CL emission spectrum can be attributed to three different surface imperfections related to incorporation of Eu^{3+}.

The CCL-SEM method revealed that similar luminescent materials are nonhomogeneous and possess a variable incorporation degree of the RE ions into the crystalline host lattice. The contribution of the host lattice emission to the apparent luminescence could be also put in evidence. The CL-images obtained in SEM in real colours can be used for a rapid examination of spatial and spectral characteristics of powder materials, produced by different technologies.

References

1. Saparin GV, Obyden SK: Colour in the microword: Real colour cathodoluminescence mode in scanning electron microscopy. *European Microsc Anal*, 7–9 (1993)
2. Grasser R, Scharmann: The optical properties of extrinsic anionic oxo-Ccomplexis in tungstates. *Phys Status*, (a) 130, K99–K105 (1990)

Effects of elevated CO_2 on canopy carbon sequestration, leaf stomatal density, and gas exchange of *quercus shumardii* and *liquidambar styraciflua*

Z.H. NING, K.K. ABDOLLAHI

Urban Forestry Program, Division of Agricultural Sciences, College of Agricultural, Family and Consumer Sciences, Southern University and A&M College, Baton Rouge, LA, USA

Introduction

National programs to plant and steward trees in U.S. cities are estimated to reduce annual CO_2 emissions by 0.5 to 0.2%.[1] Carbon storage by trees in urban forests nationally has been estimated between 660 and 990 million tons.[2] Carbon storage in individual urban forests ranges between 145,800 tons in Oakland and 854,800 tons in Chicago.[3] Many reports have detailed the effects of elevated CO_2 on growth and carbon sequestration of a variety of woody plants.[4] Dry mass increases induced by elevated CO_2 are often accompanied by increasing in net assimilation rate, at least in the short term.[5]

This paper reports some of the results of a research project aimed to assess CO_2 sequestration capacity of urban tree species in response to elevated atmospheric CO_2.

Materials and Methods

One-year-old Shumard oaks (*quercus shumardii*) and Sweetgums (*liquidambar styraciflua*) were grown for 12 months in climate-controlled environmental growth chambers at ambient (350 vpm) or elevated (700 vpm) CO_2 conditions. Net CO_2 uptake rates (Pn), transpiration (Tr), and leaf conductance to water vapor were measured during the growing season using a portable gas exchange system (Ciras-1, PP Systems, Hitchin, UK). During measurements, PPFD was supplemented to ensure saturation of Pn (> 600 $\mu mol\ m^{-2}\ s^{-1}$). A minimum of 10 plants, with three leaves of similar physiologic age per plant, were used for each measurement.

Total dry mass was quantified for leaves and stems (canopy biomass). Samples from each 20 plants were dried at 80°C to constant weight. Carbon sequestration was calculated based on the reported relation between biomass and carbon sequestration. Total plant leaf area and mean individual leaf area were measured with a leaf area meter

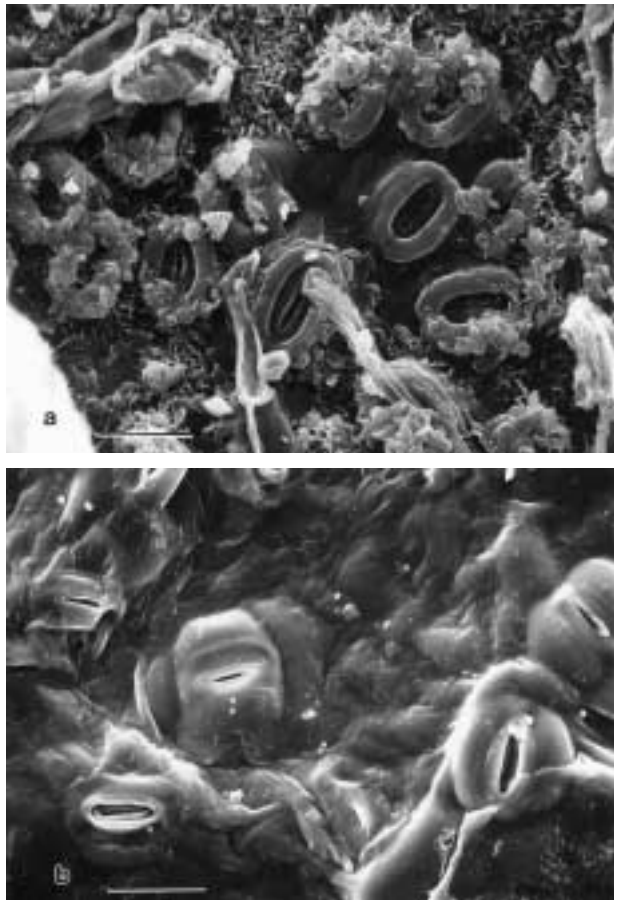

FIG. 1 Leaf lower surface shows stomates. (a) Shumard oak, (b) Sweetgum. Bar=20 um.

TABLE 1 Gas exchange, CO_2 sequestration, and carbon storage of Shumard oak and Sweetgum for elevated CO_2 and ambient growth conditions

	Net CO_2 uptake (Pn) $\mu mol\ m^{-2}\ s^{-1}$		Transpiration (Tr) $mmol\ m^{-2}\ s^{-1}$		Leaf conductance $mmol\ m^{-2}\ s^{-1}$		Canopy biomass Shoot + leaves (g)	
	Amb	Elev	Amb	Elev	Amb	Elev	Amb	Elev
Quercus	6.2	16.8[a]	1.4	1.6	104.5	110.0	25.0	72.8[a]
Liquidambar	5.5	11.5[a]	0.85	1.1	92.6	102.2	17.2	33.0[a]

[a] Significant differences between measurements at elevated (Elev) and measurements at ambient (Amb) CO_2, a=0.001.

(Model LI-3050A, Li-Cor, Inc., Lincoln, Nebr., USA) on 10 leaves from each of ten Shumard oaks and 10 Sweetgums.

Stomatal density per unit area was quantified from epidermal impressions of the leaf surface using silicon-based dental product (Provil M, Bayer, Lever Kusen, Germany). Positive impressions were made with nail varnish and viewed with a light microscope. In addition, leaves were examined under a scanning electron microscope for stomatal morphology and distribution.

Results

Gas exchange and canopy biomass production of 1-year-old Shumard oaks and Sweetgums were measured during 12 months of growth in climate-controlled environmental growth chambers at ambient (350 vpm) or elevated (700 vpm) CO_2. In both species, the elevated CO_2 treatment increased the PPFD-saturated rate of net CO_2 uptake (CO_2 sequestration) and dry matter production (carbon sequestration) (Table I). After 12 months at elevated CO_2, Shumard oaks showed significant increase in combined leaf and stem biomass (191%). Similarly, after 12 months of growth at elevated CO_2, combined leaf and stem biomass of Sweetgum increased by (92%). Exposure to elevated CO_2 for 12 months resulted in increased mean leaf area in both species and increased stomatal density (Fig. 1).

References

1. McPherson EG: Urban forests and climate change. In (Eds. Abdollahi KK, Ning ZH, Appeaning A). *Global Climate Change and the Urban Forest*. GCRCC and Franklin Press, Inc. Baton Rouge, La, USA, 17–30 (2000)
2. Nowak DJ: Atmospheric carbon dioxide reduction by Chicago's urban forest. In (Eds. McPherson EG, Nowak DJ, Rowentree RA. *Chicago's Urban Forest Ecosystem*: *Results of the Chicago Urban Forest Climate Project.* USDA Forest Service General Technical Report NE-186, Radnor, Pa. (1994c) 3–18, 140–164
3. Nowak DJ: The interactions between urban forests and global climate change. In (Eds. Abdollahi KK, Ning ZH, Appeaning A) *Global Climate Change and The Urban Forest.* GCRCC and Franklin Press, Inc. Baton Rouge, La, USA, (2000) 31–44
4. Atkinson CJ: Global changes in atmospheric carbon dioxide: The influence on terrestrial vegetation. In *Plant Response to Air Pollution.* (Eds. Iqbal M, Yumus M) John Wiley and Sons Ltd., Sussex, UK, (1996) 99–133
5. Long SP: Modification of the response of photosynthesis productivity to rising temperature by atmospheric CO_2 concentrations. *Plant Cell Environ* 14, 729–739 (1991)

Comparative study of pyrocarbon microstructure by atomic force, transmission electron, and polarized light microscopy

A. PFRANG, B. REZNIK,* T. SCHIMMEL, D. GERTHSEN*

Institut für Angewandte Physik and *Laboratorium für Elektronenmikroskopie, Karlsruhe University, Karlsruhe, Germany

Carbon-carbon composites are currently used in break assemblies because of their high wear and corrosion resistance. Pyrolytic carbon (pyrocarbon) obtained by thermal decomposition of methane is one of the attractive matrix materials. The pyrocarbon microstructure is related to the conditions of methane pyrolysis and takes a number of graphite-like forms, ranging continuously from the near amorphous-like to the highly crystalline state. The deposited carbon layers exhibit preferential orientations (textures) parallel to the substrate surface.[1,2] The arising structural anisotropy strongly influences mechanical properties of pyrocarbon-based materials.[3] However, the relationship between deposition conditions and pyrocarbon microstructure is not fully understood. For this reason, intensive attempts must be taken for the characterization of the structural organization in pyrocarbon.

In the present study, the structural anisotropy of pyrocarbon matrix layers in composites obtained by chemical vapor infiltration of carbon fiber felts was comparatively studied by atomic force microscopy (AFM), transmission electron microscopy (TEM), and polarized light microscopy (PLM). The influence of mechanical polishing and ion etching on pyrocarbon with different textures is investigated. The AFM surface topography of the ion-etched samples is compared with TEM image amplitude contrast and corresponding electron diffraction patterns, as well as with polarized light microscopy. It is shown that the roughness value R_q correlates with the amplitude contrast variations, radial broadening of the carbon 002 reflections, and extinction angles. Moreover, height differences extracted from AFM cross sections are in good accordance with the variation of mass density in pyrocarbon. The results of the present study indicate that the combination of AFM, TEM, and PLM provides a means for the correlatoin of pyrocarbon texture, mass density, and micromechanical behavior, and therefore allows a deeper understanding and interpretation of the complex pyrocarbon microstructure.

References

1. Reznik B, Gerthsen D, Hüttinger KJ: *Carbon* 39, 2, 215–229 (2001)
2. Pfrang A, Yalman I, Gliemann H, Schimmel T, Hüttinger KJ: *Carbon* (submitted)
3. Reznik B, Guellali M, Gerthsen D, Oberacker R, Hoffmann MJ: *Mater Lett* (submitted)

Microstructural characterization of serra cheese using low-vacuum scanning electron microscopy

P.J.M. REIS, F.X. MALCATA

Escola Superior Biotecnologia, Universidade Católica Portuguesa, Porto, Portugal

Serra cheese is the most important variety of traditional Portuguese cheeses made from raw ewes' milk without added starter culture[1] so it has been the subject of extensive research in the past.

In this study, Serra cheese fractured samples were directly observed (without conductive material such a gold or carbon) using a low-vacuum scanning electron microscope (LV-SEM). The test cheeses were manufactured in three different dairy farms, and pieces of those cheeses were stored in formal saline[2] dehydrated in an ethanol series, and used directly for observation.

As a result of this method (which was applied to this cheese for the first time), the microstructure of Serra cheese could be observed at > 250× magnification, and the fine microstructure of such micro-organisms as bacteria and yeasts could be resolved at 2000×. The microstructure of cheeses from the various dairy farms unfolded protein matrices with voids spaces through the protein network, but no apparent microstructural differences could be detected between samples.

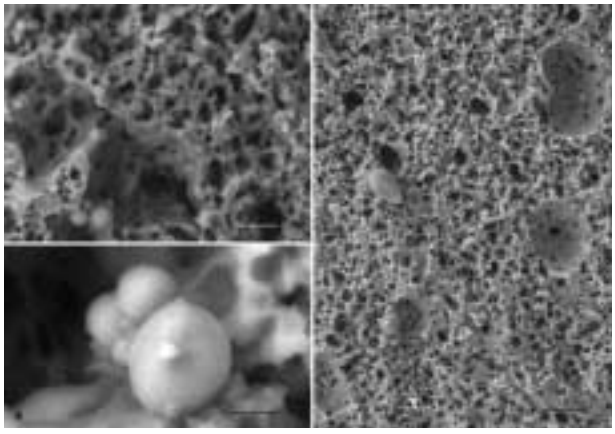

FIG. 1 Low-vacuum scanning electron micrographs of sections through inner region of Serra cheese. (a) Colonies of spherical yeast cells, scale bar = 15 µm. (b) Part of colony of yeast cells, scale bar = 5 µm. (c) Elongated and spherical yeast cells within the casein curd, scale bar = 25 µm.

References

1. Dean MR, Berridge NJ, Mabbitt LA: Microscopical observations on cheddar cheese and curd. *J Dairy Res* 26, 77–82 (1959)
2. Macedo AC, Malcata FX, Oliveira JC: The technology, chemistry, and microbiology of Serra cheese: A review. *J Dairy Sci* 76, 1725–1739 (1993)

Quantitative analytical electron microscopy of calcium in hypomineralized amelogenesis imperfecta

M.C. SÁNCHEZ-QUEVEDO, G. CEBALLOS,[*]
J.M. GARCÍA, M.E.G. GÓMEZ DE FERRARIS,[†]
I.A. RODRÍGUEZ,[†] A. CAMPOS

Departamento de Histología, Facultad de Medicina y Odontología, Universidad de Granada; [*]Servicio de Estomatología, Hospital Clínico Universitario, Universidad de Granada, Spain; [†]Cátedra de Histología y Embriología, Facultad de Odontología, Universidad Nacional de Córdoba, Córdoba, Argentina

Amelogenesis imperfecta (AI) identifies a group of hereditary alterations that affect the formation of enamel extracellular matrix.[1] This disorder is classified into 14 subgroups according to characteristics of the enamel, clinical appearance, and Mendelian mode of inheritance (autosomal dominant or recessive, and sex-linked dominant or recessive). We used scanning electron microscopy (SEM) and X-ray microprobe analysis (EPMA) to establish morphological patterns in the enamel and the concentration of calcium in enamel and dentine in canine and premolar teeth from patients clinically and genetically diagnosed as having AI.

Five normal canine and premolar and five of each with AI were immersed in Freon 22-cooled liquid nitrogen, freeze-dried, carbon-coated and examined in a Philips XL30 microscope with an EDAX DX-4 microanalytical system. Ten analyses were done for each tooth (200 measurements). Spectra were collected by pin-point electron beam at 40000x. The peak-to-background (P/B) ratio method[2,3] was used to measure the concentration.

Microscrystalline salt standards were used to quantify calcium.[4-5] The elemental weight percent (WP) of each salt standard was calculated as reported in previous publications.[6–7] Morphological study specimens were gold coated after EPMA analysis and examined by SEM.

One of the most characteristic features of AI that SEM detects is anomalous patterns, such as a decussate or superimposed filamentous pattern or an arcade-shaped outline.

Quantitative histochemical data expressed as WP showed that Ca concentration in teeth with AI was 31.59 ± 3.17 and 31.87 ± 3.86 in enamel and dentine of canine, and 32.92 ± 3.10 and 33.38 ± 3.23 in enamel and dentine of premolars. Quantitative histochemical data expressed as WP showed that Ca concentration in normal teeth was 30.19 ± 1.44 and 24.93 ± 1.41 in enamel and dentine of canine, and

31.16 ± 2.24 and 24.84 ± 1.94 in enamel and dentine of premolars. There were no differences in calcium WP of enamel between teeth affected by AI and control teeth. In contrast, there were significant differences in dentine calcium WP between canines and premolars in AI with control values. These results showed similar patterns of calcification in both types of teeth, suggesting that the biological mechanisms of the calcification are not altered in enamel. However, the calcification pattern of dentine did show significant differences between teeth with AI and control samples. Morphological study and EPMA showed that AI causes morphological alterations in enamel, with evident signs of immaturity in differentiation. However, these morphological changes were not accompanied by mineralization alterations in enamel with AI. In contrast, although the microscopical pattern in dentine was normal, WP was higher in both canines and premolars with AI.

Acknowledgments: This work is supported by PB97-0840 and AECI/98-00.

References

1. Dong J, Gu TT, Simmons D, MacDougall M: Enamelin maps to human chromosome 4q21 within the autosomal dominant amelogenesis imperfecta locus. *Eur J Oral Sci* 108, 353–358 (2000)
2. Small JA, Heinrich KFJ, Newbury DE, Myklebust RL: Progress in the development of the peak-to-background method for the quantitative analysis of single particles with the electron probe. *Scan Electron Microsc* II, 807–816 (1979)
3. Statham PJ, Pawley JB: A new method for particle x-ray microanalysis on peak to background measurements. *Scan Electron Microsc* 1, 469–478 (1978)
4. López-Escámez JA, Campos A: Standards for x-ray microanalysis of calcified structures. *Scan Electron Microsc* 8, 171–185 (1994)
5. Sánchez-Quevedo MC, Nieto-Albano OH, García JM, Gómez de Ferraris ME, Campos A: Electron probe microanalysis of permanent human enamel and dentine. A methodological and quantitative study. *Histol Histopathol* 13, 109–113 (1998)
6. Warley A, Gupta BL: *Quantitative Biological X-ray Microanalysis. Electron Microscopy of Tissues, Cells and Organelles: A Practical Approach.* (Ed. JR Harris) IRL Oxford University Press. Oxford, (1991) 243–281
7. Warley A: *X-Ray Microanalysis for Biologists.* Portland Press, London (Ed. Glauert AM) (1997) 203–246

Interactions between azoxystrobin and *Puccinia recondita*, *Erysiphe graminis*, and *Botrytis cinerea* on the microscale

S.R. SWIFT, C.A. HART,* D.W. BARTLETT,* N.D. READ

Institute of Cell and Molecular Biology, University of Edinburgh, Edinburgh; *Syngenta, Jealott's Hill International Research Station, Bracknell, Berks, UK

Fungicides are essential for the control of a wide range of economically significant fungal diseases on crop plants. The strobilurins are a family of novel, broad-spectrum fungicides that exhibit activity through the inhibition of mitochondrial electron transport at the cytochrome bc_1 complex. Azoxystrobin, a strobilurin marketed by Syngenta, is xylem systemic and has no phloem mobility or vapour phase effects.[1]

Fungicide discovery and development typically rely on large-scale, high- throughput studies to assess the biological activity of novel fungicides and new formulations. Although the scanning electron microscope (SEM) is commonly employed to study formulation deposits on crop leaf surfaces and gross effects on fungal development, the interactions between these deposits and their target organism in the infection microarena are rarely examined.

Scanning electron microscopy studies of deposits from 0.2 µl droplets of azoxystrobin formulation on wheat leaves have shown that within 30 min of contact with the leaf surface, a zone of inhibition approximately 100 µm around the deposit edge is established in all directions within which fungal spores are inhibited from germinating (Fig. 1); between 3 and 5 days spores landing between 2 and 3 mm basipetally to the deposit edge have not germinated, and development of established colonies has been arrested; after 5–7 days these effects are observed at distances of up to 5 mm basipetally to the deposit edge; and acropetally, azoxystrobin displays biological activity at >70 mm from the deposit after 3 days.

Rates of azoxystrobin translocation and its effects on target organisms have been visualised using SEM and microphosphor imaging techniques.

Despite the importance of fungicides to global agriculture and pharmaceuticals, little is known about their uptake into fungal cells. Although passive uptake mechanisms are certainly important, active mechanisms, such as endocytosis, may provide a crucial pathway for the uptake of

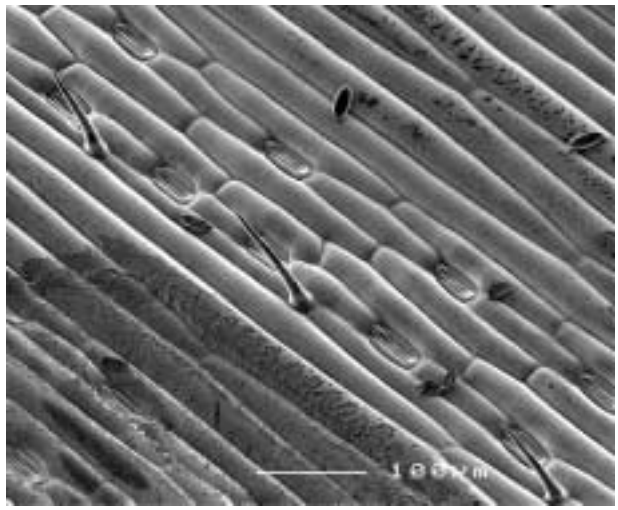

FIG. 1 Scanning electron microscopy image showing ~100 µm zone of inhibition of *Erysiphe graminis* germination around 1250 ppm azoxystrobin deposit (3 h post inoculation).

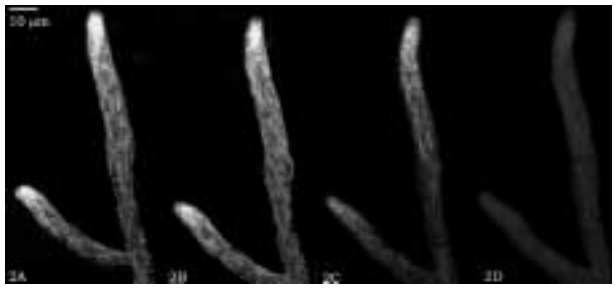

FIG. 2 Confocal laser scanning microscopy image showing decrease in fluorescence of the potentiometric probe Rhodamine 123 in mitochondria of *Botrytis cinerea*, following exposure to 5 ppm azoxystrobin solution: (a) 20 s before treatment; (b) 0 s after treatment; (c) 20 s after treatment; (d) 40 s after treatment.

some fungicidal molecules for subsequent delivery to their sites of activity.

Azoxystrobin must traverse the cell wall, plasma membrane, and both mitochondrial membranes before reaching its target site in the mitochondrial respiratory chain. Relatively little is understood about mitochondrial physiology in living fungal cells. We have explored the morphology, distribution, and organisation of mitochondria in several filamentous fungi using vital fluorescent probes in conjunction with confocal microscopy. Furthermore, we have developed an assay for mitochondrial activity using vital potentiometric markers.

Fungi exhibit highly polarised growth involving localised secretion and cell wall synthesis at the hyphal tip. The energy requirements for this region of the hypha must be considerable, particularly in species exhibiting high growth rates.[3] Hyphal staining with mitochondrion-selective vital fluorescent probes reveals a concentration of elongated mitochondria at the hyphal tip. The maintenance of a transmembrane proton electrochemical gradient is required for ATP production; small depolarisations of membrane potential can alter ATP production significantly.[2] Staining with vital potentiometric probes (whose fluorescence is variably dependent on membrane potential) demonstrates that mitochondria within this tip region are more active than those in subapical regions (Fig. 2).

Here we describe the variety and importance of techniques including low-temperature SEM, ambient-temperature SEM, microphosphorimaging, and confocal laser scanning microscopy in providing insight into the interactions between azoxystrobin and the pathogens *Puccinia recondita, Erysiphe graminis,* and *Botrytis cinerea* on the microscale, which support the conclusions outlined above.

References

1. Clough JM, De Fraine, PJ, Godfrey CRA, Rees, SB: Strobilurin analogues as inhibitors of mitochondrial respiration in fungi. In *Antiinfectives, Recent Advances in Chemistry and Structure-Activity Relationships*. (Eds. Bentley PH, O'Hanlon, PJ). Royal Society of Chemistry (1997) 176–179
2. Zoratti M, Pietrobon D, Azzone GF: On the relative relationship between rate of ATP synthesis and H^+ electrochemical gradient in rat-liver mitochondria. *Eur J Biochem* 126, 443–451(1982)
3. Bracker CE, Morre DJ, Grove SN: Laser microbeam manipulation of cell morphogenesis in growing fungal hyphae. *Int Soc Opt Engin* 2983, 67–80 (1997)

Electron backscattered diffraction on platinum corrosion

C. VIERRETHER, C. CLICK

University of Missouri at Rolla, Rolla, MO, USA

Optical glass is melted in platinum or platinum-lined crucibles to obtain homogeneity and batch-to-batch reproducibility. In addition, oxidizing gasses such as Cl_2 and O_2, are often bubbled through melts to remove residual water, to influence the redox equilibrium in the melt, and to homogenize the melt. Platinum is traditionally considered an inert metal and resistant to corrosion.[1] However, studies have shown that pits and striations are a product of Pt-Rh alloy corrosion during fused quartz melts at 1300°C.[2] Current experiments with 30 $Mg/10Al_2O_3/60P_2O_5$ melts at 1400°C produced similar grain textures on the platium crucible. Electron backscattered diffraction was used to determine the orientation and/ or misorientation of these altered grains.

References

1. Pecoraro GA, Franz H, Mackenzie JD: Corrosion of refractory metals by molten oxides. PPG Industries, University of California; *Glass Industry,* 454–458 (1970)
2. Chou TC, Mishra A, Anderson D: Loss of precious metals from Pt-Rh alloy under refractory oxide environments research and development. Englehard Corporation, Edison, New Jersey. *J Mat Sci,* V 25, 5, 2562–2568 (1990)

Microscopic examination of the development of *Onchocerca volvulus* (filarioidea: Onchocercidae) in the west African black fly, *Simulium yahense* (diptera: Simuliidae)

W.P. WERGIN, M. TRPIS,* C.A. MURPHY

Nematology Laboratory, Agricultural Research Service, U. S. Department of Agriculture, Beltsville, MD; *Department of Molecular Microbiology and Immunology, School of Hygiene and Public Health, John Hopkins University, Baltimore, MD, USA

River blindness, also known as onchocerciasis, is a tropical disease that is prevalent in humans in many areas of Africa and South America. The disease is caused by a parasitic nematode known as *Onchocerca volvulus*. This nematode is spread by black flies (*Simulium yahense*) that transmit the parasite to humans. Humans, who serve as the

host for the maturing stages of the nematode, eventually become blind because of the infection with this parasite. Scientists are attempting to develop a vaccine for this disease but must have additional information about how the nematodes develop and how they are transmitted. The current study uses Nomarski interference light microscopy and scanning electron microscopy (SEM) to view and document the development of the nematode in the black fly and to illustrate how the fly might transmit this parasite to humans.

Black flies (*S. yahense*) were fed on volunteers infected with *O. volvulus* microfilariae and then reared in the insectary of the Liberian Institute for Biomedical Research, Liberia. The infected flies were sampled and dissected to recover *O. volvulus* larvae, which were examined and measured by light microscopy. Other samples of infected flies were cryopreserved, shipped to the U.S., and revived by thawing and removing the cryoprotectant. The larval development of *O. volvulus* was photographed by Nomarski interference light microscopy and by SEM. From the examined material, the developmental times and the changes in larval morphology from microfilaria to infective larvae were determined. Observations of the larval morphology and organogenesis were concentrated primarily on the cephalic and caudal regions of the developing larvae.

Results indicated that the first, second, and third stage larvae of the nematode developed and could be found in the black fly. The third stage larvae (L3) migrated from the thoracic muscle tissue into the celomic cavity by swimming in the hemolymph. They often penetrated fly organs such as the ovaries, the antennae, palps, and, most frequently, the brain. Perhaps the random wandering of L3 through the fly body is an effort to escape their host. The fly mouth is the most natural opening for these larvae to escape from the fly and to be transmitted to a human host. Whether chemical signals are released prior to fly feeding to assist this process is difficult to determine. However, if this is the case, the signal could assist the larvae in finding the site from which they could successfully escape and enter the human body.

The destructive potential of these larvae results in serious consequences for the host flies and their survival. When *O. vulvulus* reaches the third stage in the fly, which occurs at Day 7, the fly mortality rate increases sharply; less than 1% of the flies infected with third stage larvae survive to Day 10. These results, which show the different stages of development and when they occur, will be used by research groups that are attempting to develop a vaccine to prevent this disease.

Author Index